UNIVERSITÀ
DEGLI STUDI
DI PADOVA

Sede Amministrativa: Università degli Studi di Padova

Centro di Ateneo di Studi e Attività Spaziali “Giuseppe Colombo” (CISAS)

SCUOLA DI DOTTORATO DI RICERCA IN: SCIENZE TECNOLOGIE E MISURE SPAZIALI
INDIRIZZO: MISURE MECCANICHE PER L’INGEGNERIA E LO SPAZIO
CICLO XXVI

STUDY OF INNOVATIVE TECHNIQUES FOR STRUCTURAL HEALTH MONITORING

Direttore della Scuola : Ch.mo Prof. Giampiero Naletto

Coordinatore d’indirizzo: Ch.mo Prof. Stefano Debei

Supervisore : Ch.mo Prof. Ugo Galvanetto

Dottorando : Marco Thiene

Summary

This thesis aims at developing new methodologies to determine the structural integrity of aeronautical components. The increasing use of composite materials, which present damage initiation and evolution different from the homogeneous ones, requires the development of new techniques to determine the performance of the most critical components. Structural health monitoring (SHM) is a field of research which aims at developing new methods to perform this task. One of the main concerns is given by initially barely visible impact damage (BVID), which can grow during operational time and eventually lead to catastrophic failures. The monitoring can be accomplished both with active and passive methods. In this thesis the part of SHM which concerns the development of algorithms for damage and impact detection is addressed. First a damage detection approach based on the proper orthogonal decomposition (POD) is developed. Analyses on different components are performed, in particular detecting defects without needing any baseline. Particularly important is the application of the proposed approach to a stiffened panel, which has not been deeply analysed in literature. The second part of the thesis concerns impact detection and force reconstruction. In particular the attention is focused on large mass impacts, which can produce geometrical nonlinearities in the dynamics of the system. Finally a novel impact location algorithm, based on the POD is proposed. This represents a novelty in impact location algorithms, which have previously been focused on the triangulation method. In particular the proposed approach is not dependent on the wave velocity, which is a major limitation in the application of the triangulation on composite panels. Remarkable results are obtained in this thesis. In particular experimental verifications are performed on damage detection using only data coming from a damaged system and on force reconstruction on a composite panel.

Sommario

Numerosi fattori spingono l'industria aeronautica verso l'utilizzo di materiali innovativi da impiegare nelle struttutre dei veivoli. In particolare l'esigenza di contenere il consumo di carburante, con la conseguente riduzione dei costi e delle emissioni, ha portato allo sviluppo di nuovi aerei in cui una parte della struttura è da realizzata in materiali compositi; l'esempio più recente è rappresentato dal Boeing 787 Dreamliner in cui oltre il 50% della struttura è costituito da materiale composito.

Le elevate caratteristiche meccaniche di questi materiali sono tuttavia accompagnate da meccanismi di danneggiamento non ancora del tutto conosciuti. Questo fa sì che il loro utilizzo richieda un programma di manutenzione dedicato, che influisce in maniera considerevole sui costi di gestione del singolo veivolo. Per questo motivo la ricerca scientifica si è concentrata negli ultimi anni sullo sviluppo di nuove metodologie per monitorare l'integrità strutturale dei principali componenti dei veivoli. L'obbiettivo finale di questa ricerca è sviluppare un sistema di controllo che funzioni in tempo reale, che possa cioè individuare eventuali danni nella struttura mentre il veivolo è in volo. In questo modo non solo si potrebbero evitare catastrofici incidenti, ma anche limitare le manutenzioni programmate, che spesso risultano essere non necessarie in quanto la struttura potrebbe non presentare alcuna criticità. Il campo ingengeristico che si occupa di questa innovazione è definito structural health monitoring (SHM).

Dal punto di vista del rilevamento di un possible danno nella struttura, due differenti approcci possono essere seguiti. Il primo, chiamato attivo, richiede l'utilizzo di uno stimolo che ecciti la dinamica della struttura. Dalla risposta, raccolta mediante un certo numero di sensori, è possibile determinare se un danno è presente. Il secondo approccio, denominato passivo, non richiede alcuno stimolo, in quanto un'eventuale forzante esterna è proprio l'evento che si vuole monitorare; la tipica applicazione di questo metodo riguarda il montoraggio di impatti.

La ricerca svolta in questa tesi prevede lo studio di entrambi gli approcci. Nella prima parte, una tecnica attiva, basata sulla proper orthogonal decomposition (POD) e sul gapped smoothing method (GSM), è analizzata con lo scopo di localizzare un possibile danno all'interno di tipici componenti aeronautici. Diverse posizioni del danno sono analizzate. La principale innovazione consiste nello studio di un pannello rinforzato, che in letteratura non è mai stato trattato in dettaglio con metodi basati su forme modali. Nella seconda parte della tesi è studiato un metodo passivo. Sono trattati due casi: la ricostruzione della forza d'impatto e la localizzazione dello stesso. Nel primo caso il metodo sviluppato risulta in grado di predire correttamente la forza anche nel caso in cui la risposta del componente sia nonlineare. Nel secondo caso l'applicazione della POD per localizzare impatti rappresenta una novità nel relativo campo di ricerca.

La tesi è articolata nel modo seguente. Il primo capitolo fornisce un panorama generale sul perché il monitoraggio strutturale sia importante in ambito aeronautico. I Capitoli 2 e 3 introducono la formulazione matematica utilizzata per il rileamento del danno. Nel Capitolo 4 vengono presentati i risultati relativi all'individuazione del danno mediante POD e GSM. Nel Capitolo 5 si illustra la formulazione matematica relativa ai metodi passivi. In particolare sono descritti in dettaglio gli innovativi algoritmi utilizzati. Il Capitolo 6 presenta i risultati relativi al monitoraggio d'impatti. I miglioramenti rispetto ad approcci classici sono evidenziati in modo particolare . Nelle conclusioni vengono riproposti i principali risultati ottenuti nei capitoli precedenti. Alla fine della tesi numerose appendici approfondiscono alcuni argomenti che vengono parzialmente trattati nel corso dei vari capitoli.

Acknowledgements

During the last three years many things happened to me and lots of people shared part of their lives with mine. I will try to acknowledge all of them. If someone is missing, it is due to my lack of memory, not to his/her lack of credit.

First of all I want to express my deep gratitude to Professor Ugo Galvanetto for giving me the possibility to develop my research at the University of Padova and at Imperial College London. I feel honoured of having such a great person, under both professional and human point of view, as supervisor. It would be too long to list all the opportunities he gave me during my PhD.

I would like to thank Professor Ferri Aliabadi for giving me the possibility to work at the Department of Aeronautics, Imperial College London. I can definitely say that experience changed my life and substantially improved my skills as researcher.

I would like to thank my parents Gaetano and Marialuisa for all their support throughout my entire life. Obviously I could have never achieved this result without the passion for Research they have transmitted to me since I was just a child.

I would like also to thank my relatives for all their love and support: my sister Arianna, my brother Andrea, my grandparents, Cristiano and Rosa, my uncle Roberto, my lovely nieces, Vittoria and Isabella, and my brother-in-law Andrea. A special thank you to my Aunt Dada, who still loves and supports me from somewhere far away.

I would like to acknowledge for their precious advices Dr Zaccariotto, Dr Gherlone, Dr Ghajari, Dr Sharif, Dr Bacarreza and Dr Benedetti. Most of the problems I encountered were solved with their suggestions.

For all the moments of diversion during the everyday difficulties of a PhD student life, I would like to thank all my colleagues Teo, Daniele, Riccardo, Alessandro, Giuseppe, Gianluca, Beatrice, Giovanna, Nicolo', Maurizio, Francesco, Mattia, Marco and Frank.

Then finally friends come. I have met many people in these three years, but the ones in the front line are obviously my oldest friends who helped me in particular at the beginning of my PhD: Marco, Stefano, Arianna and Aldo. When I moved to London I was quite scared about making friends. Luckily I met amazing people who made me feel at home. I want to cite in particular Niccolo', Marina, Marc, Matteo, Andrea, Alessandro, Verdiana, Gaia, Samanta, Evi, Farah, Wael, Sheldon and Sara who are the closest people I had in my London life. Thanks to all the other people who are not explicitly mentioned, but have anyway helped me with their friendship.

A special mention to my dear friend Alberto for all the unique moments we shared together, in particular our amazing trip to China.

Finally, the last but not the least, I want to thank my beloved Anna, who decided to share with me a new adventure and has supported me every single day during the last year.

List of publications

Journal papers

Thiene, M., Zaccariotto, M., Galvanetto, U., Application of proper orthogonal decomposition to damage detection in homogeneous plates and composite beams. Journal of Engineering Mechanics, 2013, vol. 39(11), pp 1539-1550.

Thiene, M., U. Galvanetto, and C. Surace, Influence of sharp stiffness variations in damage evaluation using POD and GSM. Smart Structures and Systems, 2014. In press.

Thiene, M., Ghajari, M., Galvanetto, U., Aliabadi, M.H., Effects of the transfer function evaluation on the impact force reconstruction with application to composite panels. Submitted to Composite Structures

Conference proceedings

Thiene, M.,Zaccariotto, M., Debei, S., Galvanetto, U., Damage detection using proper orthogonal decomposition applied to a plate structure. 8th International Conference on Structural Dynamics. 2011. Leuven, Belgium.

Galvanetto, U., Thiene, M., Zaccariotto, M., Gherlone, M., Damage Detection Using Proper Orthogonal Decomposition. in International Congress on Theoretical and Applied Mechanics, ICTAM. 2012. Beijing.

M. Thiene, Zaccariotto, M., Galvanetto, U., Gherlone, M., Application of smoothing techniques to damage detection using Proper Orthogonal Decomposition in International Conference on noise and Vibration Engineering, ISMA. 2012: Leuven, Belgium.

Thiene, M., Galvanetto, U., Ghajari, M., Aliabadi, M.H., A frequency analysis applied to force identification. in Fifth International Conference on Structural Engineering, Mechanics and Computation, SEMC. 2013. Cape Town, South Africa: A. Zingoni.

Thiene, M., Galvanetto, U., Gherlone, M., Aliabadi, M.H., Application of Laplacian Operators on Noisy Data to Compute Curvature with Proper Orthogonal Decomposition. Key Engineering Materials, 2014. 577: p. 241-244.

Table of Contents

List of Figures

List of Tables

Glossary

SHM	Structural health monitoring
BVID	Barely visible impact damage
POD	Proper orthogonal decomposition
POM	Proper orthogonal mode
POV	Proper orthogonal value
GSM	Gapped smoothing method
DOF	Degree of freedom
FEM	Finite element method
SNR	Signal to noise ratio
IDI	Improved damage index
FRF	Frequency response function
TF	Transfer function
IRF	Impulse response function
PZT	Piezo-electric transducer
CFRP	Carbon fibre reinforced plastic
NDT	Non-destructive technique
LNM	Linear natural mode
UAV	Unmanned aerial vehicle
ASIP	Aircraft structural integrity programme
MAFT	Major airframe fatigue test
LCC	Life-cycle cost
FBG	Fibre bragg grating
RMSD	Root mean-square deviation
(A)NN	(Artificial) neural networks
FT	Fourier transform
TOA	Time of arrival
CDF	Cumulative distribution function
$\mathbf{R}$	Correlation matrix
λ	Single POV
N	Number of samples

M	Number of sensors
φ	Mode shape
φ'	Gradient of mode shape
φ''	Curvature of mode shape
l	Laplacian operator
$p(t)$	Force in the time domain
$P(f)$	Force in the frequency domain
$u(t)$	Dynamic response in the time domain
$U(f)$	Dynamic response in the frequency domain
$h(t)$	Transfer function in time domain
$H(f)$	Transfer function in frequency domain

Introduction

The development of lighter and more efficient components for aircraft structures is becoming a fundamental requirement for the aeronautical industry. The increasing use of composite materials, which provide high specific stiffness, helps reducing the weight of new airplanes. Examples of applications of composite materials in new aircraft can be found in the Airbus A380, with the application of GLARE, and in the Boeing 787 Dreamliner, where 50% of the structure is made of carbon fibre reinforced plastic, CFRP. The consequence of this trend is a decrease in the fuel consumption with obvious savings on the costs for airlines. Moreover lower carbon emissions are nowadays a strict requirement in the performance of new aircraft. The main drawback of composite materials is related to their complex mechanical behaviour, in particular when damage is present.

For isotropic materials the main concerns, for the aeronautical field, are fatigue cracking and corrosion. In particular the first one led to catastrophic failures in the past [1]. The fatigue life prediction is certainly one of the most challenging aspects when designing a new aircraft. One of the most striking examples is given by the cracks in the lower wing of the Airbus A380, discovered just after few years of operation [2, 3], although several studies were performed to predict them [4-6]. Anyway the fatigue life prediction is a well-developed field of research, as the first study on it dates back to the 19th century [7, 8]. For composite materials, different types of damage can occur. Some examples are delamination, matrix failure and fibre failure. The initiation and evolution of these types of damage are complex and a reliable mathematical representation is still not completely developed. For this reason it is difficult to predict the life of composite panels. Due to this limitation, in recent years the attention of researchers has focused on the development of new techniques to monitor the integrity of composite structures.

Since the beginning of modern aviation, different techniques have been developed to determine the structural integrity of the most critical components. These techniques, which are currently widely applied scheduled maintenance, are based on inspections of the structure while the airplane is not operating; they are commonly referred as non-destructive techniques, NDTs. Although they are reliable, as damage can be evaluated properly, they cannot be applied while the aircraft is airborne. Moreover some of them are suitable for metals, but not for polymer-based materials [9]. The need of a more complete approach to evaluate damage in modern structures has led to the development of a new field of research, which includes different topics; this is called structural health monitoring, SHM. The target of SHM is not just the evaluation of damage in structures, but a continuous online monitoring of aircraft in order to determine if they can continue flying or if they need to land for further investigations [10]. A reliable SHM platform can be vital for the future of aeronautics, because it can increase the safety of aircraft, i.e. of passengers. Furthermore it can reduce the fuel consumption for every flight, helping preserving the

environment. The common outcome of these two results is an effective cost reduction, which can improve the incomes of the aeronautical industry and the amount of passengers, increasing the possibility of worldwide journeys and trade. The development of a robust SHM system can therefore have benefits on the global economy.

As SHM is a multidisciplinary field, a single definition of it can be difficult to give; in literature several different descriptions can be found [11]. The different branches in which SHM is divided can be summarised as:

1. Development of signal process techniques to investigate the integrity of the structure
2. Modelling of smart materials using the finite element method (FEM). This approach is also called SMART FE
3. Development of new sensors, in particular lightweight and with low power consumption
4. Development of novel manufacturing approaches, possibly with the integration of smart sensors in the structure

The focus of this thesis is on the bullet point number 1. In this topic several paths can be followed. The first distinction which can be made is between active and passive approaches [12]. This is only a simple distinction, because amongst these two approaches, several techniques can be applied. In this thesis both approaches will be studied, and for each of them numerical simulations and experimental tests will be performed.

The thesis begins with a chapter containing an overview of SHM. It gives descriptions of the standard NDT and of the modern approaches, dividing them into active and passive. The stress is given to the necessity of a reliable SHM. Examples of application in different fields are given and a review of the typical damage on aircraft is provided. A literature review of the most common techniques for damage evaluation is given at the end of Chapter 1. The following chapters are dedicated to the two approaches investigated. Chapter 2 provides the mathematical formulation of the active technique chosen. It consists on a vibrational technique based on the proper orthogonal decomposition (POD) of the dynamics of systems under a harmonic load. Chapter 3 provides further mathematical manipulations adopted to improve the results obtained with the simple POD approach. In particular it introduces the application of the derivatives of mode shapes and the smoothing technique applied. Exploiting the relationship between the proper orthogonal modes (POMs) and the linear natural modes (LNMs) of a system, the damage detection algorithm, without needing any baseline to compare with, is hence introduced. Chapter 4 contains all the results obtained with for damage detection. Different structural components and different types of damage are considered. This chapter concludes the part of this thesis dedicated to active sensing.

Chapter 5 provides the mathematical background for the passive approach investigated. The focus is given first on the evaluation of a reliable transfer function to be used for force reconstruction. Then some classic approaches for impact location are introduced before describing a novel approach based on the

POD. Chapter 6 provides the results obtained for the passive approach. First a simple model is studied, in order to choose the best approach to be adopted. Then a more realistic component is investigated both numerically and experimentally. The improvements obtained with the proposed method for force reconstruction are highlighted comparing errors, between real and reconstructed forces, with a classic approach. The last part of the chapter concerns the application of the novel impact location algorithm to the same composite plate used in the reconstruction example. Two different signals, strain and acceleration, are compared in order to determine which sensor could be more useful in a real scenario. The thesis ends with the conclusions chapter, in which the most important achievements are summarized, and with possible future applications and improvements of the research performed. After the references, several appendices can be found. They describe in depth some of the topics which are briefly introduced throughout the different chapters.

The original contribution of this thesis can be found in the both approaches for SHM which are investigated. For the damage detection approach, the novelty consists on the application of mode shape derivatives and smoothing techniques to the POD of the dynamics of the system. This allows evaluating possible damage without any comparison with a pristine status. The POD was already investigated as damage detection technique [13, 14], but in those cases still a comparison between a pristine and damaged status was required. Moreover the applicability to composite structures, with their typical damage scenarios, was not investigated. The application of this approach to a stiffened panel must be also underlined. In literature several studies can be found on damage detection based on a vibrational analysis, but all of them focus on simple beams or plates. In particular smoothing techniques were never applied to a system which presented an embedded stiffness variation, such a stringer.

In the passive method part, the stress was given to the importance of reconstructing an impact force when important nonlinearities are present in the system's dynamics. The classic frequency approach fails to predict the correct amplitude in those cases. A novel approach for determining the transfer function which links impact force and system's response is proposed and validated numerically and experimentally. A study on different parameters used in the evaluation of this transfer function is performed. Finally a novel approach for impact location using the POD is presented. This method has not been proposed before in literature, hence it represents an original approach in this field.

The main contributions of this thesis can be found both in the results obtained for damage detection in composite beams and plates using the POD and in the impact detection and reconstruction chapter. In particular the study on the through-thickness position of damage can give an outline on how a delamination can affect the dynamics of a system, when the final purpose of the investigation is its detection. Results obtained for the force reconstruction technique highlights that a proper evaluation of the transfer function should be performed and that the effects of nonlinearities in the system's response play an important role in the reconstruction of the impact force. All these results give a substantial

contribution to the SHM field and can be used to perform further research on real structures, for example curved reinforced panels, which until now have not been deeply investigated.

Chapter 1: Structural health monitoring

The interest in monitoring critical structures in different engineering fields is increasing year by year. The need for developing a reliable structural health monitoring (SHM) does not come only from the scientific field. Obviously the civil and industrial application of a reliable SHM can give vital results both for the economy of companies and for the health of people. It has been estimated that the United States spends more than $200 billion each year on the maintenance of infrastructures [10]. The mounting costs associated with aging structures have become an on-going concern. One striking example is given by airline companies. The costs they have to sustain for the maintenance of a single airplane are really high. They are based on a scheduled program of safety checks which must be performed at predefined time intervals. In between two consecutive checks, nothing can be said about the safety of the vehicle. Any unexpected failure could jeopardize the safety of the overall structure, as well as that of passengers. A continuous analysis on critical components can prevent events like this. All these considerations can be easily extended to different structures, such as bridges, plants etc. SHM has the potentiality on one hand to replace scheduled with as-needed maintenance and on the other one to prevent unscheduled safety checks. This chapter presents an overview on the analyses which can be performed to control the health of structures. Starting with a general description of the most common non-destructive techniques (NDTs) it brings the reader to the definition of SHM, throughout examples in which this can be vital.

1.1 Common non-destructive techniques

Different techniques can be applied in order to evaluate the status of structural components. For practical application the focus is on those which do not compromise the future availability of the structure. These are commonly referred as non-destructive techniques (NDTs). Before describing the principal NDTs, a classification of the methods [15], based on the level of identification is given:

- Level 1: determining the presence of damage in the structure
- Level 2: level 1 plus determination of the position of damage
- Level 3: level 2 plus quantification of the entity of damage
- Level 4: level 3 plus estimation of the residual life of the structure

The above classification starts from the simplest level, which is good only to check if any kind of variation is present, and reaches the hardest and most desired one. However this last type of investigation cannot just be performed on the component under exam, but it must be coupled with a reliable analytical or numerical model, which is often difficult to obtain, as it will be discussed in following sections.

Many methods are currently used to evaluate the presence of damage in a structure. In this section the most common NDTs are presented, dividing them into two groups: non-vibrational and vibrational. NDTs represent an assembly of tests meant to investigate the possible presence of damage in a component without destroying it. Many types of damage can be invisible, especially if they represent flaws or delamination in a composite panel. Hence simple visual inspections, which were the first investigations which could be made, were replaced by more sophisticated techniques. Some of the methods which are presented in the following are well established and commonly used in real applications. Others have been applied only to numerical cases or to very simple and controlled experiments.

1.2 Non-vibrational techniques

Conventional aircraft damage detection methods are based either on visual inspection or on different NDTs. These are the oldest techniques which were developed in order to check the health status of components. Some of them are really simple while others require advanced tools and software programs. Their common point is that they usually need the structure not to be operating; sometimes even the component to be inspected has to be removed from the main frame. This is why they can be time consuming and expensive. The process to disassemble one part of structure and put it back can require several hours; furthermore it can be difficult to provide these operations automatically without the presence of physical operators. Moreover, as they can inspect only a small portion of a system, the position of possible damage must usually be known a priori. On the other hand they are considered reliable techniques and they usually do not require any comparison with an undamaged pristine case. This step can now not appear as important as it actually is. In the following sections this advantage will be underlined in details. Some of the most common techniques are listed below. A detailed description of one of them, which is particularly interesting for aeronautics applications, is given in Appendix 1. For a more detailed description see reference [9].

- Magnetic particles inspections
- Electric inspections (Eddy current)
- Radiography
- Visual inspection
- Ultrasounds inspections
- Thermography
- Acoustic emissions
- Penetrating liquids
- Shearography

Appendix 2 provides a more detailed description of ultrasounds inspections. The choice of providing a deeper explanation of this technique is due to the fact that, although it is a local technique, it can achieve

really important results in terms of both damage identification and localization, in particular for composite materials.

1.3 Vibrational techniques

The change in the vibrational characteristics of a structure can be easily associated with damage. Techniques which can calculate these parameters allow reducing the inspection time and can be applied to generic structures. One of their main drawbacks is that they are usually based on a comparison between the response of the system in a pristine and damaged configuration. Three basic properties are used as comparison:

- Natural frequencies
- Modal shapes associated to these frequencies
- Damping factors

All these characteristics are function of the properties of the system. A variation of one of these, due for example to a reduction of stiffness caused by damage, modifies the vibrational response. A simple explanation can be found considering the 1 degree of freedom (DOF) system shown in Figure 1. Its natural frequency can be easily calculated as:

$$\omega_n = \sqrt{\frac{k}{m}} \qquad \textbf{1-1}$$

Any variation of the stiffness of the spring, which can be due to possible damage, modifies the value of the natural frequency of the system. For this simple 1 DOF case it is straightforward that a reduction in k produces a reduction of ω, but for a more complicated structure the solution is not so easy, especially with regards to the position of defect.

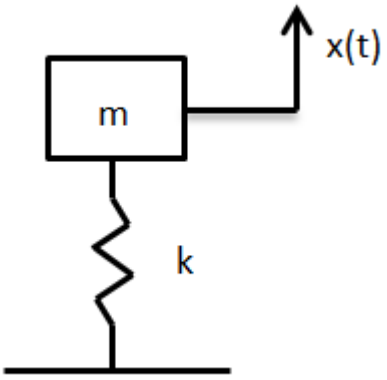

Figure 1: 1DOF system.

These methods are however limited to level 1, with the exception of modal shape analysis which can reach level 2, and can provide limited accuracy due to noise. In particular three disadvantages can be listed [16]:

- The result can depend on the experiment variables; furthermore tests can be long and expensive
- It's hard to identify a general procedure for different structures
- These methods are insensitive to small defects which can be already present in the structure

For these reasons the simple vibrational techniques which have just been presented cannot provide the necessary safety that the aeronautical field requires.

1.4 Advanced vibrational damage detection techniques

Another important way to classify different damage detection techniques regards the distinction between continuous and non-continuous monitoring [1]. An example it can be provided by a system of embedded accelerometers which monitor the integrity of a bridge towards a discrete monitoring provided only after significant events, i.e. an earthquake. This concept can easily be brought into the aeronautical field. A series of sensors mounted on critical parts of the structure could control online the safety of the airplane and provide information about the necessity of an emergency landing. This possibility becomes even more important for unmanned vehicles, as for example for spying or land control purposes, which must be controlled remotely. That is why several new techniques are nowadays studied. They can be considered vibrational, as the dynamic response of the system is used to determine its state. However they have several advantages with respect to the ones described before:

- Minor dependency from experimental setup
- Fewer sensors needed
- It is possible to establish a general methodology
- Smaller defects can be evaluated

Some examples of these methods are wavelet analysis and Lamb waves. Obviously they have also some limitations; usually the presence of noise in data can lead to error using these types of analyses. The environment in which an aircraft has to operate can contain many source of noise. These techniques are often not able to distinguish variations in signals due to noise from the one due to damage. Furthermore the variability of damage indices is another limitation which on one hand prevents these methods to obtain a high probability of detection, while on the other can produce false alarms.

The influence of the presence of small initial defects, due for example to manufacturing or assembling errors, has an influence also on these techniques and sometimes it is really difficult to individuate them. However the most challenging aspect to deal with is the treatment of boundary conditions. The validation of numerical cases, developed through analytical or numerical finite element method (FEM) models, with experiments is often very difficult. The reflections of waves from the boundaries are really difficult to

predict. That is why usually the above techniques take into account only the first part of the signal, which does not contain any reflection. When talking about a continuous control of the safety of a system, the field of research does not refer anymore to simply NDTs but to structural health monitoring [10].

1.5 Impact damage detection

All the vibrational techniques described before can be described as "active sensing methods". This means that an external stimulus is required to excite the system; then the dynamics can be acquired and processed. Another important analysis which can be performed, relates to the detection of impact energy and location. This is a passive approach, as no external stimulus is required. As impacts are one of the main sources of damage, especially for composite plates, this possibility can improve the safety of the structure. More details on this field, including a detailed literature review, will be given in a following chapter of the thesis, which is entirely dedicated to impact detection and reconstruction.

1.6 Advantages of the structural health monitoring

From all the descriptions made above, it is clear that several techniques to monitor structures exist. However all of them present some drawbacks, in particular about the possibility to locate damage, sensitivity to noise, and necessity of a comparison with a pristine case. All these limitations prevent them to be successfully applied when the structure is operating. The need for safety and cost reduction, which characterises engineering fields, requires a modern approach towards the control of operational conditions of the most crucial components of a system. The final target is the continuous monitoring of these parts through the permanent installation of sensors on a structure. This necessity is not essential just for aeronautical structures, but also for civil and mechanical ones. Researches on signal processes, which can provide all the information needed for the purpose, have been conducted throughout the last decades. However the greatest limitation was that appropriate sensors, which could be easily installed on structures, had not been developed yet. The main concern was related in particular to their size and weight. These could be a limitation especially for aeronautical and aerospace applications, in which the constraint on the mass can be very restrictive. In recent years new sensors have been developed. In particular the piezoelectric wafer active sensors (PWAS) are small, light cheap and can be produced in several shapes. They can be welded onto surfaces or attached through special resin. For a description of their properties see Appendix 3.

There can be several definition of SHM; one of these says that "SHM is a scientific process of identification, in a non-destructive way, of four topics related to the health of one component during its operational life" [11]. These characteristics are:

- ✓ Types of load, operational and environmental, which act on the component
- ✓ Mechanical damage due to those loads
- ✓ Damage growth while the component is operating

- ✓ Performances of the component as damage grows

The knowledge of the first three points, combined with the design of the component and with the operational specifications, allows the identification of the last point, which determines if the component can still satisfy its structural requirements. All the techniques used in SHM must be non-destructive and applied during the operational time of the system. They should exploit a combination of hardware and software utilities in an automatic implementation.

People apply everyday some empirical techniques to monitor the health of systems which they usually use. For example, an anomalous noise produced by a car, can be interpreted as a malfunctioning of the engine. This type of comparison, between the actual response of the system and an ideal one which is considered pristine, is the base of many monitoring techniques. A typical example of a system in which an automatic monitoring is necessary, is an unmanned airplane. Loads due to landing, aerodynamic forces, engine thrust and impacts caused by external objects, let the system respond deforming and vibrating during operations. In particular the compression load, to which the landing gear is subjected, is transmitted throughout all the structure. Embedded sensors can register this vibration in terms of amplitude of displacements, frequency content and strains. Other variables which can interact with the structure stability are temperature, corrosive elements, humidity. All these variables can have an important contribution in damage growth and evolution. While for metallic structures, analytical formulation that can represent the stress along cracks are available in literature [17], for composite materials the evolution of delamination is still a great concern, as many variables can affect the local stress and strain distribution around the damage. The possibility to detect the presence and eventual growth of defects through variation of vibrational parameters can be really important especially for new materials.

There are several reasons for which a real time monitoring while the structure is in use must be preferred. Some of them have already been presented before and concern safety and cost reduction. But there are also some engineering considerations which can be underlined. In many cases it is easier to detect the presence of a possible damage when loads applied to the structure are high. During operations, a structure can be subjected to high loads, at least the highest it was designed to. Sometimes it can be difficult and expensive to reproduce those loads in a laboratory. Furthermore these loads can have different sources; they can be also due to occasional events, such as impacts. Understating the energy and position of these impacts can be useful to determine if the system can still work or if a deeper check on its health must be performed. Detailed examples of practical advantages of SHM are given in the following sections, considering two different fields. The first one is the commercial field, so the one in which private companies can have interest in reducing costs. The second one is the military field, for which the objectives are different, but an appropriate SHM is still essential.

1.7 Structural health monitoring in the commercial field

The economic interests of private companies can give a strong push to the development of a fast and reliable SHM. One example is the case of excavating machines. In the USA, builders started to give this machines in leasing instead of selling them (and this is the case of several others fields, such as the aeronautical one). This new approach requires the constructors to keep their products at a high level of performance, in order to satisfy their clients. It was estimated that an increase of 2% of wasted working time of 20 trucks, would cost about $13 million per year. Condition based maintenance (CBM) is the application of real time monitoring of system to develop a maintenance program based not on fixed parameter, but on the real necessity of systems. For example, the scheduled oil check for a car is about every 15000 km. But at that point the oil level can still be enough or, on the other hand, it can run below the minimum level before the expected time. A CBM applied to vehicle like this would reduce the costs of maintenance and increase its efficiency. Moreover it could prevent accidents, which in certain cases can have catastrophic consequences, such if a public transportation vehicle is involved. A continuous monitoring would also reduce the inactive time of a vehicle needing a component substitution because this could be ordered in advance, before the vehicle is prevented from going on with its duties.

Focusing on the aeronautical field, in the last years the number of passengers increased consistently. This means that airports are becoming more and more crowded and that the demand of flights is increasing. Obviously every delay during take-off or landing can cause several problems to the overall air traffic. From Figure 2 it is possible to see the trend on the amount of passengers on the 10 busiest airport in the world (reference year 2012) [18]. For most of them the last ten years represented a period of small increase in the overall amount of passengers, with the exception of Dallas which suffered a reduction. It is very important to underline that the only two eastern airports which are present, Beijing Capital International Airport and Soekarno-Hatta International Airport, manifested an impressive increment of the number of passengers. Obviously the Olympic Games which took part in the Chinese capital in 2008 gave an important push to the tourism of that city. In general all the most important airports in Asia resemble this incredible trend in the number of passengers per year. In the last five years the Hong Kong airport increased its passengers by almost 9%, Suvarnabhumi (Thailand) by 18% and Dubai's even by 52%.

Although many aeronautical accidents are due to human faults, there were several occasions in which a structural failure determined important consequences. In May 2002 an airplane of China airlines broke into four pieces 20 minutes after take-off causing the death of 225 people. The cause was identified in a not properly repaired tail-strike which developed fatigue cracks. In October 2003 an air-taxi crashed in Brazil due to mechanical failure just after take-off. In December 2005 an airplane of the Alaska airlines on the route from Seattle to Burbank was hit by a luggage truck before take-off. After twenty minutes of flight the cabin started losing pressure and the pilot was forced to an emergency landing which tilted all

the regional air traffic. In February 2008 a helicopter crashed in the sea in front of the Argentina coast due to a failure of the tail rotor. On 1st April 2009 a helicopter carrying 16 people crashed due to the main rotor failure causing the death of all the passengers and members of the crew. It is clear that all those accidents were due to an inappropriate health monitoring of the structures. Particular attention should be paid especially to the first case; cracks growth is one of the most dangerous topics in health monitoring because the growth speed is often unpredictable so checks should be performed very often in order to guarantee the safety of the airplane.

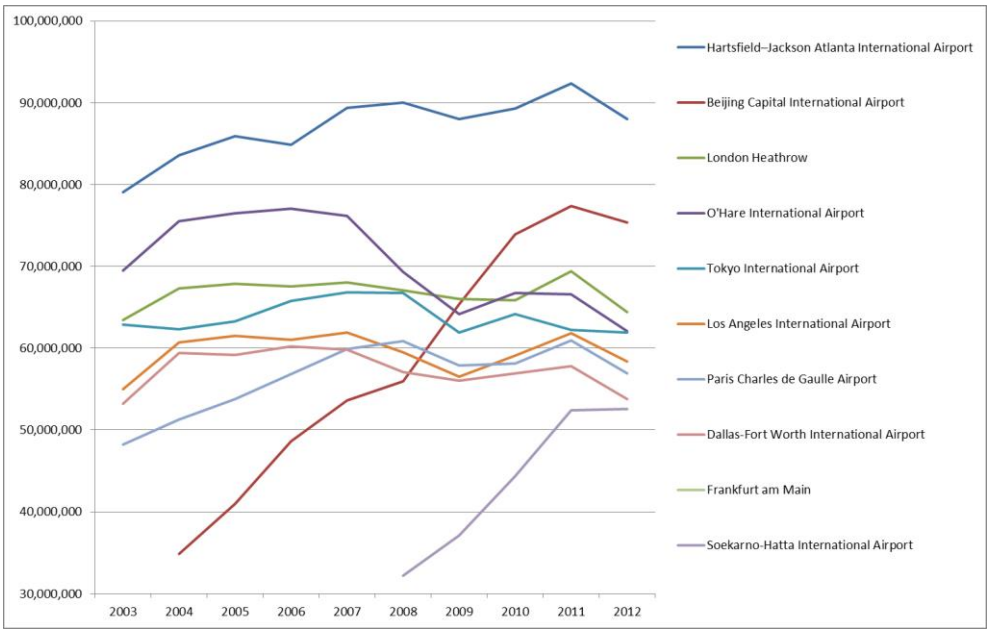

Figure 2: Evolution on the number of passengers in the last 10 years.

1.8 Structural health monitoring in the military field

Technological improvements are often first available in the military field, thanks in particular to the high budget available. However also the in this case there is the need of a change in the monitoring of systems. In 2004 the 14% of the economic resources of the Defence Department in the USA was used for maintenance of vehicles. The repair costs are growing while the replacement of old airplanes with new ones is decreasing [11]. An F-16 requires up to 25 hours of maintenance for every hour of flight. Nevertheless after an air-fight a pilot should be warned if some component is damaged such that the mission cannot be carried on any more. In recent years several improvements were also achieved in the development of unmanned vehicles, which can be used for spying purposes. A failure of one of this unmanned aerial vehicle (UAV) could lead to its destruction or loss. Sometimes it can be difficult to define which one of the two scenarios is the worst. On 4th December 2011 an American UAV was captured by Iranian forces which claimed that later they were able to build a replica of the drone. It is clear that in a world were new technologies are kept as much confidential as possible, events like this can be really dangerous, especially if the military field is involved. All these considerations can be extended to all the army divisions, like the Navy for example.

1.9 Aircraft structural damage

Materials currently used for aircraft structures include metals, such aluminium, and polymer-based composites. Damage evolution and growth depend on their ductility and homogeneity. For example microscopic cracks can generate in the grains of a metal, and then propagate due to variable loading conditions. Plastic deformation of the surface of components can occur after a severe load, such as an impact. Polymer-based composite materials are really sensitive to this type of load when developing damage. The EU Framework Programme IV included a research project named MONITOR, which performed a survey regarding the most common and important damage forms in aeronautical structures. For metallic structures the crack propagation due to fatigue resulted to be the most common one. For composite materials, impact damage was the most relevant.

Fatigue failure can have different sources; that is why there can be a differentiation in fatigue failure types [19]. Variable loads lead to mechanical fatigue or cracking. If they are in conjunction with high temperature, the phenomenon is called creep-fatigue. When aggressive agents are present, corrosion can have an important influence in fatigue life. When contact between components is involved, it leads to contact fatigue. All metallic components exhibit different stages of fatigue damage. These can be classified as [20]:

- Sub-structural and microstructural changes.
- Microscopic cracks
- Formation of dominant cracks
- Structural instability and/or complete fracture

The first fatigue research dates back to 1850s when Whöler analysed railway axles subjected to cyclic loading. The aerospace industry started to study fatigue design in 1940s. These resulted in the jet aircraft *Comet*, which however suffered for crack propagation from the rivets close to passengers' windows. A second major lesson to the aerospace industry was taught in 1988 by a Boeing 737-200 operated by Aloha Airlines on Hawaii. That case was an impressive example of combined events which can cause structural failure. The airplane had already performed lots of flights, 80,029, so that multisite fatigue cracking had formed in the upper crown skin of the fuselage. The corrosive environment, due to the proximity of the sea to the main airport in which the Boeing operated, increased the fatigue effect which at the end led to explosive cabin decompression. In the military field these types of accidents happened more often due to the difficult environment in which they have to operate. Examples include crashes of Vulcan, Harrier, Gnat and Bucaneer in the UK and B-47, F111 and F15 in USA. Different programs started in order to monitor damage in aircraft. One of them is the aircraft structural integrity programme (ASIP). This has been running for more than 25 years in the US Air Force and summarises all the different activities performed on aircraft with regard to structural integrity. Another statistical analysis, which represents an important source of information in the aerospace field, is the major airframe fatigue test (MAFT). This

test is required every time a new aircraft is designed and realised in hardware before the first flight. An example of results obtained for a Tornado is given in Figure 3, [9].

Cracks due to fatigue seem to be the most dangerous factor which can lead to the complete failure of an aircraft. As the life of an airplane increases, the possibility to develop cracks becomes more and more probable. Obviously a reliable SHM would prevent catastrophic accidents due to crack propagations, but at the moment the most effective damage detection techniques belong to the NDT field. It is very important, hence, that the mean fleet age of airlines is kept low, in order not to be exposed to dramatic fatigue failure. The average fleet age of airlines can be easily checked on the web, [21]. A summary is given in Table 1.

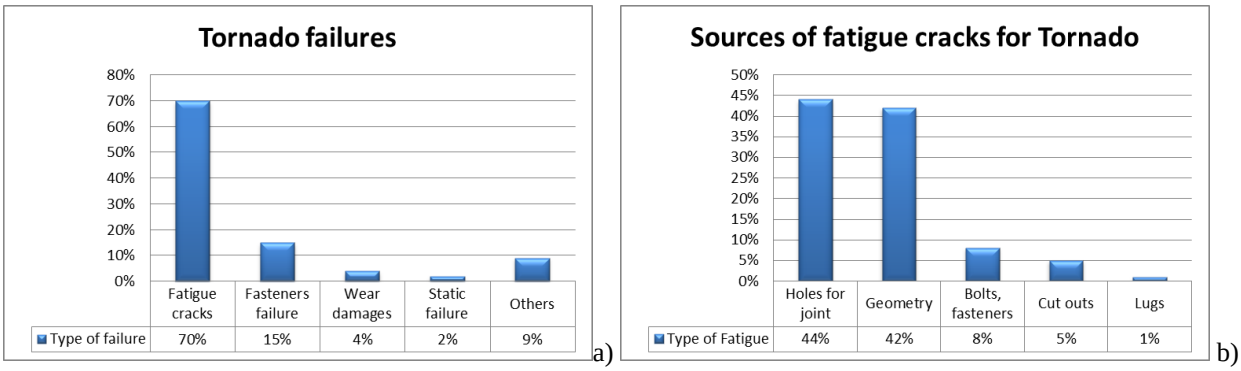

Figure 3: MAFT results for Tornado. a) Types of failures. b) Sources of fatigue cracks [9].

Table 1: Fleet age for some relevant airlines.

Airline	Number of airplanes	Fleet age [years]
Alitalia	115	8.1
Air France	253	10
Lufthansa	306	12.6
British Airways	256	13
Emirates	194	6.2
Delta	711	16.4
American Airlines	606	14.8
United Airlines	707	13.4

It is also interesting to highlight that several differences exists in aviation safety records around the world. Due to the globalization of trade and economy which characterizes the world nowadays, it is expected that the safety standards in the aviation field are similar. However studies on this topic showed that different area in the world are interested by much higher accident rate than the average. One of the main causes has to be found in the use of aircraft beyond their designed life. An important analysis on this field can be found in [22]. An on-line database can be found in [1].

1.10 Lifecycle cost of aerospace structures

The aging of existing aircrafts and the development of new types of airplanes, require an increase in the effort on inspecting and monitoring structures. However this inevitably increases operational costs. That

is why analyses on maintenance and reparations are becoming more and more important. In this section an example of estimation of life-cycle costs is given, based on what discussed in [23] and [9]. Many people think that the costs associated with an airplane, are mostly due to the manufacturing. A correct analysis should subdivide the life-time of structures in different part:

- Research and Development (R&D): this phase includes in initial planning, market-analysis, feasibility studies, research, software development, documentation, project management etc.
- Production and Construction: this phase includes material acquisition, industrial engineering, manufacturing, process development, quality control, initial logistic support, deployment etc.
- Operation and support (O&S): this is the most interesting part for this research. It consists not only in the maintenance and repair but also in storage, transportation and handling, system modification etc.
- Retirement and disposal: this last step consists in system retirement, disassembly, recycling, disposal of non-repairable systems etc.

The total cost of these stages is known as life-cycle cost (LCC). A typical Boeing 747 aircraft has a purchase cost of about $220 million, but its LCC is much higher. The purpose of an efficient LCC is the development of a detailed cost profile, which can predict the costs over the complete life-cycle. A possible example consists in dividing it in six parts:

1. Identification of all activities which can contribute to cost, throughout all the life of the structure.
2. Develop a cost breakdown structure based on the activities identified in step 1.
3. Calculation of costs estimation relationships. This can involve either self-developed procedures or parametric cost estimation models and tools.
4. Decision upon the reference date, which can be the current or future LCC value. The conversion for any given time is given by:

$$x(t_i) = \left(1 + \frac{y}{100}\right)^{t_j - t_i} x(t_j) \qquad \textbf{1-2}$$

   Where x is the cost, y is the percentage of interest per annum and t_i and t_j refer to two different time points.
5. Introduction of learning curves which can take into account improvements in technology.
6. Summary of different costs profiles within the cost breakdown structure.

A detailed example of application of this procedure, for a TORNADO, can be found in [9].

1.11 Technical approach to structural health monitoring

As already mentioned, usually SHM consists of four steps: identification of loads, identification of possible damage and prevision on damage growth and of its influence on system performances. A typical scheme of SHM is given in Figure 4. A detailed description of the most important parameters is given in the following sub-sections.

1.11.1 Sensors

Depending on the type of measurements required, different sensors can be more suitable. For example a temperature measure can be performed at a low frequency, one sample per minute, while vibrations require several kHz of sampling frequency. Sensors can be also passive, so dedicated only to acquisition, or active, able to produce a stimulus which can be later collected. Depending on the type of signal processing needed one of these two choices can be preferable. The environment in which measurements are performed must be also taken into account, as noise and other disturbances can prevent results to adhere to the expected ones. For aeronautical applications, piezoelectric sensors are the most promising ones. They are cheap, light and can reach high frequencies. They collect the strains at the surface of the component they are attached to. In particular their capability to act both as sensors and actuators makes them suitable both for active sensing, in particular with guided waves, and for passive sensing like impact monitoring.

1.11.2 Identification of loads

The first distinction which must be made is between transient and cyclic loads. For example the rotation of the engine compressor and turbine causes cyclic loads on the structure while the contact between the landing gear and the ground during landing is transient. Impacts caused by birds or hail during flight are occasional events, which however can have serious consequences. Also temperature variations can be considered external loads. The identification of the most important features of the load, such as amplitude and frequency content, can be exploited in different ways. For example an unexpected force can be due to an impact which could have damaged the structure. On the other hand, updated periodic load data can be used to update the design of the system, modifying the dimensions in order to maintain the safety factors at an acceptable level. Finally these loads can help developing a reliable damage evolution law, in case one of the components is damaged.

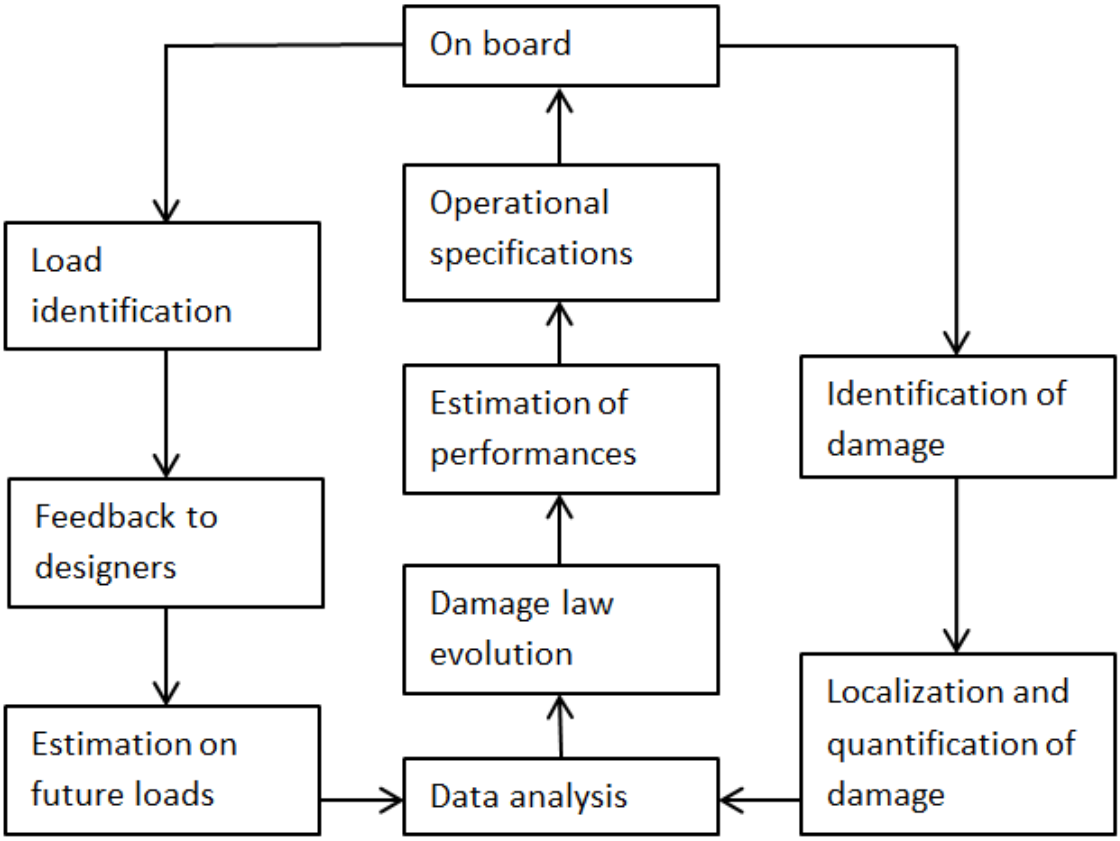

Figure 4: Technical approach to SHM [11].

1.11.3 Identification of damage

Identifying possible damage is a process which requires different steps, for example data acquisition, processing and comparison with a known status, in order to obtain useful information for the diagnosis. The difficulties do not lie only in missed identification but also in false positive cases. Sometimes changes in environmental conditions can interfere with data processing bringing to wrong damage identification. Algorithms should be also able to localize damage and identifying its size. Usually a mechanical or physical model of the system is required to determine these parameters. All this information can then be used to perform a proper check when the structure is not in use.

1.11.4 Performances prediction

Not all types of damage determine the structure to be unsafe. Often a proper monitoring of its growth and evolution can let the system continue its duties. After a certain threshold, the damage can be too extended and all the structure, or some parts of it, must be replaced in order to avoid any risk. Furthermore the knowledge of a possible malfunctioning of a part of the system can be managed by proper expedients which can reduce the stress on the structure, for example reducing the aircraft speed can alleviate the stress on wings and engines. For an airplane this can be a striking opportunity. In case of failure while the airplane is airborne, understanding if it can complete its cruise until the final destination, or if it needs to stop before, can make a considerable difference for the airline, as well as for passengers.

1.12 Bibliographic references on aeronautical SHM

Aeronautical and aerospace companies are focusing more and more on the development of reliable SHM techniques. Scientific research must then be focused not only on numerical algorithms but also on their practical application. The increasing use of composite materials makes this research even harder because of their direction dependent behaviour and all the different fracture mechanisms to which they can be subjected. However their special properties in terms of low density and high strength attract the main aeronautical constructors. Some of the main problems associated with this type of materials are listed below:

- They are really sensitive to low velocity impacts, due for example to birds, tool drops or hail. These cause the barely visible impact damage (BVID) which are the main responsible of delamination and fracture.
- Debonding between composite plates and metallic stringers.

In [12] an analysis on an impacted plate was performed both with an active and passive approach. In the first case a piezoelectric actuator was used to excite Lamb waves on the plate and the response was recorder using a scanner laser vibrometer, able to collect 567 points simultaneously. A differentiation on the in plane and out of plane waves was performed, highlighting how in the latter case the damage could be localized. In the passive approach, waves due to the impact were collected and a triangulation of signals, united to a genetic algorithm, was performed in order to localize the impact. The results were good especially in the central region of the wing box, while close to the boundary inaccurate estimations were obtained.

Another application of SHM using Lamb waves was performed in [24] were changes in Lamb waves velocity with respect to tensile strength and transverse cracks were analysed for cross-ply fibre reinforced plastic (FRP) laminates. They determined that these velocities can be an accurate estimation of the elasticity of laminates and that they are sensitive to possible damage present in the structure. An important description of the application of Lamb waves for damage detection can be found in [25]. Other recent applications of this technique for SHM can be found in [26-32].

In [33] again active and passive techniques were proposed to monitor impacts on a wing box. It was underlined that as the energy of the impact increased, higher frequency components tended to appear in the spectrum of the response; this was described as a development of micro-fractures. The active approach was applied to identify a possible debonding between the plate and the stringer. Two PZTs, one actuating and one receiving the signal, were used to analyse the waves after the damage. Results highlighted that, in the debonding case, one type of waves was not collected anymore. The reason was their lower wavelength, so their higher sensitivity to damage.

The effect of a repair on a wing was studied in [34]. In particular a composite patch was applied in a wing panel were a crack of 48 mm was discovered. Fatigue tests were performed in order to verify the

reliability of the reparation. At scheduled time interval NDT were used to monitor the possible growth of the crack. A continuous monitoring through strain gages was performed as well. It was demonstrated that the reparation could guarantee long life to the structure and that the continuous monitoring was able to determine the resistance of the patch. In particular it was underlined that the number of sensors should be adequate to obtain reliable results. Furthermore they should be resistant to environmental conditions such temperature variation, corrosion and abrasion.

Another comparison between different NDTs, ultrasounds and thermography, and a monitoring system through fibre bragg grating (FBG) was performed in [35]. First of all a plate was impacted and then fatigue cycles, correspondent to the operative life were performed. The monitoring technique was able to detect the impact; in particular a variation of the spectral component was determined after the impact. All the three techniques revealed that the damage didn't grow after the fatigue cycle.

An overview of piezoelectric impedance-based health monitoring can be found in [36], including a discussion on future applications and research in that area. In [37] an impedance-based SHM was applied to detect crack in matrix of graphite/epoxy composites. The structure was excited and sensed using ceramic PZT, and a root mean square deviation (RMSD) between the square difference of undamaged and damaged systems was used to locate cracks. This impedance-based method resulted to be more suitable for thin specimens.

The application of neural networks (NN) in damage detection procedures has been motivated by the possibility of the existence of different types of damage at several different locations within the same structure, making damage detection a complicated process [38]. They can be applied both for damage detection and localization and for impact reconstruction. Some examples of these applications can be found in [39-41].

More references on SHM research will be given in following chapters, where the specific topics will be presented.

Chapter 2: Proper orthogonal decomposition

Proper orthogonal decomposition (POD) is a statistical method which aims at obtaining a compact representation of data. The method can find applications in different fields but the basic principle is always the same. This consists in a projection of data from a space of high dimension to one of lower size, keeping most of the essential information on the system and revealing an unexpected structure. The key idea is the reduction of a big number of correlated variables in a much lower number of independent variables. This method was first developed for linear systems but it finds application also in nonlinear problems as best linear approximation of the model under exam [42]. Basically the method requires the acquisition of the dynamic response of a system, in terms of displacements, accelerations etc. and gives as outputs the proper orthogonal values (POVs) and the proper orthogonal modes (POMs). According to the field of applications they represent different features of the system.

2.1 Historical and bibliographic references

The POD, known also as Karhunen-Loève decomposition, was proposed independently by several authors, including Karhunen [43], Loève [44], Kosambi [45], Obukhov [46] and Pougachev [47]. Its fields of application can be various. However, due to the high number of data required to apply this technique, it was not used until the half of the twentieth century. It became popular with the availability of computers capable of manipulating a large amount of data. The first author who presented an application of the method was Lumley [48]. He used the POD to study turbulent flows. In this field the POMs represent the optimal distribution of kinetic energy and power, while POVs represent the contribution provided by the POMs to the total energy or power of the system. Graham and Kevrekedis [49] applied this method to the diffusion and reaction of chemical processes, Bayly et al. [50] studied the ventricular fibrillation, Epureanu et al. [51] obtained a reduced order model of viscous fluids under non stationary motion while Barnston and Ropelewsky [52] applied the technique in weather forecast.

2.2 POD in the structural field

The first application of POD in the structural field dates back to the 1990s. Fitzsimons and Rui [53] determined a reduced order model for a continuum system, Kreuzer and Kust [54] applied it to control the auto-induced vibrations on a torsional bar. Regarding the dynamic characterization of a structure, Feeny and Kappagantu [55] provided useful studies on the properties of POMs and POVs. They demonstrated how for an undamped system under free vibrations the POMs coincide with the linear natural model (LNMs) if the response is collected for a long period of time. As the critical damping factor increases, the POMs tend to diverge from the LNMs. This can be explained with a fewer number of oscillations which

the system undergoes with a higher damping factor. When the system is excited with a harmonic load, under certain conditions the relationship between POMs and LNMs is still maintained. In particular if the frequency of the load is close to one of the natural frequencies of the system, the most relevant POM, the one with the highest corresponding POV, is close to the mode shape related to that frequency. When the system under exam presents nonlinear behaviour, the POMs can be considered the best linear representation of the system while the POVs represent the deviation of the linear model from the real one [42]. The POD analysis on the dynamic response of a structure is particularly important in the damage detection field. Feeny and Liang [56] studied the behaviour of POMs for a randomly excited system. The results highlighted how even for this case the POMs are related to the LNMs if the Fourier transform of the load is convergent, i.e. zero mean and no substantial harmonics. Even in this case damping acts an important role in the convergence of the POMs to the LNMs. A detailed review of the POD, with its implications in the dynamic characterization of systems can be found in [42, 57].

2.3 Calculation of the proper orthogonal modes and proper orthogonal values

The method consists in acquiring the time response of a structure over a certain period of time T, with a fixed sampling time Δt. The output must be taken at M locations in the structure and N samples for each location must be acquired with a fixed sampling frequency. In this way it is possible to set up an NxM matrix in which each row represents a snapshot of the system at a certain instant t_i while each column represents the evolution of a single point over the entire window T. This is called the space matrix V and contains the whole history of the system.

$$\mathbf{V} = \begin{bmatrix} v_1(t_1) & v_2(t_1) & v_3(t_1) & \dots & v_M(t_1) \\ v_1(t_2) & v_2(t_2) & v_3(t_2) & \dots & v_M(t_2) \\ \vdots & \vdots & \vdots & \ddots & \vdots \\ v_1(t_N) & v_2(t_N) & v_3(t_N) & \dots & v_M(t_N) \end{bmatrix} \qquad \textbf{2-1}$$

To go on with the analysis it is important to shift the values in order to have a zero mean value, Figure 5. So from each column the average is subtracted, obtaining the matrix U, Equation 2-2. Finally it is possible to form the space correlation matrix R, Equation 2-3.

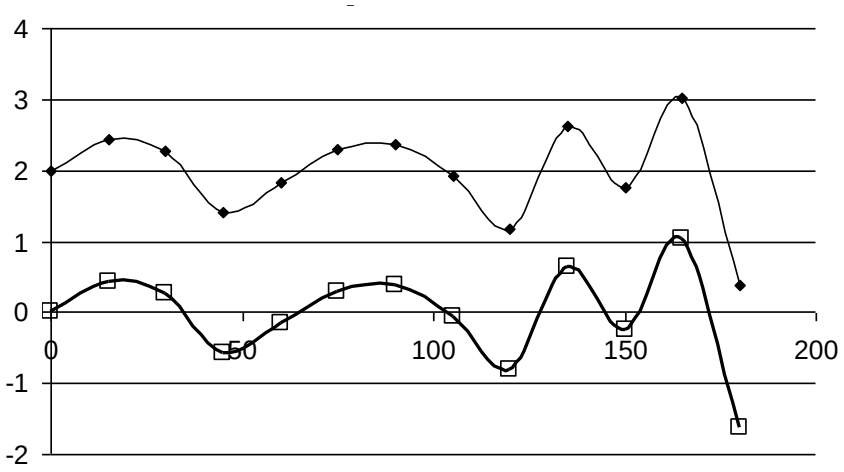

Figure 5: Possible signal before and after subtracting the mean value.

$$\mathbf{U} = \mathbf{V} - \frac{1}{N}\begin{bmatrix} \sum_{t=1}^{N} v_1(t_t) & \sum_{t=1}^{N} v_2(t_t) & \sum_{t=1}^{N} v_3(t_t) & \cdots & \sum_{t=1}^{N} v_M(t_t) \\ \sum_{t=1}^{N} v_1(t_t) & \sum_{t=1}^{N} v_2(t_t) & \sum_{t=1}^{N} v_3(t_t) & \cdots & \sum_{t=1}^{N} v_M(t_t) \\ \vdots & \vdots & \vdots & \ddots & \vdots \\ \sum_{t=1}^{N} v_1(t_t) & \sum_{t=1}^{N} v_2(t_t) & \sum_{t=1}^{N} v_3(t_t) & \cdots & \sum_{t=1}^{N} v_M(t_t) \end{bmatrix} \qquad \textbf{2-2}$$

$$\mathbf{R} = \frac{1}{N}\mathbf{U}^T\mathbf{U} \qquad \textbf{2-3}$$

This matrix results to be real, square and symmetric. In particular its dimensions are MxM. So it is possible to notice that the dimension of the problem now depends only on the number of sensors and not on the number of samples, which is normally extremely large. The eigenvalues of the matrix R are the POVs while the eigenvectors are the POMs. As explained previously, a single POM represents a single vibrational mode of the system while the corresponding POV represents the energy captured by that mode. To model the overall response of the system, it is not useful to consider all the modes, as some of them can have negligible effect. This is particularly true if the excitation frequency is close to one natural frequency of the system. An energetic approach is used to determine the number of POMs to be used. Only the first j POMs which can capture the 99.9% of energy are considered in order to proceed with the analysis, Equation 2-4. Under certain conditions this j can be even just one.

$$\frac{\sum_{i=1}^{j} \lambda_i}{\sum_{i=1}^{M} \lambda_i} \geq 0.999 \qquad \textbf{2-4}$$

2.4 POD as damage detection technique

The above described procedure can be applied to a pristine and a damaged structure. Taking the difference of the two results it is possible to verify the presence of a possible damage. This kind of approach has been investigated in previous papers, however only simple structural elements were considered.

Galvanetto and Violaris [14] applied this technique to verify the presence of a defect on a cantilever beam and on a simply supported beam: the damage consisted in a reduction of the elastic moduli in one of the elements in which the beam was discretised. Numerical investigations highlighted how the method was able to locate the damage in both configurations and with different frequencies of excitation. Furthermore different entities of damage produced different levels of damage index. The effect of noise in data was studied and results showed that the method can overcome a certain amount of noise in data, still being able to detect damage correctly.

The experimental verification was carried out by Galvanetto et al. [13] on a cantilever beam. Two levels of damage were considered, both were a transverse crack, but with different depths. Results highlighted that the damage could be located even changing the excitation frequency. The increase in the depth of the crack led to a higher value of the damage index. In [58] a similar experiment was conducted using only the damaged data.

Kershen et al. [59, 60] studied the behaviour of POVs and POMs for a cantilever beam subjected to impacts. In the analysis the beam was harmonically loaded, while at a certain position an obstacle was repeatedly hit because of the displacements of the beam. The results highlighted how a transfer of energy from the first to the second POM was present. This was explained as a capability of the method to reveal the passage from a linear to a nonlinear response of the system. Furthermore it was highlighted the capability of the method to reduce the order of the model to study continuous systems in cases were the classical modal analysis can be difficult to apply.

Placzek et al. [61] proposed a hybrid POD in which the continuous equations of the system were projected on a discrete space. They underlined that the advantage of this technique is that it does not need discretised equations, which are not always available for a given system. Another important achievement of the paper concerned the calculation of displacements of the system thanks to a reduced order model, established with the hybrid POD. Three different techniques were compared and the results showed good agreement.

Chelidze and Liu [62] applied the method to fatigue control, introducing a control on the damage index. A time and frequency analysis with the POD on a cantilever plate was carried out by Thiene [63]. In this thesis it was highlighted how the technique was sensitive to changes in boundary conditions and how the position of the damage in the plate could affect the damage index. The influence of damping and noise in data was also studied.

2.5 Advantages and drawbacks on the application of POD

The application of POD to SHM has the same advantages of typical vibrational techniques, as it can control a component in its entire dimension, providing a global inspection. Furthermore there are some aspects which make this method more convenient than classic techniques based on LNMs:

- The technique is based only on experimental data and does not require any mathematical model of the system.
- Only a few numbers of POMs are required to evaluate damage, sometimes even just one, while using LNMs several of them may be needed to have the same result. This is due to the fact that damage can be a local phenomenon which has small influence at low frequencies, while it affects more the higher ones. For this reason it is difficult to determine the correct number of LNMs to use in damage evaluation. The dominant POM is the one identified by the largest POVs, so it is uniquely determined. This advantage seems also to make the POD less sensitive to the presence of noise.
- The calculation of POVs and POMS, based on matrix operations and on an eigenvalue problem, results to be simple, fast and accurate.

However there are also some limitations on this technique:

- In order for the POMs to be coincident to the LNMs, the mass matrix of the system should be proportional to the identity matrix; however this is a drawback only when a modal analysis is performed.
- The presence of damping decreases the possibilities to apply the technique.
- The type of load, in terms of location and frequency must be carefully chosen.
- The number of sensors needed to perform experiments can be high, leading to difficulties in carrying on the procedure.

2.6 Influence of the excitation frequency

As already stated, POD determines a series of modes, POMs, and energy coefficients, POVs, which are representative of the dynamics of the system under exam. As the frequency of the force tends to coincide with the first natural frequency of the system, the predominant POM becomes more and more similar to the first linear natural mode (LNM) and its contribution to the final damage detection algorithm can be much more relevant than the variation of the other modes. Exploiting the similarity of POMs, the variations of LNMs with stiffness properties of a simple structure can provide a theoretical explanation of the relevance of the forcing frequency.

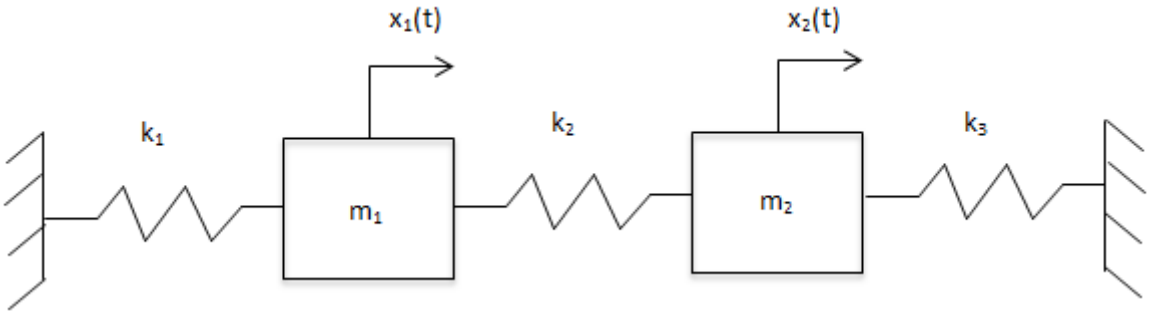

Figure 6: Example of 2 DOF system.

Consider the 2 degree of freedom (DOF) system shown in Figure 6. Following the procedure describe in [64], the equations of motion for a free vibration case are given by:

$$\begin{aligned} m_1\ddot{x}_1(t) + (k_1 + k_2)x_1(t) - k_2x_2(t) = 0 \\ m_2\ddot{x}_2(t) + (k_2 + k_3)x_2(t) - k_2x_1(t) = 0 \end{aligned} \quad \textbf{2-5}$$

The solutions of the differential equations stated above can be expressed in the form:

$$\begin{aligned} x_1(t) = X_1\cos(\omega t + \varphi) \\ x_2(t) = X_2\cos(\omega t + \varphi) \end{aligned} \quad \textbf{2-6}$$

Where X_1 and X_2 are constants that denote the maximum amplitude of the response, and φ is the phase angle. Substituting Equation 2-6 in Equation 2-5 and considering only the maximum amplitude response, as the equations must be satisfied for all the values of time t, it is possible to obtain:

$$\begin{aligned} [-m_1\omega^2 + (k_1 + k_2)]X_1 - k_2X_2 = 0 \\ [-m_2\omega^2 + (k_2 + k_3)]X_2 - k_2X_1 = 0 \end{aligned} \quad \textbf{2-7}$$

For a non-trivial solution, the determinant of the coefficients must be zero. This implies that:

$$(m_1m_2)\omega^4 - [(k_1 + k_2)m_2 + (k_2 + k_3)m_1]\omega^2 + [(k_1 + k_2)(k_2 + k_3) - k_2^2] = 0 \quad \textbf{2-8}$$

$$(m_1m_2)\omega^4 - [(k_1 + k_2)m_2 + (k_2 + k_3)m_1]\omega^2 + [(k_1 + k_2)(k_2 + k_3) - k_2^2] = 0 \quad \textbf{2-9}$$

At this point, since we want to evaluate the influence of k_2 on the mode shape, some simplifications are applied. In particular $m_1=m_2=m$ and $k_1=k_3=k$. the above equation reduces to:

$$m^2\omega^4 - [(k + k_2)m + (k_2 + k)m]\omega^2 + [(k + k_2)(k_2 + k) - k_2^2] = 0 \quad \textbf{2-10}$$

The solutions of this equation are given by:

$$\omega_1^2, \omega_2^2 = \frac{1}{2}\left[\frac{2(k+k_2)m}{m^2}\right] \mp \frac{1}{2}\left[\left(\frac{2(k+k_2)m}{m^2}\right)^2 - 4\left(\frac{(k+k2)^2 - k_2^2}{m^2}\right)\right]^{\frac{1}{2}}$$

$$\omega_1^2 = \frac{k}{m} \qquad \textbf{2-11}$$

$$\omega_2^2 = \frac{k+2k_2}{m}$$

The ratios between the amplitudes of the response of the two masses are given by:

$$r_1 = \frac{X_2(\omega_1)}{X_1(\omega_1)} = \frac{-m\omega_1^2 + k + k_2}{k_2} = 1$$

$$r_2 = \frac{X_2(\omega_2)}{X_1(\omega_2)} = \frac{-m\omega_2^2 + k + k_2}{k_2} = -1 \qquad \textbf{2-12}$$

The above equations suggest that the two mode shapes, which are characteristic of the system under exam, are not sensitive to k_2 nor k. This implies that a change in those parameters, due for example to damage, would not then be captured by the mode shapes, which could not therefore be used as damage indicator.

If instead $k_1=k_2$ the results are different, as it is possible to see from Figure 7. The mode ratios change with a modification of k_3. Moreover the variation is different between the two modes**.**

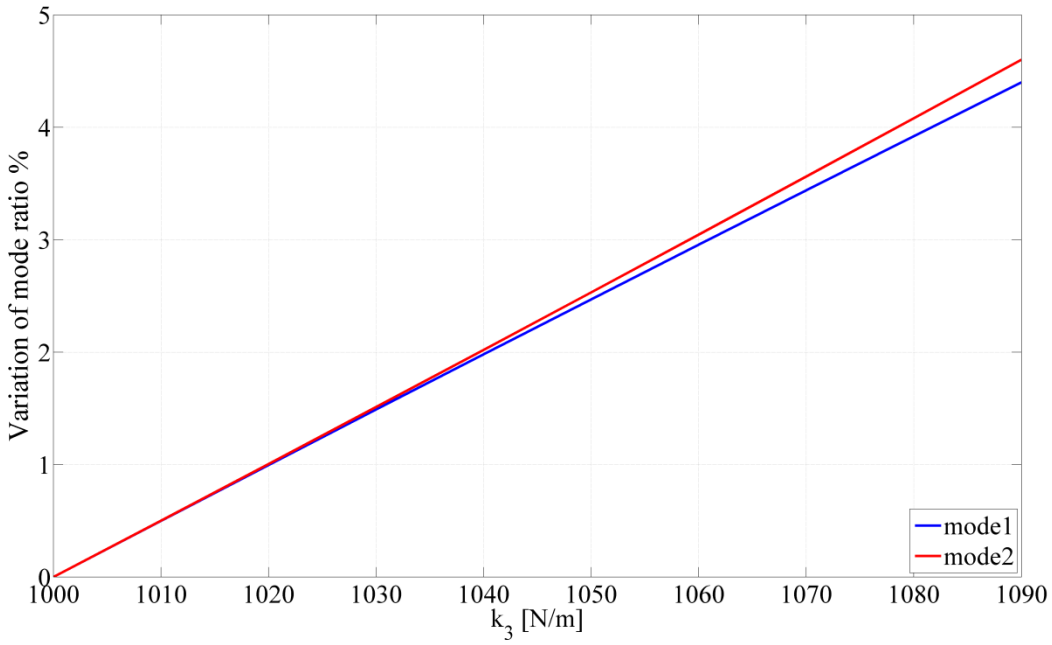

Figure 7: Percentage variation of mode ratio with respect to k3.

The above considerations suggest that, depending on the mode shape chosen, the value of the damage index can be different. That is why the frequency of the load applied to compute the POD has a relevant role. Generally the first natural frequency of the system under exam is chosen; this is actually what was done in previous works. In [14] a more detailed analysis on the influence of the excitation frequency on a simple beam can be found. In the following sections, the first natural frequency of the system under exam is generally considered for the analysis. When a different frequency is adopted, this will be explicitly highlighted.

Chapter 3: Advanced POD

As mentioned in Chapter 2, usually a comparison with a pristine case is needed in order to evaluate the presence of damage inside a structure when a vibrational method is performed. This was the case applied in previous application of POD as damage detection technique. However a modern and effective SHM must not rely on pristine data, because in many situations they are not available. That is why further mathematical manipulations can be applied to the classic POD in order to avoid that comparison. As the modes evaluated with the POD are strictly related to the natural modes of a system, an approach already successfully applied in modal analysis will be adopted also in this thesis in order to develop an improved version of the POD. These improvements consist first of all in using the derivatives of the POMs as damage index, not the POMs themselves, and then in the application of a smoothing technique on the damaged curvature, in order to avoid any comparison with the pristine case.

3.1 Computing the derivatives of mode shapes

Curvatures of mode shapes are widely used as alternative to damage identification from mode shapes changes [38]. Previous papers demonstrated how the curvature of the mode shape is more effective in locating damage. The reason lies in the fact that the curvature of a mode shape is more sensitive to local changes in the structure, being also directly related to its bending stiffness [65]. Denoting with E the elastic modulus of a beam, I the moment of inertia and M the bending moment, the curvature of a beam under bending conditions can be expressed as:

$$-\frac{M}{EI} = \varphi''(x) = \frac{d^2\varphi}{dx^2} \qquad \textbf{3-1}$$

The curvature of a mode shape can be calculated with different approximation techniques. The most common way uses the central difference method:

$$\frac{d^2\varphi}{dx^2} \approx \frac{\varphi(x-h) - 2\varphi(x) + \varphi(x+h)}{h^2} \qquad \textbf{3-2}$$

In the above equation, φ refers to the value of the mode shape at a certain grid point in the beam and h to the uniform distance between two consecutive points in the grid, Figure 8. Equation 3-2 is valid for the beam case. For a bi-dimensional case the corresponding equation is simply the sum of the curvature in the two directions x and y:

$$\varphi''(x) = \frac{\varphi(i-1,j) - 2\varphi(i,j) + \varphi(i+1,j)}{h_x^2} + \frac{\varphi(i,j-1) - 2\varphi(i,j) + \varphi(i,j+1)}{h_y^2} \qquad \textbf{3-3}$$

In Figure 9 the meaning of the indices is explained. It must be noted that the curvature is obtained using the central difference method. In this way only the internal points of the grid can be calculated whereas for the points on the boundary a forward or backward difference method is applied. Alternatively an extrapolation of the nearby values can be used. This can be a limitation of the method, especially when the number of points is low or when noise is present in data. Both of these concerns will be discussed in the following sections.

Even if the curvature of mode shapes is widely considered a reliable index for damage detection purposes, it suffers from several limitations. These include the sensitivity to noise, to the effects of boundary conditions and to the number of grid points, and their relative distance, used to collect the dynamic response of the system under exam. For this reason it can be useful to perform the algorithm proposed using only the first derivative of the POMs, i.e. their gradient. Although it is not directly related to the bending stiffness of a beam, it can highlight discontinuities in the POM, enhancing the damage detection performance. The gradient of a POM is calculated with the following equation:

$$\varphi'(x) = \frac{\varphi(x+h) - \varphi(x)}{h} \qquad \textbf{3-4}$$

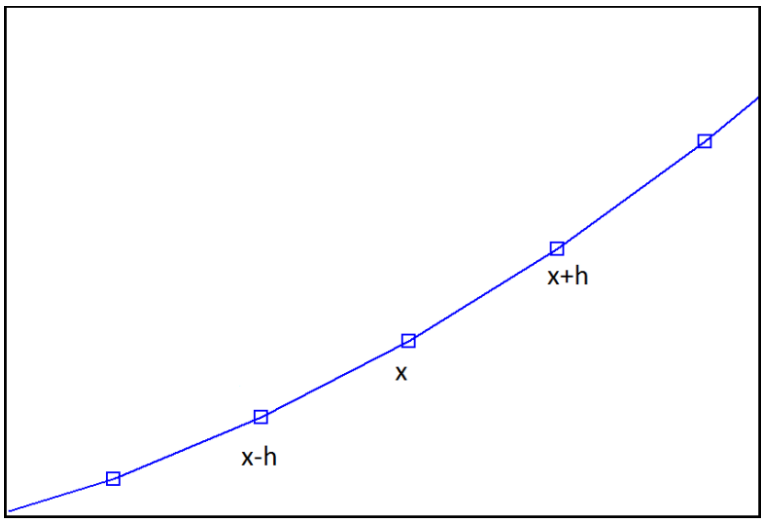

Figure 8: Grid points for the curvature calculation, beam case.

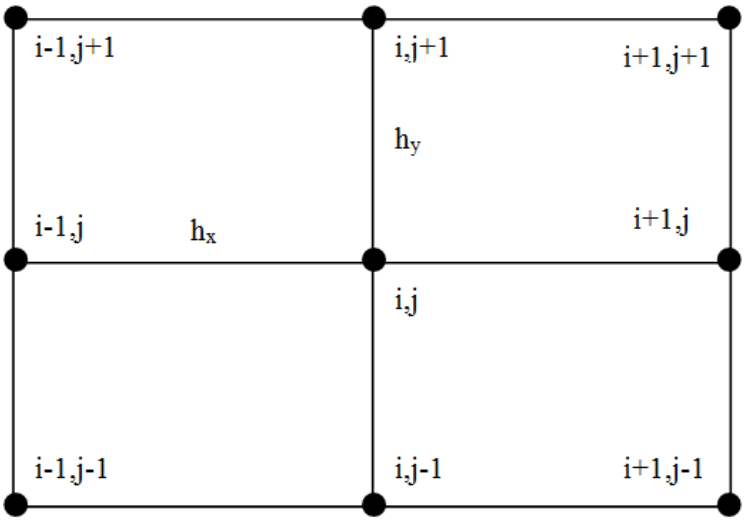

Figure 9: Schematic representation of the 2d curvature calculation.

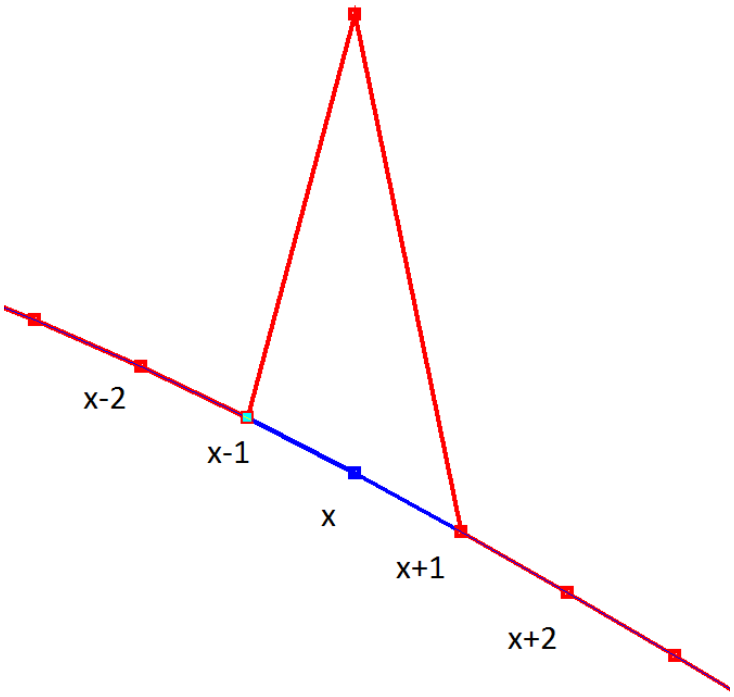

Figure 10: Interpolation for a beam case.

3.2 Gapped smoothing method

The gapped smoothing method was proposed by Ratcliffe [66, 67] as a powerful method to locate a sudden change in the curvature of a beam. The principle of this technique is that any damage present in the structure causes a discontinuity in the curvature of the mode shape. The basic concept consists of interpolating the curvature at each grid point using a cubic spline:

$$\varphi''(x) = a_0 + a_1 x + a_2 x^2 + a_3 x^3 \qquad \textbf{3-5}$$

Where x is the position of the grid point and the coefficients a_i are determined using four neighbouring points, Figure 10. The interpolation can smooth the discontinuity, hence providing a shape more similar to a hypothetic undamaged case.

A similar equation could be used to extend the GSM to the bi-dimensional case [68]. However Yoon, [69] proposed a slightly different method, which can take into account the differences in the neighbouring conditions at the boundary points. In this case a minimization problem is set up as follows:

$$\varphi''_{i,j} = g_{i,j}{}^{T} \vartheta_{i,j} \qquad \textbf{3-6}$$

$$g_{i,j}{}^{T} = [1, x_i, y_j]; \;\; \vartheta_{i,j}{}^{T} = [a_0, a_1, a_2] \qquad \textbf{3-7}$$

Where $\varphi''_{i,j}$ is the curvature at the interpolation point, $g_{i,j}$ refers to the position of the point and $\vartheta_{i,j}$ is the array containing the interpolating coefficients. In order to calculate the coefficients, a matrix equation can be set-up:

$$\lambda_{i,j} = G_{i,j}{}^{T} \vartheta_{i,j} \qquad \textbf{3-8}$$

Where:

$$\lambda_{i,j}{}^{T} = [\varphi''_{i-1,j-1}, \varphi''_{i,j-1}, \varphi''_{i+1,j-1}, \varphi''_{i-1,j}, \varphi''_{i+1,j}, \varphi''_{i+1,j-1}, \varphi''_{i+1,j}, \varphi''_{i+1,j+1}] \qquad \textbf{3-9}$$

$$G_{i,j} = [g_{i-1,j-1}, g_{i,j-1}, g_{i+1,j-1}, g_{i-1,j}, g_{i+1,j}, g_{i-1,j+1}, g_{i,j+1}, g_{i+1,j+1}] \qquad \textbf{3-10}$$

In general the matrix G is not square, so it's not always possible to perform a direct solution of equation 3-8 in order to calculate the coefficients a_i. In such case a least square approximation is required:

$$\hat{\vartheta}_{i,j} = (G_{i,j} G_{i,j}{}^{T})^{-1} G_{i,j} \lambda_{i,j} \qquad \textbf{3-11}$$

Finally the smoothed curvature at the point (x_i, y_j) can be computed:

$$C_{i,j} = g_{i,j}{}^{T} \hat{\vartheta}_{i,j} \qquad \textbf{3-12}$$

Equations 3-9 and 3-10 are valid for a grid point which belongs to the inner part of the plate. For a boundary point the size of the matrices are different, being them dependent on the number of neighbouring points. It is possible to see in Figure 11 how the coefficients for the boundary points are calculated.

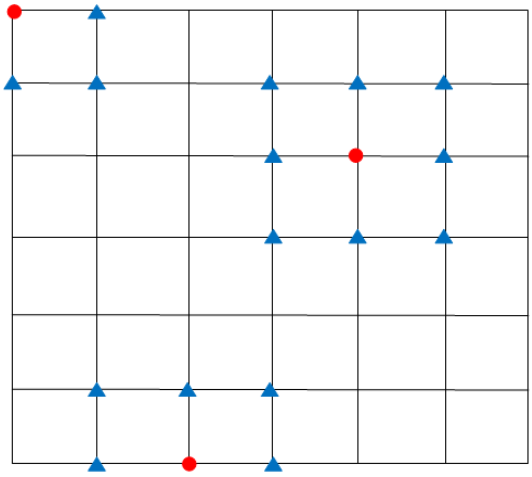

Figure 11: Application of the 2D GSM. The red circles are the points at which the curvature is smoothed while the blue triangles refer to the neighbouring points used for the interpolation.

3.3 Influence of the number of sensors in the calculation of the mode shape derivatives

The number of points used to compute a modal shape of a system can considerably influence the result of the application of a damage detection technique. This is due to both a correct representation of the mode shape and a correct evaluation of its derivatives. Consider as a simple example the second mode shape of a cantilever beam of length 0.6m. A good sampling of this shape can be obtained with 41 grid points with a spacing of 0.015m. A bad sampling is obtained using only 9 points at a distance of 0.075m. The results of the relevant shapes are presented in Figure 12. It is clear that with the bad sampling some of the features of the mode shape can be not correctly predicted. These can include also possible damage.

The applications of derivative operations can exaggerate this problem. An estimation of the error in the calculation of the gradient with equation (7) is given by a Taylor series:

$$u(x_i + h) = u(x_i) + h\left(\frac{\partial u}{\partial x}\right)_{x_i} + \frac{h^2}{2!}\left(\frac{\partial^2 u}{\partial x^2}\right)_{x_i} + \frac{h^3}{3!}\left(\frac{\partial^3 u}{\partial x^3}\right)_{x_i} + \cdots \qquad \textbf{3-13}$$

This equation can be rearranged as:

$$\frac{u(x_i + h) - u(x_i)}{h} - \left(\frac{\partial u}{\partial x}\right)_{x_i} = \frac{h^2}{2!}\left(\frac{\partial^2 u}{\partial x^2}\right)_{x_i} + \frac{h^3}{3!}\left(\frac{\partial^3 u}{\partial x^3}\right)_{x_i} + \cdots \qquad \textbf{3-14}$$

The second term in Equation (3-13) is the truncation error. When *h* is small enough, the left hand of Equation (3-14) is a correct representation of the gradient of a function; otherwise the truncation error becomes relevant. Similar considerations can be derived for the curvature. An example of the gradient of the considered mode is given in Figure 13.

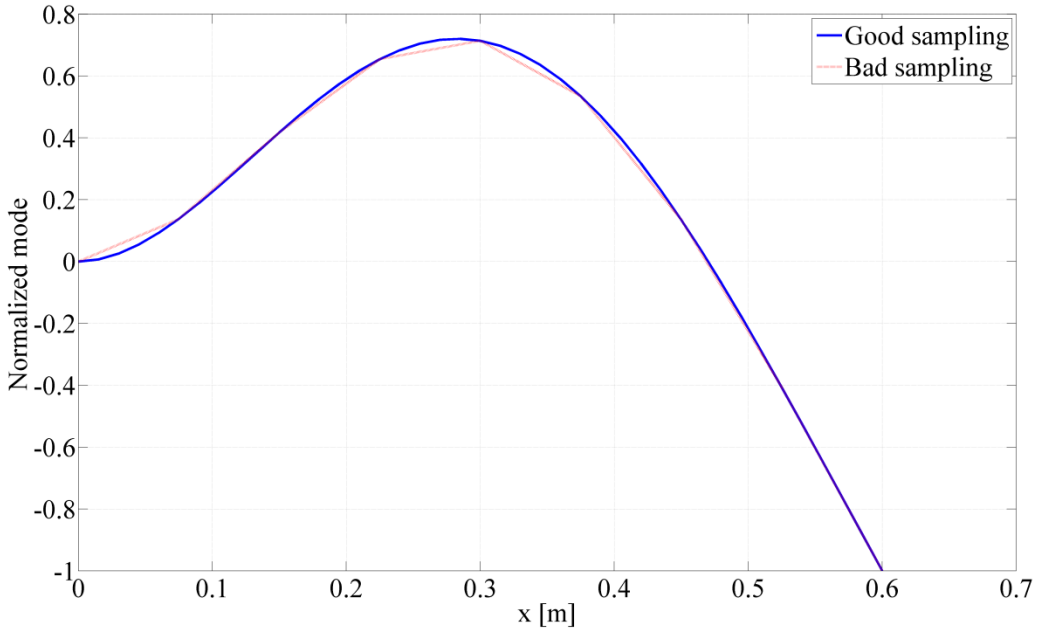

Figure 12: Examples of good and bad sampling in the evaluation of the mode shape.

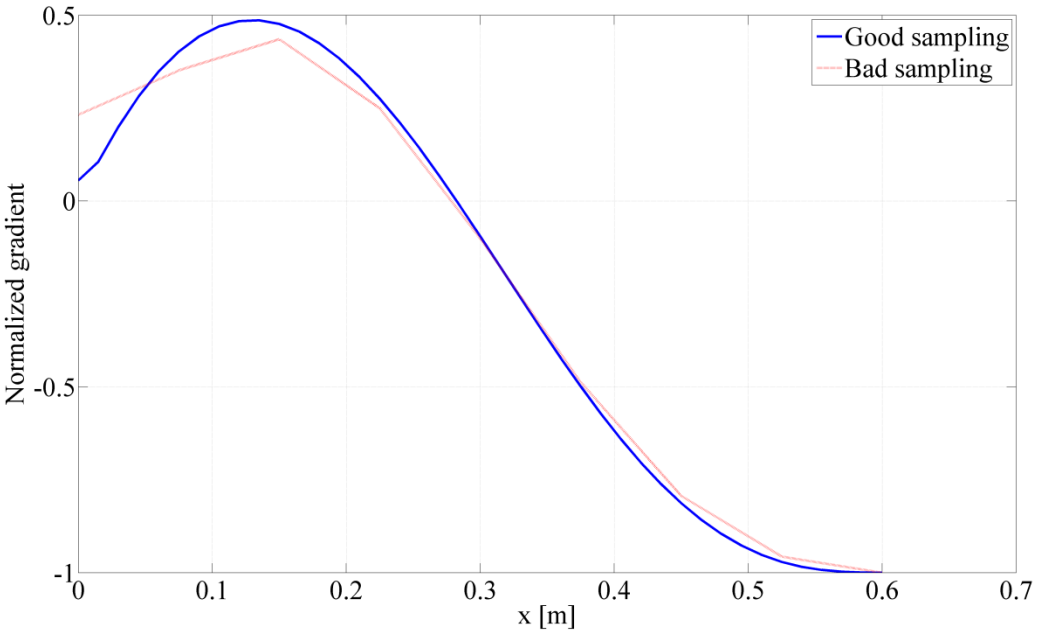

Figure 13: Examples of good and bad sampling in the evaluation of the gradient of the mode shape.

Chapter 4: Numerical and experimental verification on the damage detection method based on POD and GSM

In this chapter the POD technique is applied to different structural elements. In Section 4.1 a cantilever beam, modelled with continuum elements is analysed in depth, considering different positions of possible damage. Section 4.2 provides an experimental verification on an isotropic beam. An extension to a bi-dimensional case is provided in Section 4.3. Results obtained experimentally on a cantilever plate are presented in section 4.4. The influence of noise was investigated and a method to overcome this problem is shown in section 4.5. Finally the application of the method to a more complicated structure is presented in section 4.6. Some remarks on the applicability of the method conclude this chapter of the thesis, Section 4.7.

4.1 Cantilever beam

The first model under exam is a composite cantilever beam. Previous works have investigated the performance of POD on isotropic components, [13, 14, 58], but an analysis on delamination in a composite beam has not been performed yet using the POD. Although this is a simple model, it allows a deeper analysis to be conducted, as solid elements, instead of the simple beam elements, have been used to model it. In particular delamination in a composite system can be modelled decoupling the corresponding nodes of two facing elements and linking them with gap elements. These provide the facing nodes from overlapping when in contact. Furthermore the initial opening of the delamination can be chosen. On the other hand the use of this type of elements is computational expensive. That is why an application of the above techniques has been conducted on simple beam. A cantilever beam made up of several layers has been modelled in two ways: a two-dimensional plane stress model and a fully three-dimensional model; its dimensions are 300x6x6mm^3 and it is formed by 8 layers of equal thickness. In the first case the beam is meshed with quadratic two-dimensional continuum elements, cps8 provided by Abaqus (the use of quadratic elements prevents the model from shear-locking during bending loading, Sun [70]). 400 elements are used along the length and 8, one per layer, through the thickness. The inhomogeneous nature of the beam is described by defining different Young's moduli for the various layers, as shown in Table 2, layer 4 is separated by layer 5 by the symmetry plane of the laminate.

In the second case the beam is modelled as a 3-D continuum system, meshed with c3d20 elements of Abaqus. 400x8x8 elements of an orthotropic material are used with the following properties: E_{11}=146.9

GPa, $E_{22}=E_{33}=10.89$ GPa, $G_{12}=G_{13}=10.89$ Gpa, $G_{23}=6.4$ GPa, $\nu_{12}=\nu_{13}=0.38$, $\nu_{23}=0.776$, $\rho=1.5\cdot10^{3}$ kg/m^{3}. The stacking sequence is $[0/45°/-45°/90°]_s$. In both models three positions of delamination through the thickness and three along the length are investigated, for a total of 9 positions. However in each numerical analysis delamination is present at only one location, no multiple delamination locations are taken into consideration in the present investigation. Delamination is introduced by decoupling two adjacent layers of elements through the thickness and connecting the corresponding nodes with gap elements; in the analysis an initial gap of 10^{-3}mm is introduced. At each location delamination affects 16 elements in the direction of the axis of the beam for a total length of 12mm. The 2-D model can only describe delamination affecting the whole width of the beam whereas in the 3-D case delamination may affect even only a portion of the width. The beam is excited with a harmonic load with a frequency of 90 Hz applied to its free end. This is close to the first natural frequency of the structure, which was calculated to be 87.2 Hz. The use of continuum elements did not provide only the possibility to introduce delamination in the beam, but also to investigate possible variations in the effectiveness of the method due to the position of the sensors used to capture the accelerations: nodes on the upper or lower surface of the beam can represent sensors applied to that surface. A case of composite beams and POD based damage detection has already been considered in [71] where, however, delamination has not been taken into account.

Table 2: Mechanical properties for the 2-D model

Layer	E [GPa]	ν
1	146.9	0.38
2	35	0.38
3	35	0.38
4	10.89	0.38

4.1.1 2-D continuum model

The schematic model of the beam is presented in Figure 14. The different positions of the delaminated zones along the length and the thickness are shown by red dots. For this kind of model two time integration methods are adopted, an implicit method ,Hilbert et al. [72], and a modal dynamic method, [73]. The second method requires much less computational time but the use of gap elements can introduce some form of non-linearity in the model so that a comparison of the results obtained with the two methods was carried out, which revealed no noticeable differences.

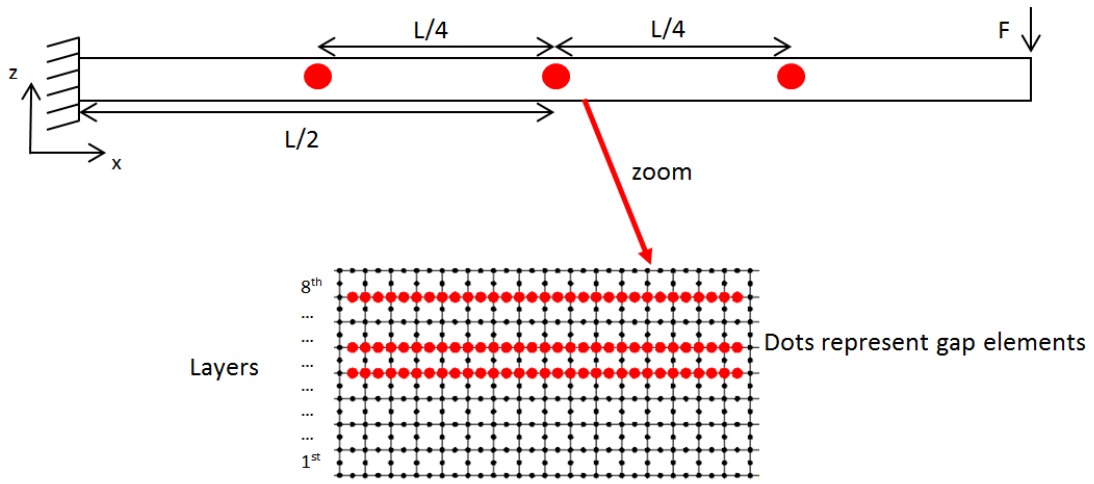

Figure 14: Position of the delamination. Three possible positions along the length are indicated by red circles. In the zoomed area the positions through the thickness are highlighted.

From Figure 15 it can be seen that the method can locate the presence of the delamination in all different positions. Figure 16 shows the difference in the damage index computation using upper or lower sensors. The evaluation of the POD gives considerable differences when the damage is located between the 7th and 8th layers. Figure 17 shows the result obtained computing the damage index from the gradient of the POM. This represents its first derivative and, although it is not directly related to the bending stiffness of the beam, it can provide more accurate results. The application of this index can be effective when the calculation of the curvature can't be performed correctly due to the issues described in the previous section.

Three remarks can be drawn:

- The method seems to be more sensitive to damage locations closer to the constraint, as shown in Figure 15b, in particular a damage located closer to the constraint led to a higher value of the damage index.
- Delamination placed between inner layers causes greater differences in the slope of ΔPOM, as shown in Figure 15a.
- The possibility to locate damage in the outer layers is strongly influenced by the position of the sensors, as shown in Figure 16.

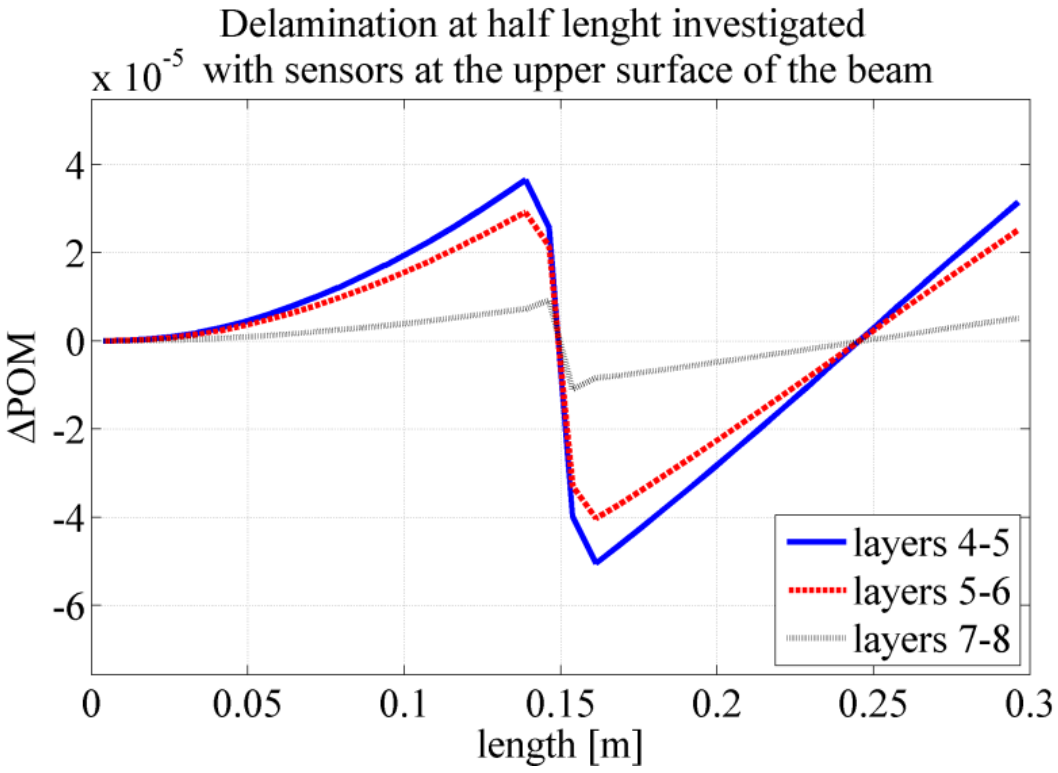

a)

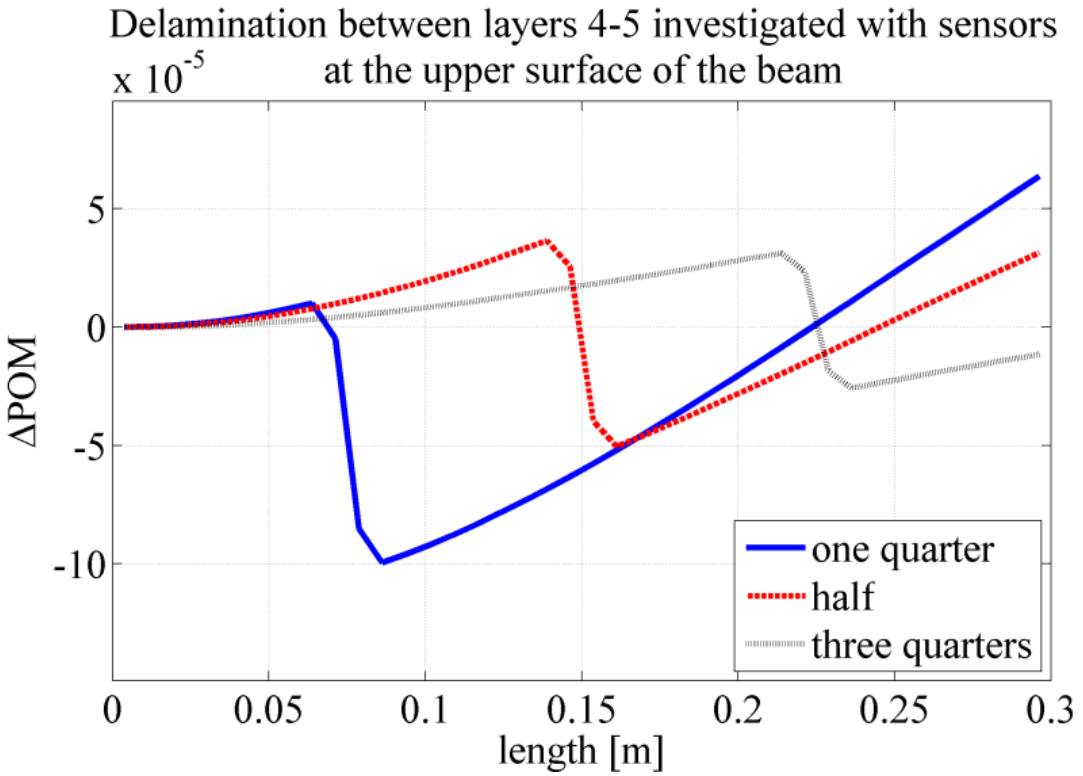

b)

Figure 15: Damage indices computed with the classic POD for the full width delamination. a) Variation of damage index through the thickness. b) Variation of damage index along the length.

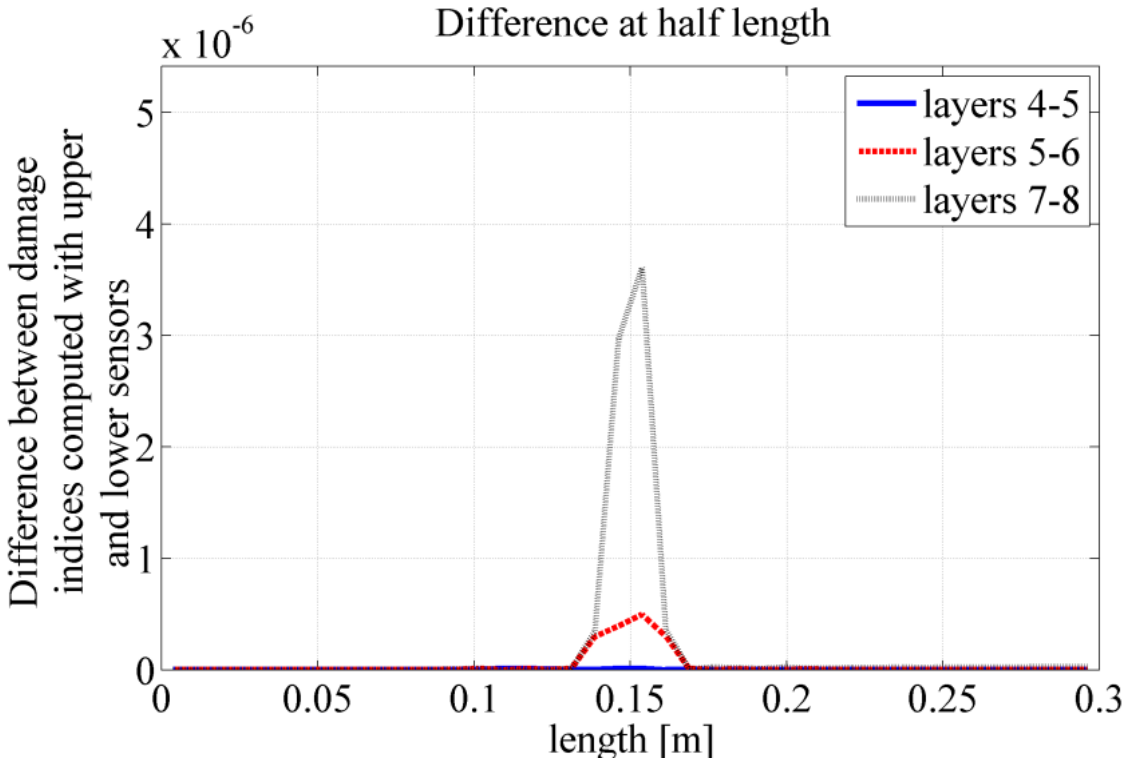

Figure 16: Difference in the ΔPOMs evaluated using upper and lower nodes data.

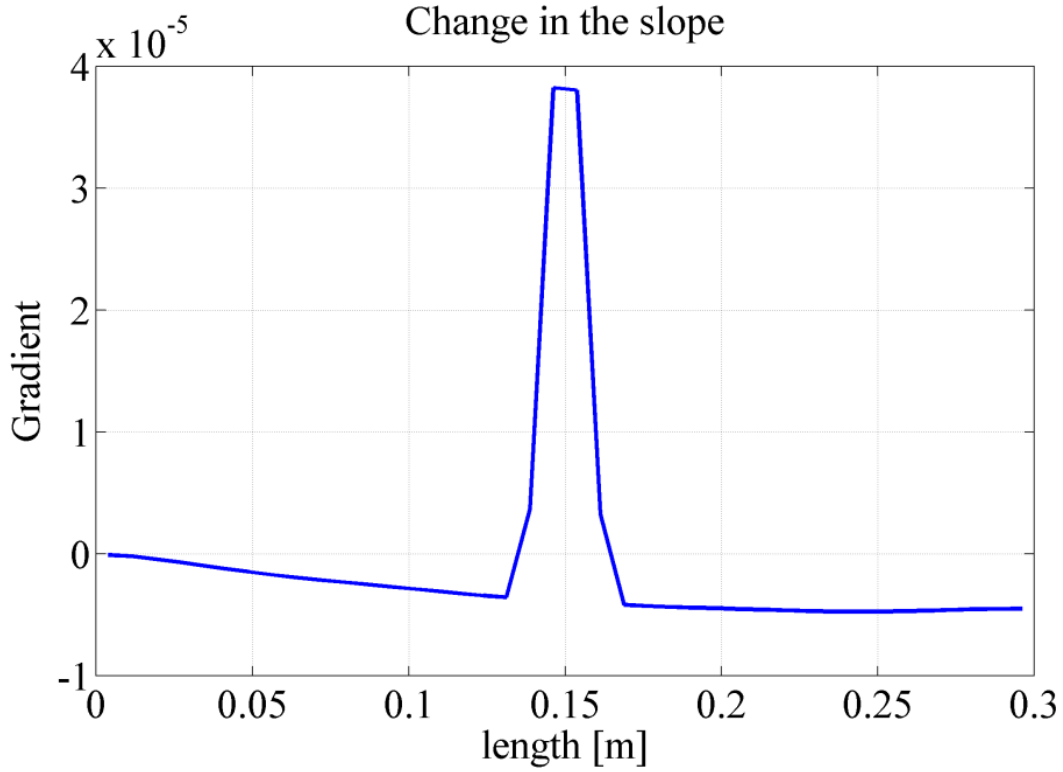

Figure 17: Change in slope of ΔPOM for a delamination placed between 4th and 5th layers at half length.

4.1.2 3-D solid model

Thanks to the three-dimensionality of the model, two sizes of damage were analysed: in the first case delamination affected the whole width of the beam, in the second case just two rows of elements, as shown in Figure 18. In the first case the analysis is conducted with the modal time integration method for all cases referring to the whole width delamination, the implicit method was applied only to the cases referring to the delamination at the half-length of the beam as an additional check which did not reveal any substantial difference with the other integration scheme. For the partial width damage, the implicit method was used as it provided more accurate results. This can be explained with the local variation of dynamics due to the small defect, which could not be completely captured by a modal superposition integration method.

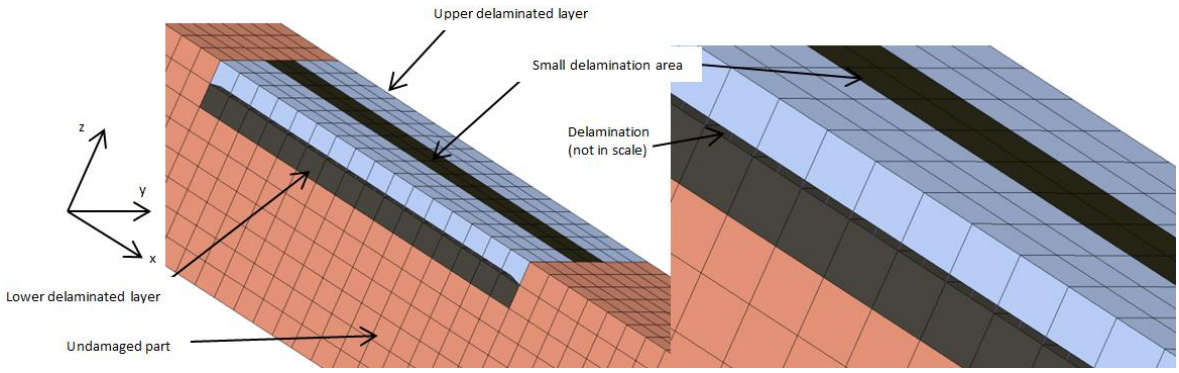

Figure 18: Delamination width: dark grey refers to the case in which the delamination affects just a portion of the width (small delamination).

In the case of whole width delamination numerical results in 3-D are very similar to those obtained with the 2-D model. However results seem to be slightly more sensitive to the position of the sensors. The following pictures show the results obtained with the partial width delamination a case which cannot be examined in 2-D. As it can be seen in Figure 19 the magnitude of the damage indicator is greatly reduced with respect to the case of whole width delamination and therefore it is more difficult to locate exactly the position of the damage because there is a global change in the shape of ΔPOM which partially hides the local change due to damage. In this case the application of the curvature as damage index seems to be necessary; this can be seen from Figure 20 and Figure 21. Now the damage is well defined for all the three positions along the length and also the differences between the evaluations with upper or lower sensors are presented.

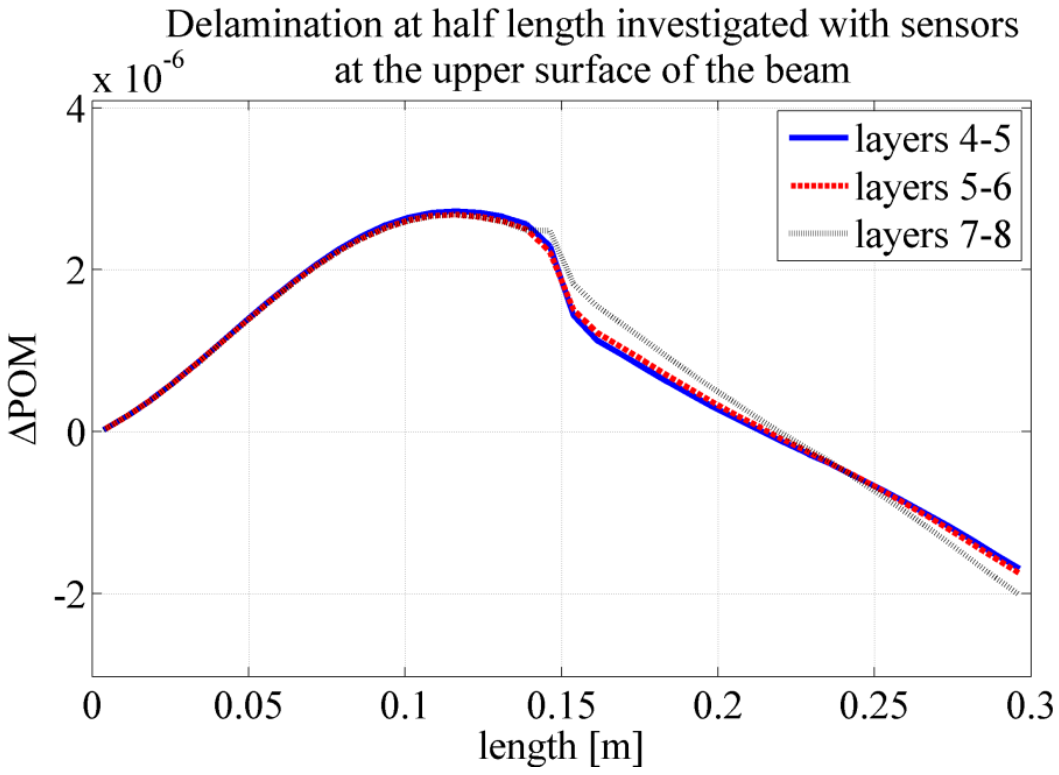

a)

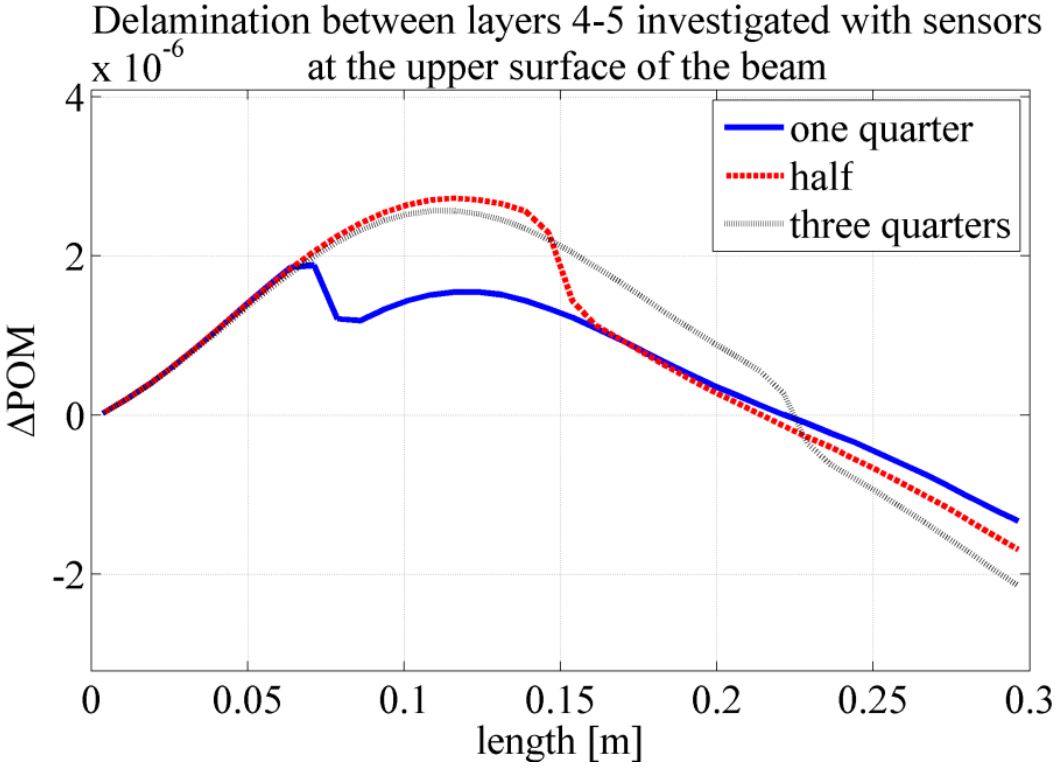

b)

Figure 19: Damage indices computed with the classic POD for the partial width delamination. a) Variation of damage index through the thickness. b) Variation of damage index along the length.

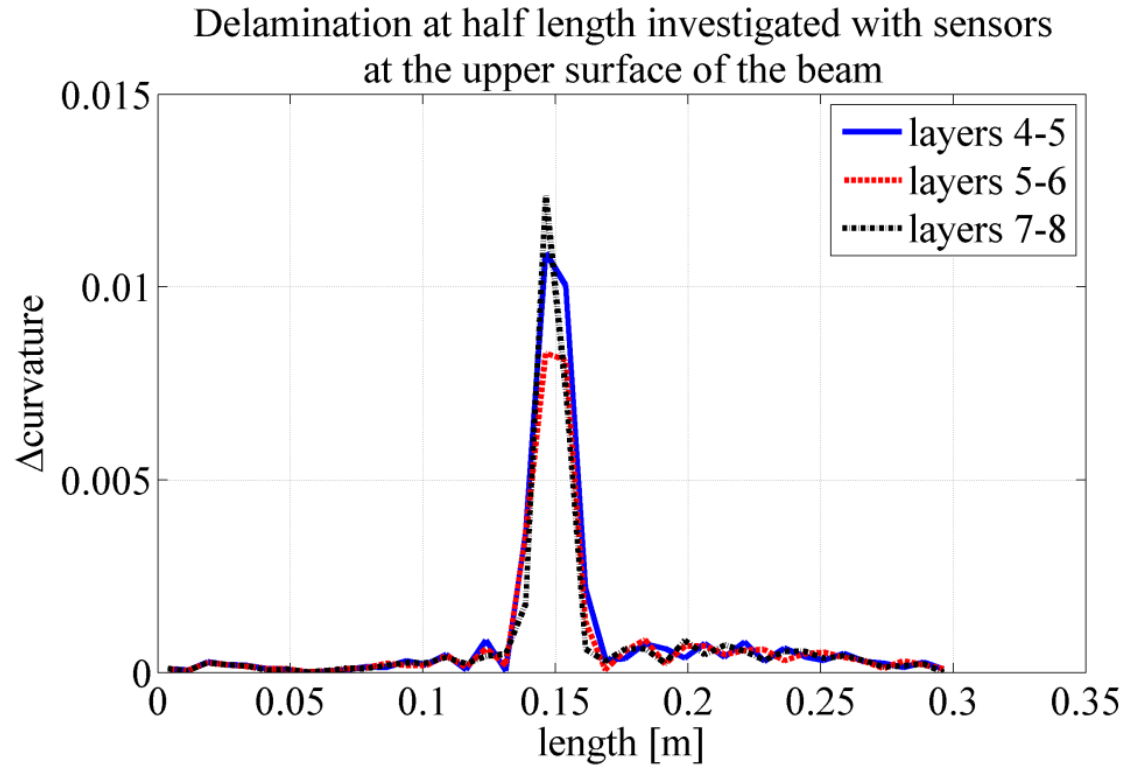

a)

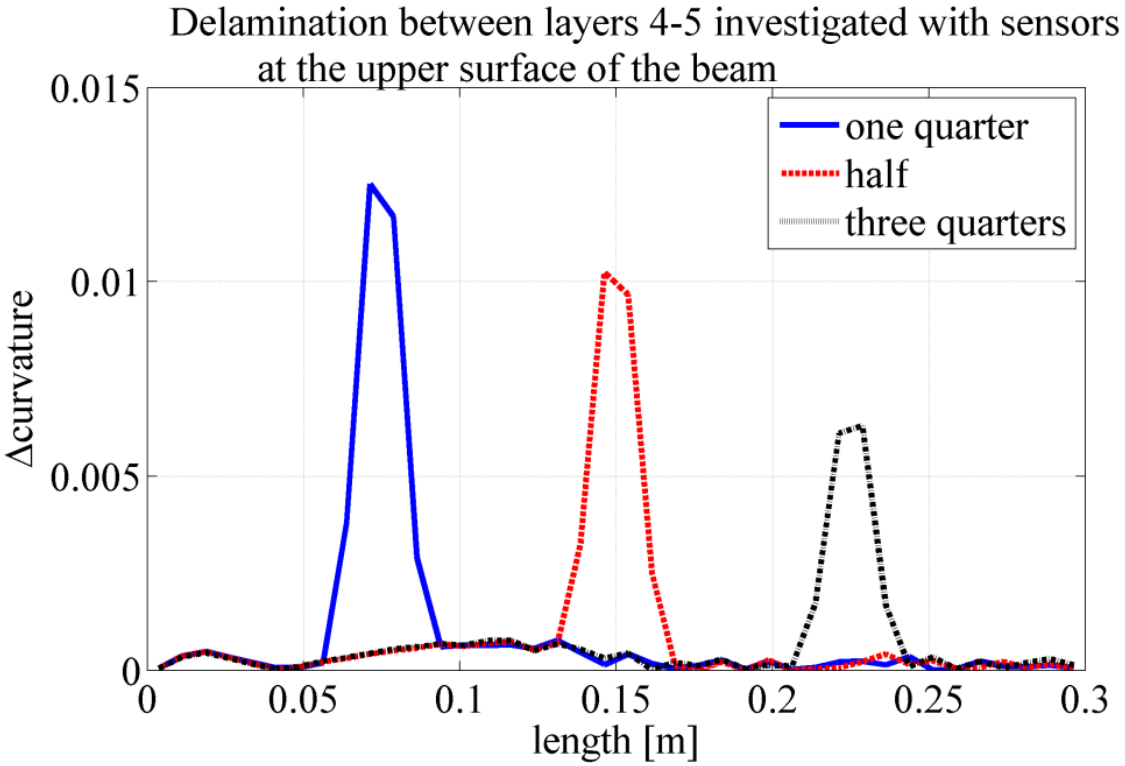

b)

Figure 20: Damage indices computed with curvature of the POMs for the partial width delamination. a) Variation of damage index through the thickness. b) Variation of damage index along the length.

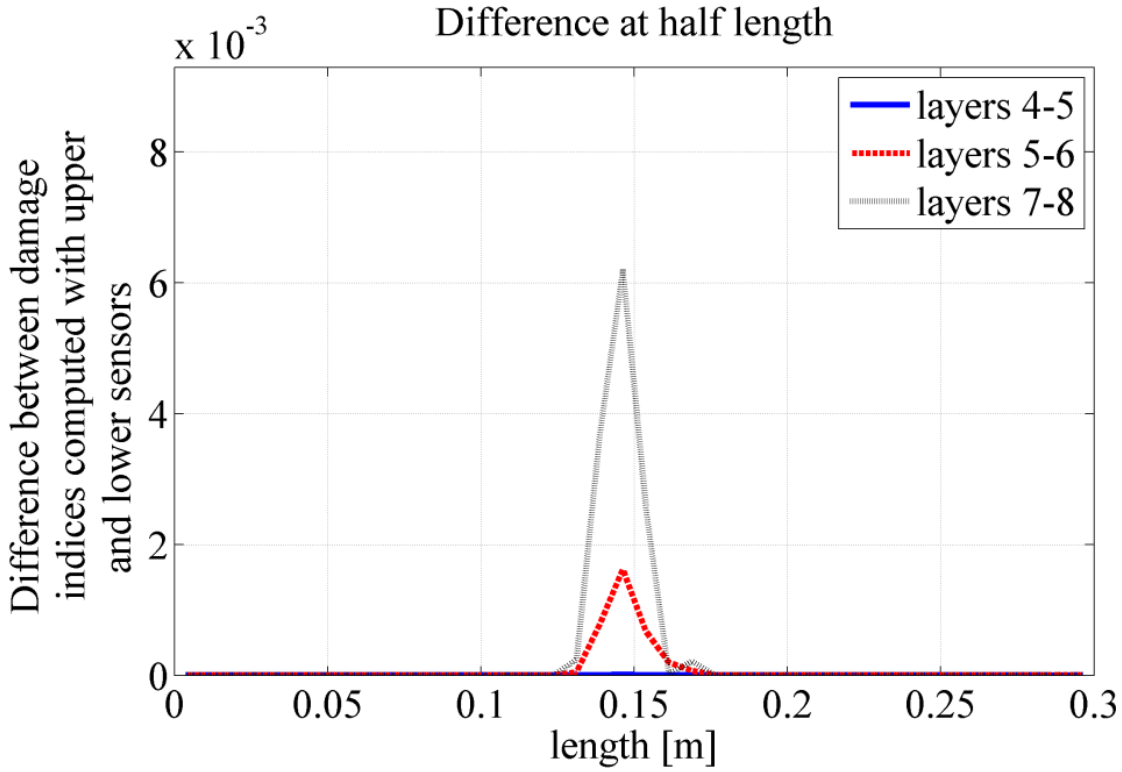

Figure 21: Difference in the curvature damage indices evaluated using upper and lower nodes data.

4.1.3 Application of the GSM to the composite beam case

The capability of the gapped smoothing method to locate damage in a beam, without using any information about the pristine status, is now addressed. The model under analysis is the 3d beam just investigated with the classic POD. Both full and partial width delamination are considered. The Some results for the damage detection are sown in Figure 22. It is clear that the damage is well detected.

Figure 23 shows the values of the normalized damage indices for the two types of damage and for their different locations. The conclusions which can be given for the damage detection results on the composite beam using POD and GSM are similar to the cases already presented:

- The damage index is higher when the delamination is placed closer to the boundary
- A delamination between the inner layers is better identified than a possible one in the outer layers; an exception is given by the short width delamination, in which the most external one is more easily detected than the other two
- The method can give an estimation of the entity of the damage, as wider delamination produces higher variation of the curvature

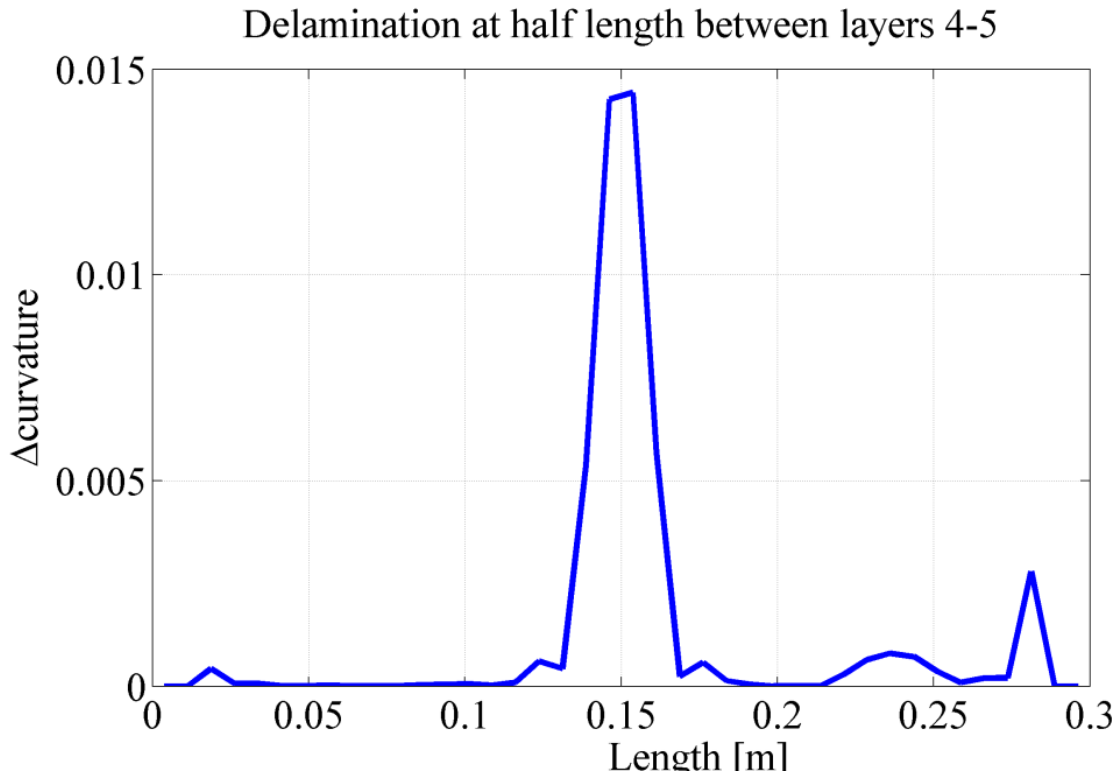

a)

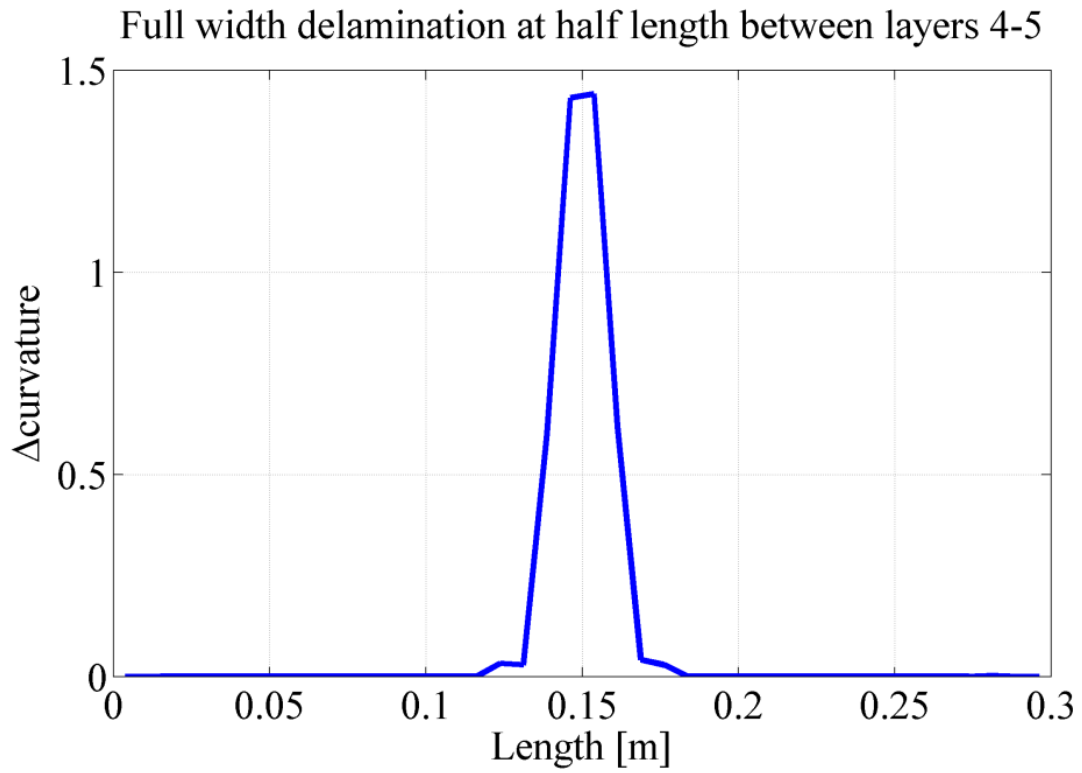

b)

Figure 22: Example of damage detection using GSM on the composite beam for a delamination placed at half length. a) Partial damage. b) full width damage.

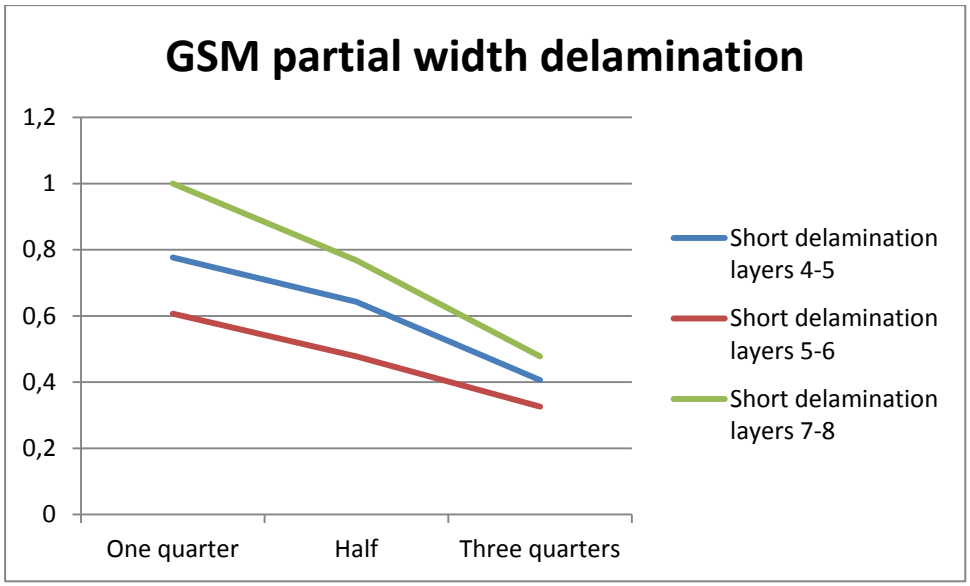

a)

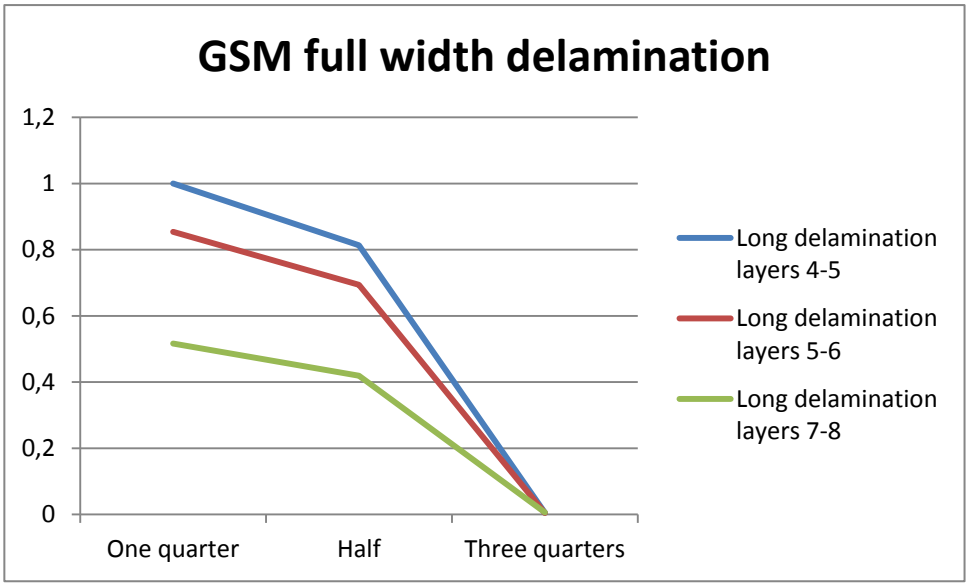

b)

Figure 23: Variation of damage index with the position of the delamination. a) Partial width delamination. b) Full width delamination.

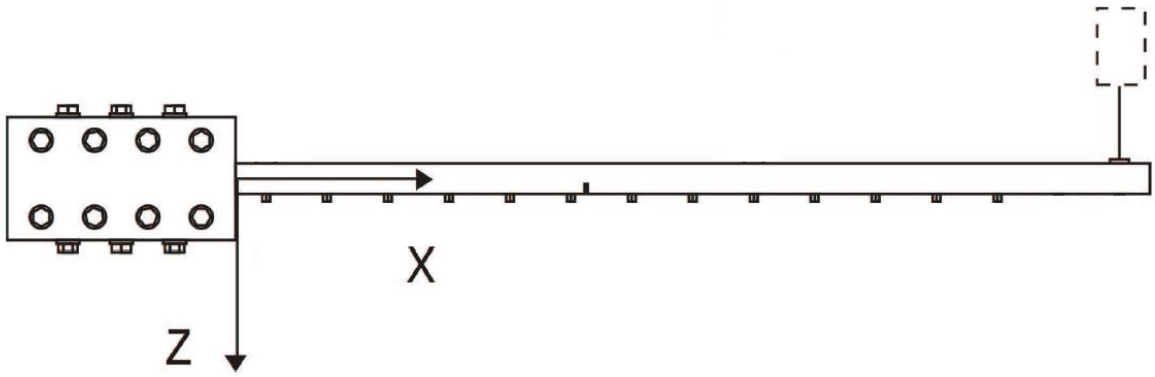

Figure 24: Experimental setup for the cantilever beam. The saw cut is visible after accelerometer 6; the position of the shaker at the end of the beam is also highlighted.

4.2 Experimental verification on a cantilever beam

The results obtained by Galvanetto in [13, 58] are updated in this section with the application of the advanced POD. In the first paper only the comparison between two different states of the beam were used to calculate the damage index. A first attempt to apply a smoothing technique on that experiment was performed in [58]. However in that case the smoothing technique was applied to the weighted POM, not to the curvature, and a numerical fitting of the experimental data obtained was performed. Now the analysis is extended using derivatives of the POMs and the GSM, without artificially increasing the number of data. The system under exam is a cantilever beam, with length L=600 mm and square cross section A=400 mm^2. The material is steel AISI 1030. 13 accelerometers, from x=20 mm to x=500 mm with 40 mm spacing were used to acquire the beam's response, under sinusoidal excitation at 40 Hz, produced by a shaker placed close to the free end of the beam. A saw cut of 1 mm was produced at x=230 mm, between accelerometers 6 and 7, Figure 24. The POD is applied and then the gradient of the POMs calculated. In particular the first two POMs are considered in the damage evaluation. The application of the curvature could not be accomplished, as the number of sensors used in the experiment was limited, and the space grid between sensors is too large (this is a typical issue when dealing with curvature calculation). In Figure 25 and Figure 26 it is possible to see how the method can locate the saw cut using data coming only from the damaged beam. Comparing the damage index computed with the gradient of the POMs to the one presented in [58], it is possible to notice that the value increases, especially when the second POM is considered.

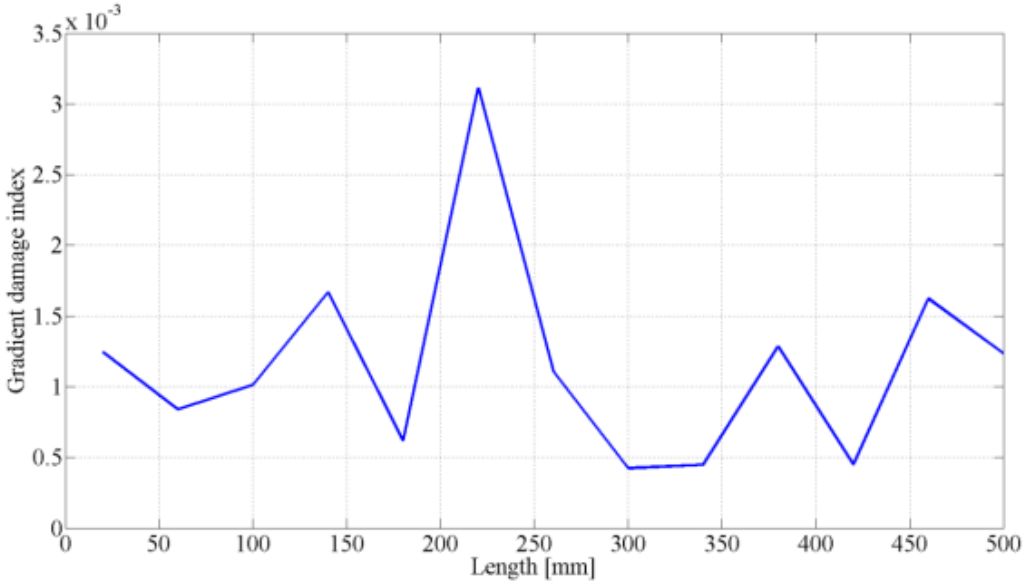

Figure 25: Experimental verification on a cantilever beam. First POM gradient damage index.

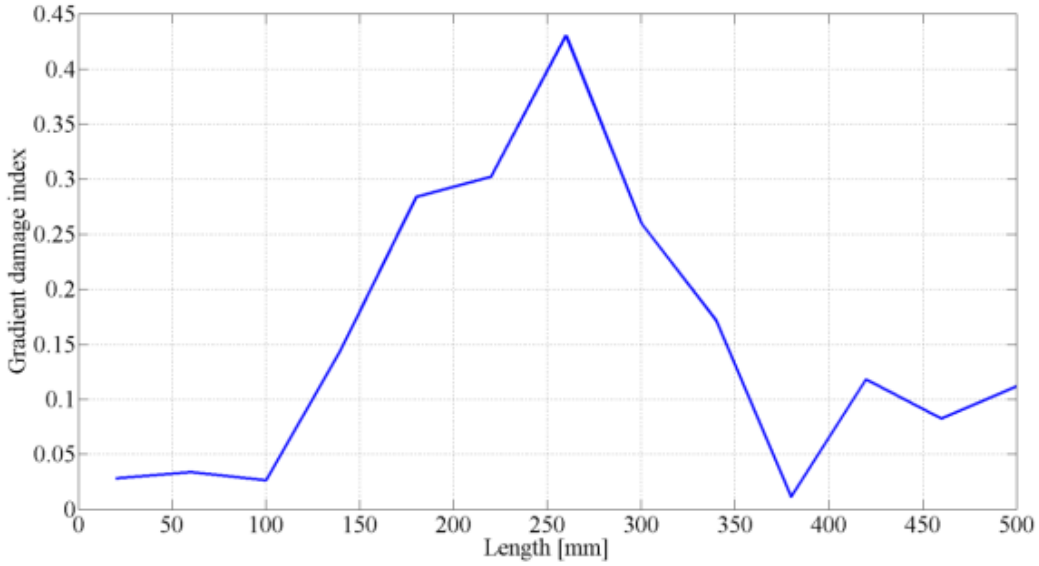

Figure 26: Experimental verification on a cantilever beam. Second POM gradient damage index.

4.3 Cantilever plate

After demonstrating the capabilities of POD and GSM to locate damage in a beam, numerical analyses were conducted on a composite cantilever plate. The dimension of the plate was 300x400 mm^2 in the plane and 2.7 mm in thickness. The laminate consisted of 8 plies with the following configuration [0°/45°/-45°/90°]s. The 0° fibres were aligned to the longest edge, while one of the short edges was clamped.

The load consisted in a harmonic concentrated force, applied next to one of the free corners, with frequency close to the first natural frequency of the system. A schematic representation of the plate is given in Figure 27a) while the FEM model, with damage and location of 117 sensors, in Figure 27b). The material properties are summarized in Table 3. In this case the choice of continuum elements in modeling the plate would have led to an extremely long computational time. For this reason the system was modeled with S4r shell elements provided by Abaqus. Even if they have some limitations with respect to the elements chosen to mesh the beam, their representation of the dynamics of a plate is reliable. One possible concern is given by the introduction of the damage. However this was modelled with facing shell elements, representing the plate over and under the delaminated plane, with gap elements between the corresponding nodes which prevented the elements to overlap. This revealed to be an effective approach. Two positions of the damage in the plane and three in the thickness were considered. The damage was introduced as a delamination of 4cm^2. The positions of the damage are shown in Table 4. Regarding the position in the thickness, three different simulations were carried for each damage position: between the 4^{th} and 5^{th} layers, between the 5^{th} and the 6^{th} and between the 7^{th} and the 8^{th}. A second concern regards the impossibility to check any variation of the damage index when sensors are placed on the bottom or top surface of the plate. This is due to the fact that shell elements, and therefore their nodes, are representative of the middle plane of the plate, while the thickness, given as a property of the element, is not physically

modelled. However this analysis was already performed in the beam case, so that no different results are expected for a bi-dimensional case.

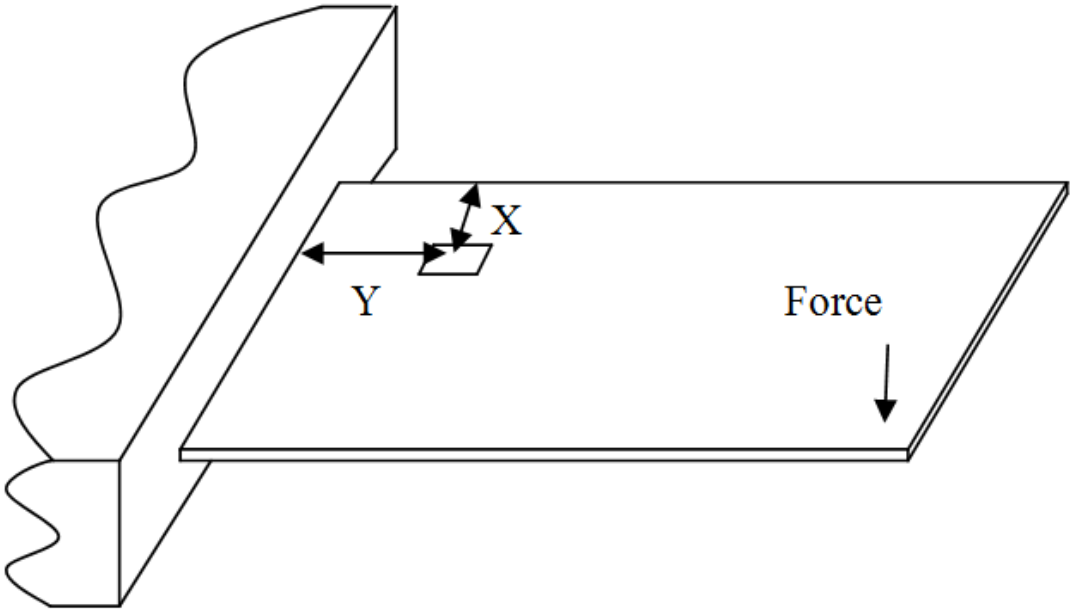

a)

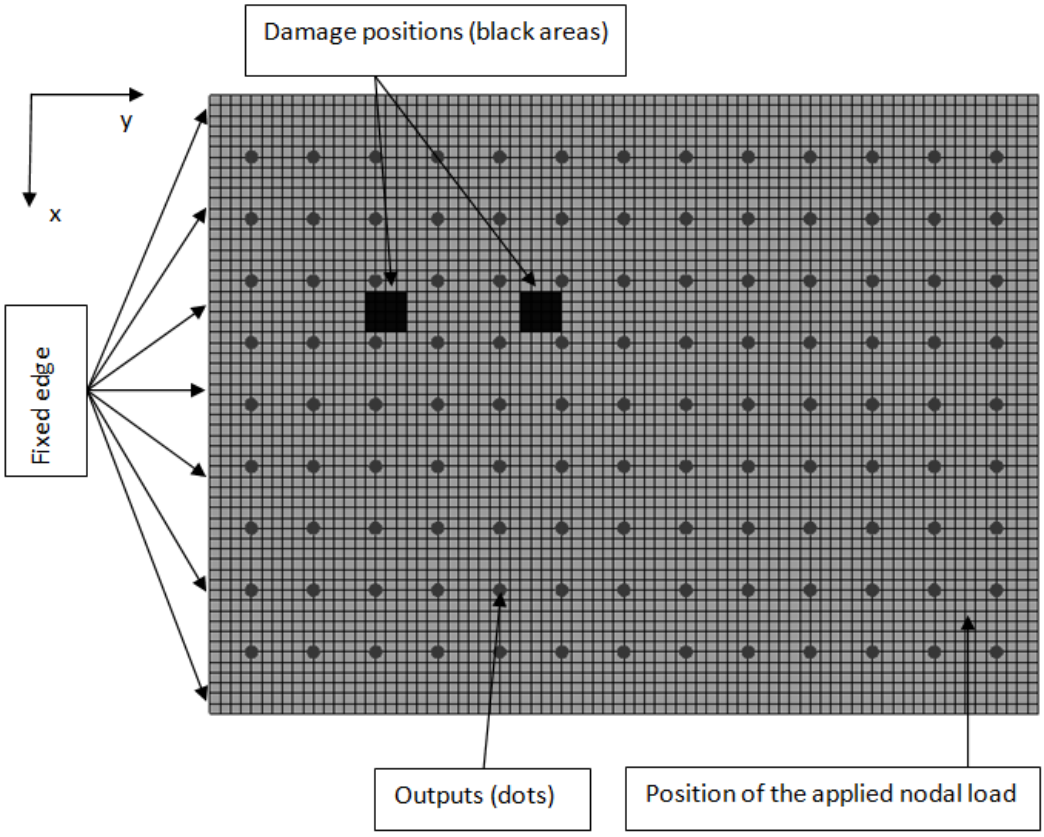

b)

Figure 27: a) Schematic representation of the plate. b) FEM model with highlighted the two damage positions, the sensor locations and the applied force.

Table 3: Mechanical properties of the material.

E11	E22	G12	G13	G23	v	ρ
140GPa	9.7GPa	5GPa	5GPa	5GPa	0.3	1715kg/m^3

Table 4: Position of the damage along the plate.

Coordinate	Position 1	Position 2
X	105mm	105 mm
Y	85 mm	160 mm

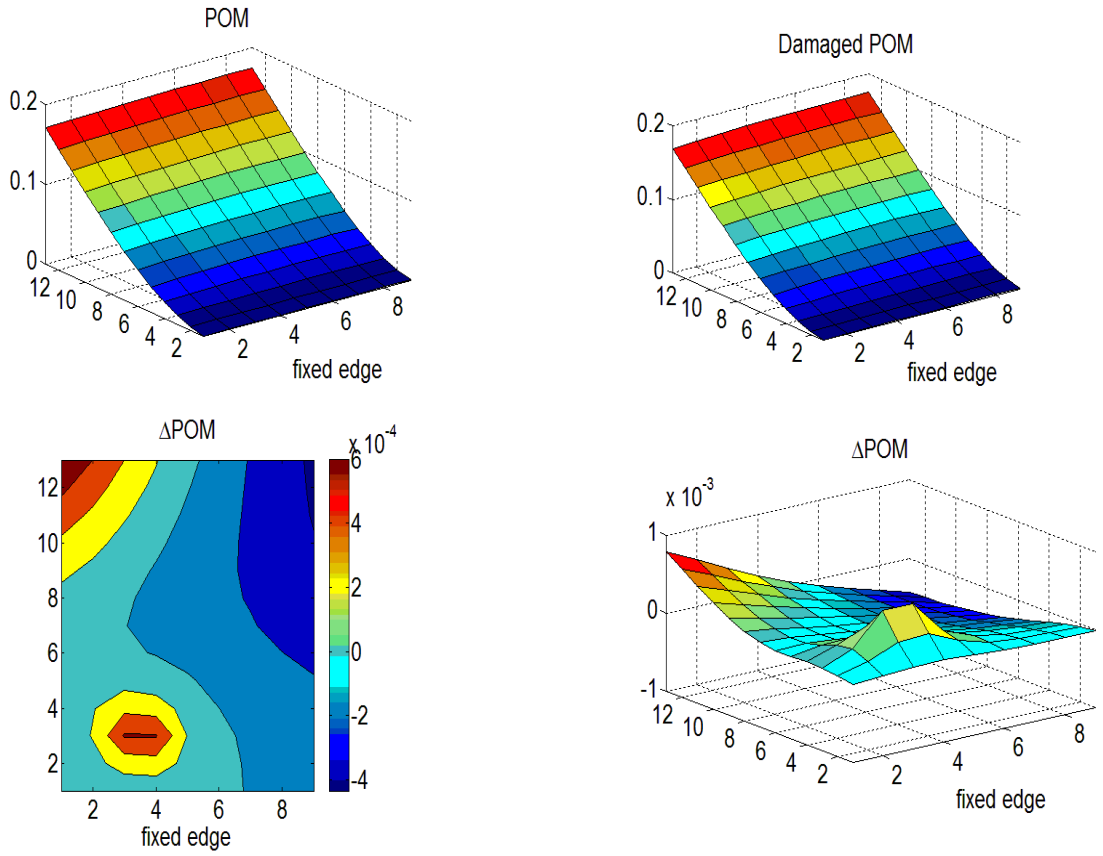

Figure 28: Result obtained for damage at position 1.

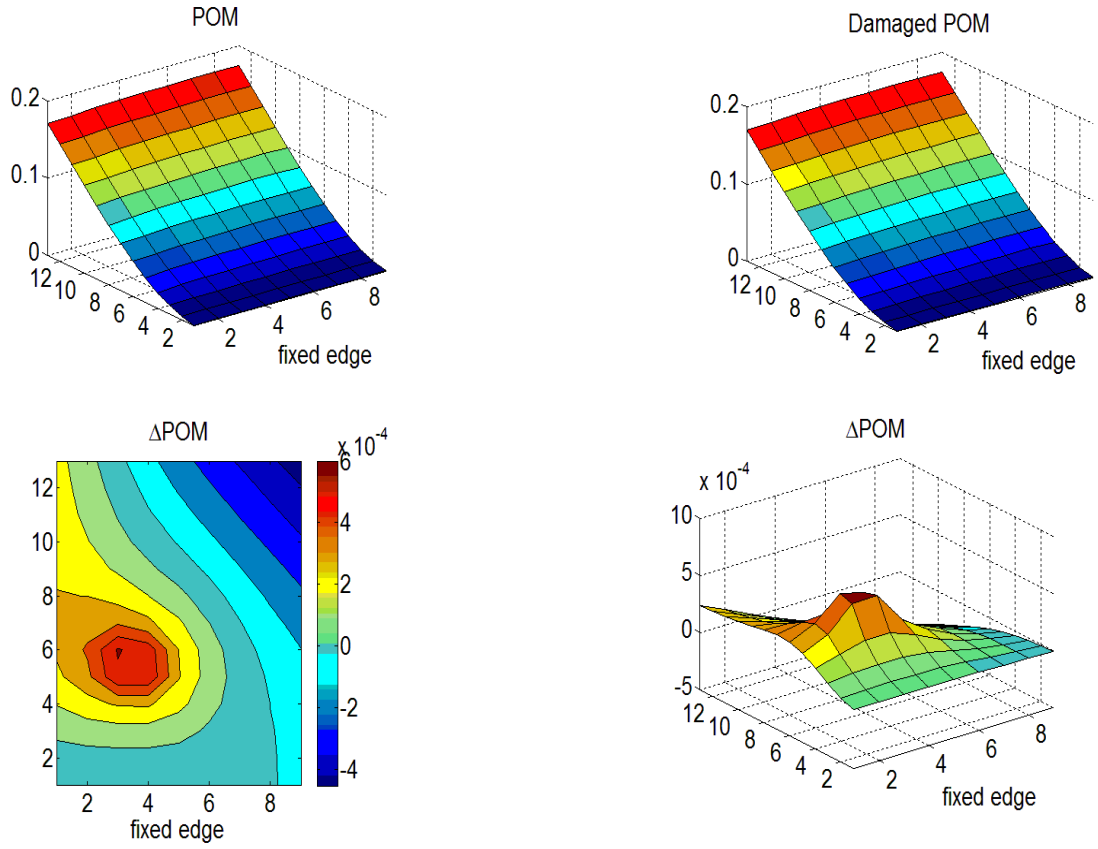

Figure 29: Result obtained for damage at position 2

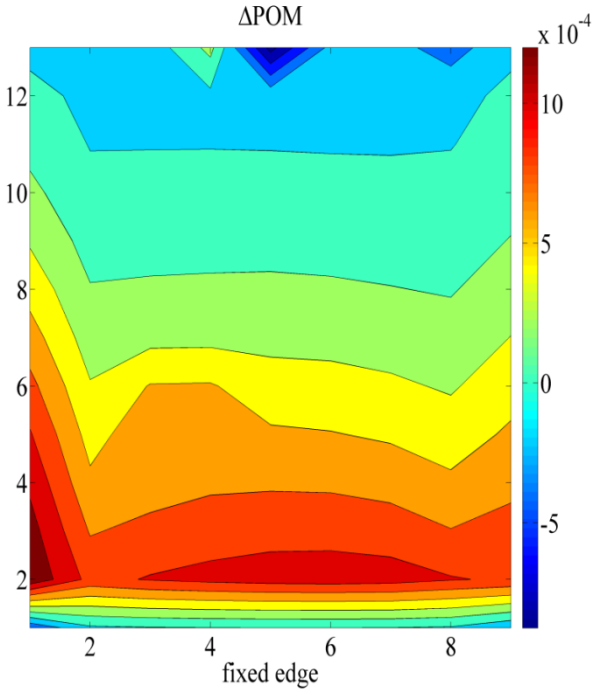

Figure 30: Example of damage index after the application of GSM to the weighted POM.

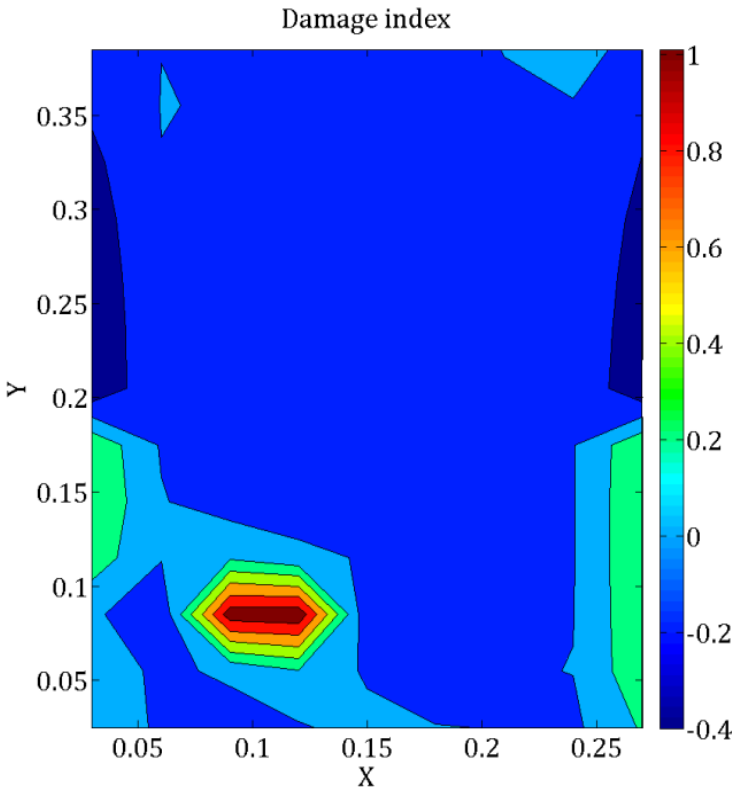

a)

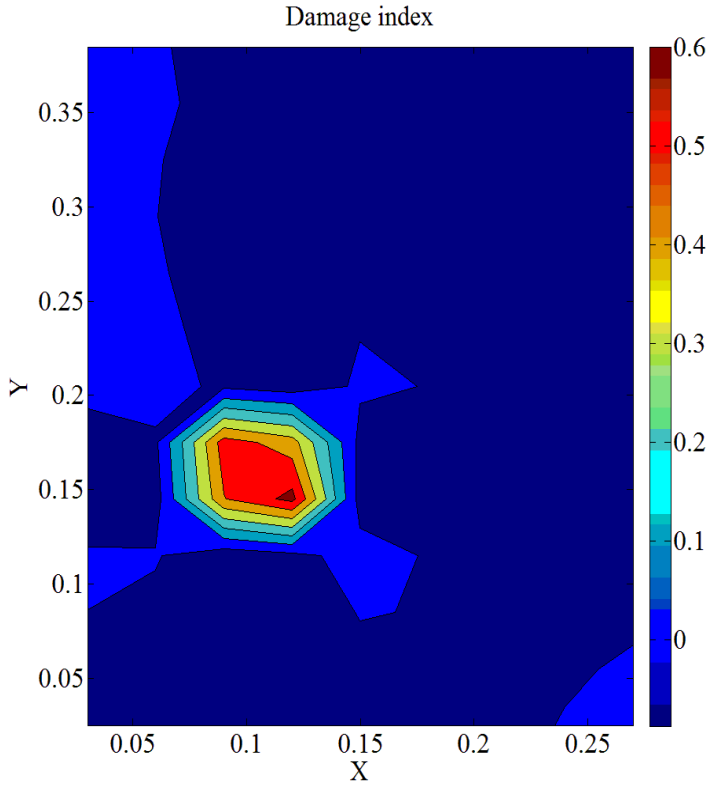

b)

Figure 31: Results obtained with the curvature. a) Damage in position 1. b) Damage in position 2.

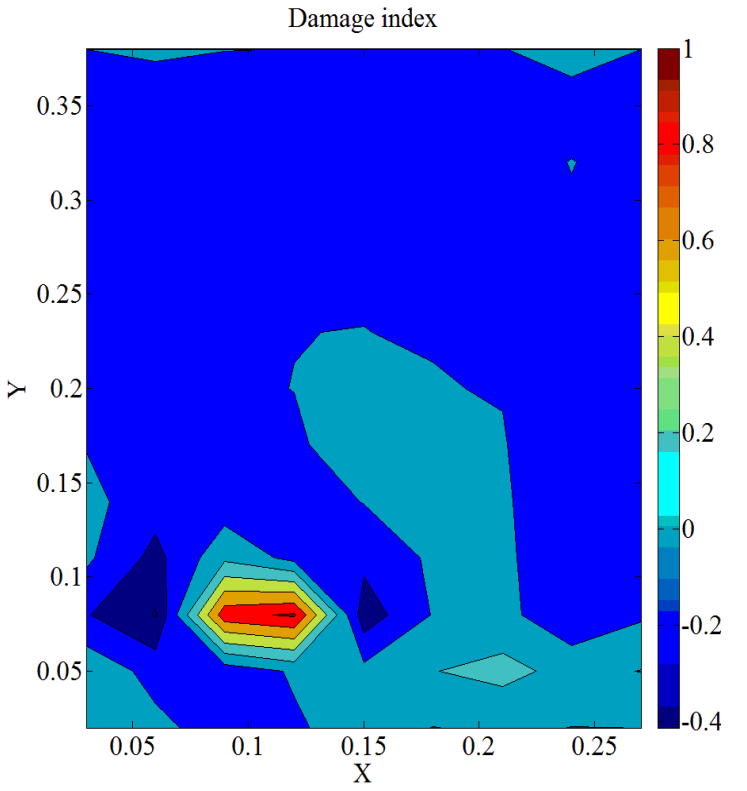

a)

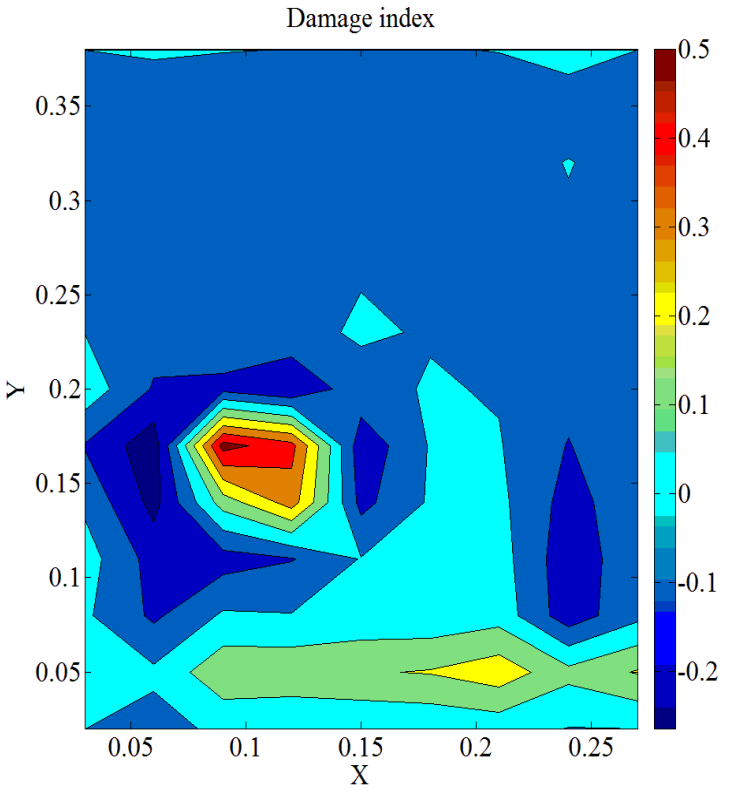

b)

Figure 32: Results obtained with the smoothing technique. a) Damage at position 1. b) Damage at position 2.

From Figure 28 to Figure 33 several numerical results are presented. Some considerations can be derived from them. First of all the damage index calculated with the curvature is much higher than the one

computed with the simple POM. Furthermore the high level of damage index is concentrated only around the damage in Figure 31 and Figure 32, while in the cases represented in Figure 28 and Figure 29 there is an oscillation of the damage index close to the free edge of the plate. It is important to notice that this behaviour was already seen in previous works on POD [14, 63]. This is due to the fact that the curvature can exaggerate minor singularities between consecutive points, while it is not sensible to a general trend of the ΔPOM.

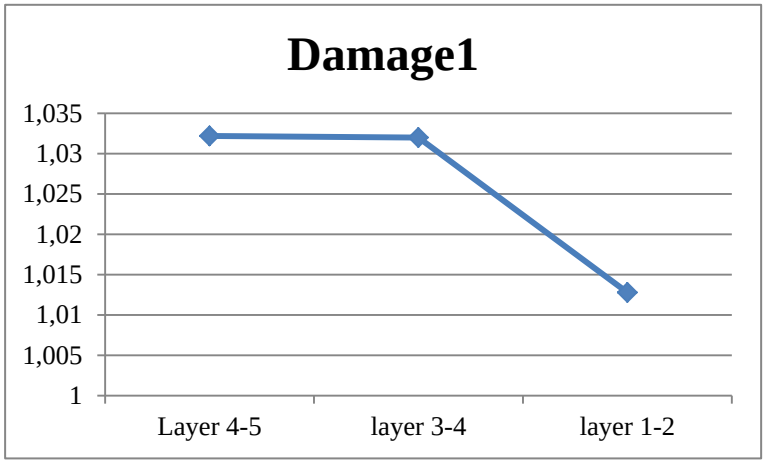

a)

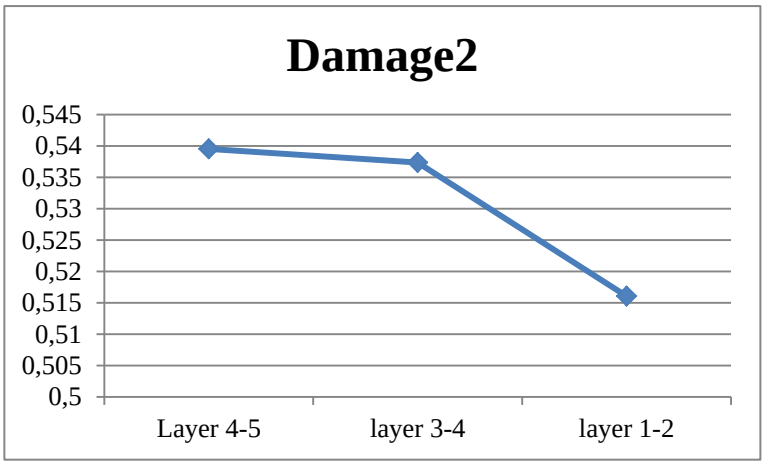

b)

Figure 33: Maximum values of the damage index with respect to the layer interested by the delamination. a) Position 1. b) Position 2

The GSM presented in Section 3.2 was applied to this system. Figure 32a) and b) show the results obtained using only the dynamic response of the damaged plate. The results obtained are comparable to the classic POD approach an in all the cases analysed, damage was correctly located. It was found that the level of the damage index resulted to be a bit smaller than the one calculated with the standard POD and that it is less concentrated around the damage, as some spurious peaks appears around it. This however didn't affect much the result. The application of the GSM to the POM, instead that to the curvature, didn't provide results similar to the classic POD, Figure 30. This reinforces the idea that, for damage detection using the POD, curvatures of the mode shape are essential in order to obtain reliable results.

4.4 Experimental verification on a cantilever plate

Another experimental verification of the method was carried out on a cantilever plate. This was excited with a shaker, placed close to one of the free corners. The velocity of several points in the plate was acquired through a laser scanner vibrometer (LSV), see Appendix 4. These experiments though didn't provide good results at a first glance, highlighted that the simple curvature of a mode shape, computed with the central difference method, cannot be properly evaluated when noise is present in data. In this section some examples of data collected with the LSV are presented. As the POD results were not the expected ones, a deeper analysis on the effects of noise will be presented in the following section.

4.4.1 Filtering data

The time history collected resulted to be very noisy, especially in the points very close to the constraint, Figure 34 and Figure 35. In order to obtain better results with the POD, data were filtered with a low pass filter, using the command "filtfilt" of Matlab, and the phasing shift was applied to the filtered data, Figure 36. However the shape of the POM still resulted to be irregular, especially closer to the free edge. To verify the actual mode shapes of the system, the software Testlab was used. However, also in this case, the shape of the first mode resulted to be irregular. The actual reason for this inconvenient is unknown, but a possible explanation can be found in mistakes of the acquisition software while computing the amplitude of the signal. Probably small differences in the reflectivity of the plate caused a non-homogeneous reflection of the incoming laser beam

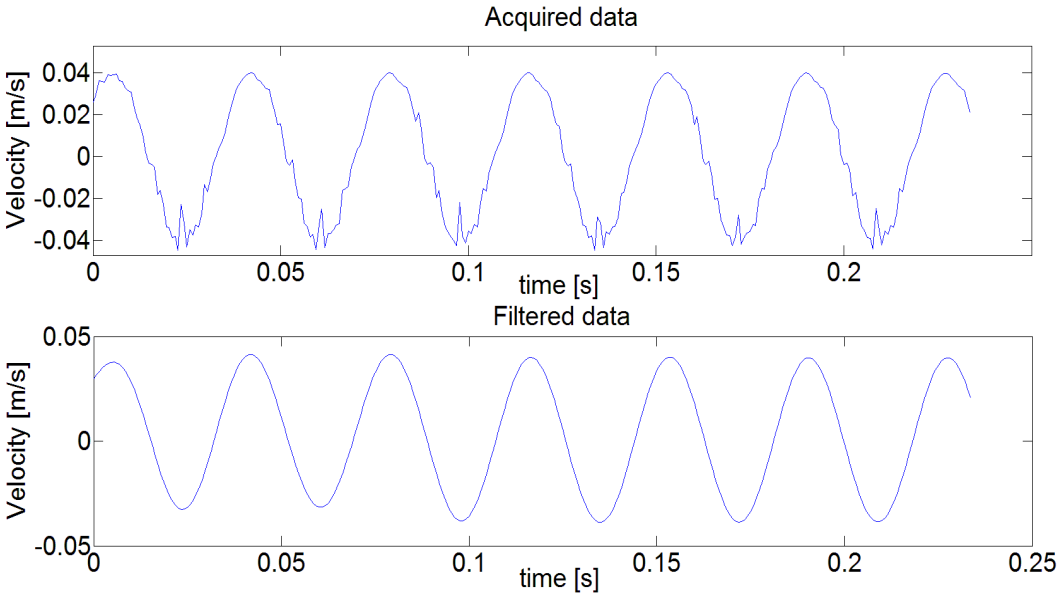

.

Figure 34: Reducing the amount of noise. Point close to the free edge.

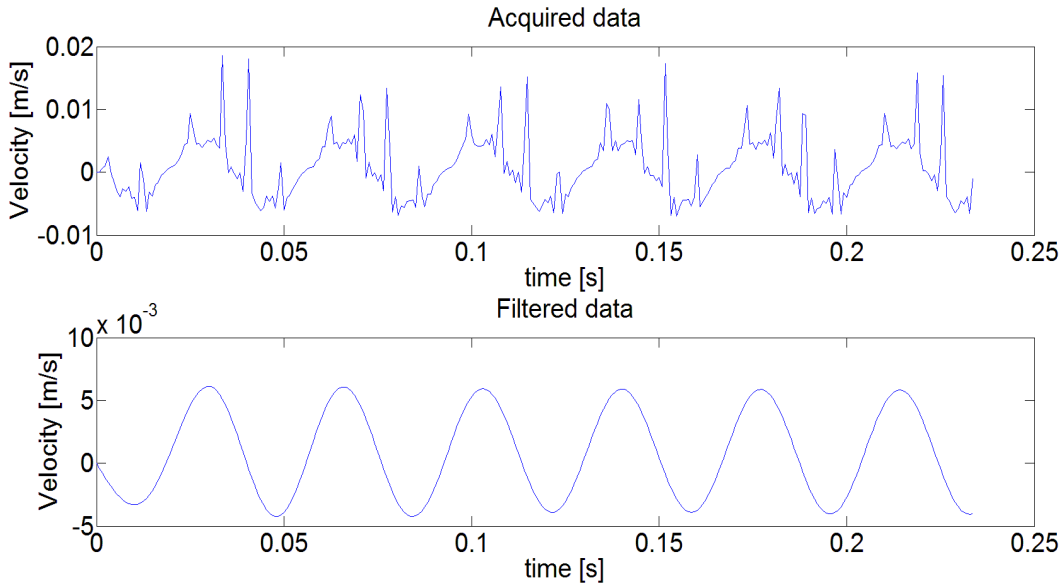

Figure 35: Reducing the amount of noise. Point close to the constraint.

Unfortunately even with filtered data, the results didn't reflect the numerical ones. Even if the overall shape of the POM was similar to the numerical one, when the curvature was calculated the effect of the imperfections on the POM, due to residual noise and other experimental issues, prevented not only to detect damage, but also to compute the expected curvature of the corresponding mode. This issue revealed one of the greatest problems which arise when this parameter is used in damage detection. In literature this topic has not been discussed deeply. A contribution on that can be found in [65] in which an isotropic beam was analysed. In the following section details of this reference will be given and an analysis with POD on noisy data will be computed on the same system and on the previous composite plate.

4.5 Influence of noise in the calculation of the curvature

One of the main concerns about using the curvature for damage detection technique is its sensitivity to the presence of noise. This is obviously a great problem when implementing a damage detection technique, especially if the target is to apply it not in a controlled environment. An investigation of this sensitivity was carried out by Cao and Qiao [65] on an analytical model of a cracked beam. The technique consists on the calculation of different curvatures and the application of different filters to them in order to reduce the amount of noise. In this section finite element model, representative of the mentioned analytical one, is presented. Results obtained with the POD are comparable to the ones in [65].

After showing the capability of POD to perform also a multi-resolution curvature analysis on a cantilever beam, the method is extended to a bi-dimensional case. The system under exam is the plate described in Section 4.3. In this case no damage was introduced in the plate. A certain amount of noise was added to

data and different curvatures were calculated. Experimental verification on the system described in Section 4.4 is given below.

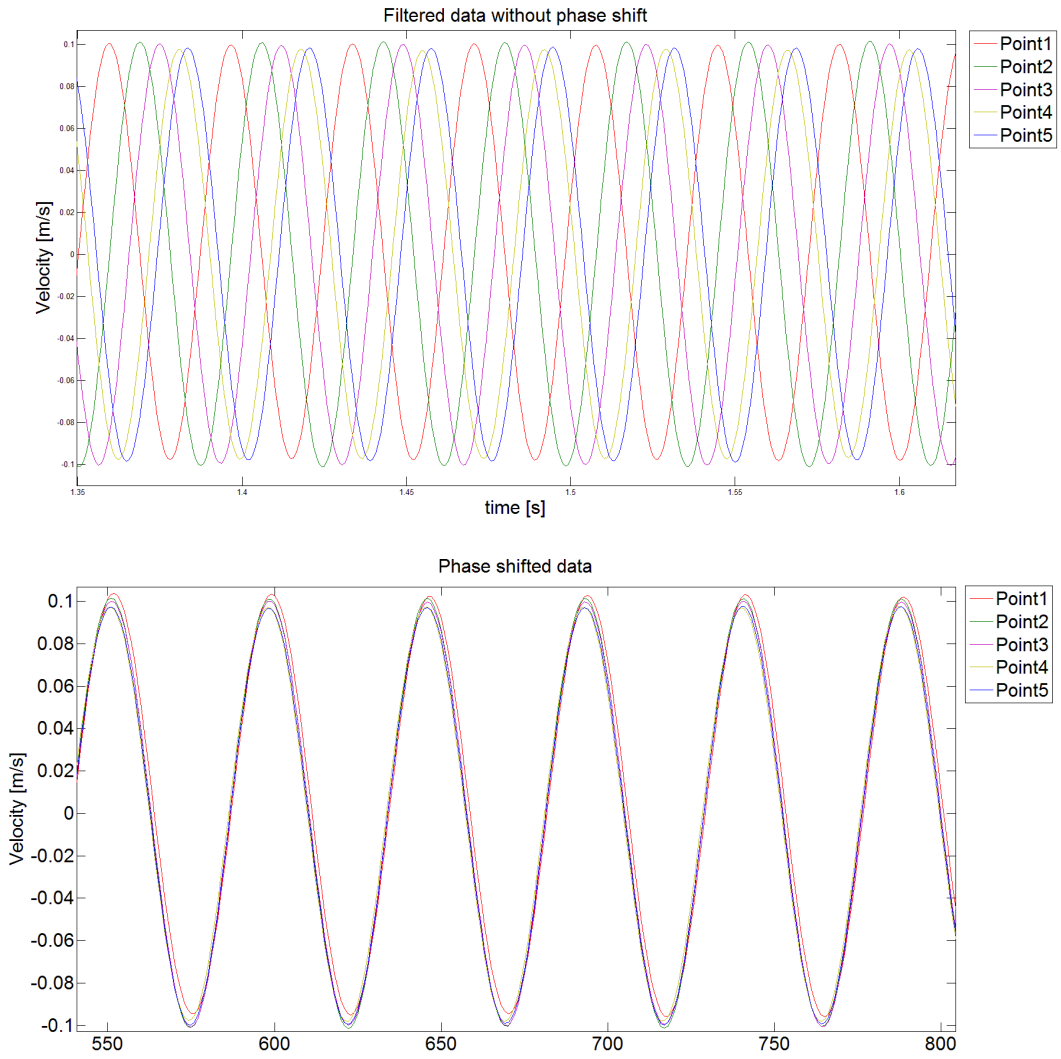

Figure 36: An example of data. a) Before phase shift. b) After phase shift.

4.5.1 Modified à trouse Laplacian operator

The equation used to calculate the curvature of a beam was expressed in section 3.1. With the exception of the denominator, that equation represents the convolution between a mode shape $\varphi(x)$ and an operator l *= [1 -2 1]*, which is hereafter called "Laplace operator". The Matlab expression for convolution, which can be found in the help manual of the software, is:

$$\varphi''(k) = \sum_j l\,(j)\varphi(k-j+1) = \varphi * l \qquad \textbf{4-1}$$

In order to prevent the calculated curvature to be affected by noise, a modified Laplace operator is used:

$$l_j = \left[1, \theta_j, -2, \theta_j, 1\right], \quad j \in N \qquad \textbf{4-2}$$

θ_j is a vector containing j-1 zeros. The generation of these l operators is very similar to the à trouse wavelet transform [74]. This is why here is called à trouse Laplace operator. In this way a different number of l operators can be produced, depending on j. The different curvatures are then called multi-resolution modal curvatures. A coarser resolution has the capability to overlook at the noise in the curvature, reflecting just structural variations. Examples of different Laplace operators are given in the following equations.

$$l_1 = [1\ , -2\ , 1] \quad \textbf{4-3}$$

$$l_2 = [1, 0, -2, 0, 1] \quad \textbf{4-4}$$

$$l_3 = [1, 0, 0, -2, 0, 0, 1] \quad \textbf{4-5}$$

4.5.2 Results for the cracked beam case

A finite element method (FEM) model of the cracked beam proposed in [65] was analysed with the POD. Data obtained from the numerical model were corrupted with white gaussian noise with a signal to noise ratio (SNR) equal to 50. In Figure 37 it is possible to see the main POM of the beam and its curvature calculated with Equation 3-2. It is clear that the amount of noise has a negligible influence on the POM but it completely hides not only the damage, but also the overall shape of the curvature. In Figure 38 all the different orders of curvature, evaluated from the main POM, are presented. They were calculated using different Laplacian operators, up to the eighth order. The ellipse highlights the position of the crack in the model. As it is possible to see the use of higher order Laplacian operators increases the possibility to detect damage with further application of smoothing techniques, such as the already proposed GSM. Results obtained with this technique are comparable to the reference ones [65].

It is worth to underline that the application of a convolution technique creates discontinuities at the edges of arrays. The higher the order of the Laplacian, the lower the accuracy that can be obtained at the boundaries of the beam. To overcome this problem a third order polynomial interpolation can be used at the boundary grid points or, in alternative, the backward or forward finite difference method, instead of the central one. However as the level of noise increases, this boundary effects become more and more relevant. This is obviously a limitation of this approach as a damage placed close to one end of the beam cannot be identified. Anyway for real application the positions of sensors must be carefully studied in order to obtain the desired area of inspection. This obviously can include also the issues regarding the different orders of curvature.

The two main differences between this approach and the one presented in [65] are that the dynamics of the system is calculated through the POD and that in this case the noise was added to the time response of the system and not to the mode shape. In all the figures presented in this section, the number of grid points used to perform the analysis was 121. A larger number of points increased the resolution on the

crack detection. Furthermore Laplacian operators with higher orders usually require lots of grid points to compute the convolution. However in real applications it is usually difficult to deal with a high number of sensors.

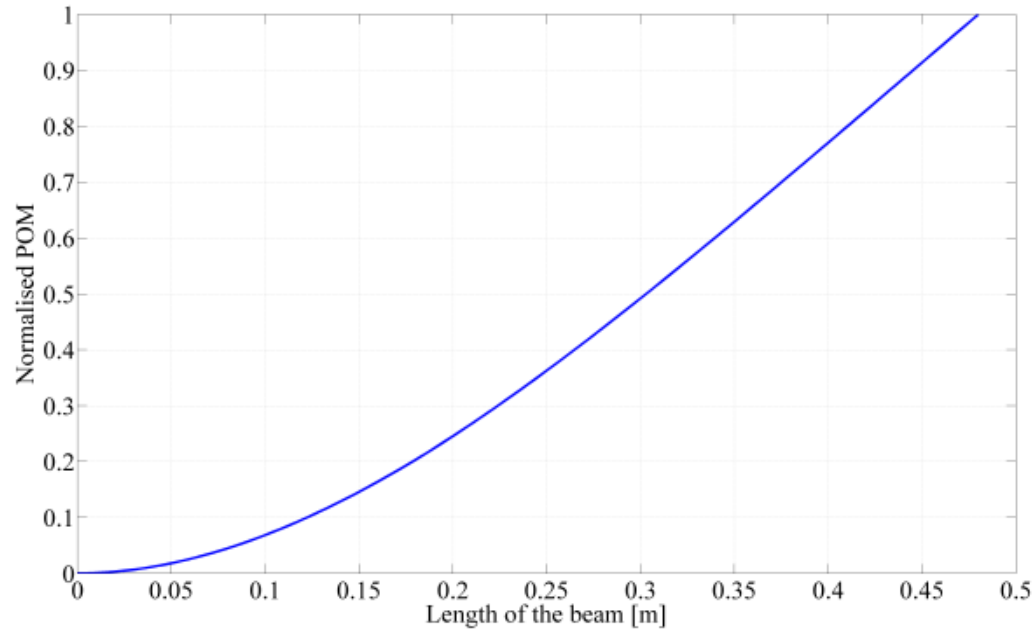

a)

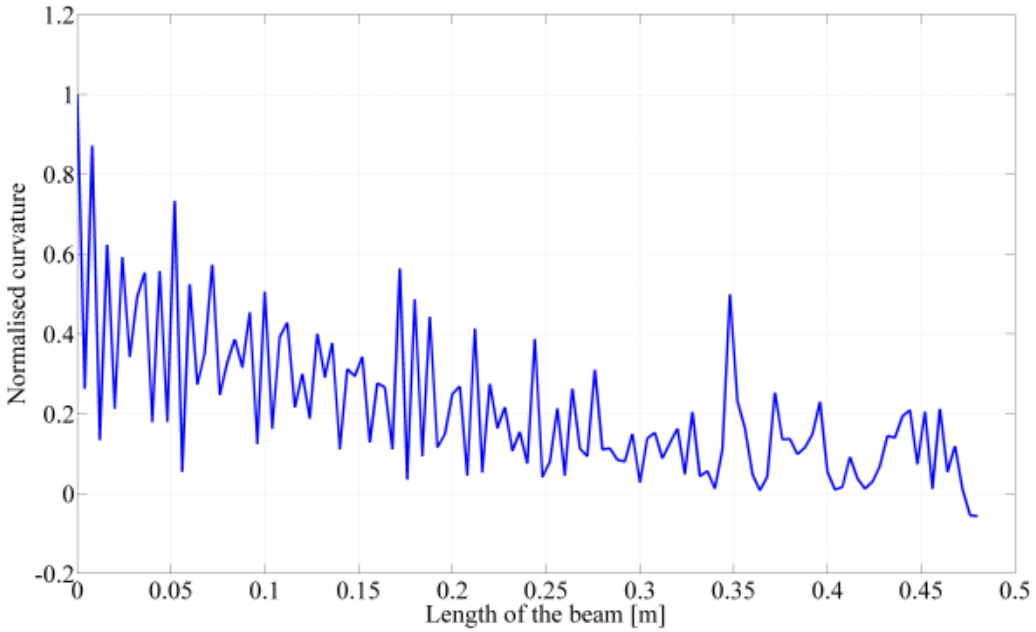

b)

Figure 37: POD result after the addition of noise. a) POM. B) First order curvature.

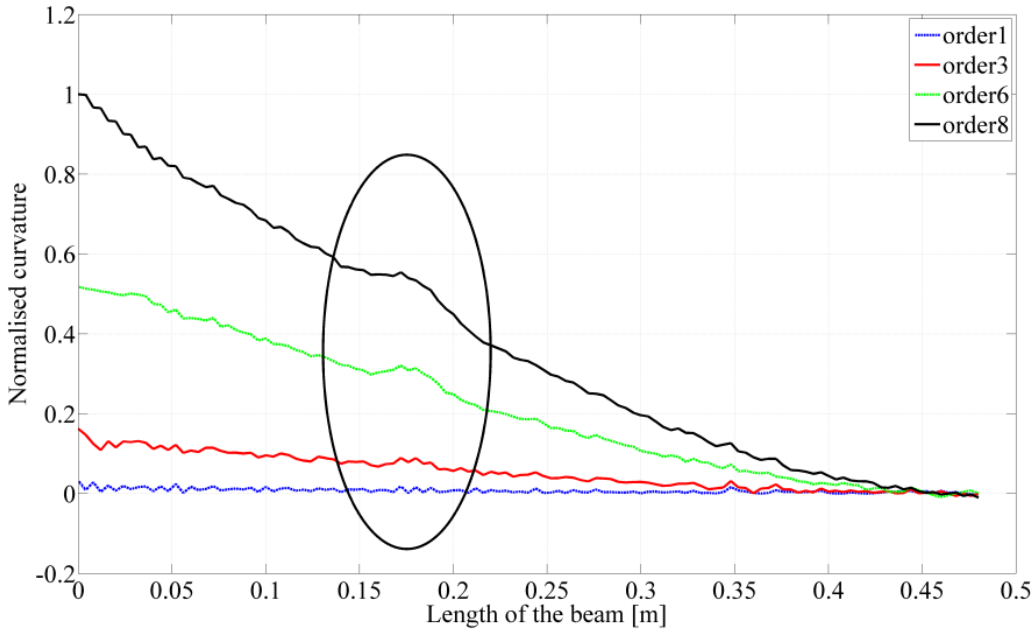

Figure 38: Comparison of different curvatures.

4.5.3 Extension to a plate case

After the application of POD was validated with a comparison to an analytical model, the method is extended to a two-dimensional case. The model under exam is the composite plate described in Section 4.3. In this case, to study the effect of the Laplacian order, the number of output positions is 1008. This is due to take into account the boundary effect explained previously. Even for this case the amount of noise hides completely the curvature as shown in Figure 39. In order to overcome this issue, different curvatures were calculated using up to the eighth Laplacian order. From Figure 40 it is clear that the methodology proposed is suitable also for a two-dimensional case. An example of the method applied to the experimental case described in Section 4.4 is given in Figure 41. In this case, due to the limited number of sensors (117), only the third order Laplacian for the curvature could be properly calculated. However, also in this case the improvements in curvature calculation are remarkable. This approach is hence suitable for a possible application on damage detection. Anyway still some issues about the boundary conditions and the number of outputs available have to be investigated in order to produce a reliable damage detection algorithm.

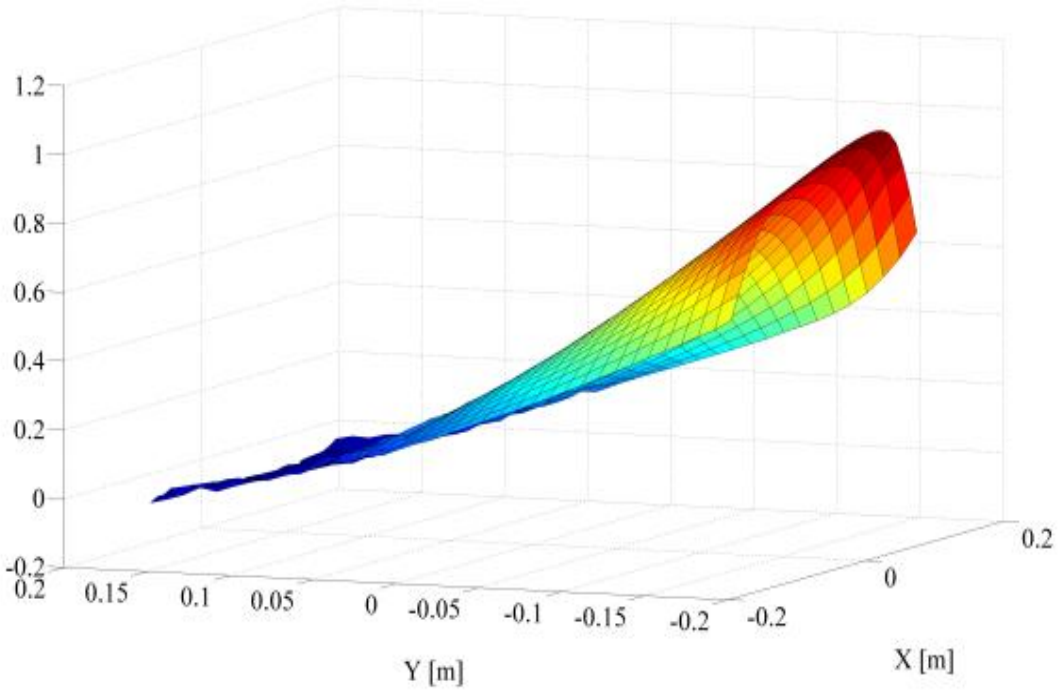

a)

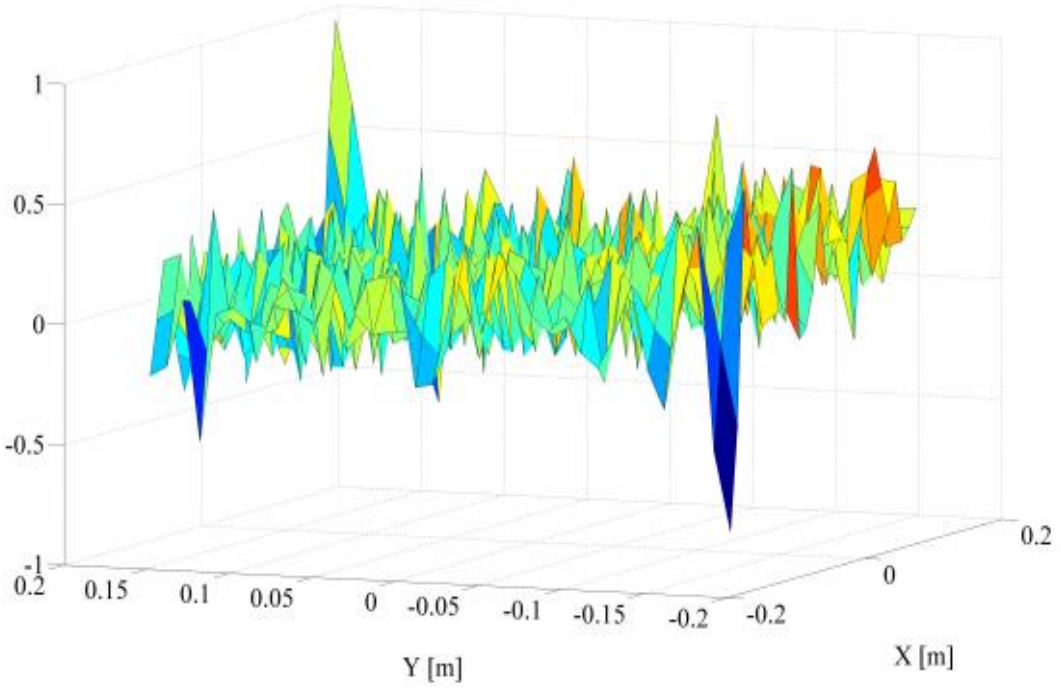

b)

Figure 39: example of standard curvature normalised to 1, calculation before and after adding noise to data.

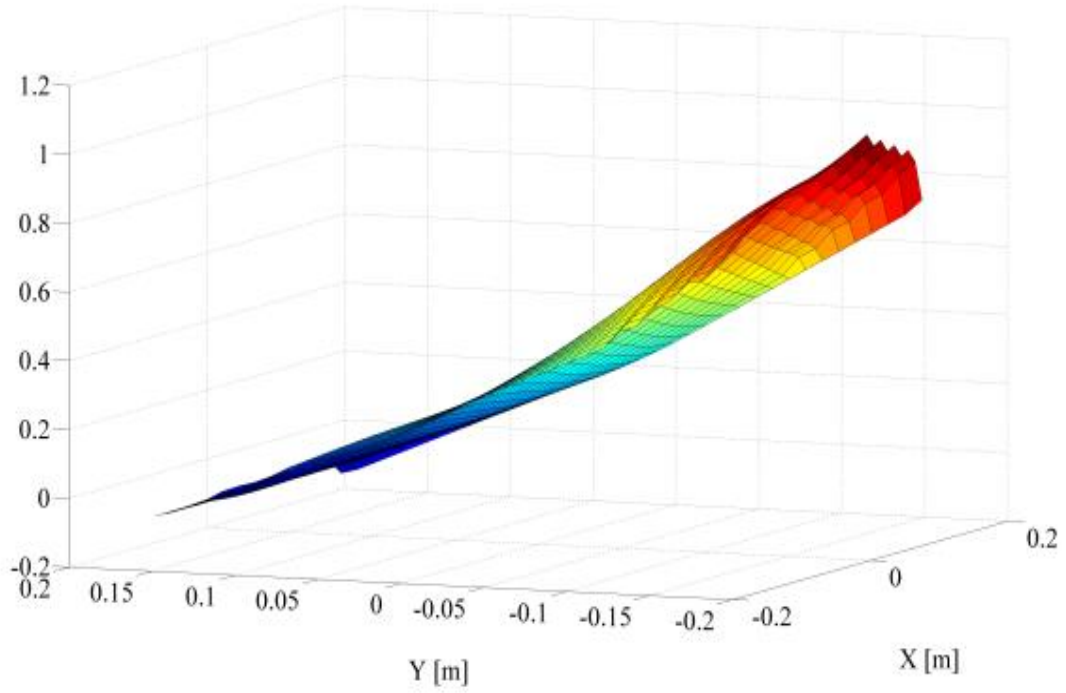

a)

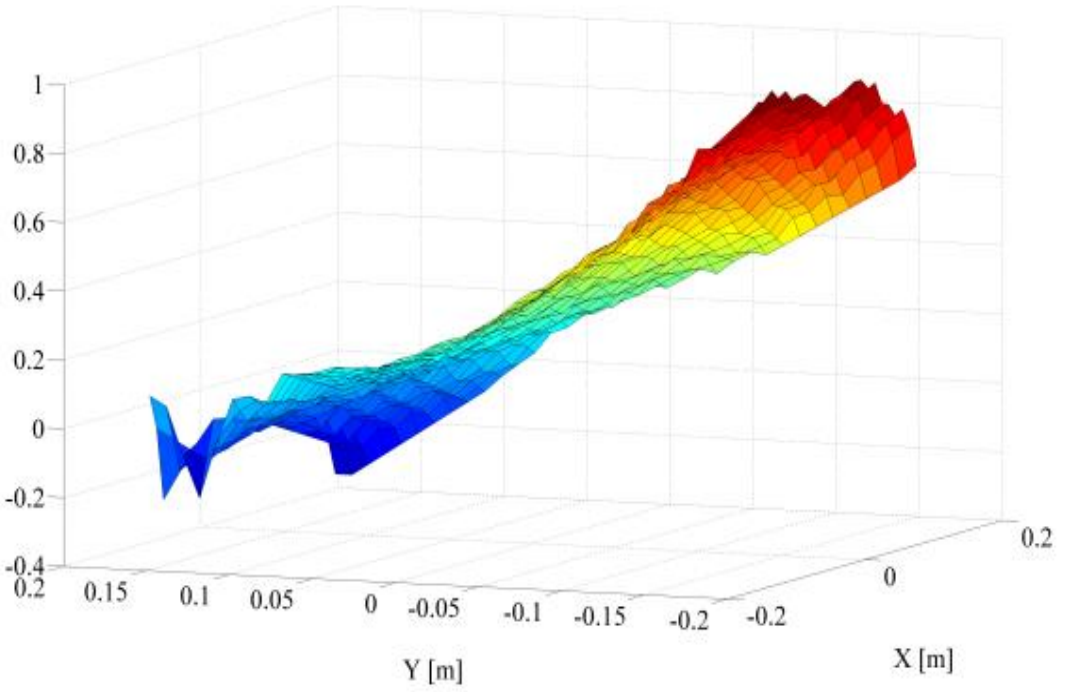

b)

Figure 40: Eighth order normalised curvature before and after the addition of noise.

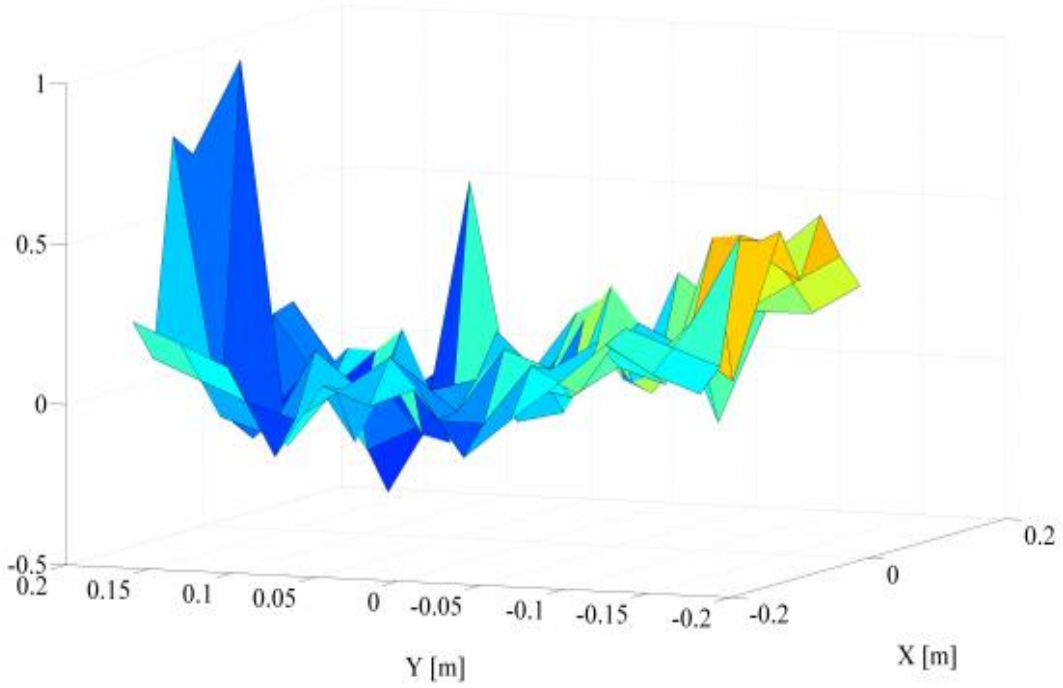

a)

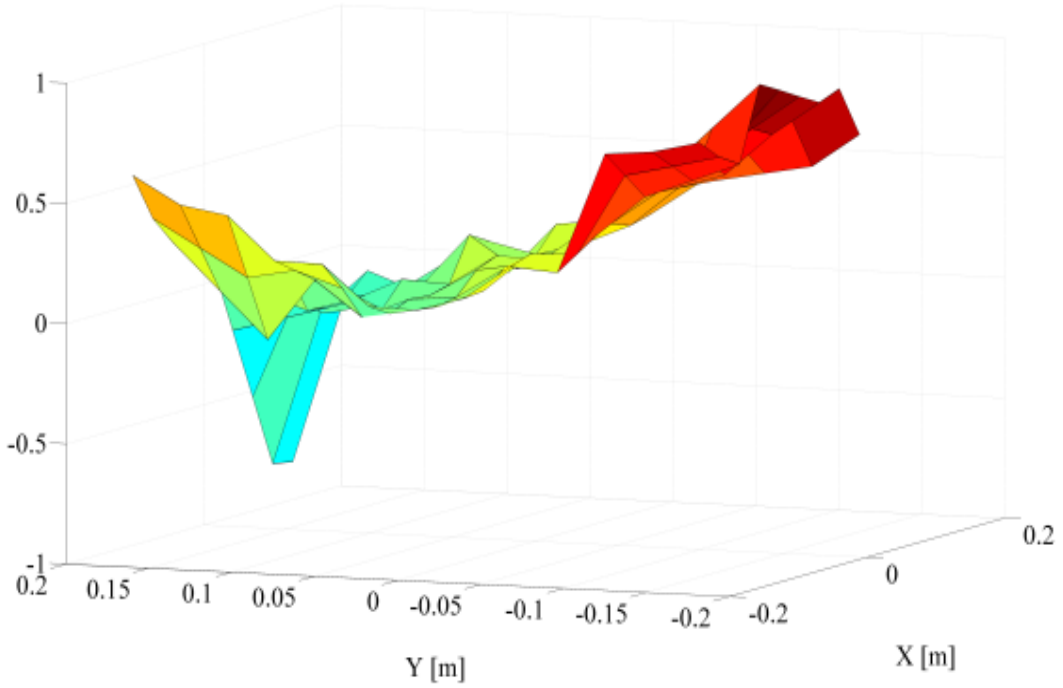

b)

Figure 41: Result obtained with experimental data. First and third order normalised curvature.

4.5.4 Remarks on the modified Laplacian operator approach

The experimental verification carried out on a delaminated composite plate, highlighted the sensitivity of the curvature of the POMs to noise. Although a filter was applied before performing the POD, still damage could not be located. Moreover even the curvature was completely different from the expected one. In order to overcome this problem, a modified Laplacian operator was adopted to calculate higher order curvatures. Results highlighted that this approach is able to delete the influence of noise in data and

to provide a better computation of the curvature. Numerical and experimental verification of the method were presented and they showed promising results. Further tests with proper equipment should be performed in order to verify the capability of this approach to detect possible delamination in panels.

4.6 Stiffened plate

In the previous figures it was shown that the GSM coupled with the POD, applied to a simple component, is able to locate one defect. However in that ideal case the only contribution to the change in the local stiffness of the plate was due to the presence of damage. Plates commonly used in the aeronautical field are usually stiffened with stringers. These obviously create a sharp change in the local stiffness, which usually is much higher than the one produced by low level damage. For this reason it can be useful to study the effect of this kind of structural elements when a technique such the GSM is applied to damage detection. The model which is analysed is a composite plate, pinned at all the edges, with a stringer. Both the plate and the stringer are made of composite layers. The model of the plate can be seen in Figure 42a) while in Figure 42c) the scheme of the stringer is presented. The material properties and other information on the system can be found in Table 5. Different positions and entities of damage are considered. One type of damage is the softening of a local area in the plate, shown in black in Figure 43. Two levels of this type of damage are considered: softening of the two innermost layers and softening of all the layers, both of 90% of the original elastic moduli. Another typology of defect is a local debonding between the stiffener and the plate. Two different sizes for this debonding are considered: small, black area on the stringer in Figure 43, and big, area enclosed in the black rectangle in Figure 43. The external load is distributed on the free flange of the stiffener in the direction normal to the plane of the plate. Intensity and frequency of the load are 50 kPa-230 Hz. An analysis with a point load applied to the top of the plate, with the same frequency, was also conducted but the results were not as satisfactory as in the present case. Before presenting the result of the analysis it is important to highlight the two main features of the structure: the presence of the stringer and the system boundary conditions which are applied to all the edges of the plate and not on just one as in the cantilever case. Furthermore in this case the rotations at the boundary nodes are not constrained.

Numerical results show that the influence of the stringer is strong, hiding in most of the cases the presence of the defect. In particular in the case of low level damage it was not possible to have a clear evidence of the softening in the plate. For the high level damage it resulted that damage at position 2 was the easiest to locate whereas position 1, Figure 44, and position 3 weren't clearly identifiable. Also for the deboning case it was found that the smaller damage was difficult to detect. However the deboning was easier to identify than the softening at the corresponding position (case 3). In all cases, both for the classic POD and the GSM, position 2 was the one that led to the highest value of the damage index, as indicated in Table 6. Finally it is worth to observe that in this case, with boundary conditions applied to all edges, the algorithm does not seem to work better when the damage is close to the constraint, as in the case of the cantilever plate.

Table 5: Mechanical properties for the stiffened panel case

E11=150.15GPa	E22=8.35GPa	G12=4.2GPa	G13=4.2Gpa
G23=4.2Gpa	ν=0.27	ρ=2100kg/m^3	Boundary condition: 4 edges pinned
Plate dimensions: 300x400x2mm^3		Layup (plate and stringer): 8 layers [0°/45°/-45°90°]s	

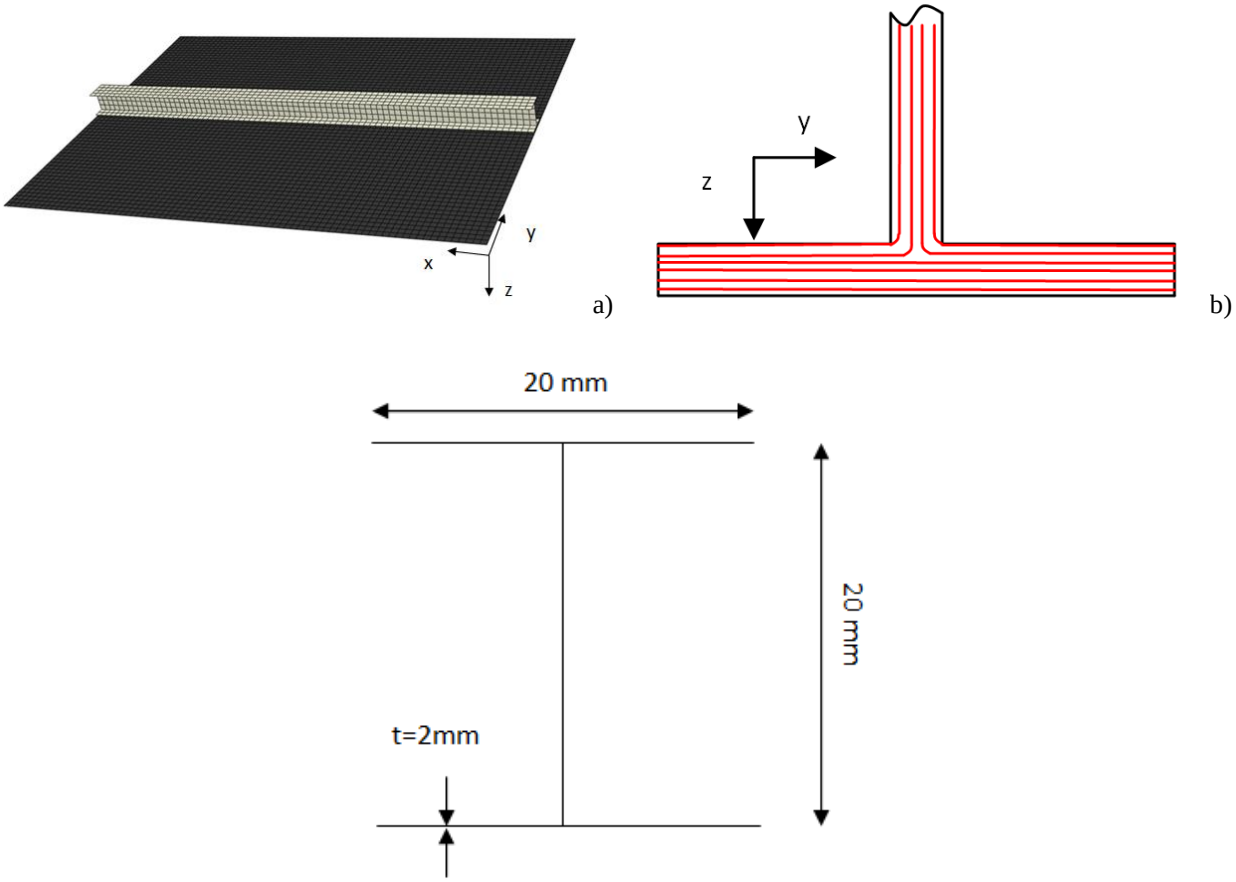

Figure 42: a) 3D view of the stiffened panel. b) Stratigraphy of the stringer cross section. c) Scheme of the stringer.

Table 6: Normalised damage indices for the high level damage cases.

Damage position	1	2	3	Debonding
Classic POD	0,661645	1	1,90E-01	0,667553
POD + GSM	0,615102	1	0,556338	0,838576

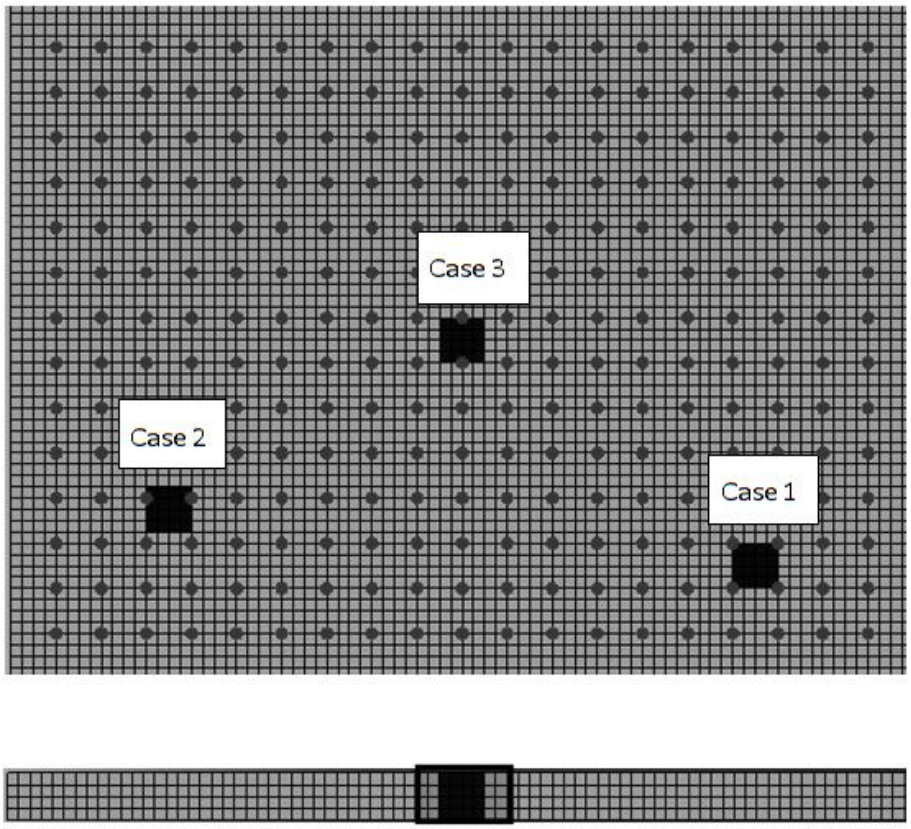

Figure 43: Stiffened panel with damage positions.

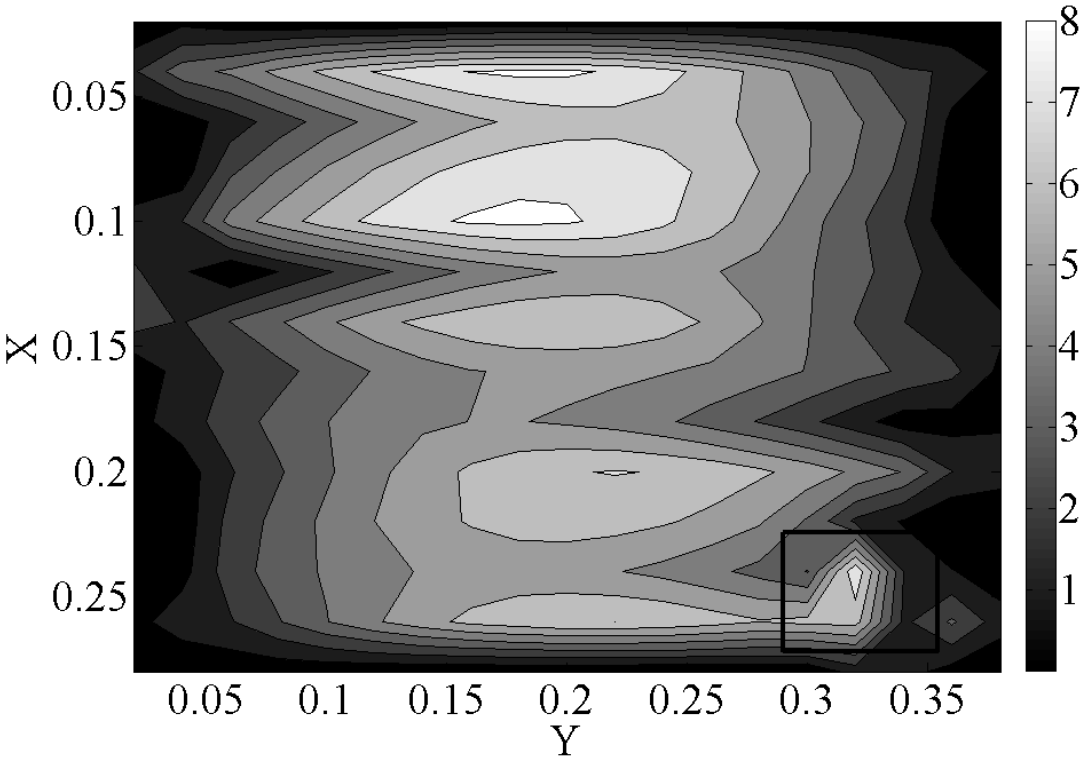

Figure 44: Damage index evaluated with the GSM for case 1 high level. The black rectangle shows the damage position. Dimensions of the axes in m.

4.6.1 Threshold approach

In the previous paragraph it was shown that the simple GSM coupled with POD and applied to a stiffened plate could not locate precisely the damage, as the stiffener creates a sharp change in the curvature which can hide the one due to the defect. A possible way to avoid this problem is studied in this paragraph. The first consideration concerns the opportunity to create a baseline from a single measurement. In a single acquisition there can be different sources of noise, but also other causes of temporary stiffness changes, like a temperature or humidity variation. In this situation it can be useful to calculate a baseline from different sets. Before providing the procedure applied in this research it is convenient to mention that similar considerations were used in a damage detection application with a different interpolation approach [75, 76].

An average of different acquisitions, all of them having different small local discontinuities due to different sources, can smooth these variations, keeping all the common features. These can then be deleted when a comparison with a damaged case is needed. In the case under examination the common feature which must be deleted in the damage evaluation is the stringer, while damage which was introduced is considered as possible stiffness change. In this way a new baseline is created, to which each single damage case is then compared to create an improved damage index, IDI. This IDI is then compared to a chosen threshold, in order to set to zero the IDI values at all the grid points where it doesn't overcome a certain value. The step by step procedure is the following one:

- Application of the POD plus GSM approach to all the damaged cases under examination. In this way several different damage indices can be calculated. All of them share the contribution of the stringer.

- Average all the damage indices calculated, in order to find a baseline which takes into account different conditions of the plate, not just a hypothetic undamaged status. With this step the contribution of the different damages is weakened while the influence of the stiffener is still present.

- Calculate the damage index for a single case and compare it with the baseline, defining the IDI.

- Define a threshold, if the result obtained with the previous step at each point is lower than the threshold, set it to zero (modified IDI).

The most challenging aspect of this approach is to find a threshold which is valid for most of the cases. Obviously it should be able to highlight the presence of damage without deleting even its contribution. For all the low level damage cases this approach results to be impractical, as the contribution of the stiffener is still too high to find the defect. Nevertheless it must be noted that the level of damage in those cases is low and that the baseline is computed considering also the high level damage cases.

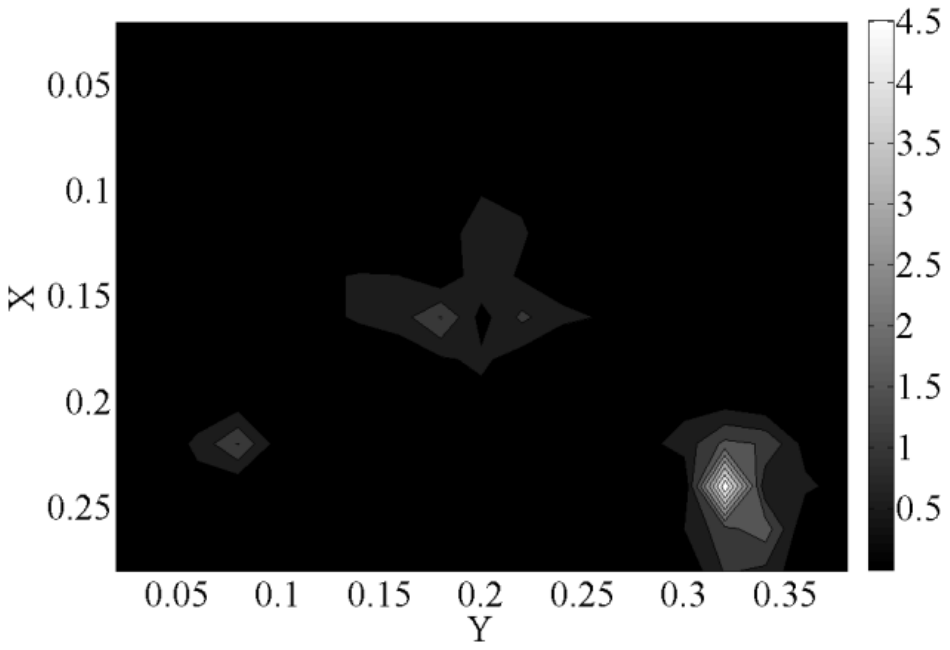

a)

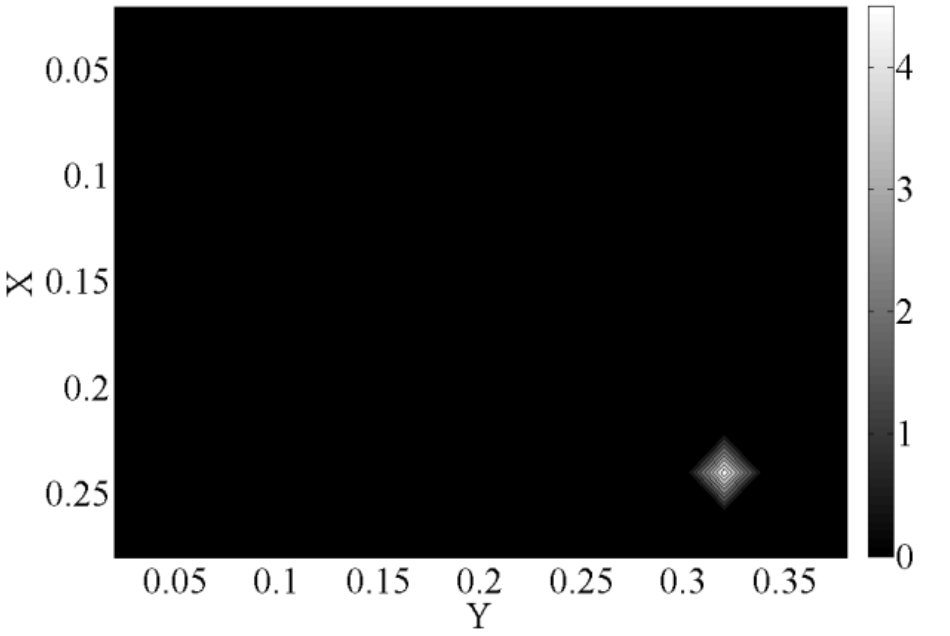

b)

Figure 45: a) IDI for case 1 high level. b) IDI after threshold. Dimensions of the axes in m.

However for certain cases, damage 1 and 2 high level and big debonding area, the method provides good results. After the IDI has been defined in point 3, its absolute value was considered. The mean *M* and standard deviation *S* were then calculated and the threshold was calculated as:

$$threshold = M + \alpha * S \qquad \textbf{4-6}$$

Where α is a parameter which can be adjusted in order to suit most of the cases. In this case it was chosen equal to 5.5. This empirical value was appropriate for the three cases mentioned above. From Figure 45a) it is clear how the IDI for case 1 high level presents the highest value close to position 1, but some other

peaks are present. After the threshold approach all these heights are deleted and only the damage contribution remains, Figure 45b). The results for the other two valid cases are presented in Figure 46.

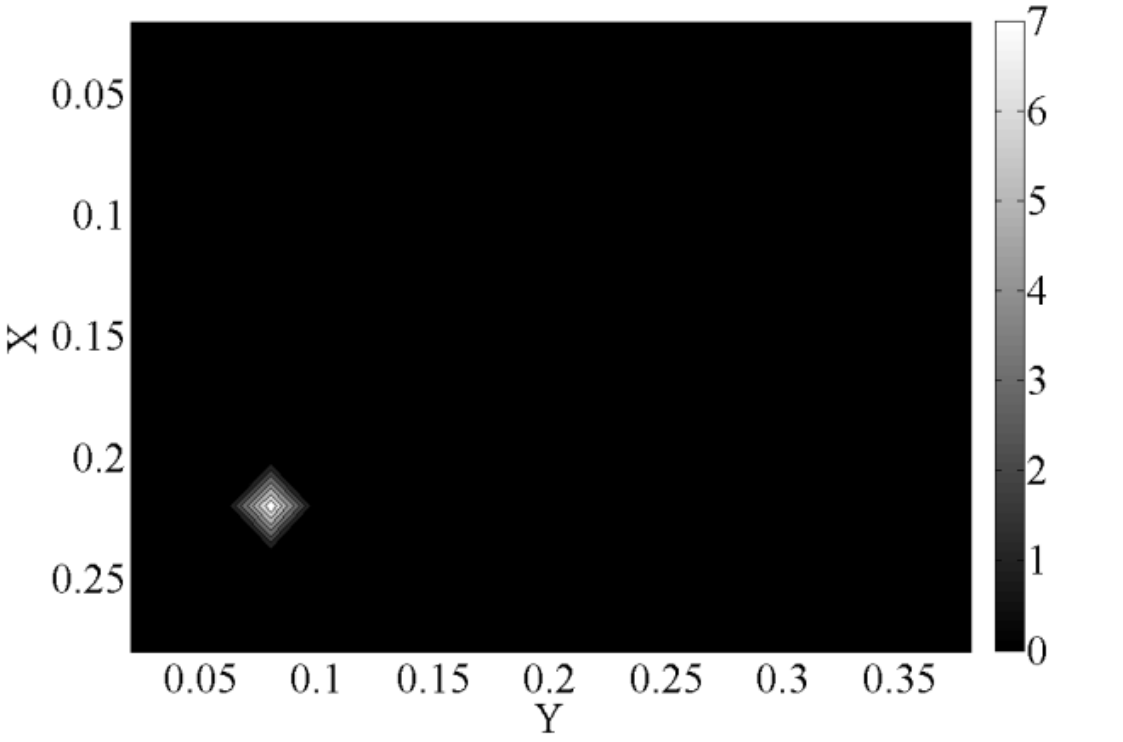

a)

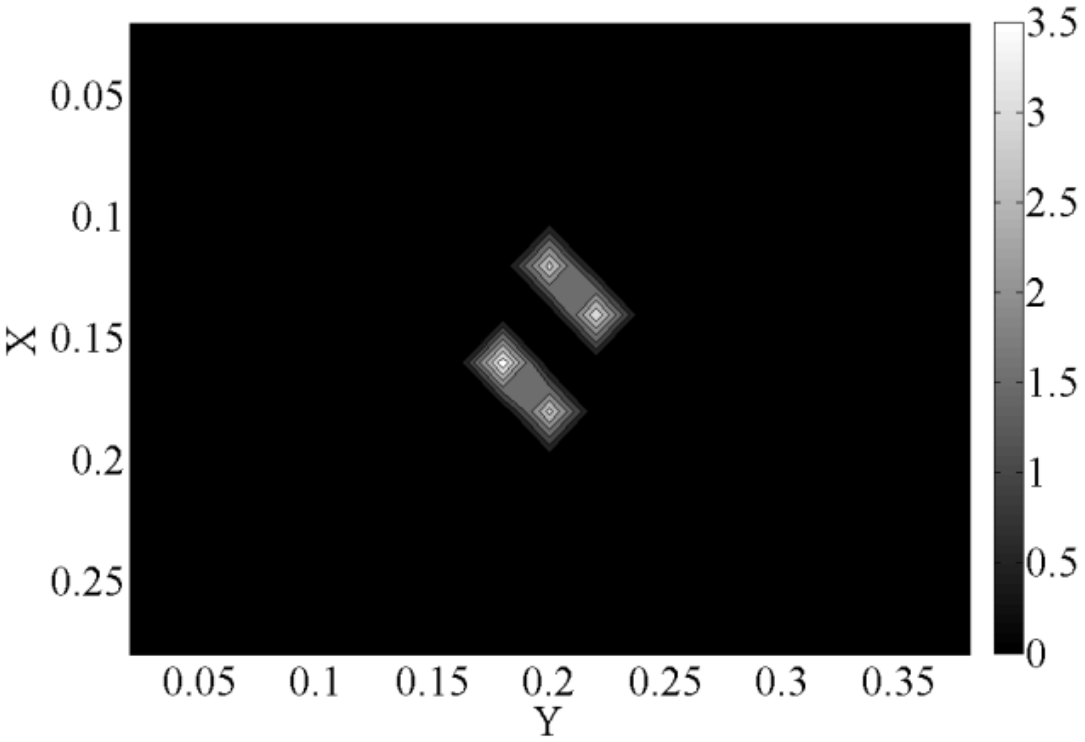

b)

Figure 46: Modified IDI. a) Case2 high level. b) Big debonding. Dimensions of the axes in m.

4.6.2 Influence of noise

As already stated in Section 4.5, the presence of noise in the data can have an important influence on the performance of damage detection techniques. It can hide the effects of damage, as well as produce "false positive" cases. Mode based damage detection is affected by the level of noise present in data, and each mode can manifest different sensitivities towards it [77]. Recently a thorough study on the effect of noise on the dynamics evaluation of systems was performed [78]. In that case the nonlinearity of the system's response was monitored and it was highlighted that noise level can modify the threshold at which the nonlinear effects, which can be easily referred as local damage, become relevant. Furthermore it was highlighted that the excitation frequency for the system should be close to its first natural one, in order to optimize the determination of the monitored feature.

Also POD can be affected by the presence of noise. The problem was already considered in [14]. In that case, however, still a comparison between a pristine and a damaged case was performed. A preliminary investigation of a probabilistic POD for noise reduction is given in [79]. The application of the curvature of mode shapes in damage detection further stresses the influence of noise in data.

In the present study an analysis similar to the one presented in Section 4.6.1 was performed adding white Gaussian noise to the data used to compute the POD. In particular two levels of noise are presented here. The command *awgn* available in Matlab was used with levels of signal to noise ratio, SNR, equal to 40 and 20. Higher values of SNR (100, 80 and 60) provided results comparable to the uncorrupted case. An example of the standard damage index with SNR equal to 40 is given in Figure 47 where damage cannot be detected. The application of the IDI and threshold approach revealed that the influence of noise can be overcome, as the averaging technique is able to remove noise effects. The explanation of this can be found on the nature itself of the white Gaussian noise, which has a flat power spectral density, normal distribution, zero mean and finite variance.

The noise is hence expected to corrupt the dynamic response of the plate with a zero mean, and a finite variance σ. This obviously affects the POMs; furthermore its effects are even amplified when a double differentiation is applied. The application of the threshold can therefore delete also the influence of this variation, if its level is below the threshold itself. The value of the variation is determined from the given SNR [80]. The corruption of the signal is obtained with Equations 4-7, 4-8 and 4-9:

$$noise\_level = 10^{-\frac{SNR}{10}} \quad \textbf{4-7}$$

$$noise = \sqrt{noise\_level * randn} \quad \textbf{4-8}$$

$$data\_noise = data + noise \quad \textbf{4-9}$$

Where the variable "*randn"* in Equation 4-9 refers to a random number.

Results for the first position damage case are presented in Figure 48,Figure 49 and Figure 50. The same results for the first and second damage cases were obtained even after the addition of noise while for the big debonding the chosen value of alpha resulted to be appropriate only for the case of SNR equal to 40. The difference between the case without noise, in which the same value of alpha was used for these sets, and this case with noise in which it could not be used successfully, is explained with the variance of the noise, which in this case overcomes the threshold level. A summary of the results obtained with the addition of noise can be found in Table 7.

Table 7: Summary of the results obtained after the addition of noise.

Case	Noise level SNR	
	40	20
Damage 1high	detected	detected
Damage 2 high	detected	detected
Damage 3 high	missed	missed
Small debonding	missed	missed
Big debonding	detected	missed

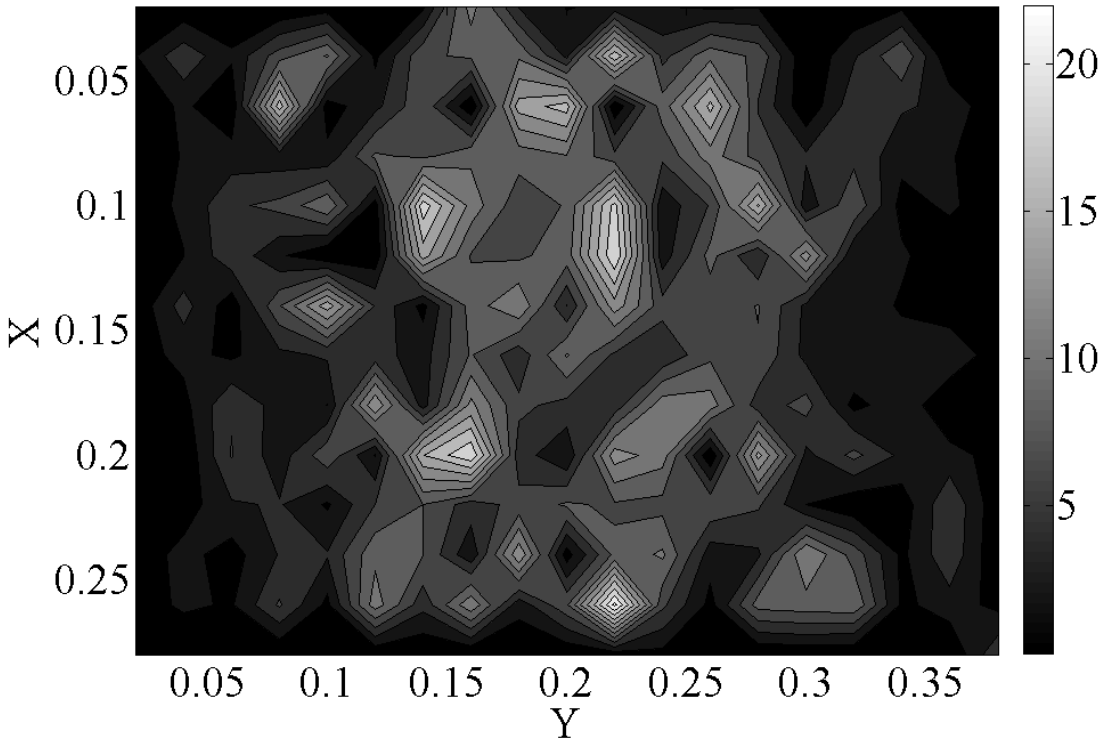

Figure 47: Case 1, standard index, SNR 40. The noise hides the damage. Dimensions of the axes in m.

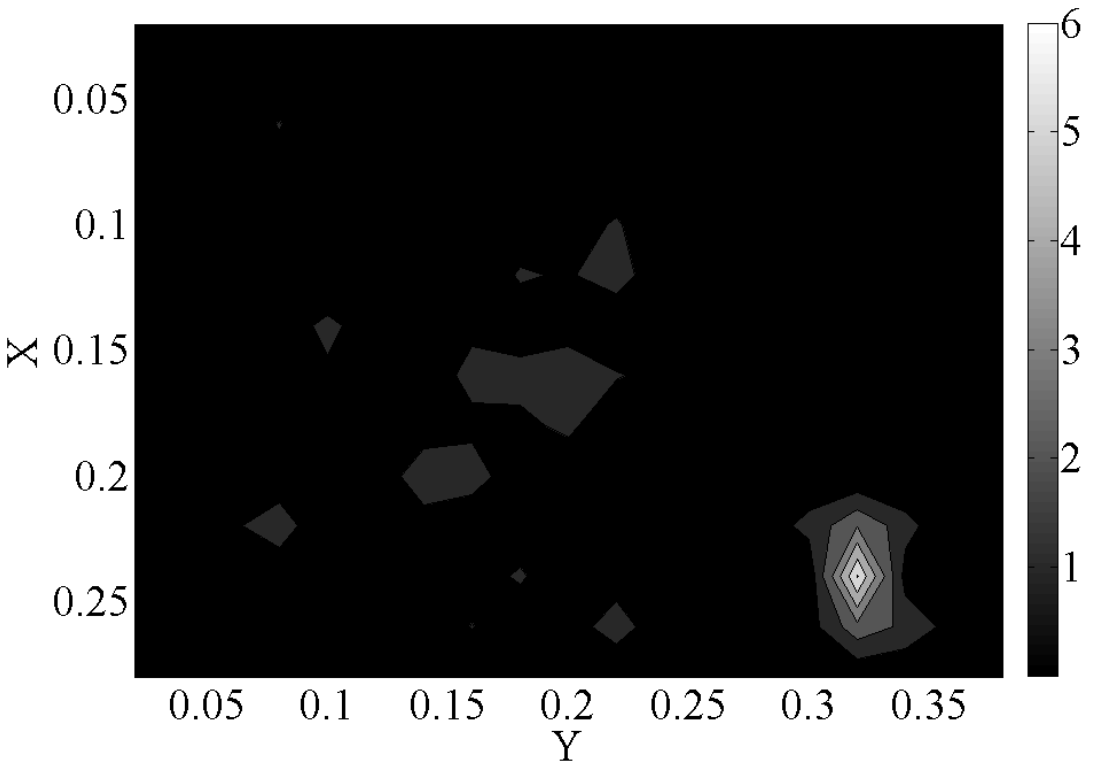

Figure 48: Case 1, IDI SNR 40. The damage is clearly identified. Dimensions of the axes in m.

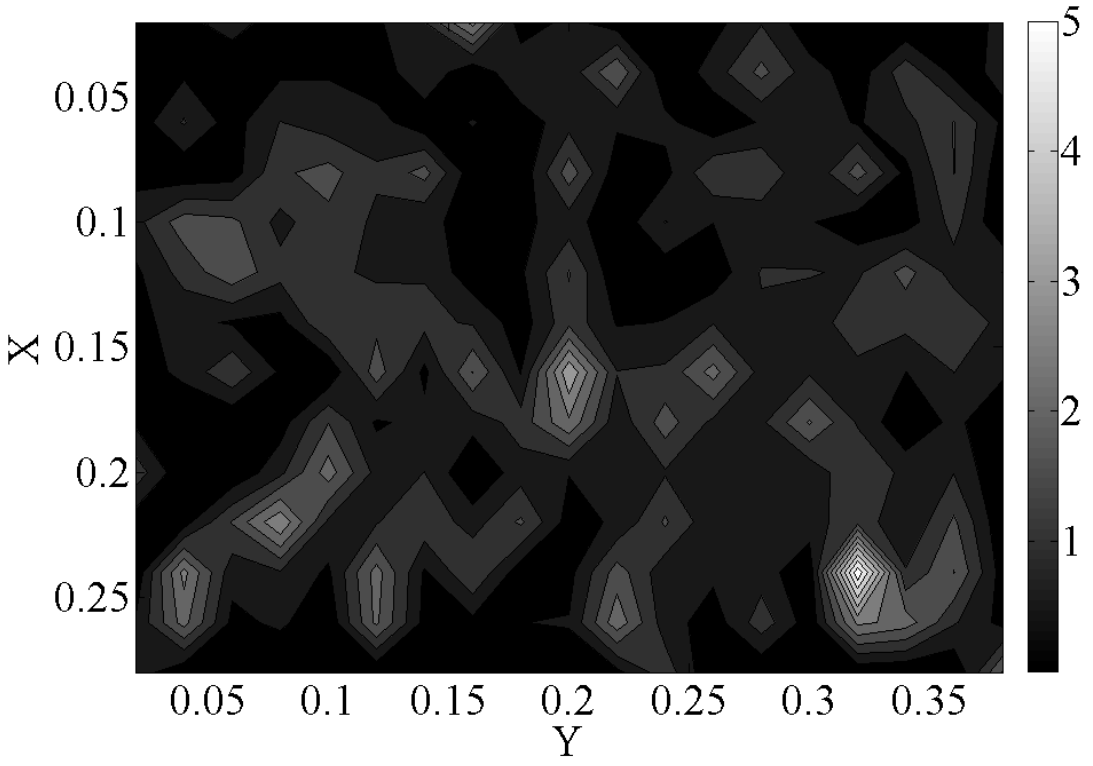

Figure 49: Case 1, IDI SNR 20. The damage is identified. Dimensions of the axes in m.

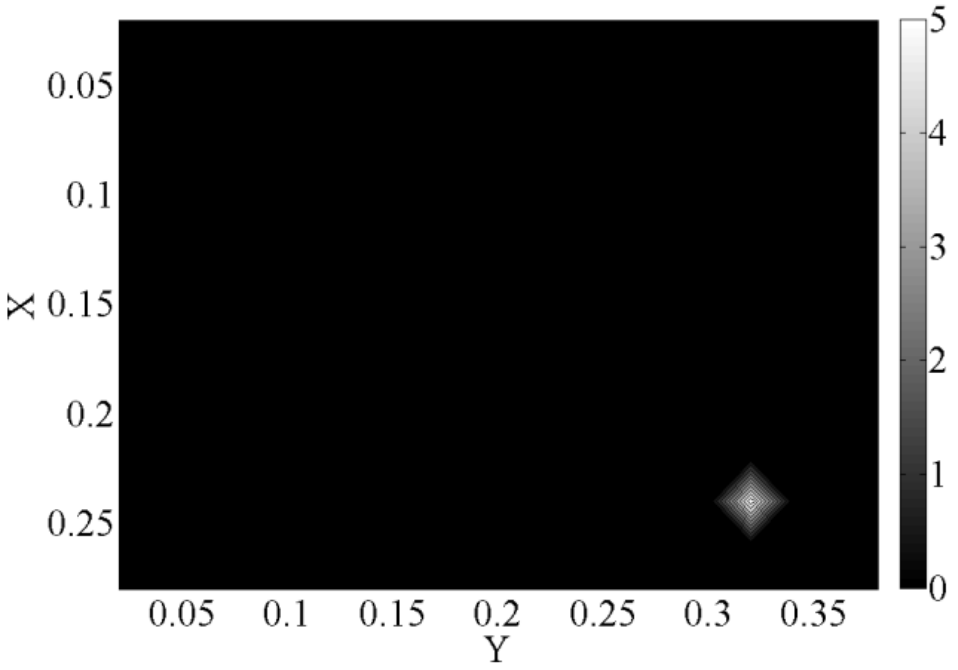

Figure 50: Case 1, modified IDI SNR 20. The damage is clearly identified. Dimensions of the axes in m.

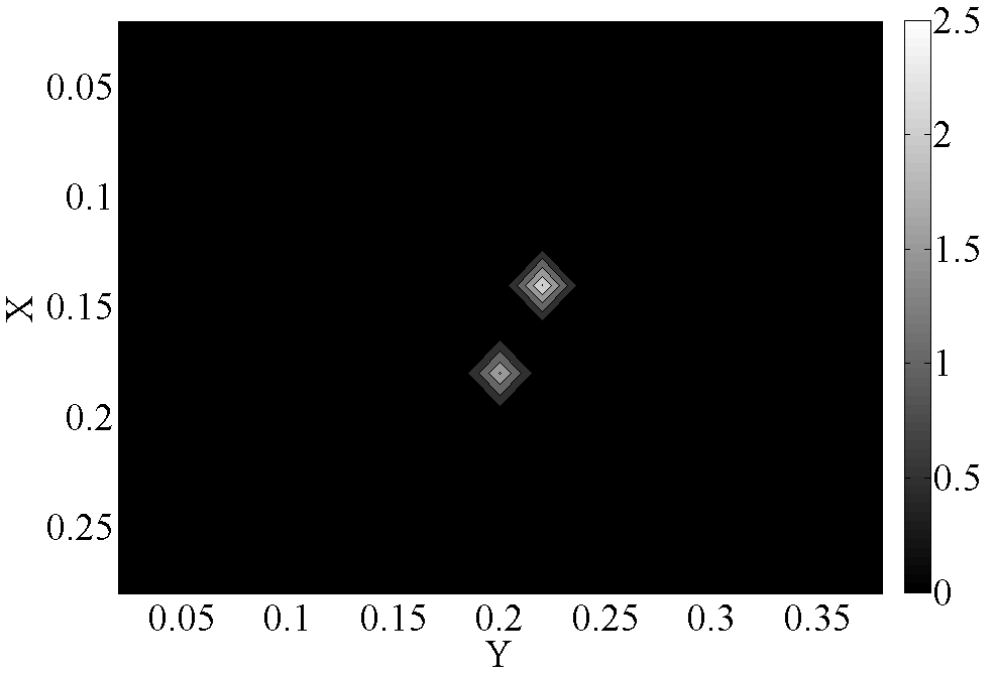

Figure 51: Big debonding 100 Hz, modified IDI, SNR=40. Dimensions of the axes in m.

4.6.3 Modification of the load frequency

In order to study the influence of the load frequency on the final results, the same approach described in the previous paragraph was applied to data obtained on the same system under a harmonic load with frequency equal to 100 Hz. In this situation the dynamics of the system captured by the POM is different but the method should still be able to identify possible damage, as previous studies confirmed [13, 14]. An example for the big debonding case, after corrupting data with SNR equals to 40 is presented in Figure 51. In general it was found that the amplitude of the modified IDI was lower than in the case in which the frequency was higher, and that the number of missed detection increased. This is due to a lower

level of the system‘s response, as in the first case the frequency was close to the first natural frequency of the system. These results agree with the theoretical explanation given in Section 2.6.

4.6.4 Considerations about the number of sensors

In most cases, the number of sensors needed to perform a reliable damage detection using modal data can be high. This is due to the fact that a correct determination of modal shapes and hence curvatures, needs a fine grid mesh, in order to describe properly the dynamic behavior of the system. This is particularly true for a two-dimensional case. Mathematical explanation of this has been given in Section 3.3. In the stiffened plate case under examination a 50% reduction of the number of outputs prevented the location of the damage. A more accurate analysis of their location with respect to that of damage could be useful to determine the sensitivity of the method to sensor density and location. However it is worth to notice that the determination of a possible debonding between plate and stringer doesn’t necessarily need to be evaluated using data from a bi-dimensional grid. As the part of the system which is interested by this particular failure is narrow, only the dynamic of the plate over the stringer can be considered. In this section the POD plus GSM approach is applied using data only from sensors placed over the stringer. In particular the 19 nodes encircled by the line in Figure 52 were considered; the full black square represents the small debonding while the black rectangle the big debonding. In Figure 53 it is possible to see the results obtained for the two debonding cases using 19 outputs. The results were normalized in order to show the increase in the damage index when the debonding size was wider. Analyses with a smaller number of sensors were conducted in order to study the capability of this approach to locate the debonding also with fewer data. In particular two cases are shown: one in which 10 sensors were used (every other node from the first to the last in Figure 52) and one in which 9 sensors were used (every other node from the second to the last but one in Figure 52). The results indicate that for the main POM it is difficult to locate the damage. However using the second POM to perform the GSM the localization provides better results. This is also consistent with what found in Section 4.2. The damage indices calculated from the gradient of the second POM are shown in Figure 54. Figure 53a), Figure 54a) and Figure 54b) present the same behavior of the damage index in proximity to the debonding. Two consecutive peaks are present close to the damage. However in the fewer nodes cases a spurious peak is also present at one node close to the boundary.

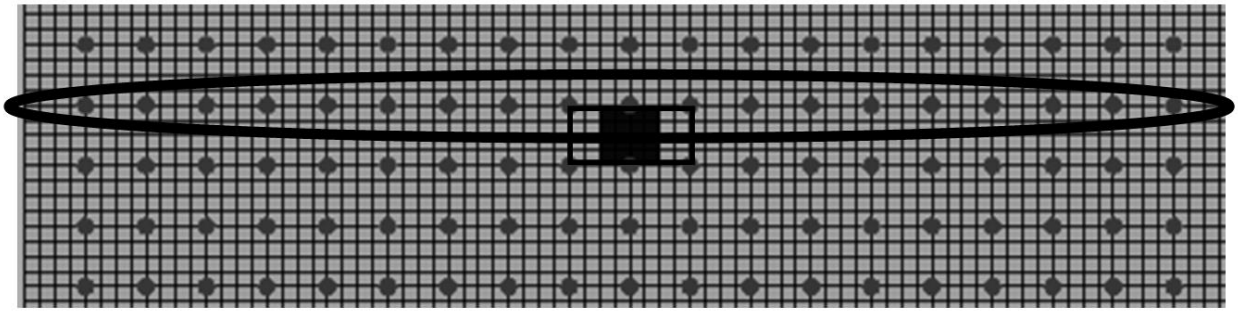

Figure 52: Nodes used to perform the POD.

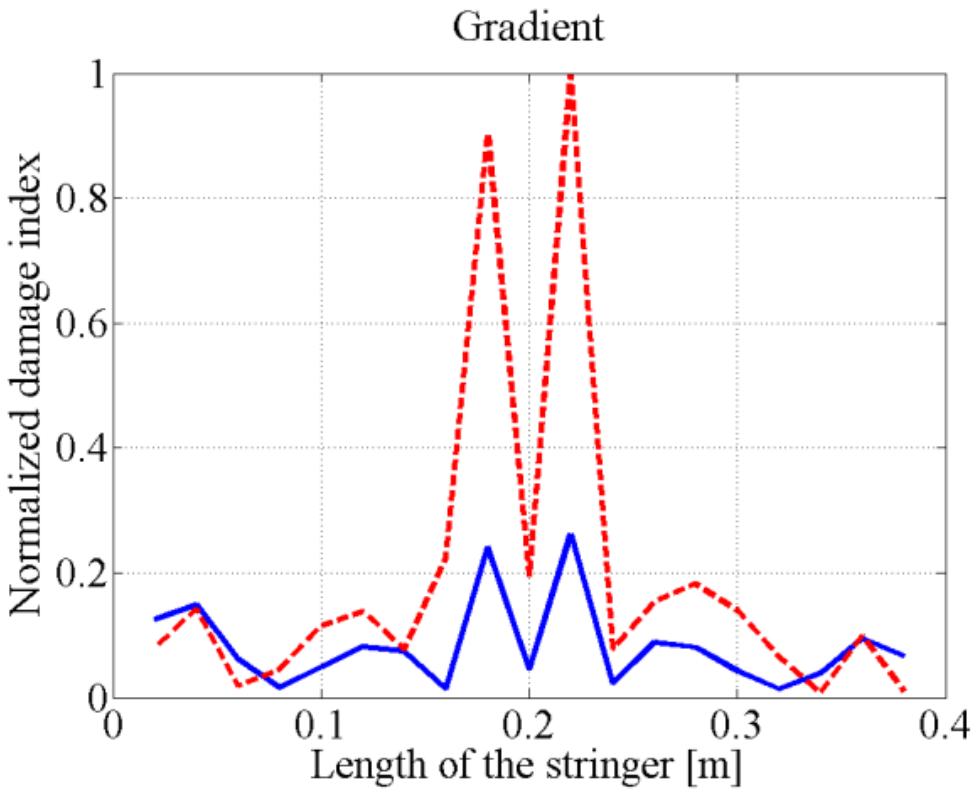

a)

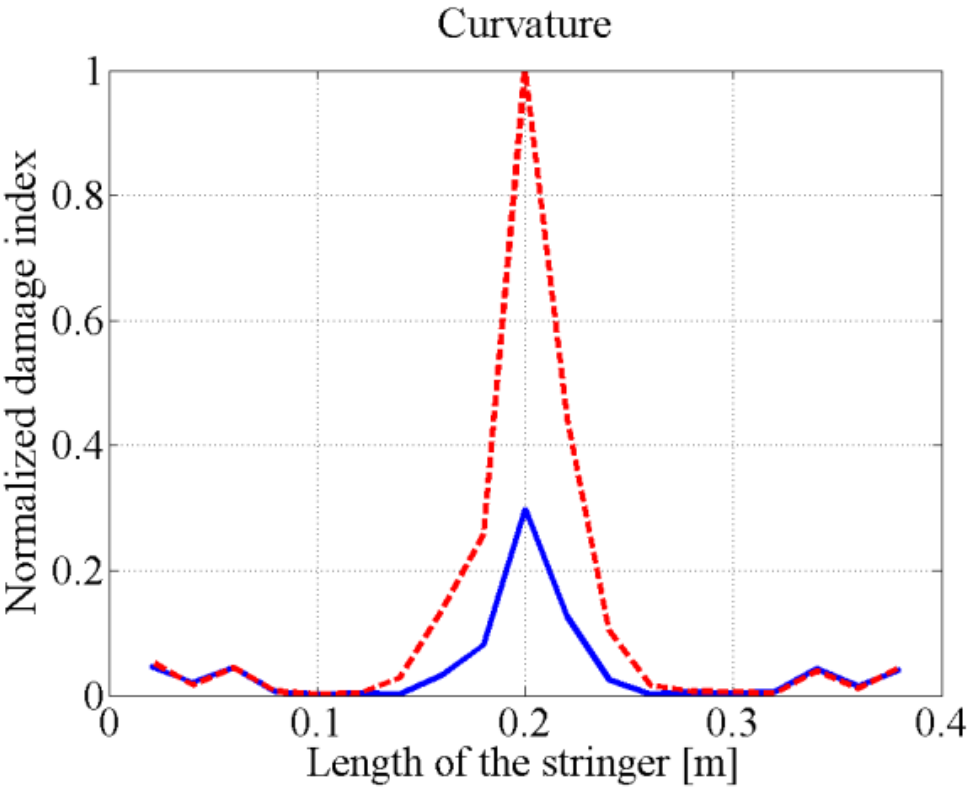

b)

Figure 53: Normalized damage index with 19 outputs. The solid lines refer to small debonding while the dashed lines to the big debonding. a) Gradient damage index. b) Curvature damage index. Damage is correctly located.

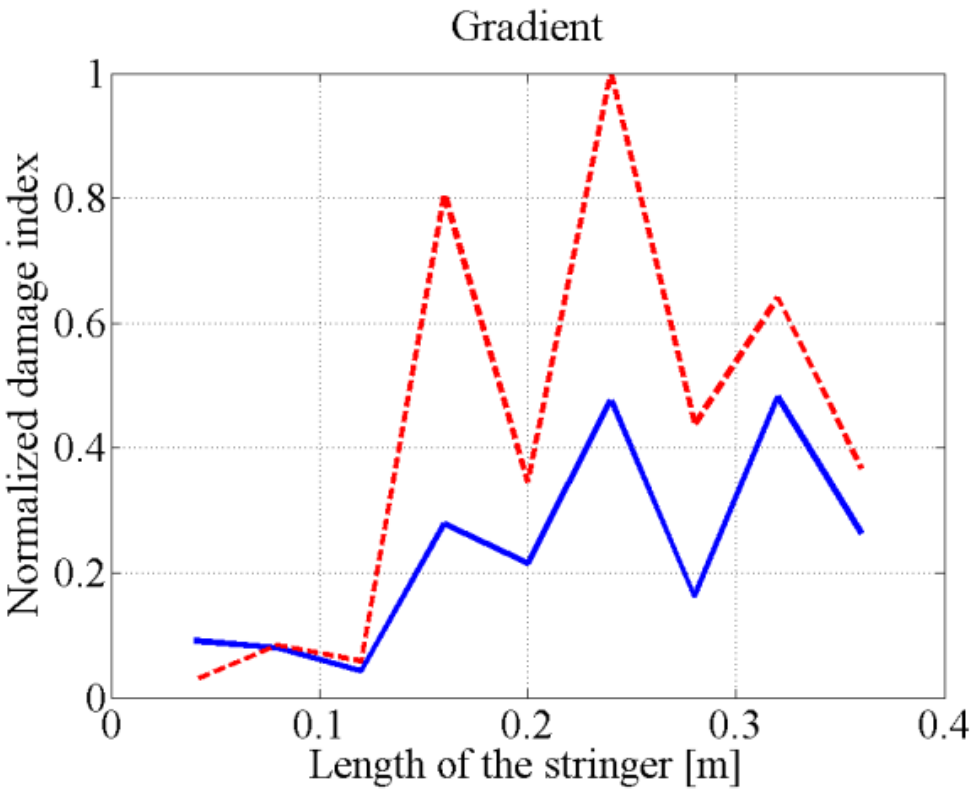

a)

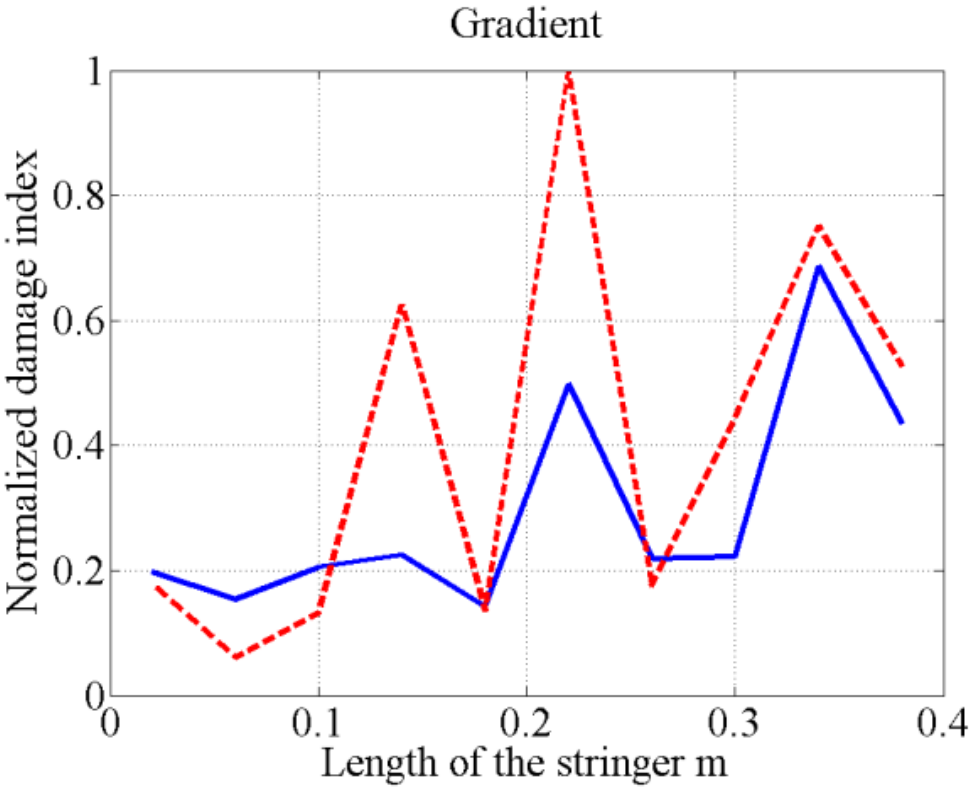

b)

Figure 54: Normalized damage index using the gradient of the second POM. The solid lines refer small debonding while the dashed lines to the big debonding. a) 9 nodes case. b) 10 nodes case.

4.7 Final considerations about the application of proper orthogonal decomposition as damage detection technique

In this chapter the application of POD to damage detection was investigated on different structural elements. The influence of the position of damage was studied and its effects on the calculated damage index evaluated. The application of the gapped smoothing method resulted to be an appropriate tool to avoid the necessity of data belonging to the pristine case. The difference between the derivatives of the proper orthogonal modes and their smoothed representations were used as damage indicator.

The first examples represented simple structural components, as cantilever beams and plates. In each of these cases it was shown that the damage index was higher when defects were placed close to the fixed edge. Moreover it was found that a delamination place at the middle plane caused a more relevant variation of the curvature. The position of this type of damage through the thickness of a composite was further analysed with a three dimensional model of a cantilever beam. What could be investigated more in detail was the reliability of the method with respect to the mutual position of sensors and damage. It was shown that if the delamination is located between two layers which are close to the free surface of the beam, it is better located by sensors which are placed on that surface, and that this difference has a certain influence on the level of the damage index. This is particularly true when the damage dimension is small.

An experimental verification on a homogeneous beam was conducted. In this case, due to the limited number of sensors, the first derivative of the proper orthogonal modes was used as damage index. In particular the first two modes were considered. Results showed that the method provided good results in terms of damage location, and that the damage index calculated was higher than the one related to the classic POD, which was presented in a previous work.

The influence of noise on data was also studied. It is well known that the curvature of a mode shape, due to the equation through which it is calculated, is much more sensitive than the mode itself to disturbances in the signal. This obviously can have a fatal effect on the damage detection algorithm. A different evaluation of the curvature, with the application of a modified Laplacian operator, was proposed. First a validation of the method, with respect to an analytical case present in literature was conducted. After having shown that the POD also in this case is a good alternative also when noise is involved for a simple homogeneous beam, this approach was extended to the proposed composite plate. The results showed that also in a bi-dimensional evaluation the noise can completely hide the shape of the curvature. An experimental verification was conducted and promising results were obtained. Even if damage detection was still not accomplished, the shape of the curvature could be obtained with good agreement with the numerical model. Some issues which still have to be investigated are related to the limited number of grid points which can be investigated experimentally. In fact the application of higher order Laplacian operators requires a large number of nodes to provide a consistent result, especially close to the boundaries.

The last example proposed represents the most relevant novelty of this chapter. The application of vibrational damage detection techniques to stiffened panels is something which has not been deeply studied in literature, in particular with reference to the POD and GSM. The model under exam was representative of a typical aeronautical component. The influence of the stringer on the calculation of the curvature was studied and it was highlighted that its influence is much more relevant than the one due to damage. That is why a simple GSM was not effective in locating defects. A more advanced approach, based on a multiple set of training data was proposed, and numerical results showed that this was effective in deleting the influence of the stringer, keeping only variations due to damage. The influence of noise was also taken into account and the algorithm resulted to be valid also with this type of uncertainty included in signals. Analyses with a load applied with a frequency different from the resonant one revealed that this parameter is important also with this more complicated model. The application of a frequency close to the first natural one still resulted to be preferable to locate damage. A possible solution useful to locate debonding between plate and stringer was proposed using only one raw of sensors.

From all the considerations made above, it was demonstrated that the proper orthogonal decomposition, which was already applied as damage detection technique to homogeneous beams comparing pristine and damaged cases, can be successfully applied also to more complicated structure, and that it can be connected to the gapped smoothing method in order to use only real-time data to perform the damage detection [81-83].

Chapter 5: Impact detection and reconstruction

5.1 Overview

In the previous chapter, examples of application of active sensing based on proper orthogonal decomposition were proposed. It was shown that several parameters can influence the damage detection results. They include the type of force applied to the system as well as the boundary conditions. For many applications an active sensing can be difficult to implement, especially during the operational life of the structure. In such cases a passive approach can be preferable, as only data recorded by sensors mounted on the system are required. The input is usually provided by an external event, which typically is the one which must be monitored.

This second type of SHM finds its most relevant application, for aeronautical purposes, on impact detection and reconstruction. In this case the aim is not to detect a possible damage inside a structure, but to identify a possible damaging load just after it occurred on the component. A typical example is given by impacts both during assembling/maintenance (i.e. tool drops) or during the operating time (i.e. hails, bird strike, etc.). The main advantage of this approach is that the mathematical background is simple, as a linear relationship can be established between the force applied by the impact and the signal collected by the sensors. The impact energy and location can be obtained from sensors' response solving an inverse problem. The main disadvantage is that it can be difficult to calculate the exact relationship which relates force and signal, especially for complicated structures. Furthermore the linear representation of this problem is valid only when the energy of the impact is low. When this is not the case, large deflections of the structure under the load are expected; therefore the relationship between the acting force and the response of the system becomes more and more nonlinear. Previous papers evaluated this relationship either analytically, using a Finite Element Method (FEM) approach, or experimentally. However those approaches could be performed only on few impact cases.

In the past two decades several authors have studied the problem of impact reconstruction on different structures. The relationship between impact and strain was investigated in [84], by studying different methods to better evaluate the impact. An important contribution to the inverse problem was given in [85, 86], where the influence of boundary conditions on the transfer function was studied as well as the difference between a time domain and frequency domain approaches. A method for determining the location of low velocity impacts on a sandwich plate was proposed in [87]. In [88] a system identification method was established to reconstruct and locate small mass impacts on a stiffened panel. However, it was shown in [89, 90] that, if the energy (i.e. the mass and/or velocity) of the impact increases, the

reconstruction technique can fail. Recently, an artificial neural network (ANN) approach has been proposed to both locate and reconstruct impacts, with different energies, on composite plates [28, 41, 89, 91, 92]. An experimental verification of a methodology to determine impact damage on a CFRP plate was reported in [93]. Although the focus of this paper was on damage detection, rather than force reconstruction, it demonstrated that it can be useful to use experimental frequency response function (FRF), collected on an undamaged specimen, to perform further analyses on the same system when it is in operation. The problem of determining a robust transfer function, which represents the mathematical relationship between input and output in a mechanical system, is certainly the most critical issue in the force reconstruction problem. This is due to the fact that numerical models of a mechanical system always contain some approximations, particularly in relation to boundary conditions, which can compromise their accuracy. This can lead to incorrect force reconstruction results if the FRF of the system is obtained numerically.

In this chapter the inverse problem will be addressed. The mathematical background of the method will be presented, highlighting two possible approaches, time and frequency analyses, which can be adopted. In particular a novel frequency approach to compute the transfer function will be introduced in Section 5.4. In the following chapter numerical and experimental results will be presented. The application of this technique, which will be presented in the following chapter, includes some preliminary analyses conducted on a simple model in order to verify which of the two approaches is more suitable for the case under exam, Section 6.1. After showing the main advantages and drawbacks of both, the chosen one will be applied to a more realistic case, providing an accurate numerical model and experimental verification. Once the numerical model is validated, a more detailed investigation is carried out considering different positions of the impact, Section 6.5. The last part concerns the application of POD to impact location, which represents a novelty in this field, Section 6.6.

5.2 Mathematical background

The dynamic of a linear system, subject to a generalised force, can be described using a convolution integral:

$$u(t) = \int_0^t h(t-\tau)p(\tau)d\tau \qquad \textbf{5-1}$$

Where *u(t)* is the response of the system, e.g. displacement, velocity, strains, etc., *p(t)* is the load and *h(t)* is the transfer function, which is commonly defined as the impulse response function. Equation 5-1 represents a direct problem, in which the response of the system is calculated from the force and the transfer function. For SHM purposes, it is important to perform a so-called inverse analysis, which consists in the reconstruction of the force applied to a system, for example an impact on a plate, from the response of the system itself. In real cases, this response can be recorded during loading by using sensors

attached to the structure. However, to reconstruct the force by using Equation 5-1, the transfer function, *h(t)*, should also be determined. One more problem is the inversion of Equation 5-1, which cannot be straightforwardly applied in the time domain. The application of the Fourier transform (FT) to discrete signals in the time domain allows working in the frequency domain. The convolution theorem says that a convolution of two signals in the time domain corresponds to their product in the frequency domain. Equation 5-1 then can be rewritten as:

$$U(f) = H(f)P(f) \qquad \textbf{5-2}$$

Where *H(f)* is the FT of the impulse response function. For linear applications, it represents the frequency response function (FRF) of the system. *U(f)* and *P(f)* represent the FTs of *u(t)* and *p(t)*.

Now that the basic mathematical principle has been explained, two different approaches were introduced to perform the inverse analysis: one in the time domain and another one in the frequency domain. For every approach different paths can be followed to compute *h(t)* or *H(f)* and to reconstruct the force. In the following sections two different techniques, one in the time and one in the frequency domain will be described.

5.3 Frequency domain approach

Equation 5-2 is the fundamental one when performing an analysis in the frequency domain. Once *U(f)* and *H(f)* are known, the FT of the load can be estimated, component by component, with a simple division:

$$P(f_n) = U(f_n)/H(f_n) \qquad \textbf{5-3}$$

The above equation can be considered the solution to the inverse problem. However, a simple inversion of equation 2 is not always possible, especially in experimentally analyses. This is due to the fact that the matrix *H(f)* can have zero values in its diagonal; in such cases there is no information on the force at certain frequencies. Usually the presence of boundary conditions in the structures amplifies this problem, [85]. To overcome this, a small amount of random noise can be added to the matrix. The equation is the rearranged as:

$$H_n{}^{*}U_n = [H_n{}^{2} + R_n]P(f) \qquad \textbf{5-4}$$

Where * indicates the complex conjugate, n indicates the frequency component and R_n is the random noise evaluated for each component. According to the number of sensors used in the analyses, the equation which provides the frequency components of the force is modified. If two sensors are available this equation can be written as:

$$P_n = \left[\frac{H_1{}^* U_1 + H_2{}^* U_2}{H_1{}^2 + H_2{}^2 + R}\right]_n \quad \textbf{5-5}$$

The way the transfer function *H* is determined, depends on the equipment which is available. In the following chapters, which present the numerical and experimental results, two different approaches will be presented. Although they basically give an estimation of the same function, which is the FRF of the system due to a load at a certain position, they follow different paths to calculate it. They will be described in Section 5.4. Before introducing the time domain approach, a description of the meaning of Fourier analysis is given.

5.3.1 Fourier analysis

Frequency analysis of periodic and non-periodic functions can be accomplished thanks to the mathematical theory, developed by Joseph Fourier, known as Fourier analysis. In this chapter a description of the technique used to describe a time domain signal using its frequency content is provided. It must be underlined that this is not a complete mathematical description of the Fourier analysis, which can be found in any mathematics book [94], but a useful engineering characterization which will help to understand the analyses which will follow.

Consider a periodic function *s(t)* with period *T*. Under certain hypotheses it can be represented with an infinite sum of sine and cosine functions. This series is called the Fourier series of the signal. It can be expressed in the form:

$$s(t) = \sum_{n=-\infty}^{+\infty} S_n e^{-i2\pi nft} \quad \textbf{5-6}$$

Each S_n coefficient is related to a particular frequency of the signal, which is a multiple of the fundamental frequency *f=1/T*. It is calculated as:

$$S_n = \frac{1}{T}\int_0^T s(t) e^{-i2\pi nft} dt \quad n = 1,2,3,\ldots. \quad \textbf{5-7}$$

Indicating with * the complex conjugate of a coefficient, each S_n has the property that:

$$S_{-n} = S_n^* \quad \textbf{5-8}$$

This simplifies the calculations of the coefficients, as only the positive spectrum needs to be calculated. The main features of the frequency spectrum of a real and periodic function are:

- It is complex, as each S_n is a complex number
- It is discrete, as only and all the frequencies multiple of the fundamental *f* one are present

- It is conjugate, as for each positive frequency there is the equivalent negative one

In some cases it is possible to extend this analysis to non-periodic functions. The fundamental approximation lies in the fact that they are considered periodic with infinite period. In such case the fundamental frequency tends to zero and the spectrum becomes a continuous function. These new mathematical formulations are called direct and inverse Fourier transform.

$$G(f) = \int_{-\infty}^{+\infty} g(t) e^{-i2\pi f t} dt \qquad \textbf{5-9}$$

$$g(t) = \int_{-\infty}^{+\infty} G(f) e^{i2\pi f t} df \qquad \textbf{5-10}$$

5.3.2 Discrete Fourier Transform and Fast Fourier transform

In practical applications, a continuum function is usually not available. A real signal is discrete, hence formed by several samples, acquired consecutively over a certain period of time *T*. The parameters which define the acquisition process are, apart from *T*, the sampling time ΔT and the number of samples *N* which is actually dependent on the previous two with the relationship $N=T/\Delta T$. Another important parameter, which is directly related to the sampling time, is the sampling frequency $f_s=1/\Delta T$. The above process corresponds to consider the function *s(t)* in equation 5-6 equal to zero but in the window [0, T]; its value is known only at N points, equally spaced in time by the sampling time ΔT. As the available function is discrete, the corresponding *S(f)* can be computed only at certain frequencies, submultiples of the sampling frequency:

$$f_o = 0, \quad f_1 = \frac{1}{N\Delta T}, \quad f_2 = \frac{2}{N\Delta T}, \quad \cdots, \quad f_{n-1} = \frac{N-1}{N\Delta T} \qquad \textbf{5-11}$$

In this way the Discrete Fourier Transform (DFT) can be expressed as:

$$G_k = \frac{1}{N} \sum_{n=0}^{N-1} g(n\Delta T) e^{-i\frac{2\pi k n}{N}} \qquad \textbf{5-12}$$

In equation 5-12 k=1, 2,…, N-1 refers to the frequencies while n=1, 2,…, N-1 refers to the samples. The Inverse Discrete Fourier Transform (IDFT) can be expressed as:

$$g(n\Delta T) = \sum_{n=0}^{N-1} N G_k e^{i\frac{2\pi k n}{N}} \qquad \textbf{5-13}$$

It is possible to notice that, in order to obtain N frequency components from N samples, it is necessary to perform N^2 operations on complex numbers, which can be very expensive in some applications. A similar technique, which can obtain the same result with less operations, $N*\log_2(N)$, is the Fast Fourier

Transform (FFT). This is commonly used in signal processing software programs. Equation 5-12 is rearranged in a matrix form:

$$\{G\} = \frac{1}{N}[A]\{g\} \qquad \textbf{5-14}$$

The array $\{G\}$ contains the Fourier coefficients, $\{g\}$ is an array containing the samples and $[A]$ is a square matrix, *NxN*, containing complex numbers all with unitary modulus. Each row of $[A]$ represent one frequency, in particular the first one represent the constant component, *f*=0.

5.4 Computation of the transfer function in the frequency domain

As discussed in Section 5.3, an important step in the reconstruction of an impact force is to calculate the FRF of the system. Numerical estimation of the FRF may be inaccurate due to differences between actual and modelled boundary conditions, material behaviour, etc. In this section, two methods for determining the FRF are presented.

The first one, which can be easily implemented numerically, consists in calculating the FRF of the system under exam using numerical software. For example Abaqus provides a solver called "steady-state analysis" which calculates the linear response of the system under a harmonic load in a defined frequency range. This method is fast and provides accurate results, as it will be shown in Section 6.1. From an experimental point of view, this approach can be performed only with the appropriate equipment and software. Modifications of the boundary conditions between this evaluation and the real impact case can produce wrong results. For those reasons an alternative approach is studied in this thesis.

When performing an impact during laboratory tests, for example using a drop tower, not only the response of the system can be recorded using one sensor, but also the force can be recorded with the aid of an instrumented impactor. In this way, two signals are available: the impact force history, *p(t)*, and the response history, *u(t)*. The easiest way to calculate the spectral response of the system would be computing the FFT of both signals and using the convolution theorem, Equation 5-3. However, this method did not provide acceptable results for force reconstruction, which agrees with the findings of [10]. Hence, a more accurate approach is proposed in this work.

Consider a system with an impulse response *h(n)* and let *x(n)* be a discrete sequence of input values. Equation 5-1 can be written as:

$$y(n) = \sum_{k=-\infty}^{\infty} h(n-k)x(k) \qquad \textbf{5-15}$$

The autocorrelation function for the output process is given by:

$$s_{yy}[n, n+m] = \mathrm{E}[y[n]y[n+m]] \quad \textbf{5-16}$$

Where E[] denotes the expected value of the variable. After some manipulations, which can be found in [95], it is possible to write:

$$s_{yy}[m] = \sum_{l=-\infty}^{\infty} c_{hh}[l]\, s_{xx}[m-l] \quad \textbf{5-17}$$

Exploiting the convolution theorem, it is possible to move to the frequency domain:

$$S_{yy}(f) = C_{hh}(f)S_{xx}(f) \quad \textbf{5-18}$$

Where S_{yy} and S_{xx} are called power spectra of the output and input. They are defined as:

$$S_{yy}(f) = Y(f) \cdot Y^*(f) = |Y(f)|^2$$
$$S_{xx}(f) = X(f) \cdot X(f) = |X(f)|^2 \quad \textbf{5-19}$$

Going back to Equation 5-2 and applying the definition of power spectrum, it is possible to write:

$$S_{yy}(f) = [H(f)Y(f)] \cdot [H(f)Y(f)]^* = [H(f)Y(f)] \cdot [H(f)^*Y(f)^*] = |H(f)|^2 S_{yy}(f) \quad \textbf{5-20}$$

Therefore, C_{hh} turns out to be the module of the transfer function:

$$C_{hh}(f) = H(f)H^*(f) = |H(f)|^2 \quad \textbf{5-21}$$

Hence, an estimation of the module of the transfer function can be obtained through the power spectrum of input and output of the system. However, the module of the transfer function does not contain any information on the phase of the system. To calculate the complete transfer function, the cross correlation is needed:

$$s_{yx}[n, n+m] = \mathrm{E}[x[n]y[n+m]] \quad \textbf{5-22}$$

Moving again to the frequency domain, the equation becomes:

$$S_{yx}(f) = H(f)S_{xx}(f) \quad \textbf{5-23}$$

The transfer function can be calculated from the above equation. In the present paper, the power density spectrum was obtained thanks to the calculation of the periodogram [94], which provides better power

spectrum estimation for discrete signals, which can present relevant amount of noise. Given a set of data, which includes one input and one output arrays, it is possible to calculate the relative power spectrum and cross correlation. A more detailed description of this approach can be found in [94, 96, 97]

The transfer function of the system under exam, component by component, is then given by:

$$H(f_n) = S_{yx}(f_n)/S_{xx}(f_n) \qquad \textbf{5-24}$$

With Equation 5-24 it is possible to determine the transfer function to be used in Equation 5-3. Theoretically, for a linear system, transfer functions obtained from different impact data are the same. However, as nonlinear effects are present in the dynamics of the system studied in this work, differences are expected. Hence, Equation 5-24 was applied to some impact cases with different impact energies and *H(f)* was defined as the average of the results. In [84], it is underlined that this is a reliable approach when different sets of experimental cases are available. After *H(f)* has been determined, the force due to an unknown impact can be reconstructed by applying inverse FFT on the results of Equation 5-3). The algorithm, shown in Figure 55, is summarized as follows:

- Determine the number of frequency components, N, to be used in the reconstruction technique
- Carry out a set of impacts and collect force/response data to compute H(f)
- Choose a single case to be reconstructed
- Perform the reconstruction

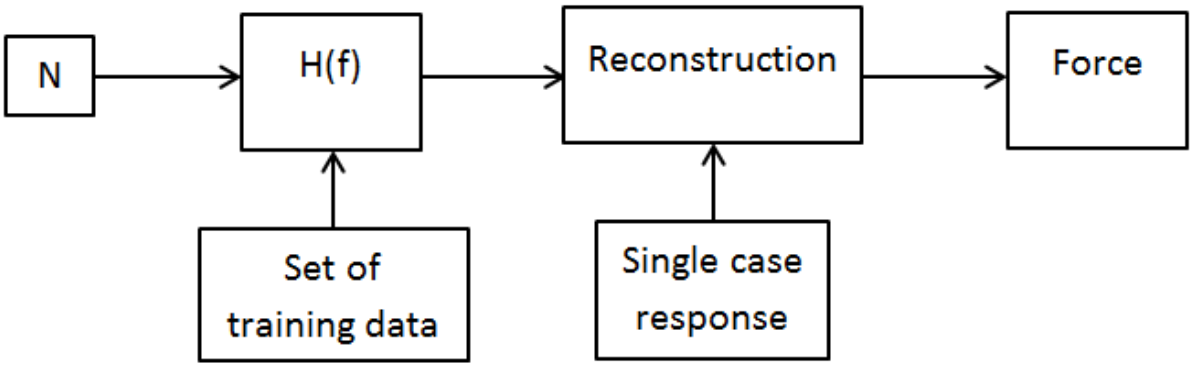

Figure 55: Block diagram of the algorithm.

It should be noted that the number of frequency components which are available from the FFT of a signal depend on both the sampling frequency and the total time of acquisition, T. The highest frequency components usually contain noise, which in experiments can be due to several sources like temperature variation, electric fields, rotating machineries, etc. These components can adversely affect the reconstruction results. Choosing a limited number of frequency components can improve the results and accelerate the algorithm. A deeper explanation of this topic can be found in [90].

5.5 Time domain approach

The strength and the weakness of the Fourier method is that it establishes a one to one relationship between the frequency components. Reflections from the boundary surface of the system can result in total loss of information at certain frequencies [85]. Although an inversion of Equation 5-1 can be difficult to obtain, due to the presence of the integral, when working with a discrete signal the integral is replaced by a summation. This enables the equation to be inverted more easily. A possible approach, based on a "wavelet deconvolution", was proposed by Doyle [86]. The starting point is similar to the one given by Equation 5-6, but in this case the force and displacements are not expressed with the Fourier coefficients, but as a sum of basis functions:

$$P(t) = \sum_{m=1}^{M} \tilde{P}_m \phi_m(t) \quad M < N \qquad \textbf{5-25}$$

Where N is the number of samples captured in the analysis. $\phi_m(t)$ is a basis function, which is used as training for the structure. In order to calculate the response of the system to different inputs, $\phi_m(t)$ is shifted in time, in order to have a set of M basis functions. The choice of $\phi_m(t)$and of M is very important as the shift of the basis function should span all the expected duration of the unknown force and its frequency content must exceed that of the measured response, [86]. The chosen basis function is a triangular pulse. However some limitations of this choice will be underlined further.

$$\phi(t) = e^{-(\frac{t-t_0}{\alpha})^2} \qquad \textbf{5-26}$$

Where α is a parameter which determines the width of the pulse. An example of training wavelet and of the typical response of one system is given in Figure 56.

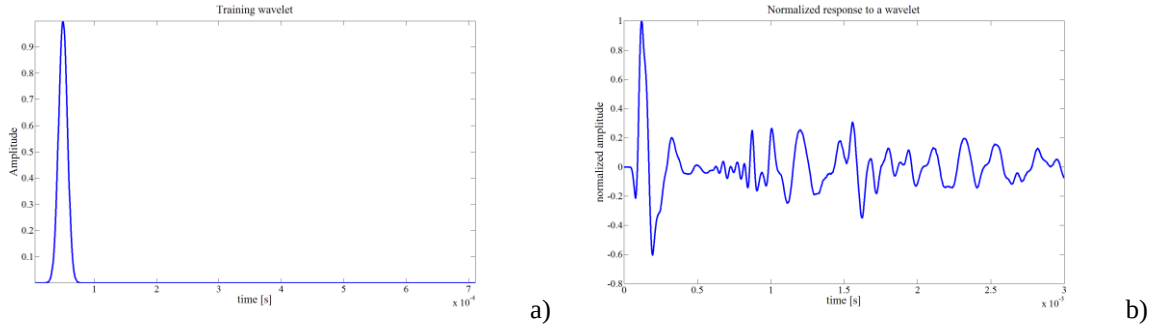

a) b)

Figure 56: a) Typical training wavelet. b) Typical response.

Introducing equation (21) in equation (1) leads to:

$$u(t) = \sum_{m=1}^{M} \tilde{P}_m \int_0^t G(t-\tau)\phi_m(t)d\tau = \sum_{m=1}^{M} \tilde{P}_m \psi_m(t) \qquad \textbf{5-27}$$

In this case the functions $\psi_m(t)$ are the equivalent of the frequency components of the FRF in the previous analysis. They are simply the response of the system to the pulse $\phi_m(t)$. In particular it is important to underline how there is the need to calculate only one $\psi(t)$ because all the others are obtained by simple shifts. The problem now consists of determining the coefficients $\tilde{P}_m$ that best fit the response information. It can be formulated as:

$$[\tilde{G}]\{\tilde{P}_m\} = \{\tilde{u}\} \qquad \textbf{5-28}$$

Where:

$$[\tilde{G}_{i,j}] = \sum_k \psi_i(t_k)\psi_j(t_k) \qquad \{\tilde{u}_i\} = \sum_k \psi_i(t_k)u(t_k) \qquad \textbf{5-29}$$

The matrix $[\tilde{G}]$ is square and symmetric with size *MxM*. This method provides better results when the frequency content of the force is very high, but the fact that the shift must span all the presumed unknown force can lead to mistakes in the force reconstruction analysis. Moreover the choice of the basis function must be appropriate. This prevents this method to be "general", because it depends on the choice of some parameter which greatly affects the final result. Examples of these drawbacks will be given in the following chapter.

5.6 Algorithms for impact location

The calculation of the transfer function is not the only concern in the inverse problem. The other main issue is related to the determination of the position of the impact. The transfer function does not only depend on the geometry, material and the boundary conditions of the system but also on the mutual position between the load and the sensors at which the dynamics is measured. This means that, in order to reconstruct the impact force, the transfer function must be known at the impact location. As in real cases this is unknown, the inverse problem involves the determination of the impact position and the determination of the transfer function at that point.

As for the determination of the transfer function, also for the one of the impact position several approaches can be followed. One of the most common is based on the triangulation of the signals collected at three (or more) points. This method is based in the calculation of the time of arrival, ToA, of the waves generated by the impact. Once this is known, the distance between one sensor and the possible impact location can be computed with:

$$r = v * ToA \qquad \textbf{5-30}$$

In this equation v represents the velocity of the wave, while r the radius of the circumference where the impact could have occurred. When three sensors are available the three circumferences intersect at one point, which is the actual impact position. The application of Equation 5-30 is subjected to the knowledge of the wave propagation speed in the system. For isotropic materials this can be easily calculated from the relationship:

$$v = \sqrt{\frac{E}{\rho}} \qquad \textbf{5-31}$$

Where E is the elastic modulus, uniform in all directions and ρ is the density. When working with anisotropic materials, Equation 5-31 is still valid, but the elastic modulus is not constant anymore; it depends on the direction of propagation. As this is generally not known, being exactly what the inverse problem should calculate, the wave speed cannot be determined. In [98] the classic triangulation method was coupled with an optimization procedure based on genetic algorithms in order to locate impact on a composite plate. A three layer identification approach, based on ToA was proposed in [99]. In [100], the wave speed on a composite panel was first determined experimentally in different directions, and then this information was exploited in an optimization procedure to locate the impact position. Anyway the need to know the velocity of the wave in different directions makes this approach difficult to implement on complex structures.

Another possible approach for impact location was proposed in [88]. In this case the estimation was based on the power of the signal computed as:

$$P_i = \frac{1}{t_f - t_0}\int_{t_0}^{t_f} |s_i(t)|^2 dt \qquad i = 1,\ 2,\ 3,\ 4 \qquad \textbf{5-32}$$

In the above equation $s_i(t)$ refers to the signal collected at sensor I, while t_f and t_0 represent the final and initial sampling time. When Equation 5-32 has been calculated for all sensors, the position of the load can be estimated as:

$$\bar{x}_c = \frac{\sum P_i x_i}{\sum P_i} \qquad \bar{y}_c = \frac{\sum P_i y_i}{\sum P_i} \qquad \textbf{5-33}$$

The terms x_i and y_i refer to the coordinates of each sensor.

Another possible approach is the one based on artificial neural networks (ANNs). This is based on a set, usually very large, of training data which is used to "train an algorithm about the response of the system under exam for impacts occurring at different locations. Different features of the signals can be used to train the network like the time after impact of maximum response, magnitude of maximum response, peak to through range of the response etc. [92]. Examples of the application of this technique can be found in [28, 41, 91, 92].

5.7 Novel approach for impact detection

In this thesis a novel approach for impact detection is presented. It is based on the proper orthogonal decomposition of the signals collected at certain positions. A former application of POD on impacts was performed in [42, 101] but in those cases the application consisted in finding nonlinearities in the system, which was a vibrating beam harmonically impacting a fixed tool. The first POM is considered as representative of the power collected by each sensor. In the network formed by the PZTs, which in the case presented is a structured one, the square formed by four adjacent sensors which can capture the most of the energy is considered and Equation 5-33 is applied to locate the impact. This method resembles what proposed in [88], but no integration of the signals is involved, this can save computational time, especially when many sensors are involved. The aim of this approach is to exploit the already mentioned capability of the POD to extract from a large number of variables only the most relevant ones, reducing the dimension of the system. An outline of the algorithm is shown in Figure 57. The step by step procedure can be summarized as:

- Acquisition of signals at different positions on a structured grid
- Performing the POD and calculate the main POM
- Determine the grid point at which the POM has its maximum value
- Determine the corresponding grid, based on the POM value at the neighbouring points
- Determine the position of the impact with Equation 5-33

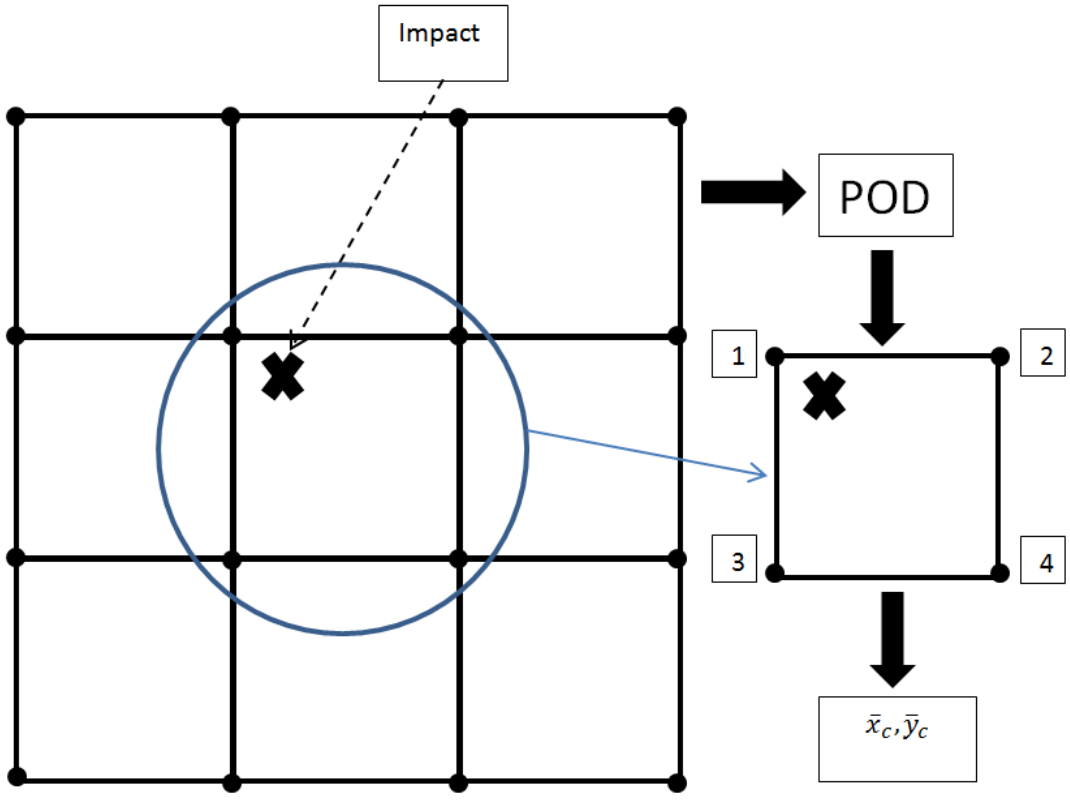

Figure 57: Impact location outline.

It is worth to notice that this application does not consider the energetic approach proposed in the damage detection algorithm. As no fundamental harmonics is excited, being the load just a short period impact, the energy cannot be concentrated in just few POMs. For this reason only the first POM is considered. As the considered time response of the system is short, the most energetic mode is the one which can contain most of the information on the impact.

Chapter 6: Inverse problem analyses

In this chapter results obtained with the solution of the inverse problem are presented. First a simple model was investigated in order to determine which method, time-based or frequency-based, is more suitable for typical aeronautical cases. In this example the position of the load was known. After determining the most appropriate method, simulations of impacts where its position was not available where conducted. After showing promising results the model was changed to a more realistic one and the reconstruction was performed based on what explained in section 5.4 both with numerical simulations and experiments. Finally the POD was applied for impact location, as described in section 5.7.

6.1 Determination of the most suitable approach

In order to show the capability of the method, first a simulation is conducted on a composite plate in which all the edges are pinned. This example will be used also in the following section. The model was chosen because both analytical and experimental evaluation of the impact force where provided in [102]. The properties of the model are presented in Table 8.

Table 8: Properties of the system

System		T800H/3900-2 CFRP plate, simply supported	
Size		127.0x76.2x4.65 mm	
Layup		$[45/90/-45/0]_{3s}$	
Density ρ		1540 kg/m^3	
E11	129 GPa	G12	3.5 GPa
E22	7.5 GPa	G13	3.5 GPa
V12	0.33	G23	2.6 GPa

In this case an impact on the plate was modelled using a non-linear spring with a mass attached to one end, and the other end connected to the plate. Just to validate the model, one case is presented with a mass of 6.15 kg and a velocity of 1.76 m/s, which is a case presented in [102]. The equation for the spring behaviour is based on the Hertzian contact law:

$$F = k * \alpha^{3/2} \qquad \textbf{6-1}$$

Here $k = 0.6x10^9 N/m^{3/2}$ as suggested in the above mentioned paper.

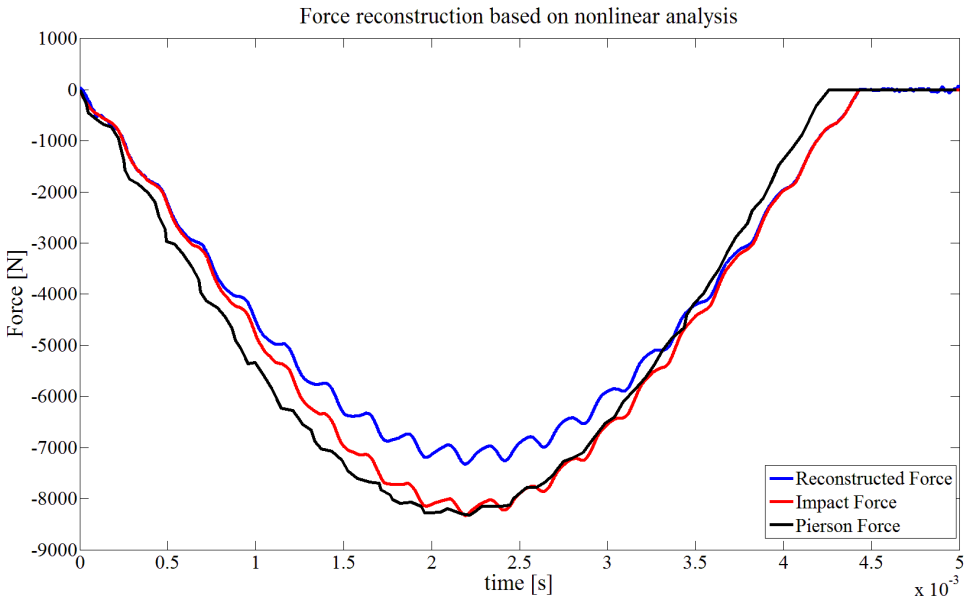

a)

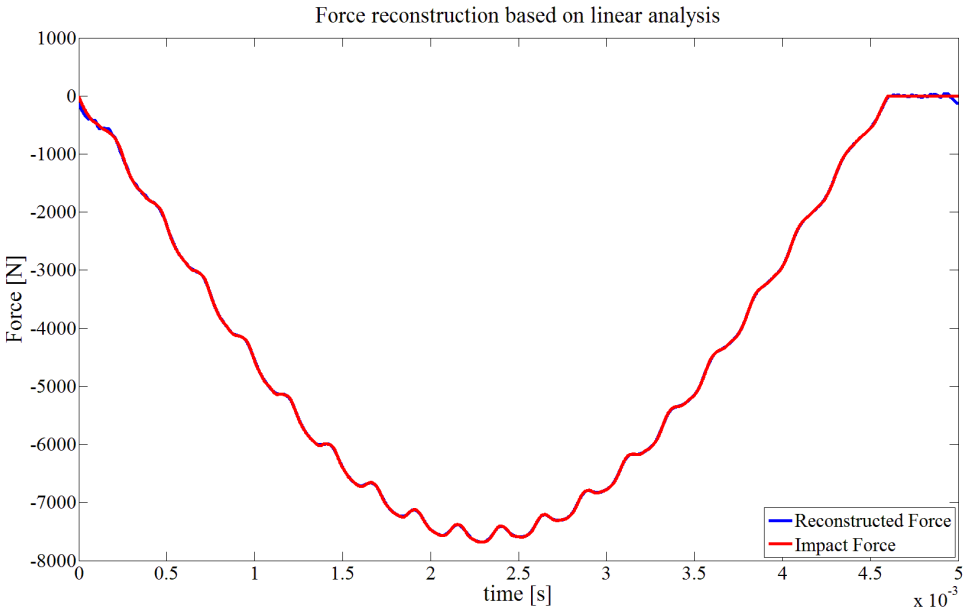

b)

Figure 58: mass 6.15 kg, velocity 1.76 m/s. a) nonlinear analysis. b) Linear analysis

Comparing the result provided by the spring-impact model, red curve, with the one provided by literature, black, it is possible to notice how the result is good and the model can be used to simulate low velocity impact, Figure 58a). The reconstructed force, blue line, is very similar to the calculated one, except for the magnitude at the highest value. This because the force applied is very high and it leads to a nonlinear deflection of the plate. As the method applied to reconstruct the force is based on a linear relationship between displacement and force, the result is affected by the actual nonlinearity in the system. In order to verify this conclusion, an impact simulation was carried out in Abaqus considering only linear geometrical deformations. The result of the analysis and of the reconstruction is presented in Figure 58b). As it is possible to see the results match completely. As the influence of the nonlinearity creates a high difference between the maximum amplitudes of the actual and reconstructed force, new simulations were

made with lower impact energy. The new parameters were: mass 6.15 kg and velocity 1 m/s. In Figure 59a) it is possible to see that the influence of the nonlinearity, although still present, is not as relevant as before. Figure 59b) shows that the method can reconstruct the force even when a certain amount of noise is added to data (SNR=30). Clearly the reconstructed force is much noisier than the real force. A possible solution to overcome of this issue will be presented in Section 6.4.

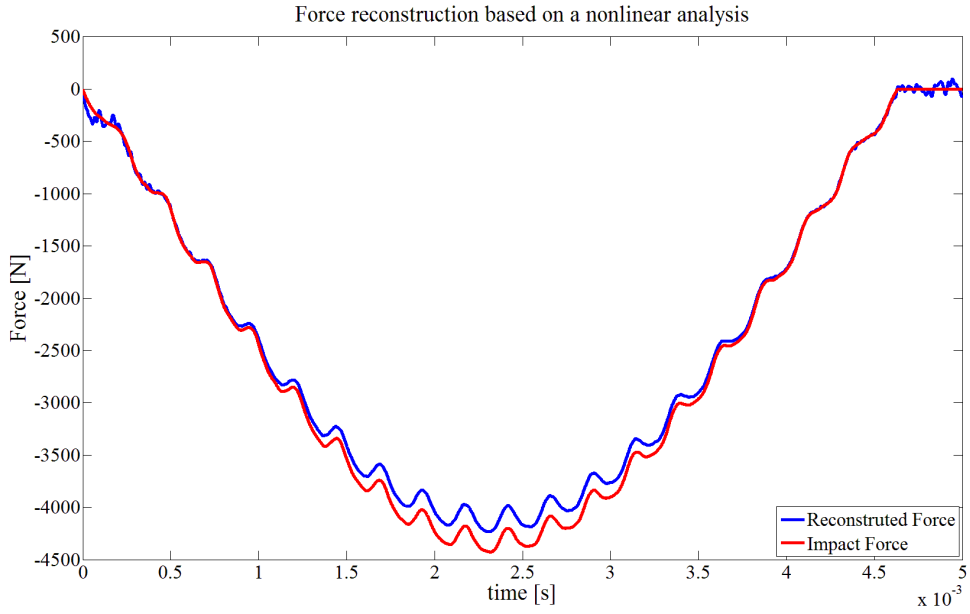

a)

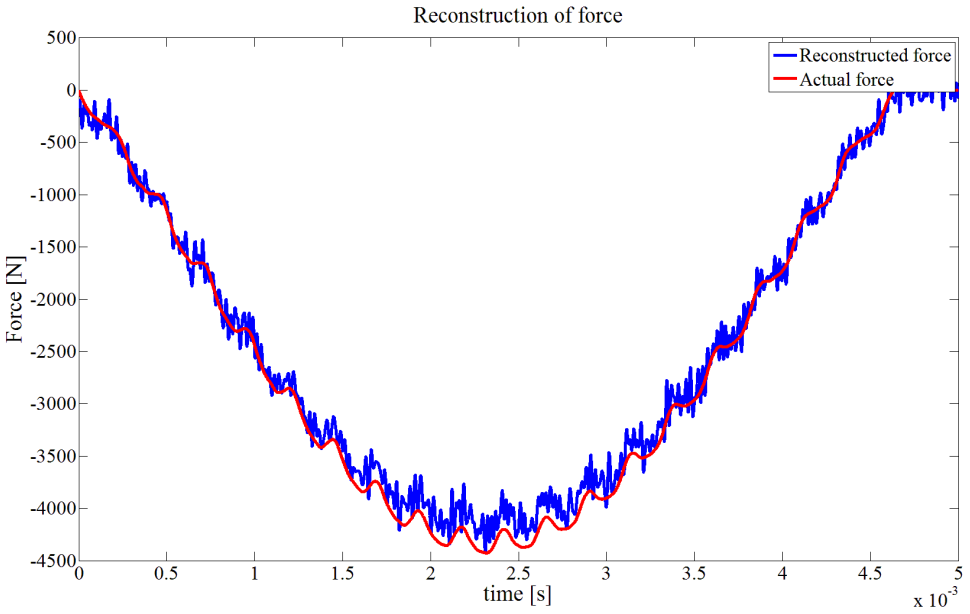

b)

Figure 59: Reconstruction of force. a) Without noise. b) With noise, snr30.

The time-based method was then applied to the impact case with mass 6.15 kg and velocity 1 m/s. One great issue was that the time span of the actual force high. As the shifted wavelet should span all the presumed force [86], the computation resulted to be very long and also the result was affected by this drawback. From Figure 60a) it is possible to see that the reconstructed force presents at the beginning an

anomalous peak with amplitude greater than the force itself. Deleting this peak, Figure 60b), the result highlights how the nonlinearity of the force leads to a difference between the amplitude of the actual and reconstructed force. This result is achieved also when the response of four sensors is used, Figure 61. The change of the load type, for example a high frequency sine pulse Figure 62, leads to better results. However when the load has a lower frequency content, as in the impact case, the chosen training wavelet resulted to be not completely suitable for the case under exam. In particular the reconstruction took much computational time and the results presented some peaks at the beginning or end of the reconstructed force which had to be filtered on a second step. Therefore it can be concluded that this method revealed not to be suitable when the frequency content of the load is low .An analysis with different wavelets can be performed in order to optimize the analysis also in the impact case. Anyway for the impact cases of interest the frequency-based method is preferable; hence it will be used in the following analyses.

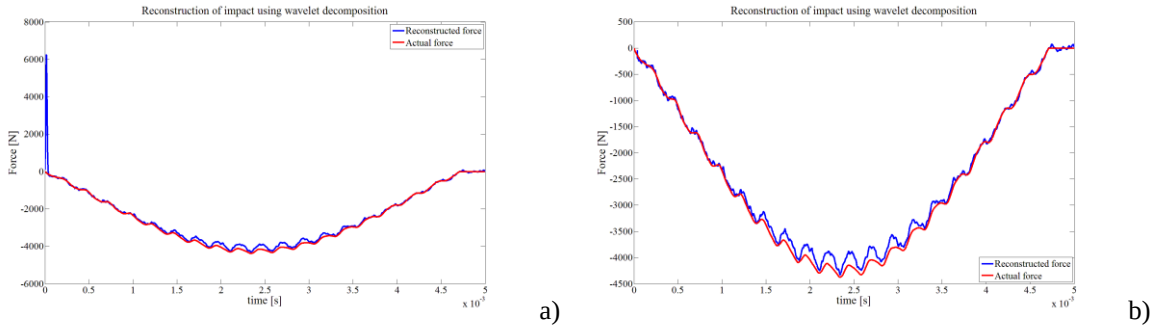

a) b)

Figure 60: Reconstruction of impact with the wavelet deconvolution using 1 sensor. a) Result of the analysis. b) Result deleting the peak at the beginning.

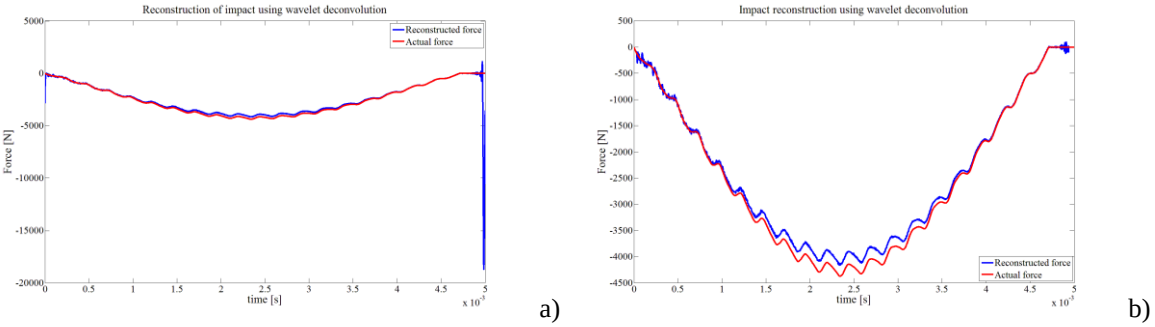

a) b)

Figure 61: Reconstruction of impact with the wavelet deconvolution using 4 sensors. a) Result of the analysis. b) Result deleting the peak at the beginning.

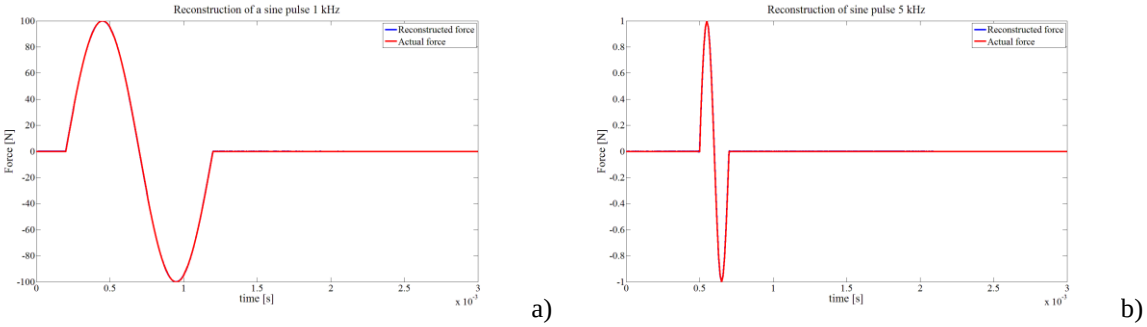

a) b)

Figure 62: Reconstruction of force with the wavelet decomposition. a) 1 kHz sine. b) 5 kHz sine.

6.2 Second simulation: unknown position of the impact

For most of the real cases, the position of the impact is not known, so the method described in Section 5.3.15.3 cannot be applied straightforwardly. However the technique can still be applied if the position of the load and the corresponding matrix *H* are estimated from the sensors' response. A possible approach is given in [88] for the force location. In this research the first part of that procedure is applied, while the updating technique is different. In order to evaluate the matrix G for a random force location, the plate was trained calculating the matrix G at four points, for four different positions of the load; in this way 16 transfer functions were available. Each point had the matrix G corresponding to four different load positions. In Figure 63 the scheme of the plate is given. The four sensors (circles) represent both the location of the output points and the location of the training forces. In the picture the positions of the load cases (crosses) are also highlighted.

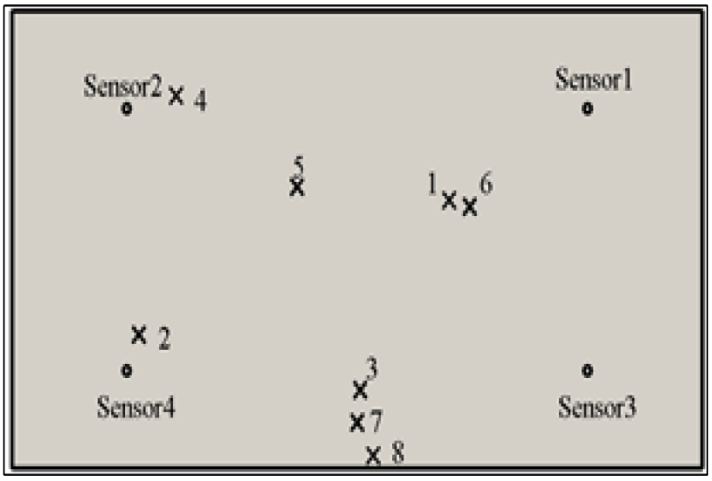

Figure 63: Schematic representation of the model under analysis. All the four edges are simply supported

Table 9: Coordinates of sensors and impact positions.

Position	1	2	3	4	5	6	7	8	Sens 1	Sens 2	Sens 3	Sens 4
X [m]	0,016	-0,036	0	-0,0315	-0,0105	0,0195	0,0005	0,005	0.04	-0.04	0.04	-0.04
Y[m]	0,006	-0,018	-0,028	0,022	0,008	0,005	-0,023	-0,033	0.02	0.02	-0.02	-0.02

After the displacements were acquired at the sensors' location, an initial estimation of the load position was made with Equations 5-32 and 5-33. Based on this position, the matrix *H* for each sensor was interpolated in order to apply the inverse problem. The reconstructed displacements were calculated together with the reconstructed force. Comparing the real displacement with the reconstructed one at each sensor, the position of the load was updated and so the force reconstructed again. With this approach the location and reconstruction of impact are performed together with a single updating procedure. A schematic representation of the iterative method is given in Figure 64.

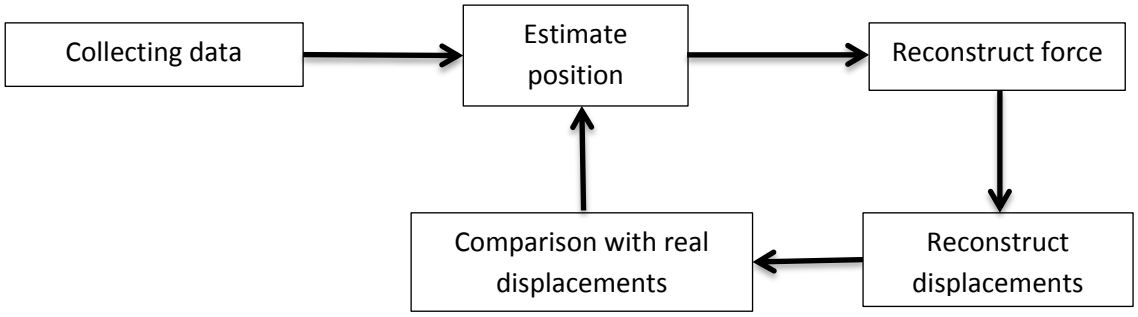

Figure 64: Schematic representation of the method.

The convergence of the method is based on the minimization of the error in the displacement integral of Equation 6-2, while the error in the calculated position is determined by Equation 6-3.

$$error = \frac{\int_0^T |s_{imp}(t) - s_{rec}(t)| dt}{\int_0^T s_{imp}(t)\, dt} \qquad \textbf{6-2}$$

$$error\_position = \left| \frac{position_{imp} - position_{rec}}{position_{imp}} \right| \qquad \textbf{6-3}$$

In the above equations, the subscript *imp* refers to the real signal or position, whereas *rec* refers to the reconstruct ones. The term *position* represents the vector from the centre of the plate to the impact position.

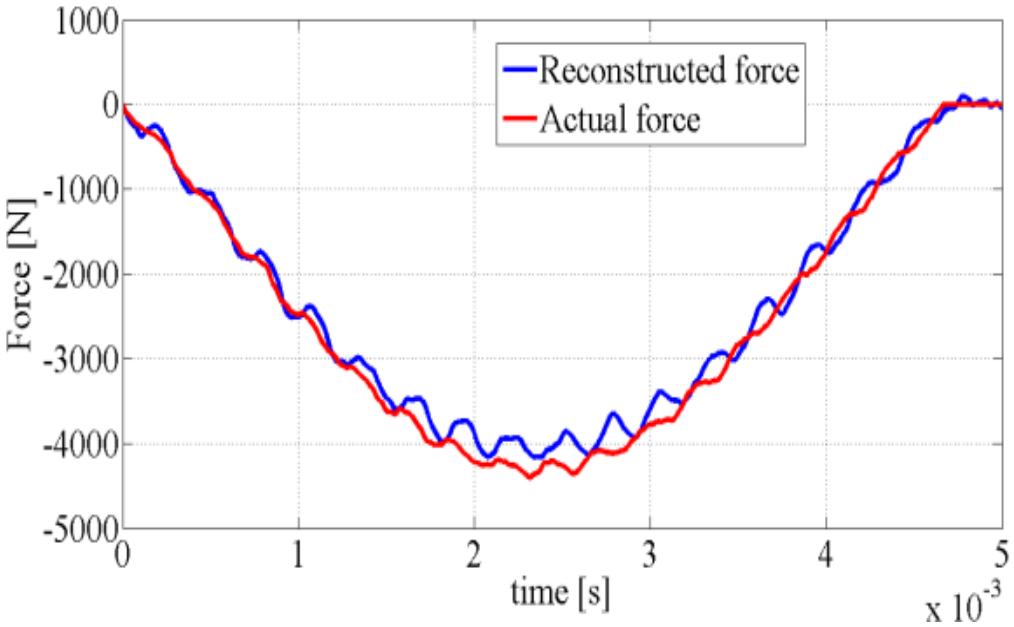

Figure 65: Reconstruction of the impact at position 5.

6.3 Numerical results on the simple model, unknown location of the impact

The load case under exam is an impact caused by a mass of 6.15 kg with an initial velocity of 1 m/s. the impact is modelled as discussed in section 6.1.

This part of the analysis is certainly more challenging as it represents the most of the real cases. The analysis highlighted that the present approach is suitable for the purpose of both locating and reconstructing the impact under certain circumstances. In particular it was found that the relative position of the impact point with respect to the sensors can influence the final results. In some cases the position of the load was wrongly calculated and so the interpolation of the transfer matrix was incorrect. However, for certain cases the results were accurate in terms of both force and displacement reconstruction.

From Figure 65 to Figure 68 the result corresponding to the impact position 5 is presented. It is clear that both the force and the displacements are reconstructed correctly. In particular Figure 66 shows that the error between the energy of the real and calculated displacements converges quickly. The convergence of the reconstructed displacement to the real one is also highlighted in Figure 67 and Figure 68.

In Figure 69 and Figure 70 other two cases are shown, referring to position 6 and 7. The first one refers to another good reconstruction while the second to a failure in the method. When the impact was located outside the rectangle formed by the sensors, the interpolation approach gave incorrect results. This was due to an error in the position calculation, which was very different from the real one. An explanation is given in Figure 71 in which the error in position calculation of all the cases under exam is presented. While for most of the cases this error is low, for three impact cases it is really high. In order to investigate the method also when the load was applied at those positions, the output locations were changed and the area of that rectangle increased. However the results were not satisfactory, probably because of the proximity of the boundary condition which affected the FRF. The problem related to boundary conditions in damage detection based on wave propagation is well known. These cause reflections which sum to the incident waves, causing a loss of information about the impact [85, 103]. A more detailed modelling of the effects of boundary conditions will be presented in the Section 6.5.

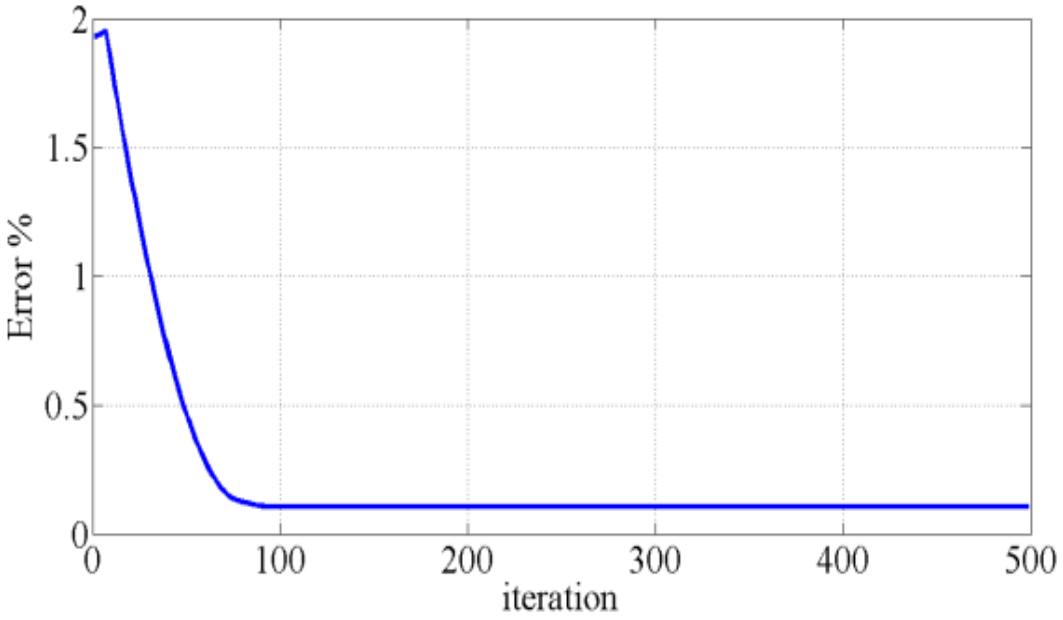

Figure 66: Convergence of the algorithm for the impact at position 5.

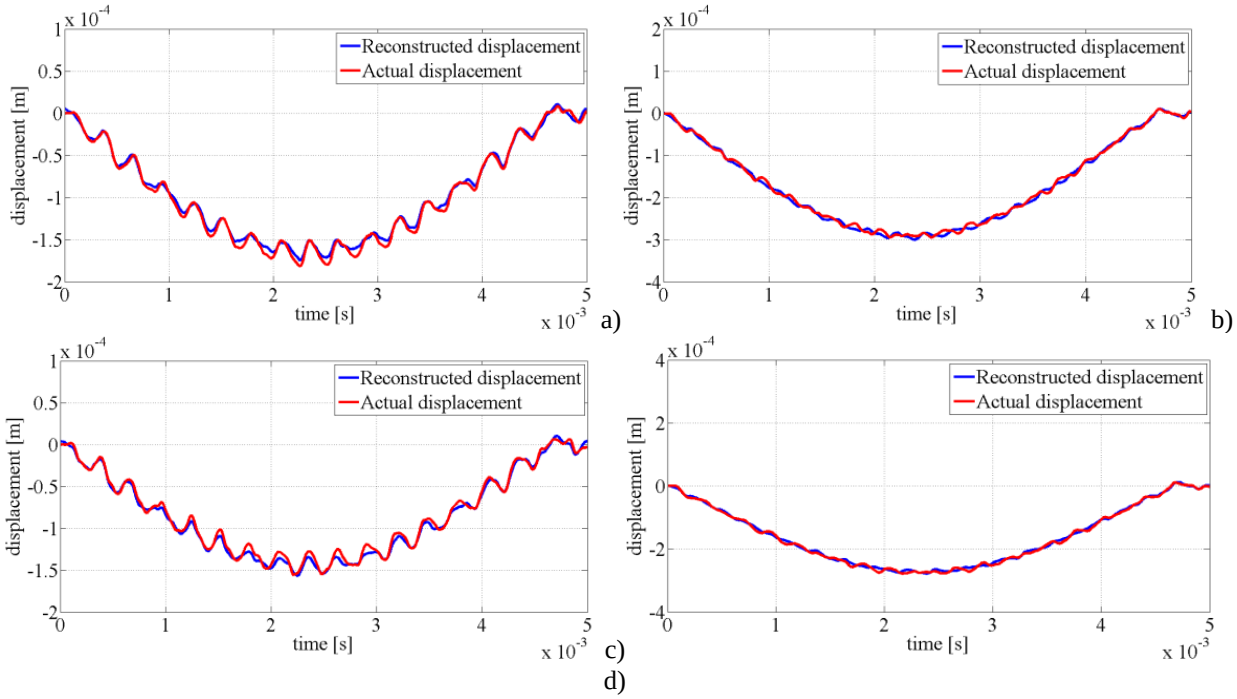

Figure 67: Result obtained for the impact at position 5. Displacement reconstruction for sensor 1-4

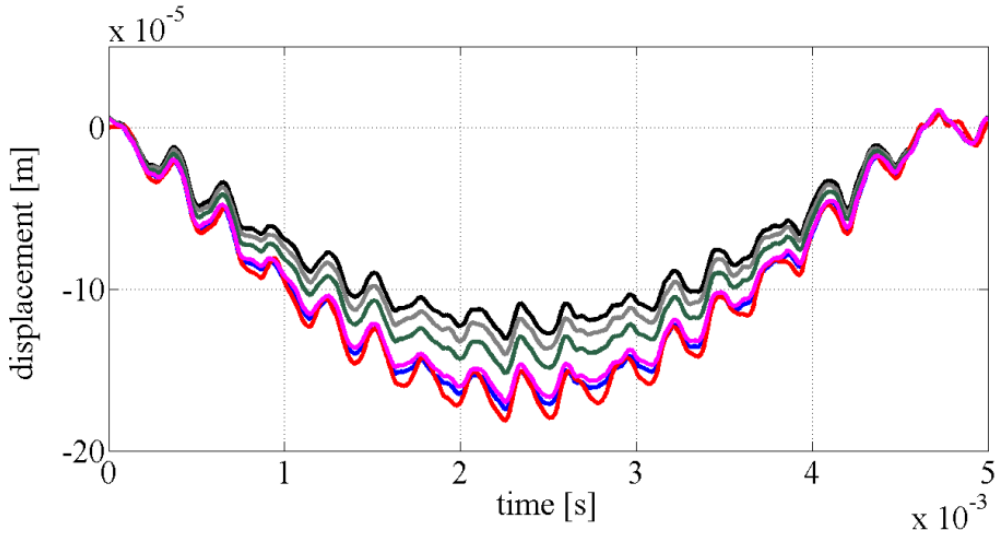

Figure 68: Example of convergence of the reconstructed displacement. The black line represents the first iteration, the blue line the last iteration and the red line the real displacement.

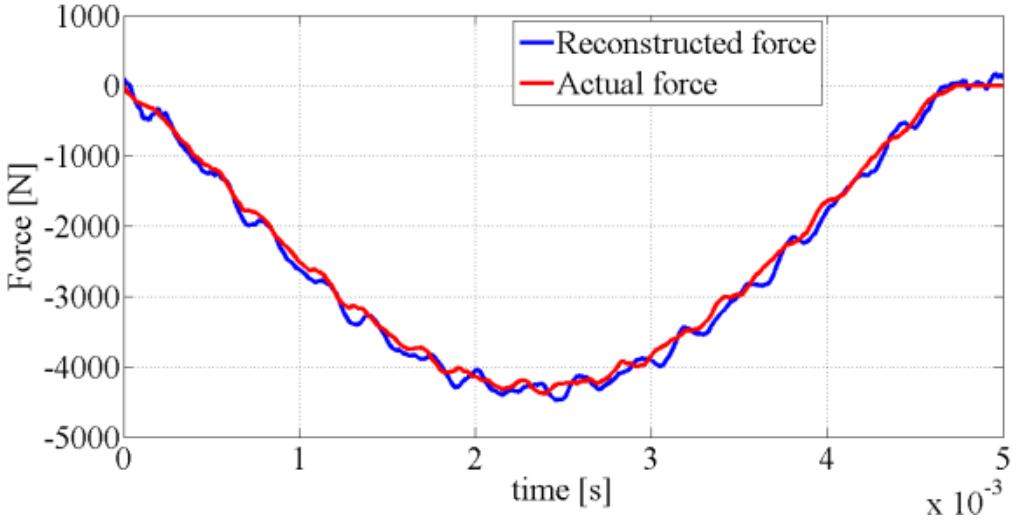

Figure 69: Result obtained for the impact at position 6.

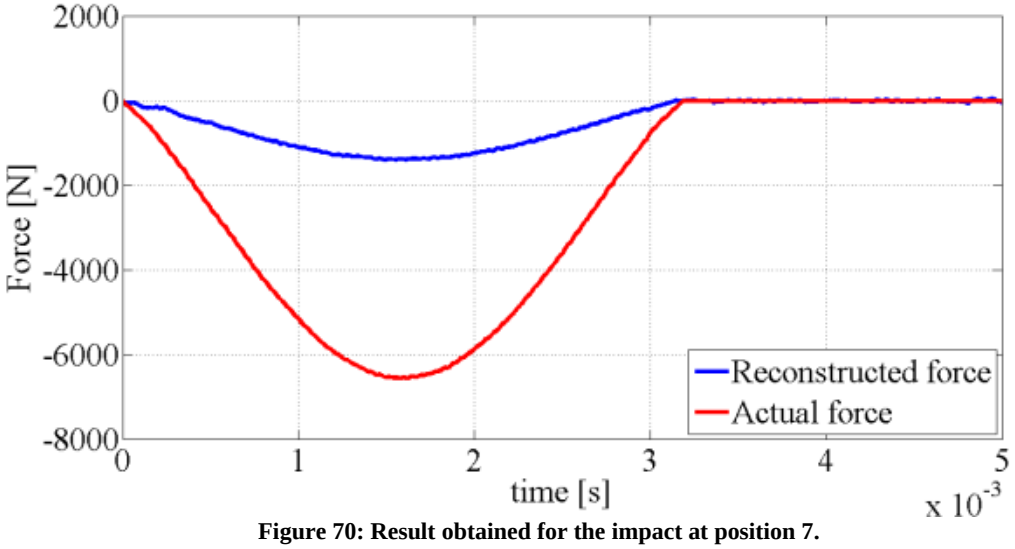

Figure 70: Result obtained for the impact at position 7.

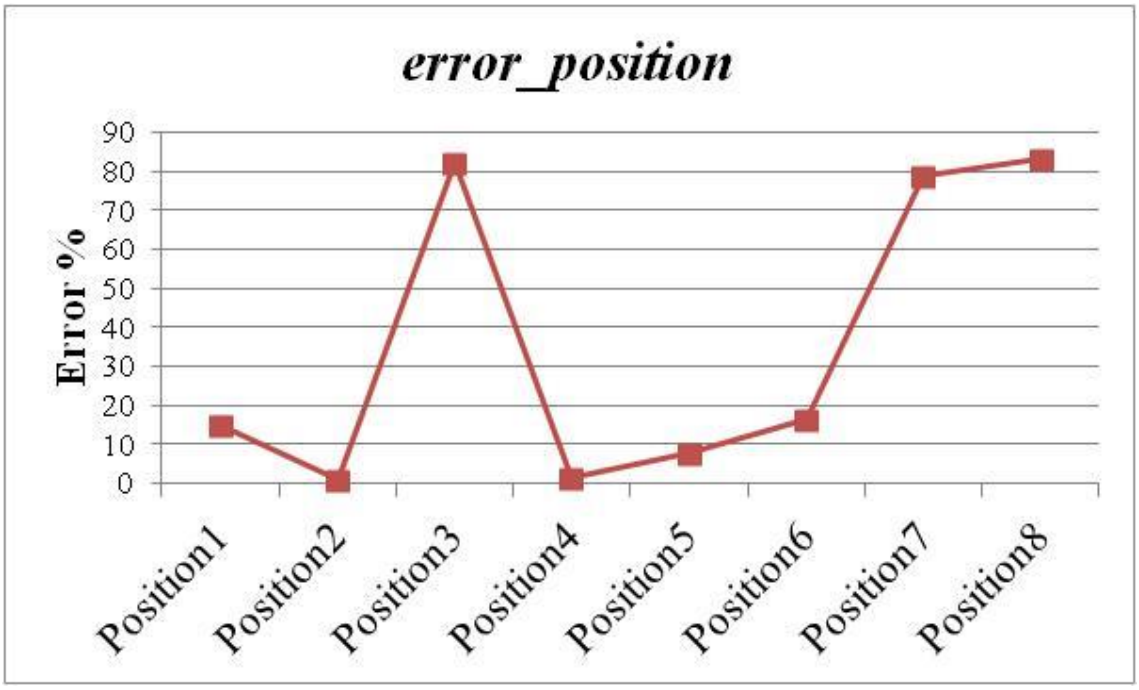

Figure 71: Error in the position calculation.

6.4 Influence of noise

The presence of noise in the data can affect the result, as previously observed in section 6.1. Especially in real applications the quantity of noise can be really high so an investigation of the method under a certain level of noise was conducted. In such situation the possibility of performing the analysis using fewer modes can be really helpful, as typically noise affects the highest frequencies in a signal. In the simulation, the signal of the sensors were corrupted using the command "awgn" in Matlab, with a signal to noise ratio (SNR) of 30. Results obtained using all the modes and just 20 of them, for the position 1 load case, are presented in Figure 72. In the first case the reconstructed force is corrupted; the lower frequencies seem not to be affected by the noise, while at high frequencies, oscillations appear. This suggests that the amount of noise affects more the high frequency components of the spectrum. The application of the frequency domain approach is therefore useful to filter the presence of noise in data. Moreover it can increase the speed of the algorithm, as matrices with smaller dimensions are involved. In particular if only the maximum amplitude of the force is of interest, even less that 10 modes can be used [104]. In Figure 72b) the reconstruction of the impact using only 20 frequency component is presented.

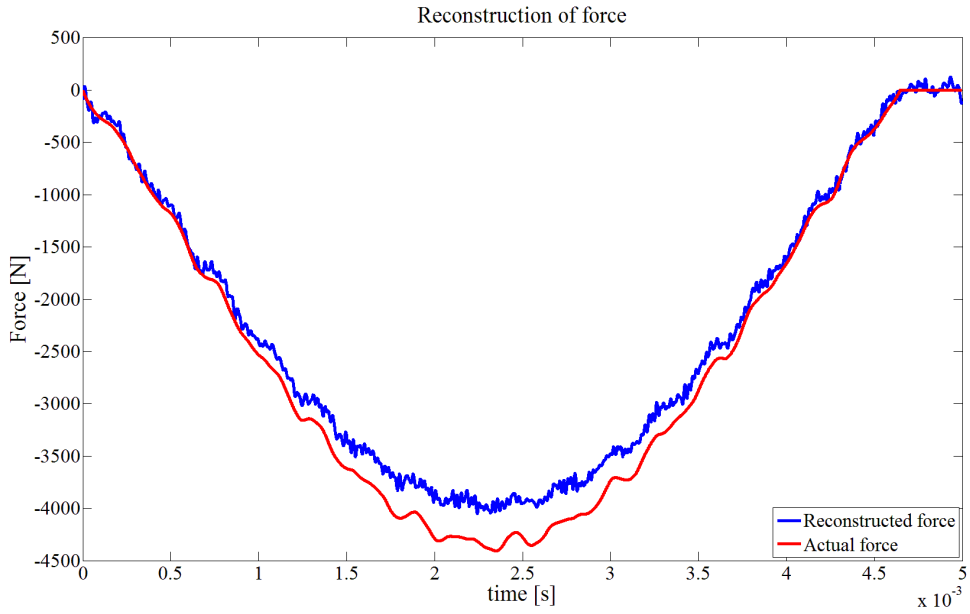

a)

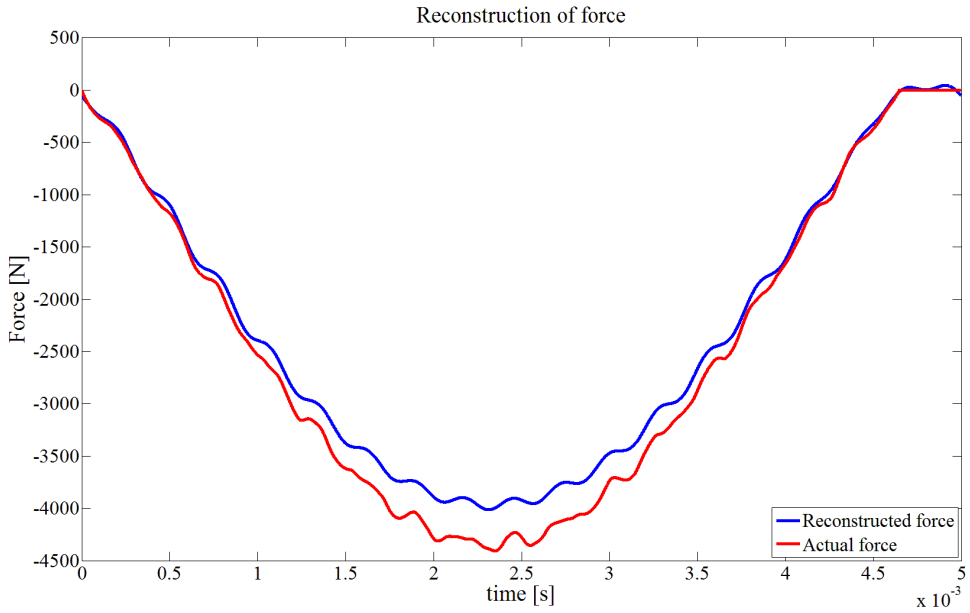

b)

Figure 72: Reconstruction of force and displacement after adding noise, SNR 30. a) Force, all modes. b) Force 20 modes.

6.5 Second model: numerical and experimental verification on a thin composite plate

Further analyses have been conducted on a plate with bigger dimensions. The frequency domain approach was used to reconstruct the force history. In particular the transfer function was computed using different sets of impacts as training, with the second approach discussed in Section 5.4. Experiments using a drop tower were conducted to validate the algorithm, while a numerical model was then developed to further investigate different parameters. In this reconstruction the position of the impact was always known. The variable was the impact velocity. The purpose of this investigation is to develop a method which can overcome the already presented limitations about the amplitude of the contact force due to the impact.

Creating a transfer function which contains information about different impact velocities can improve the reconstruction results, limiting the effects of the nonlinearity in the system's dynamics. The first two sections describe the experimental setup and numerical model. Results are presented from Section 6.5.3. The first are obtained with a classic FRF approach, as the one used previously. The incapability of that standard approach to predict the correct force reinforces the necessity of a different approach to calculate the transfer function. After that both experimental and numerical results obtained with the novel approach are presented and compared.

6.5.1 Experimental setup

Impact tests were carried out on a composite plate. The plate was placed between two steel fixtures, which provided simply supported boundary conditions. Two piezoelectric (PZT) sensors were attached to the top surface of the plate in order to collect the in plane strains due to the impact. The fixture was placed underneath a drop tower. Details of all these configurations can be found in Figure 73. The drop tower consists of a dropping mass of 2.41 kg, which is magnetically attached to a frame which can move on rails. Once the parameters of the experiment are set, the frame is moved to the desired height and then the mass is released, leaving it free to fall on the plate. Once the mass hits the plate, a servo-mechanism is activated to prevent a second impact. The force history is measured with a load cell attached to the end of the impacting mass. A photocell, activated by the passage of the mass, has the task to activate both the trigger for the acquisition box and for the servo-mechanism. All the system is controlled by a dedicated software program which provides data processing capabilities. More information about the drop tower can be found in Appendix 7.

The acquisition system has three channels. The first is connected to the load cell and the other two to circular PZT sensors (PIC 255 material), 10 mm diameter and 0.5 mm thickness, which measure strains at the top surface of the plate. The sensors were attached to the plate with an epoxy resin (Araldite 2011). The three signals are simultaneously acquired thanks to the trigger. This is essential for the inverse analysis, as the input (force) and output (sensor) signals must be synchronised. The signals were collected with a sampling frequency of 200 kHz, which is high enough to avoid any source of aliasing in the sampled signal. The impact heights, presented in Table 10, were the same as those used for the numerical analyses. Three different tests for each height were performed in order to verify the repeatability of the experiment. Only the impact at the centre of the plate could be studied with the available configuration.

Table 10: Different impact heights tested during the experiments.

Impact 1	Impact 2	Impact 3	Impact 4	Impact 5	Impact 6	Impact 7
33 mm	43 mm	53 mm	73 mm	93 mm	113 mm	133 mm

Particular attention must be paid to the connection between the PZT sensors and the acquisition system. This has a limitation on the maximum input voltage, which must be in the range ±10V. Due to the nature of the signal provided by the PZT, the raw signal exceeded this threshold even for the lowest impact height. In order to overcome this issue, the signal provided by PZT was reduced with an electrical circuit,

shown in Figure 74. This operation, which apparently performs only a reduction of the amplitude of the signal, may make other modifications to the signal. This topic is discussed in more details in the results section.

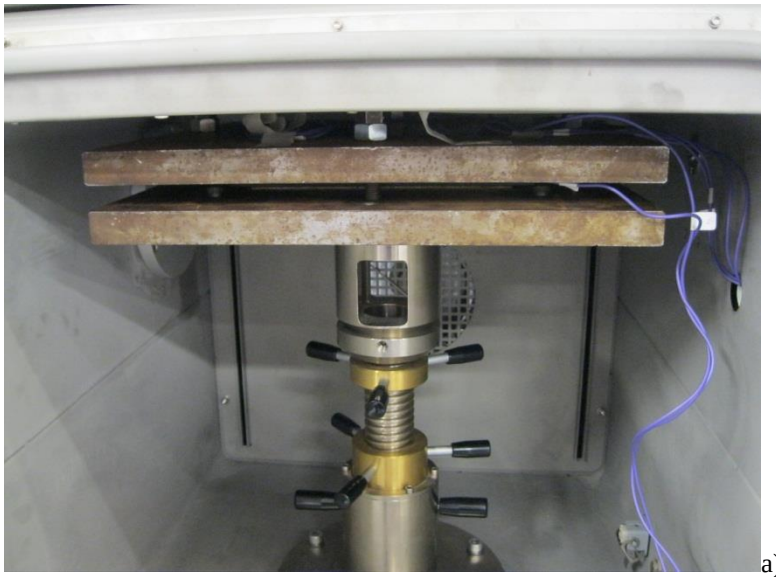
a)

b)

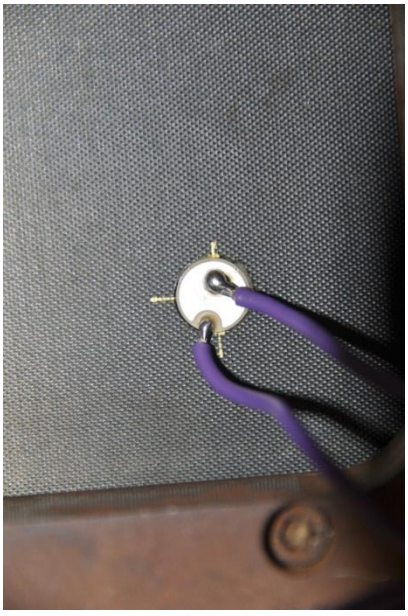
c)

Figure 73: a) Plate and fixtures placed inside the drop tower chamber. b) Drop tower. c) Highlight on one PZT

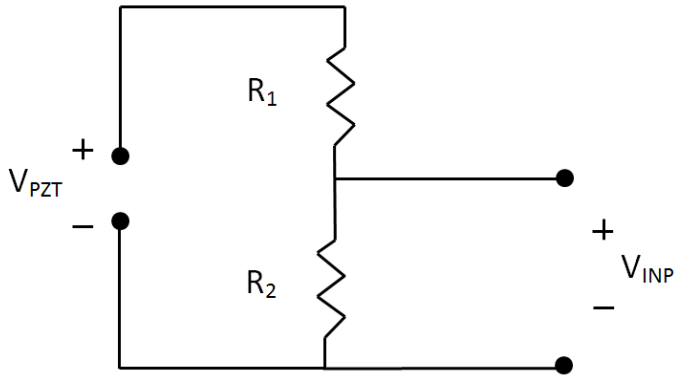

Figure 74: Voltage divider.

6.5.2 Numerical model

The system under study is a composite plate, made up of HTA/6376 carbon fibre-reinforced polymer with layup [0, +45, -45, 90, 0, 0, 90, 0, +45, -45, 0, 90]s and thickness 3.4 mm. The material properties of the composite can be found in Table 11. A schematic representation of the plate is shown in Figure 75. It can be noticed that the boundary conditions are applied in a window of 200x200 mm. The model, shown in Figure 76, consists, apart from the plate, of three rigid surfaces. The cylindrical one, with hemispheric end, represents the impactor, and the other two surfaces represent the two parts of the impact fixture, which act as boundary conditions.

The contact between the rigid surfaces and the plate was modelled with the penalty contact algorithm, considering a 0.3 friction coefficient. This allows the plate to slide between the two rigid surfaces during the impact, dissipating mechanical energy. To constrain the plate, the bottom rigid surface was kept fixed, while at the top one, a 10^{-4} mm displacement was applied, which produced a 400 N compressive load.

The plate was modelled with 38272 reduced integration continuum shell elements (SC8R) provided by Abaqus explicit [57]. In order to decrease the possible shear-locking effect which this type of continuum elements can introduce [70], two elements through the thickness of the plate were introduced. The impact was modelled with a "hard contact" formulation. The analyses were conducted using Abaqus explicit and the outputs at two locations were extracted. This consisted of both in-plane strain components, LE11 and LE22, and the out of plane displacement. It is well known that in FE analyses the calculation of the displacements is straightforward, while all the other responses are derived from them. This is why displacements should be preferable to strains, but, as in the experimental analyses PZT sensors were applied, strains were calculated also in the numerical model. In this chapter the results using the strains are shown. In Appendix 8 some of the results obtained using the displacements are presented; no considerable difference can be noticed. The PZT sensors were modelled adding one integration point at the top of the composite layup, as suggested in [28]. A detailed modelling of PZT sensors is not the purpouse of this thesis; for a detailed analysis on this topic, the reader can refer to other publications [2, 105, 106].

Table 11: Material properties of the system under exam [107].

HTA/6376C	E_1 [GPa]	E_2 [GPa]	ν_{12}	$G_{12} = G_{13}$ [GPa]	G_{23} [GPa]	ρ [kg/m^3]
	145	10.3	0.3	5.3	3.95	1590
PIC 255	E [GPa]	ν	ρ [kg/m^3]			
	100	0.38	7800			

The impact was modelled at three different positions, respectively at the centre of the plate P0 (0, 0) at P1 (20mm, 25mm) and P2 (-20mm, 25mm). Different initial heights were considered (Table 10). The related increasing velocity of the impact was expected to increase the nonlinear response of the plate. As it was highlighted in [89, 90], the nonlinearity of the response of the plate can lead to a mismatch between the real and the reconstructed force when a linear equation is used. In the following results, it will be shown that the proposed method can provide good results even if the impact force is high enough to cause nonlinear dynamics of the system.

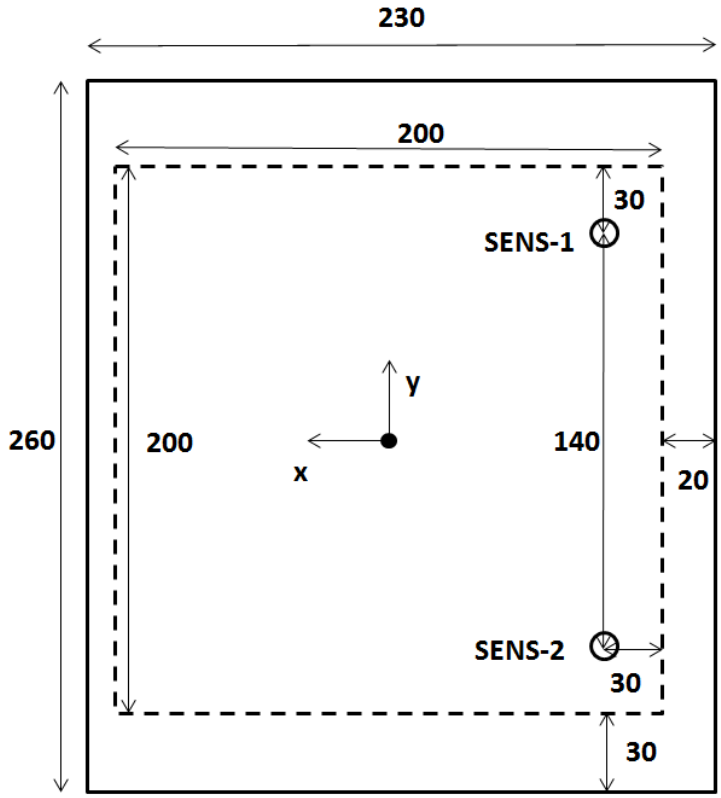

Figure 75 : Schematic representation of the plate, dimensions in mm. Dashed lines represent the position of boundary conditions

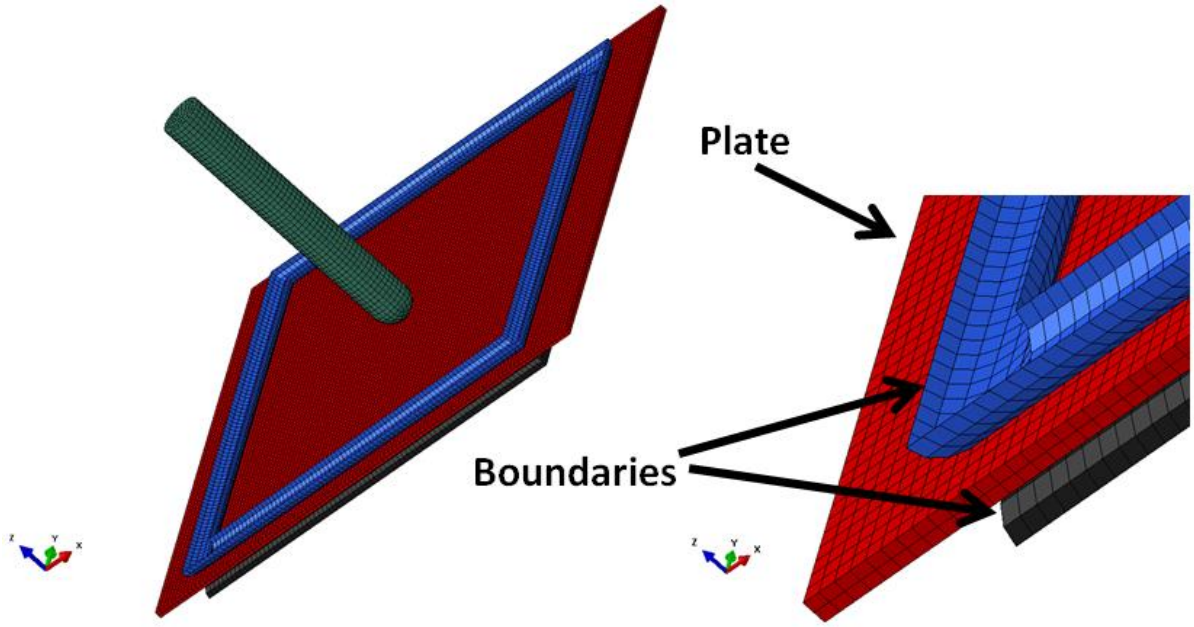

Figure 76: FE model of the system and zoom on the plate and rigid boundaries.

6.5.3 First example: force reconstruction on a simple supported plate using a classic FRF

In order to shown the improvements of the novel algorithm proposed in Section 5.4, the standard approach was first applied to the system under exam. The two impact velocities were respectively 0.78 m/s and 1.62 m/s, which correspond to a drop height of 33 mm and 133 mm, while the mass of the impactor was 2.41 kg. The maximum deflection, obtained for the impact at 1.62 m/s, was 3.3mm, almost 100% of the plate thickness. As indicated in [108], when the maximum deflection under impact reaches this percentage, strong nonlinearities in the dynamics are expected. The results obtained for the two different impacts are presented in Figure 77.

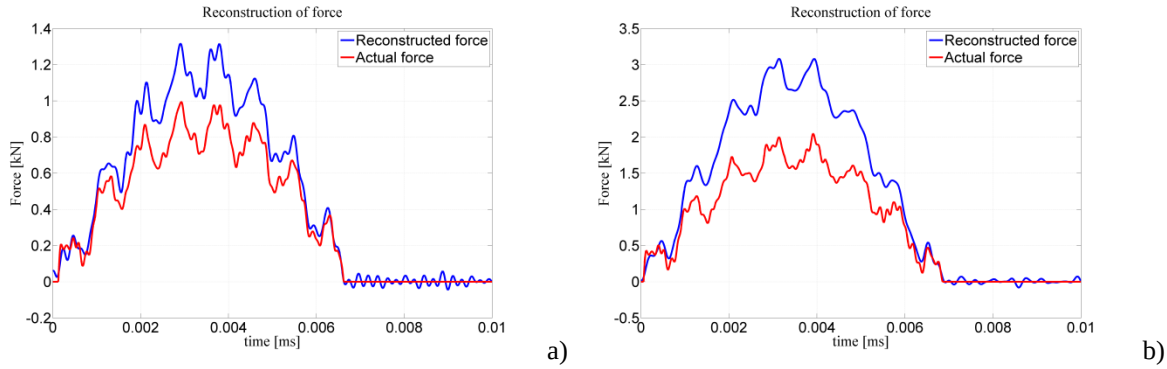

a) b)

Figure 77: Reconstruction of force with the classic FRF. a) Impact velocity 0.78 m/s. b) Impact velocity 1.62 m/s.

From Figure 77a) it is clear that the inverse problem based on the classic FRF fails to determine the correct maximum value of the force. Although the shape of the reconstructed force is similar to the actual one, their peaks are different. This mismatch becomes even more relevant as the initial velocity of the impactor increases, Figure 77b). For structural health monitoring applications, this mismatch is not acceptable, especially if higher energy impacts are expected. The results shown in the following sections

will highlight that the new method proposed can obtain a better agreement between the actual and reconstructed force.

6.5.4 Comparison between numerical and experimental impact response

To verify the validity of the numerical model, in this section a comparison between the forces calculated with the FE model and the ones evaluated during the experiments is presented. It can be seen in Figure 78 and Figure 79 that the model provides accurate predictions, and is therefore suitable to perform more detailed numerical investigations. It is worth noting that the impact force calculated using continuum shell elements was much closer to the experimental force than the one computed using conventional shell elements. A possible explanation of this lies in the fact that the impact mass is very large, compared to the mass of the plate. As conventional shell elements do not allow a local reduction in thickness during impact, the model can be stiffer than expected and consequently, the contact force can be higher. The better representation of the impact with continuum shell elements is especially achieved after the peak of the force has been reached.

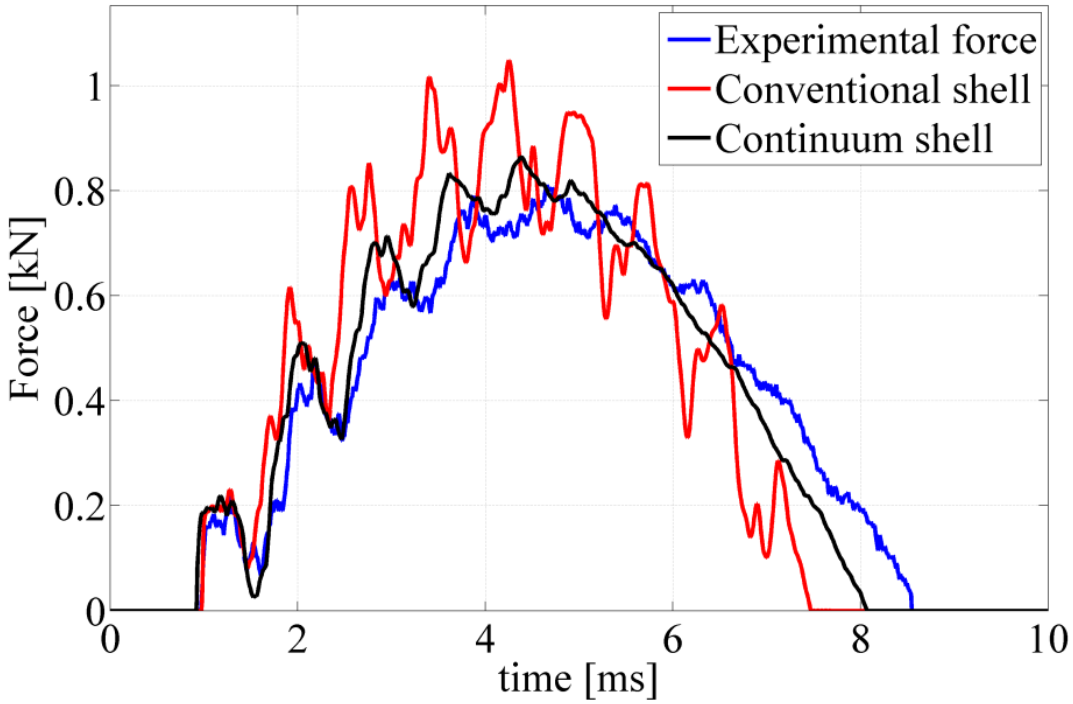

Figure 78: Comparison between numerical and experimental forces. Impact height 33 mm.

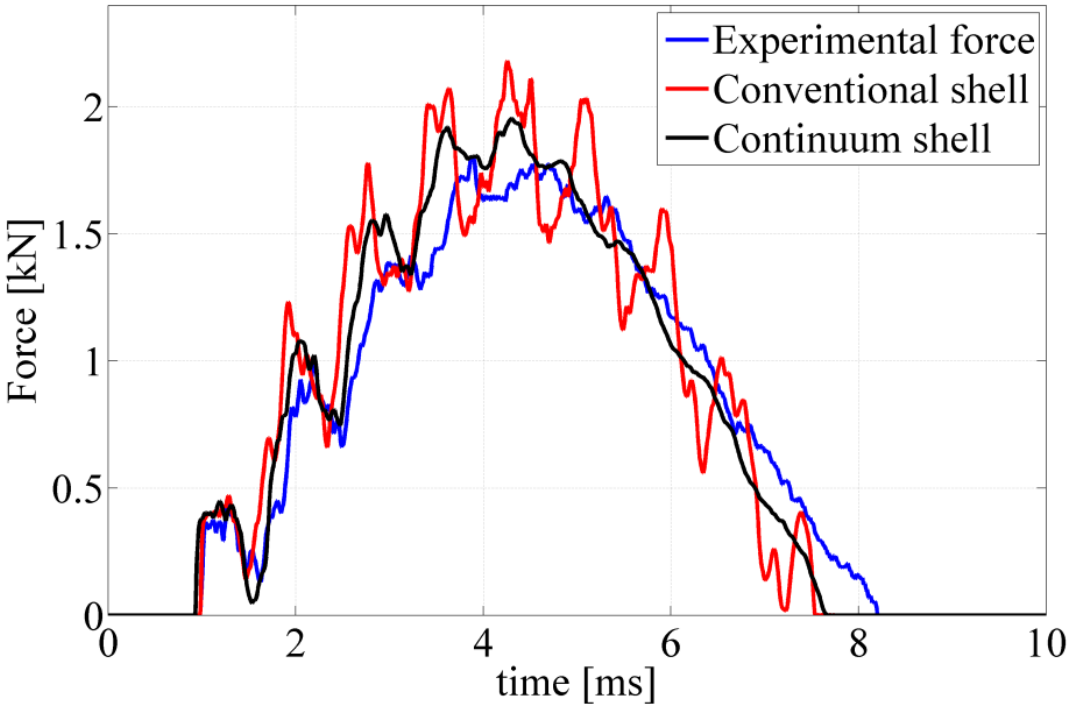

Figure 79: Comparison between numerical and experimental forces. Impact height 133 mm.

The experimental and numerical strain signals were also compared. As no conversion was possible from the raw signal of sensors to the actual value of strain, only a comparison between data normalized to the first peak value could be made. First of all an explanation of the needing of the voltage divider is given in Figure 80. The strain was acquired without voltage divider using an additional sensor, not one of the two used in the analysis. As it is possible to see the strain presents an initial bell shape and then tends to oscillate around the zero value. The maximum deflection is cut by the threshold of the data logger, so that in this situation the algorithm cannot be performed.

In Figure 81 and Figure 82, the numerical results are compared to the experimental ones, using the voltage divider. As it is possible to see in Figure 83, after an initial agreement, they start to be very different. The FE results indicate a bell-shape signal, which is in-phase with the impact force. When the impactor rebounds, the system oscillates around the zero value and tends to stop. This behaviour is actually expected from a large mass impact (Davies and Olsson, 2004). Moreover this is actually what it was found in the experimental results without using the voltage divider. When this was introduced, experimental results did not show that deflection. A possible explanation of this mismatch can be given with the influence the voltage divider has in the overall electrical circuit. Probably it could act as a high pass filter. However, this seems not to have a critical influence on the overall reconstruction process as it will be shown in the results.

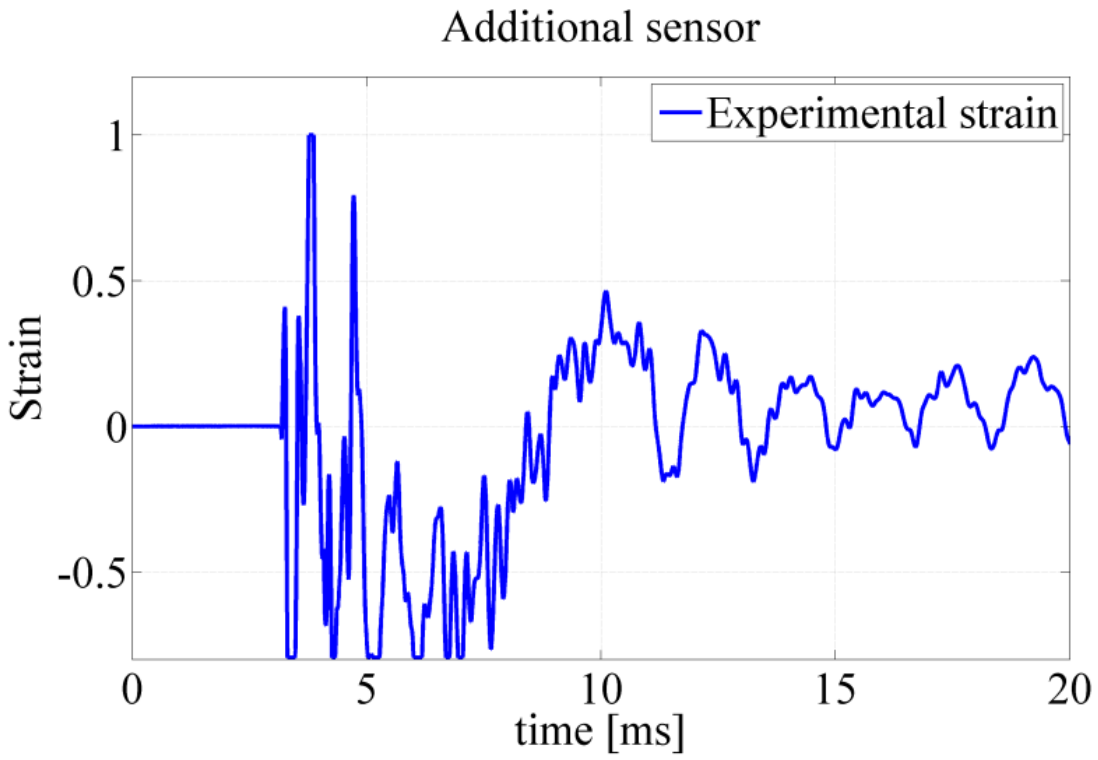

Figure 80: Undivided strain. Impact height 33 mm.

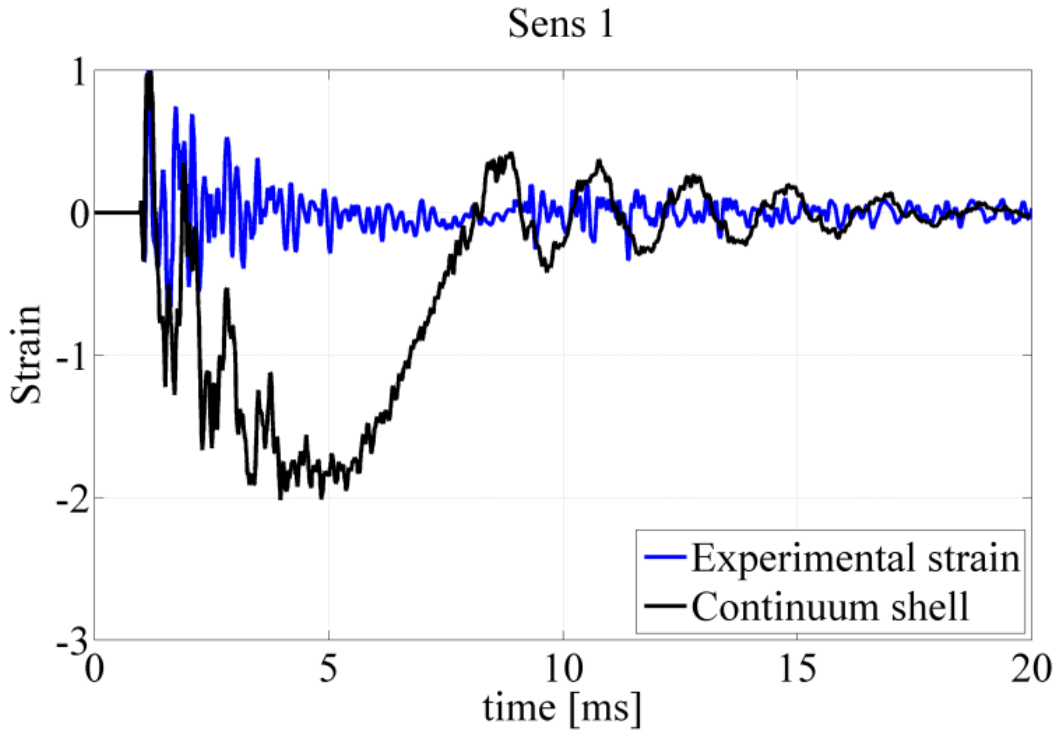

Figure 81: SENS-1 normalized response. Impact height 33mm.

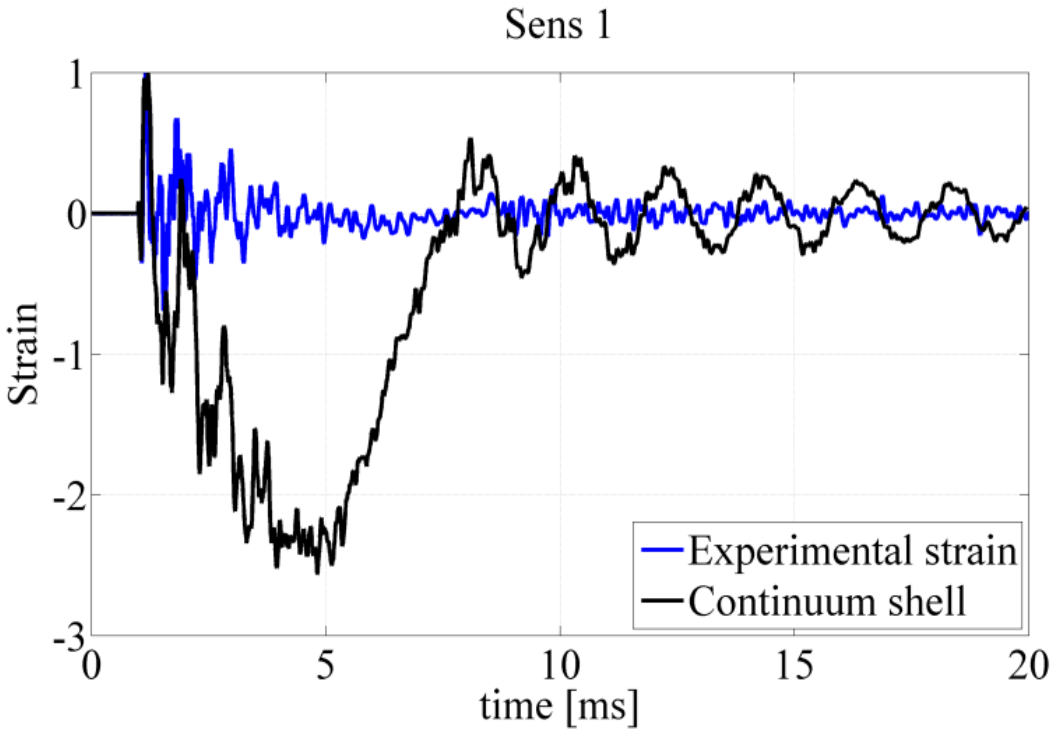

Figure 82: SENS-1 normalized response. Impact height 133mm.

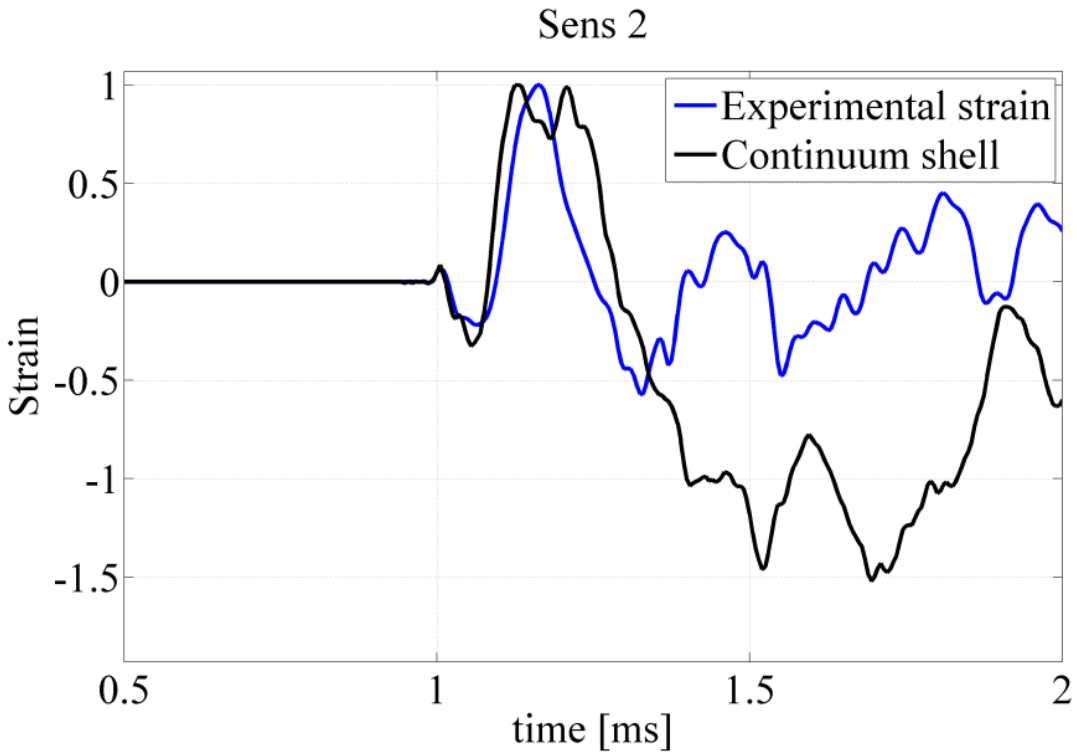

Figure 83: Comparison of the initial strains. Impact height 33 mm.

6.5.5 Repeatability of the tests

Another important aspect which was verified during experiments was the repeatability of tests. For all the different heights chosen for impacts, three different tests were performed in order to verify the validity of the experimental setup. The results showed that both forces and strains were consistent, as shown in Figure 84, indicating that the tests were repeatable. This reinforces the accuracy of the tests performed.

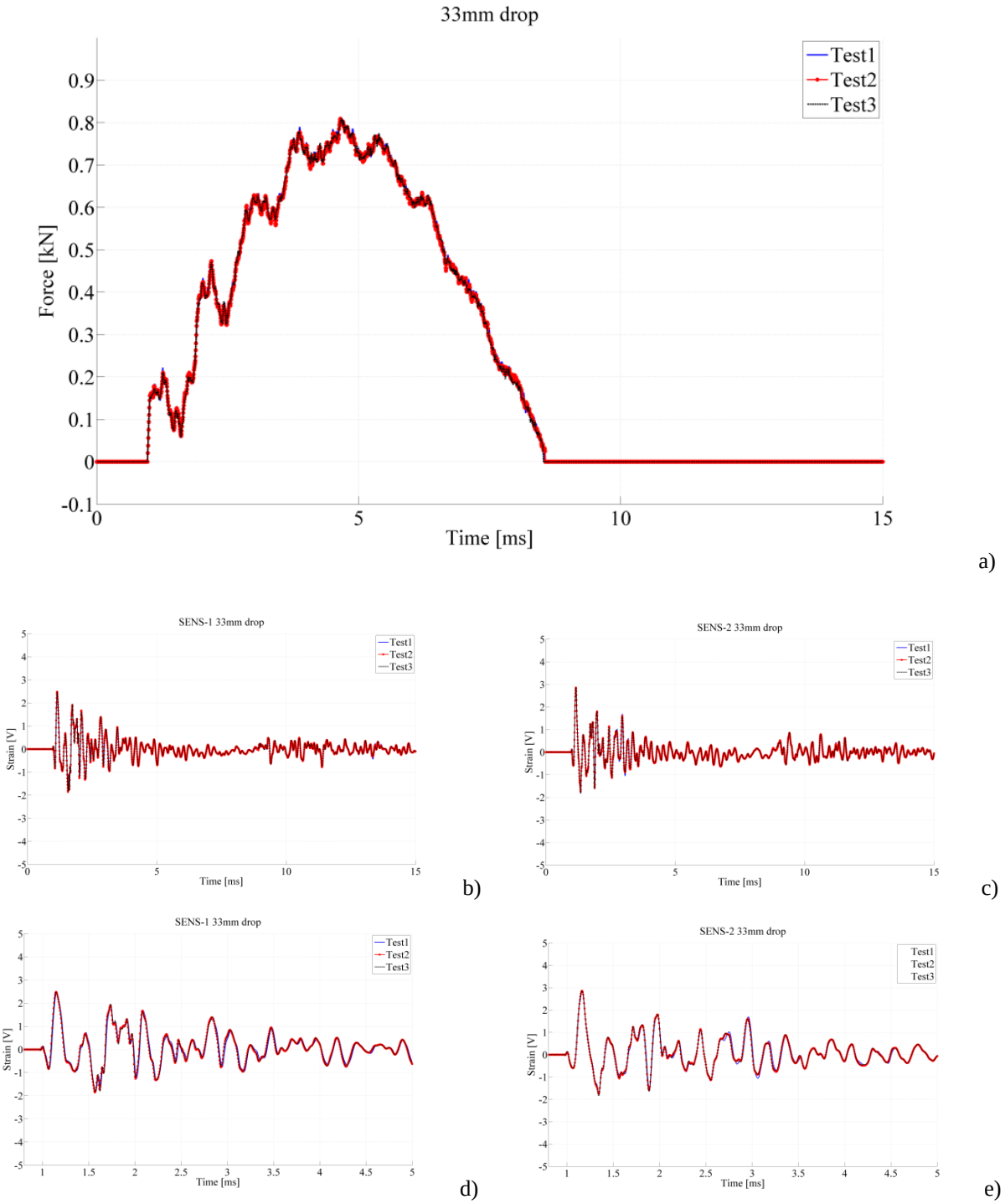

Figure 84: Comparison of results obtained with a 33 mm drop test. a) Impact force. b) Strain at sensor 1. c) Strain at sensor 2. d) Zoom of the strain at sensor 1. e) Zoom of the strain at sensor 2.

The experiments were set up properly so that the repeatability was guaranteed. This ensures that no other disturbances were introduced in the analyses, and that the transfer function approach can be considered reliable, based on the signals acquired. It is also interesting to compare the transfer functions evaluated for different impact heights. Figure 85 shows an example of three different transfer functions evaluated at different heights. It can be seen that the overall FRFs are very similar, but still some small variations, due to different dynamics excited when higher forces are introduced, are present. These results reinforce the

idea that a simple FRF, calculated for example in a modal dynamic approach as performed in the previous analyses, is not always representative of the real response of the system.

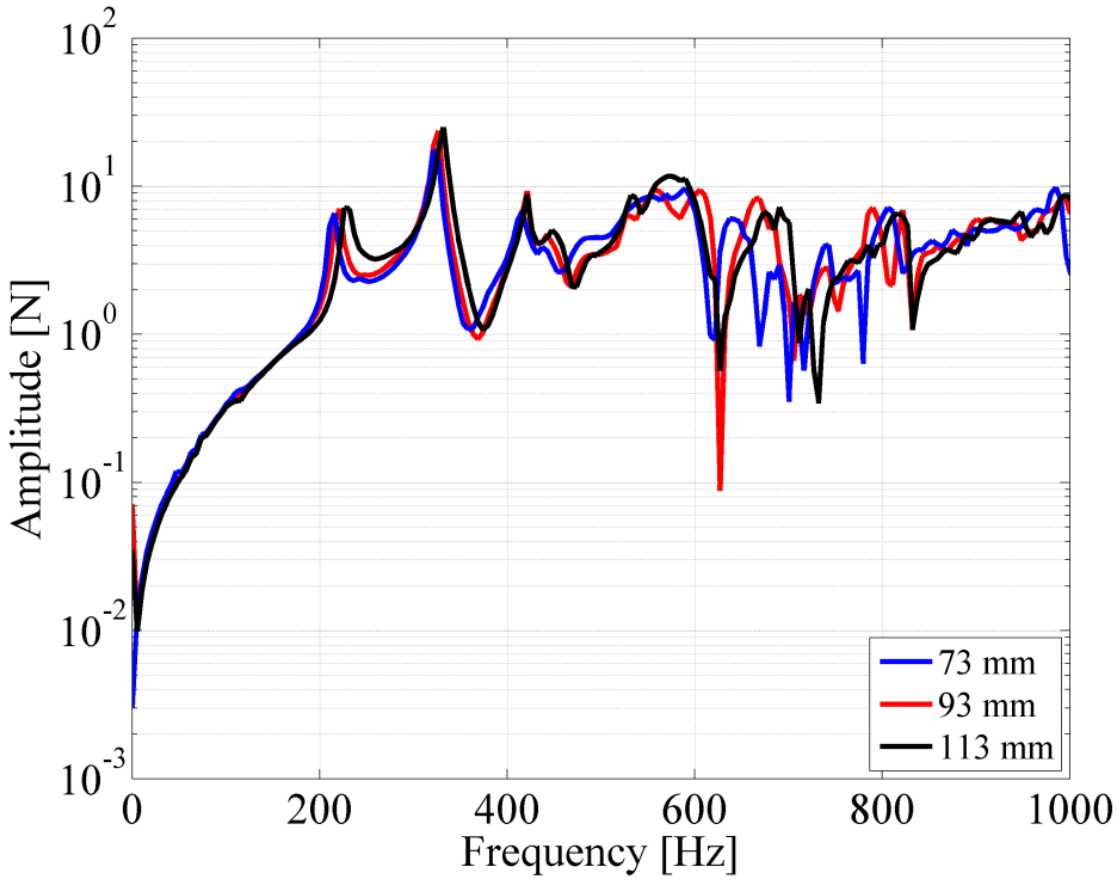

Figure 85: Different experimental FRF calculations, sensor 1.

6.5.6 Force reconstruction results

For numerical cases, only one impact result was available for each height. In this case, only the influence of different heights in the evaluation of the transfer function could be studied. For experimental analyses, the results obtained from the first test were used to determine the transfer function, while the ones belonging to the other tests were reconstructed. It is clear that a better result can be found for the case which lies in between the cases used to evaluate the transfer function. Some examples are presented in the following pictures. Different sets were used to evaluate the FRF. A list of them can be found in Table 12.

Table 12 : Different sets used to evaluate the transfer function.

Set	Cases
1	33-1/43-1/53-1/73-1/93-1/113-1/133-1
2	43-1/53-1/73-1/93-1/113-1
3	43-1/53-1/73-1
4	93-1/113-1/133-1
5	73-1/93-1

The error in the reconstruction of the force can be calculated in several ways. In this paper the approach proposed to calculate the error is based on the integral of the force. This is given by the following equation:

$$Error = \frac{\int_0^T |Force_{real}(t) - Force_{reconstructed}(t)|dt}{\int_0^T |Force_{real}|dt} \quad \textbf{6-4}$$

T is the total time of integration, which can be the time of recording or an appropriate interval of it where the amplitude of the force is significant. This error can be related to the impulse generated by the impact which can be correctly reconstructed by the algorithm.

From Figure 86 to Figure 88 it is possible to see that the method proposed provides good results in all the range of impacts under exam. Note that when an experimental case is presented, the test number is presented at the top of the figure (e.g. 113mm-2), while in the numerical case only the height is given, as mentioned at the beginning of this section. As mentioned above, the best result is obtained at the medium impact height; this can be easily verified from Figure 87 in which it can be seen that the agreement between the real and reconstructed force is better than in Figure 86 and Figure 88. Moreover a similar behaviour can be seen in these two cases. After a period in which the agreement between the forces is good, these start to diverge. This happens after the force reaches its maximum amplitude. After that the mismatch between the real and reconstructed force starts to be higher. The reason for that can be found in the fact that the transfer function works well when the force is low, even if it is not calculated for a similar velocity. After a certain value of the force, the mismatch between the transfer function parameters and the real impact parameters starts to have a certain influence on the reconstruction. However in the cases presented this influence is still negligible.

A remarkable consideration can be made regarding the capability of the method proposed to correctly estimate the force amplitude even in the 113 mm height case. In previous papers [89, 90] it was underlined that, as the nonlinearity of the event increases, the inverse problem based on the convolution method fails to correctly estimate the maximum amplitude of the force. In the present case, due to the fact that the transfer function contains information about different impact cases, the possible mismatch is reduced.

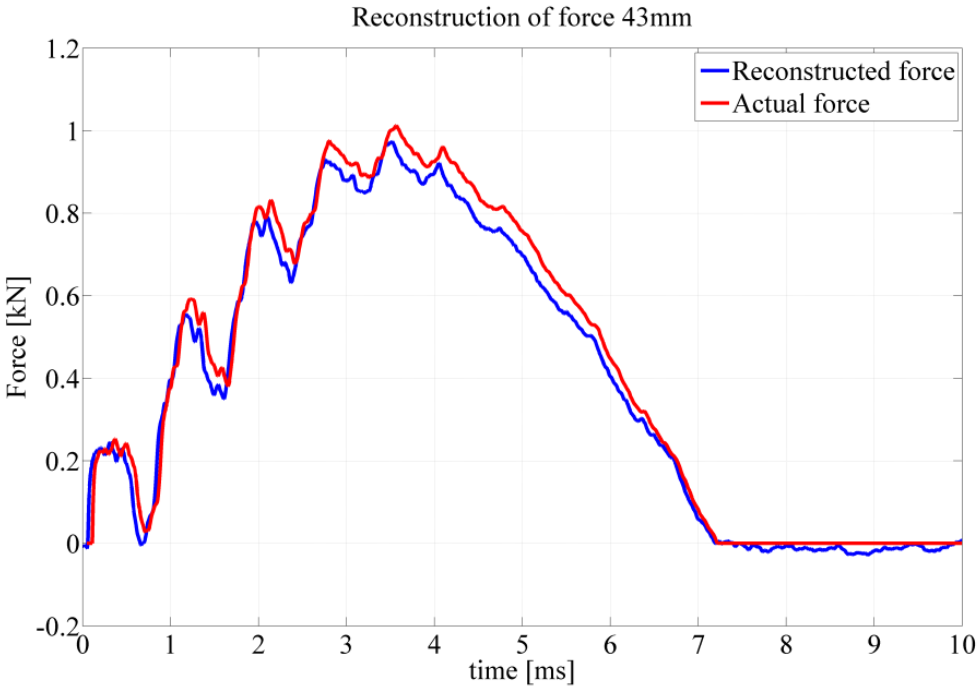

a)

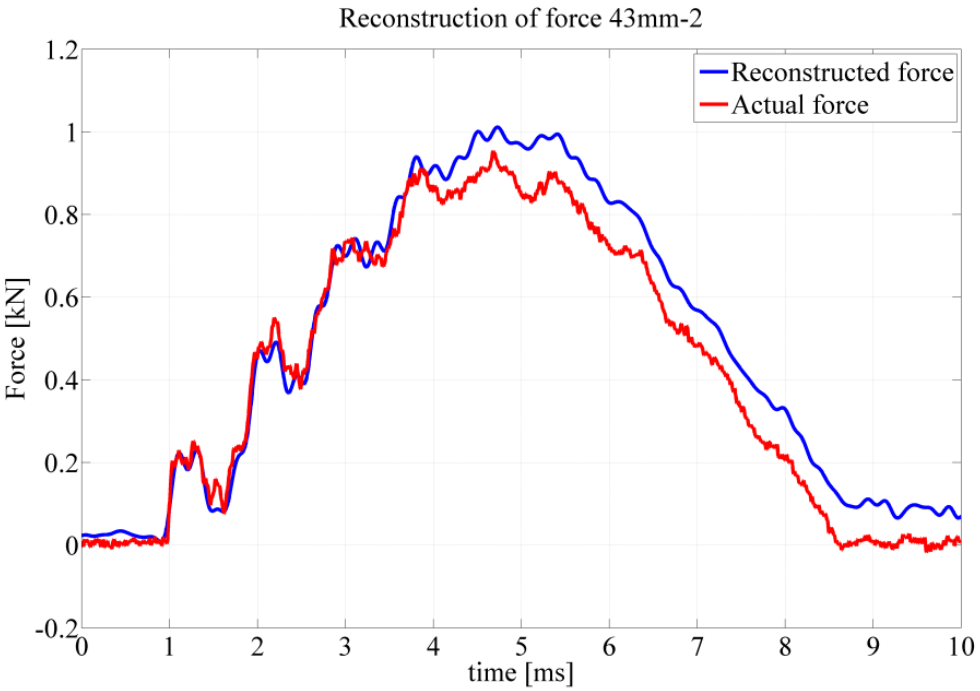

b)

Figure 86: Results using set 1, for the 43-2 case. a) Numerical reconstruction. b) Experimental reconstruction.

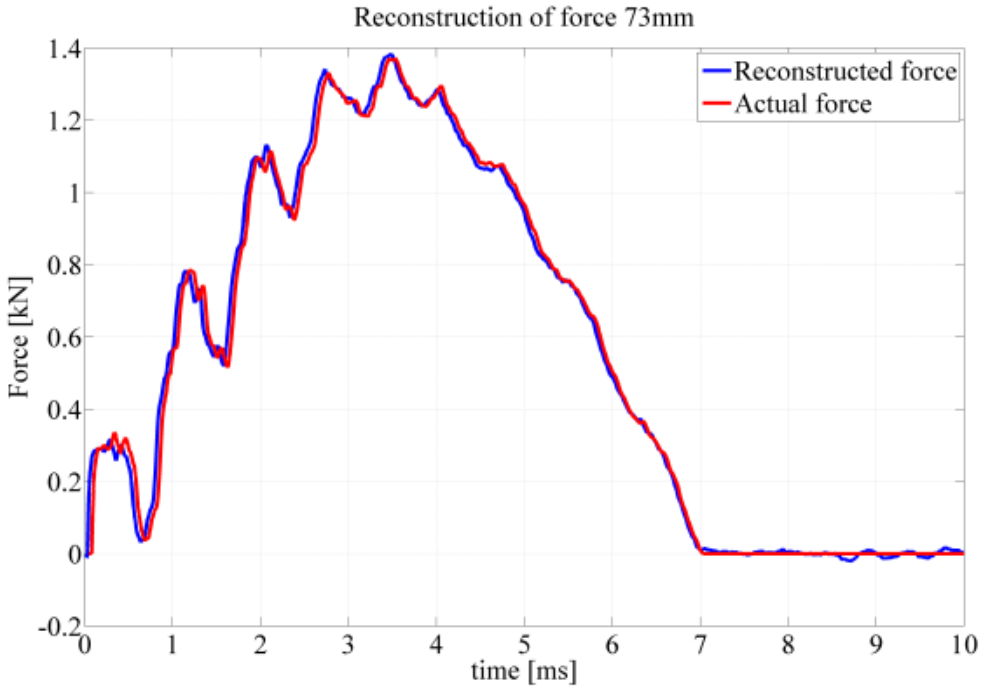

a)

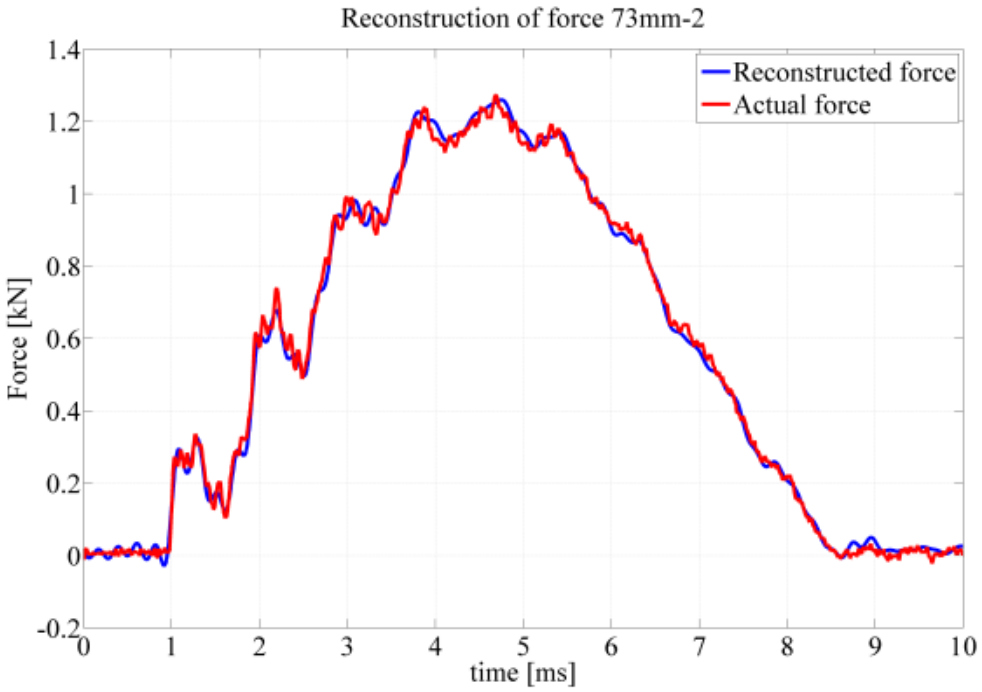

b)

Figure 87: Results using set 1, for the 73-2 case. a) Numerical reconstruction. b) Experimental reconstruction.

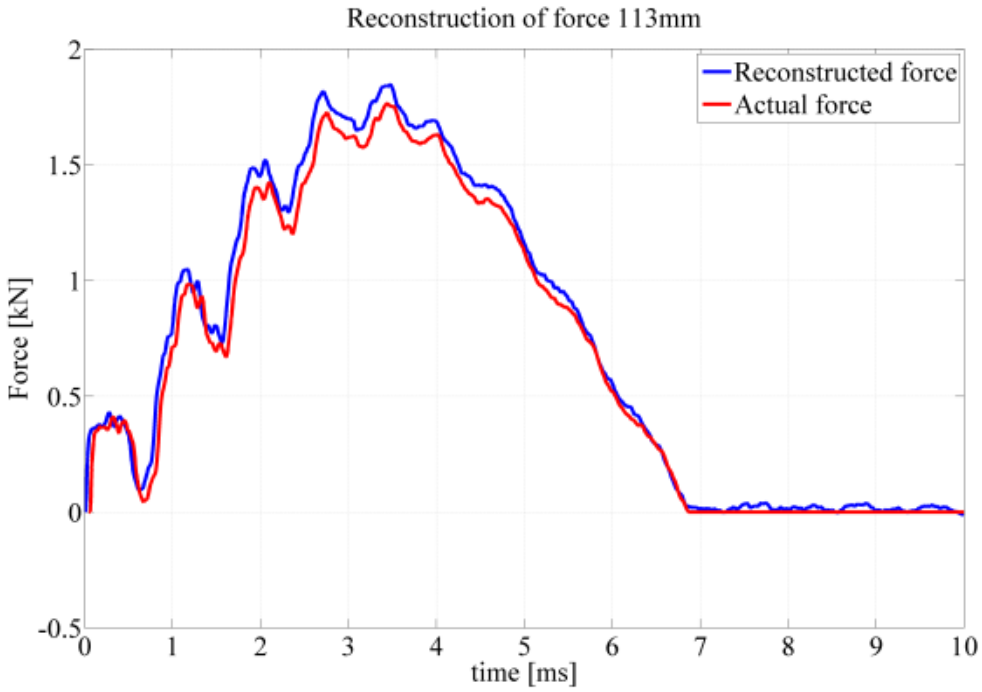

a)

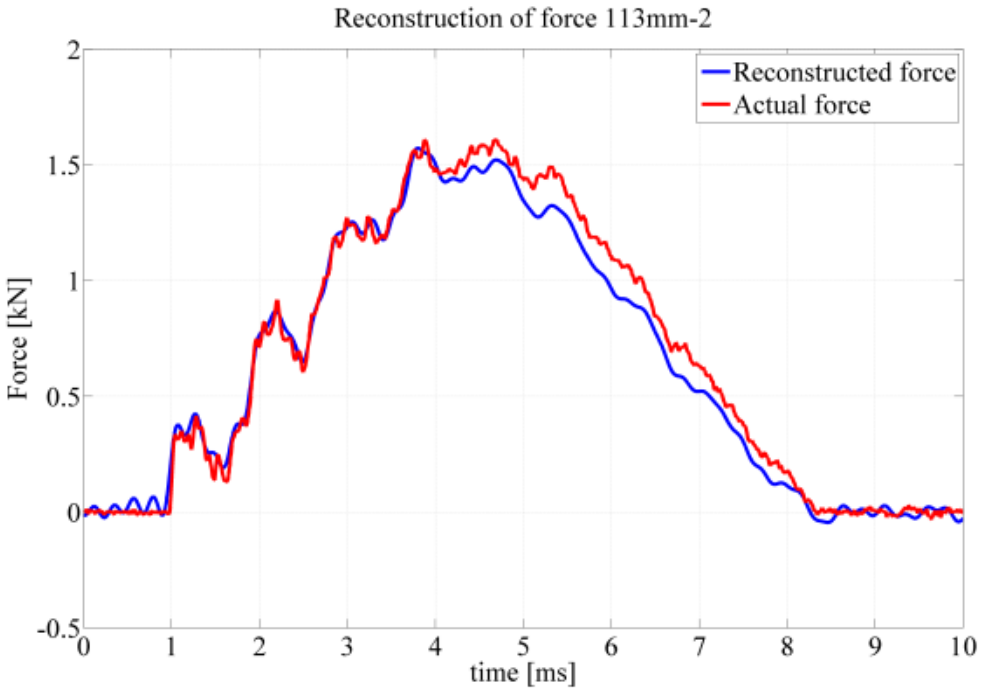

b)

Figure 88: Results using set 1, for the 113-2 case. a) Numerical reconstruction. b) Experimental reconstruction.

The overall error, computed with Equation 6-4, is a good indicator of the global performance of the reconstruction technique. Its values for the different cases displayed in Table 12 are presented in Figure 89 for the numerical cases. Some remarks can be made from the above picture. Set 1 and Set 2 present very small differences in their results. Their overall errors are similar throughout all the different impact heights. The best result is achieved in correspondence to the mean impact height (73 mm), but in general the error does not change much throughout the other impacts. The other three sets present low values of the error in correspondence to impact heights similar to the ones used to build the transfer function. In

particular it can be seen as Set 3 provides the best results in the left part of the figure (lower heights) while set 4 in the right part. It is worth to observe that the error obtained with this approach is much lower than the one obtained with the classic FRF proposed in Section 6.5.3. Table 13 presents a comparison between the errors computed for the two cases presented in Section 6.5.3 and the highest and lowest errors at the same heights, computed with the proposed algorithm. It is clear that the improvements are remarkable.

Figure 90 presents the errors in the force reconstruction for the experimental analyses. Similar conclusions can be drawn. The first two sets present similar results; with the minimum reached at 73 mm. Set 3 on the other hand gives the best results at the lower heights while Set 4 at the highest. In general the error resulted to be slightly higher in the experimental simulations. However, considering only the best case for every set, the errors in the numerical and experimental evaluations resulted to be similar. A small difference is obtained for Set 4 where in the numerical case the best result was obtained at 113 mm, while in the experimental one at 133 mm. A summary of this is given in Table 14.

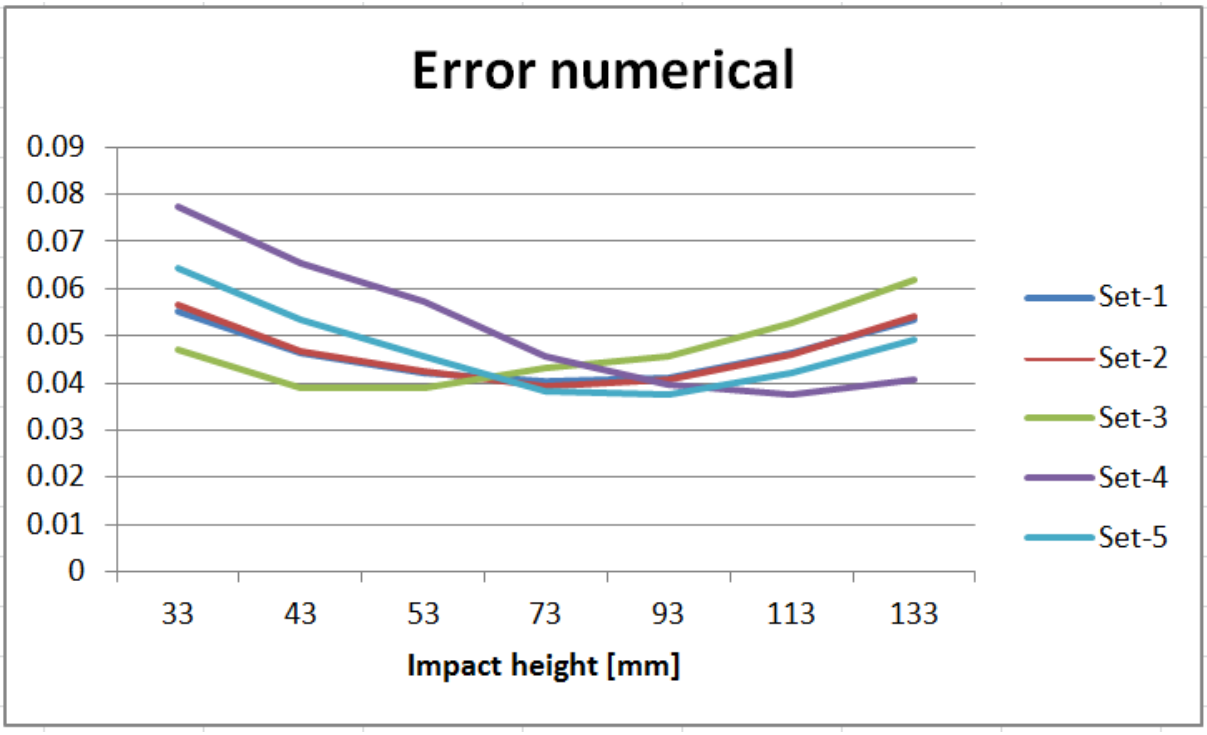

Figure 89: Error for different sets, numerical analyses.

Table 13: Comparison between the errors computed with the classic approach and the ones with the proposed algorithm.

Height	Classic approach	Proposed approach worst case	Proposed approach best case
33 mm	23%	7.7%	4.7%
133 mm	35%	6.2%	4.1%

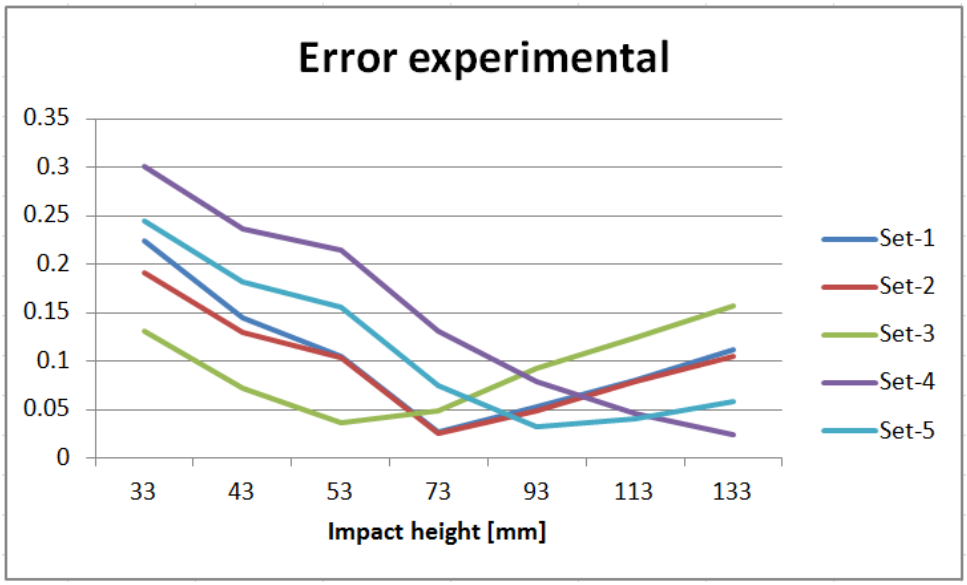

Figure 90: Error for different sets, experimental analyses.

Table 14 : Lowest errors obtained for every set.

Set	Height [mm]	Numerical error	Experimental error
1	73	4.1%	2.7%
2	73	3.9%	2.5%
3	53	3.9%	3.6%
4	113	3.8%	4.5%
5	93	3.7%	3.3%

From the above results it is clear that, in order to create a reliable transfer function for a wide range of impact velocities, different training cases should be considered. These should include cases which are representative of the expected loads. Obviously the best set would be the one which contains data coming from impacts which are representative of real load conditions. The proposed algorithm provided better results than the one based on the classic FRF and the experimental results confirmed what expected from the numerical investigation.

Another interesting topic is related to the possibility of detecting multiple impacts, happening consecutively. This can be a typical scenario of a tool dropping, which bounces on a system and falls again. In the experiment involving the 33 mm impact height, it was possible to perform two consecutive impacts before the servo-mechanism held the impactor. A good opportunity to test the method with a double impact case was hence given. The transfer function was obtained with data coming from the 43-1 test, which included only one impact. The results for impact force reconstruction at 33 mm were all satisfactory and the double impact was always successfully reconstructed in all the three different tests performed at that height. An example is given in Figure 91. This result shows that the proposed algorithm is suitable also to reconstruct multiple impacts at the same position, which can be common in aeronautical structures, especially during the assembling of components.

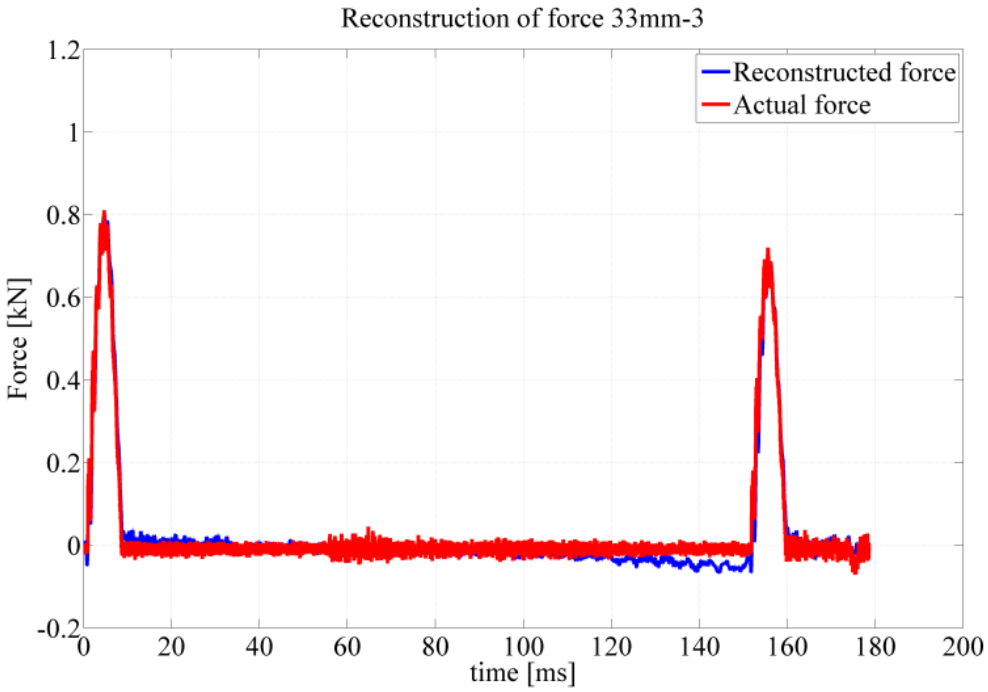

Figure 91: Reconstruction of impact 33 mm-1.

6.5.7 Different position of the impact

Once the reliability of the algorithm was verified with experimental results, it was possible to study the effect of different positions of the impact. Numerical simulations were performed in order to study if it could affect somehow the result of the proposed algorithm. Two different positions were considered: P1 (20 mm, 25 mm) and P2 (-20 mm, 25 mm). As can be seen in Figure 92 and Figure 93, the method provided good results also with these configurations, indicating that it is not affected by the location of the load. In general the same conclusions which were derived for the impact at the centre of the plate are valid also in these cases.

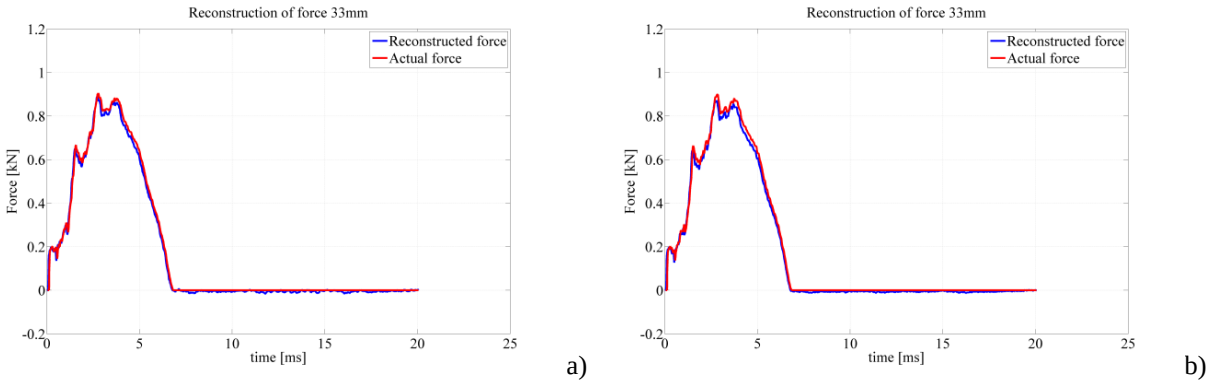

Figure 92: Reconstruction of 33 mm impact with TF from 43 mm. a) P1. b) P2.

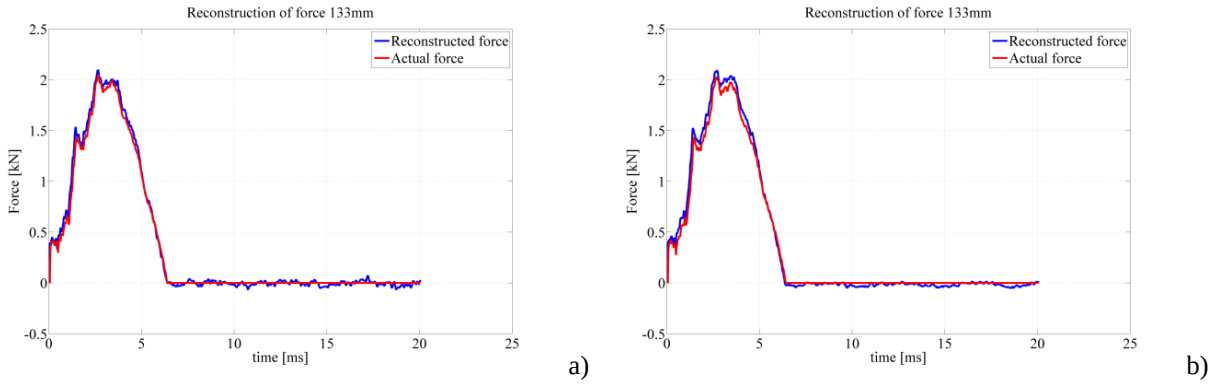

Figure 93: Reconstruction of 133 mm impact with TF from 73 mm. a) P1. b) P2.

Figure 92 and Figure 93 show that, as long as a transfer function can be built for the expected position of impact, the force can be reconstructed correctly for a certain range of velocities. In real cases, impacts can occur in positions which are different from the ones in which data to compute the transfer functions are available. In these cases the typical solution is to estimate the impact position, through time of flight or other techniques (for instance see [28]), and then calculate a new transfer matrix with an interpolation [88]. This approach usually requires the transfer function to be known for several impact cases, in terms of location. Thanks to this, when the position of the impact is calculated, a transfer function related to this position can be calculated, performing an interpolation of the transfer functions available from the training sets; this represents also what was performed in Section 6.3. From a practical point of view, this kind of approach is difficult to perform, at least with the current experimental tools. The aim of this section is not to perform again this type of study, but to test the influence of small variation of the real position of the impact with respect to the one for which training data are available.

Two different small offsets for the impact were considered: P3 (10 mm, 0 mm) and P4 (-10 mm, 5 mm). In Figure 94, it is possible to see the results obtained. The training data were calculated by using the impact data of the 43 mm drop at position P0 (0 mm, 0 mm). The impact cases represent 33 mm drops in positions P0, P3 and P4. From Figure 94 it can be seen that the reconstruction of the force is extremely good even when the impact is slightly moved from the expected position. Figure 94(d) shows that the integral error is the same in P0 and P3, while it is a bit higher for P4. This is obviously due to the fact that P4 is further from the centre of the plate than P3. These results showed that the method can still be applied even when the real impact does not occur exactly at the expected location.

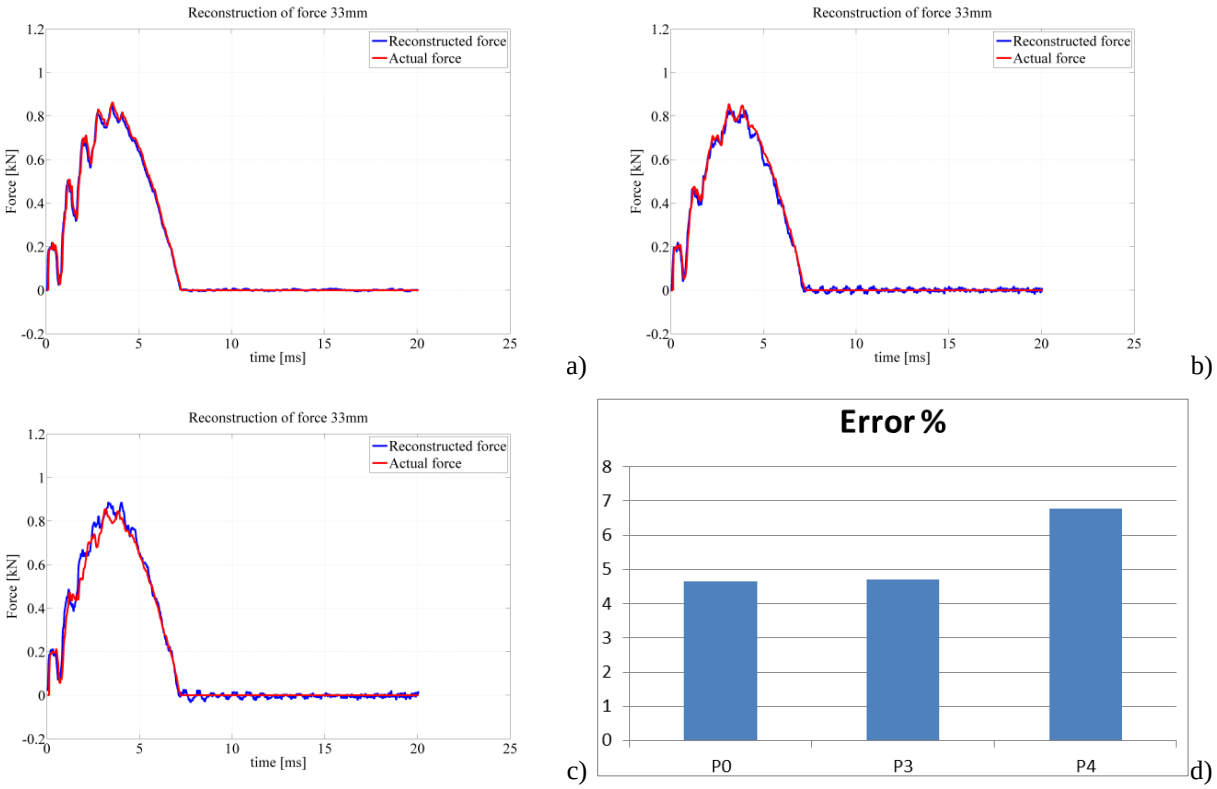

Figure 94: Reconstruction of forces with small offsets. a) P0. b) P3. c) P4. d) Integral errors.

The influence of the training set chosen to evaluate the transfer function is studied also with numerical simulations. The positions under exam are P1 and P2, which were reconstructed using training data coming from the same position, and P3 and P4 in which training data related to the centre of the plate were considered. Three different sets were considered (Table 15). The integral error was computed for the 33 mm impact case. As expected from the previous results, the best set was the one containing data closer to the impact under exam, which is set 2 (set1 also contains 33 mm impact data but it includes also the 133 mm case). The set which provided the poorest result was set 3. It is clear that the optimal set would be the one containing the same velocity as the impact under exam, but this situation is difficult to achieve in real cases. The values of the normalized integral errors computed in this analysis can be found in Figure 95. This result reinforces what already found with the experiments i.e. that an appropriate set of training data should be chosen when reconstructing the impact force. This should contain data from impacts which have conditions similar to the conditions of the expected events. From all the results obtained with this analysis however, the proposed algorithm resulted to be appropriate to determine the impact force due to a large mass drop on a thin composite plate. What is remarkable is that different impact velocities were considered and the method was still able to determine the contact force correctly. This represents an improvement in this field of research, which is usually limited to small contact forces with dynamics of the systems very close to the linear behaviour.

Table 15: Different sets considered.

Set	Cases
1	33/43/53/73/93/113/133
2	33/43/53
3	73/93/113

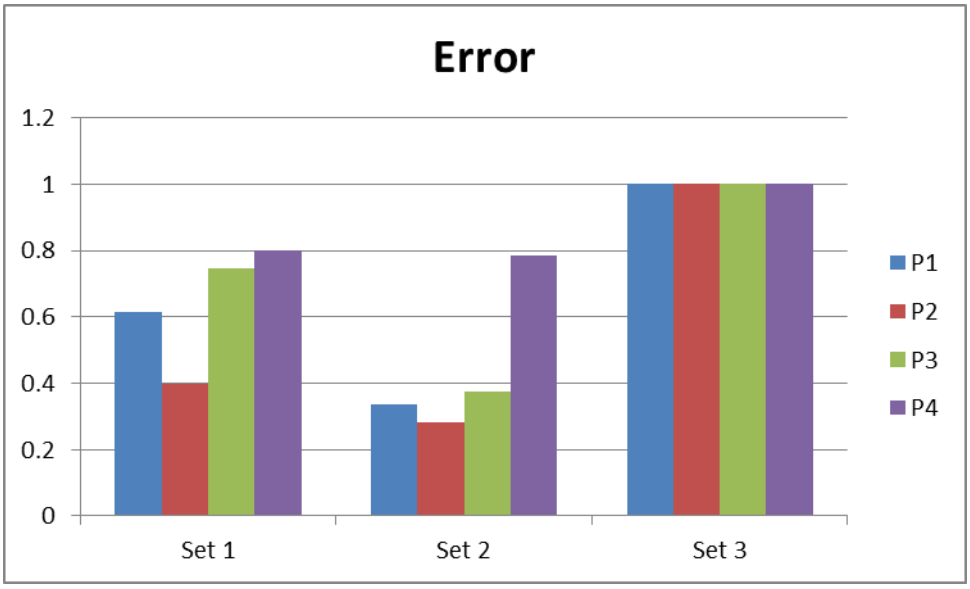

Figure 95: Normalized integral error for the reconstruction based on

6.6 Impact location results

This section provides the results obtained with the application of the POD to the problem of finding the impact location. The algorithm adopted can be found in Section 5.7. The model under exam is the same described in the previous section. A total of 25 different impact positions were simulated. For every impact, the dynamics of the system at 9 positions was evaluated. These are given in Table 16, while in Table 17 the 25 different impact locations are provided. Two different types of response were considered: strain collected by PZT sensors and accelerations. This was done to evaluate the performance of the method with different inputs. Only the first part of the signals, the first 1.1 ms, was considered in the analyses. There are two main reasons for that. First of all the information containing the position of the impact is usually included in the first part of the response. After that reflections from the boundary conditions can superimpose on the wave due to the impact. The second reason is related to the comparison between numerical and experimental analyses. As was shown in Figure 81 and Figure 82, the experimental PZT response was different from the simulated one, due to the presence of the voltage divider. However in the first period, the two signals are similar. In this way the numerical results which are now provided has a solid basis, as the experimental strain was proved to be comparable in the time range used in the analyses, Figure 96. In order to determine also if the application of PZTs sensors should be preferable also in this case, the analyses were conducted also applying the POD to the accelerations of the systems at the same positions were the PZT sensors were placed.

Table 16: Positions of the sensors.

Sensor	1	2	3	4	5	6	7	8	9
X [m]	0.075	0	-0.075	0.075	0	-0.075	0.075	0	-0.075
Y [m]	-0.075	-0.075	-0.075	0	0	0	0.075	0.075	0.075

Table 17: Positions of the impact.

Impact positions	x	y
1	0.01	0.01
2	0.03	0.06
3	0	0.05
4	-0.03	0.05
5	0.04	0
6	0.03	-0.01
7	0.005	-0.04
8	-0.05	-0.06
9	0.06	0.01
10	0.02	0.08
11	-0.05	0.07
12	0	0.08
13	-0.08	0.07
14	0.05	0.01
15	-0.03	-0.01
16	0.001	-0.085
17	0.085	0.085
18	0.01	0.06
19	-0.04	-0.08
20	-0.01	0.03
21	-0.02	-0.065
22	-0.06	-0.01
23	0.04	-0.05
24	0.05	-0.06
25	-0.02	-0.05

The results obtained for the impact location are presented below. The POD successfully located most of the impacts within an acceptable error. From Figure 97 and Figure 98 it is clear that the estimated positions are very close to the real ones. In these figures the black solid line represents the boundary of the plate, while the dashed green one the border of the sensors' grid. It can be also noticed that the PZTs seem to provide better results than the accelerations. Further manipulation of the results is performed in order to obtain a better evaluation of the impact location. For SHM purposes, it is important to determine the maximum error, in terms of position, at which a certain amount of impacts can be located. A probability analysis is therefore conducted in order to determine this minimum error.

The probability of detecting one impact is investigated through the cumulative distribution function (CDF) of the error in the position estimation. The histogram of the errors is calculated; this provides two

sets of data: one refers to the intervals of error and the other to the number of times, n, one evaluation falls in one of those intervals. The CDF is then evaluated as:

$$CDF = \frac{cumsum(n)}{sum(n)} \qquad \textbf{6-5}$$

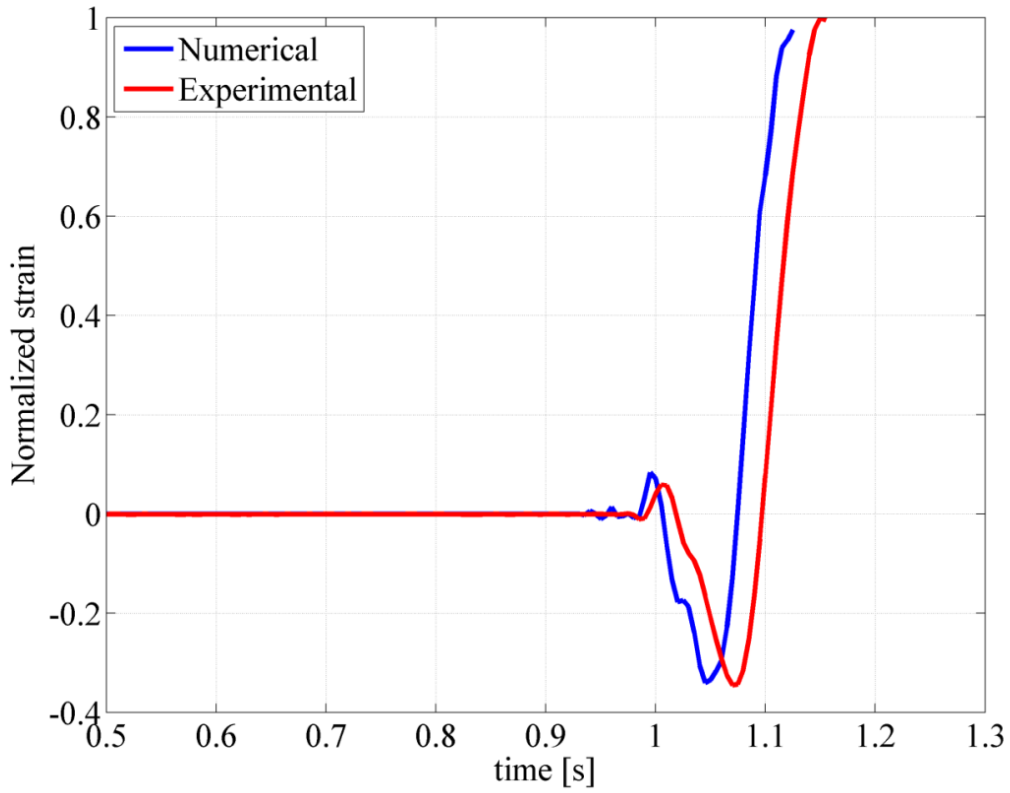

Figure 96: Comparison between the initial signals

Figure 99 shows the CDF evaluation for both the data containing accelerations and strains. It is now clear that the application of the method to the response collected by PZTs provides better results. In particular more than 80% of the impacts are estimated in between 25 mm from the actual position. Comparing the CDF with the results showed in Figure 98 it is possible to see that in most of the cases in which impacts are located closer to the boundary of the system the error is high. This is consistent with what previously found in the preliminary analyses on the small specimen analysed in Section 6.3 and with what usually can be found in literature. The results obtained showed that the POD can be applied also to the field concerning impact detection. The error in the estimation of the impact position resulted to lie in an acceptable range, in particular when impact occurs inside the sensors' grid. This represents a novel application of the POD, which possibly overcomes the typical problem arising when composite plates are under investigation, like for example the uncertainty associated to the correct evaluation the wave speed. These analyses provide a new look on the possibility, in the structural health monitoring field, of proper orthogonal decomposition which till now was applied only as damage detection method.

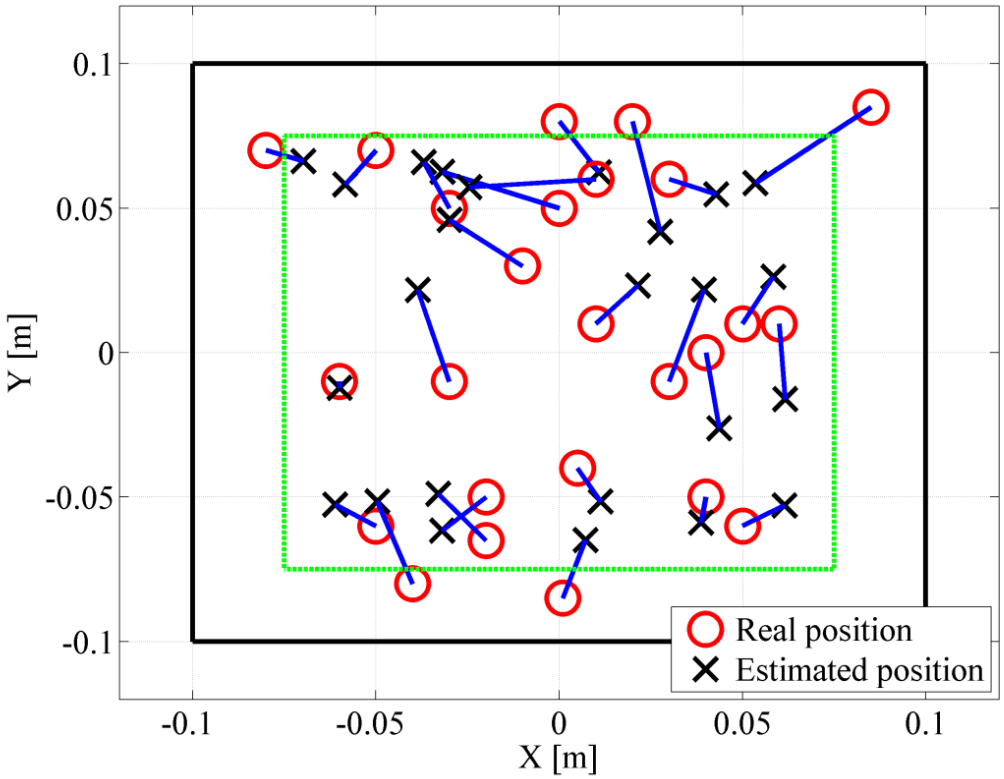

Figure 97: Comparison between estimated and real position of the impacts using accelerations.

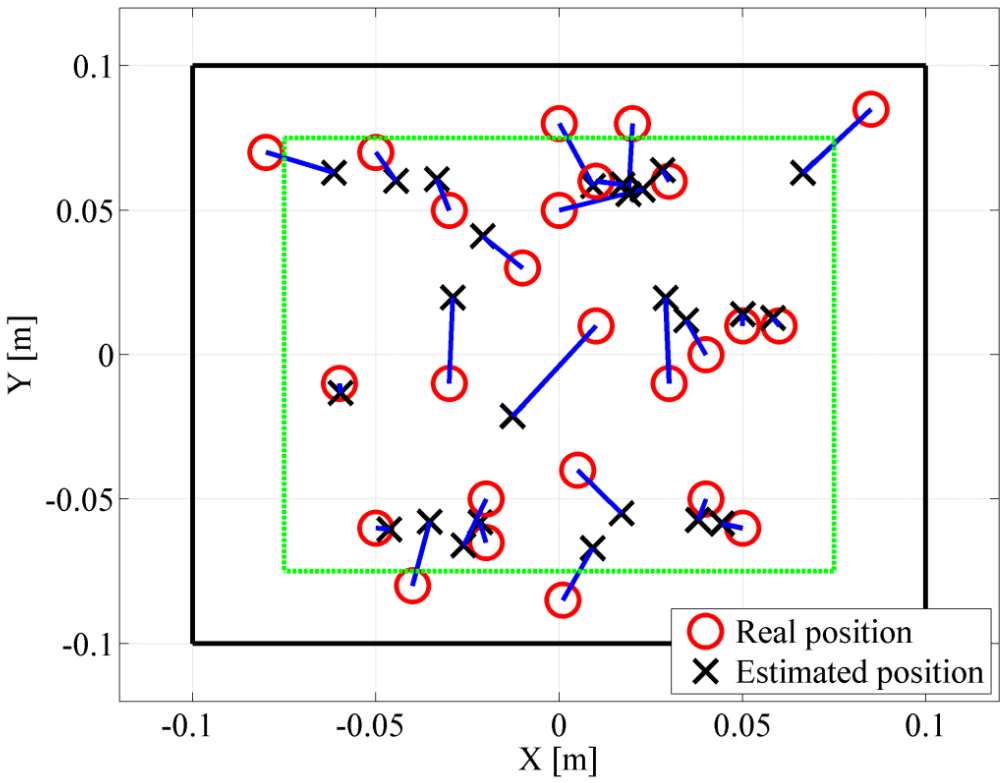

Figure 98: Comparison between estimated and real position of the impacts using PZTs.

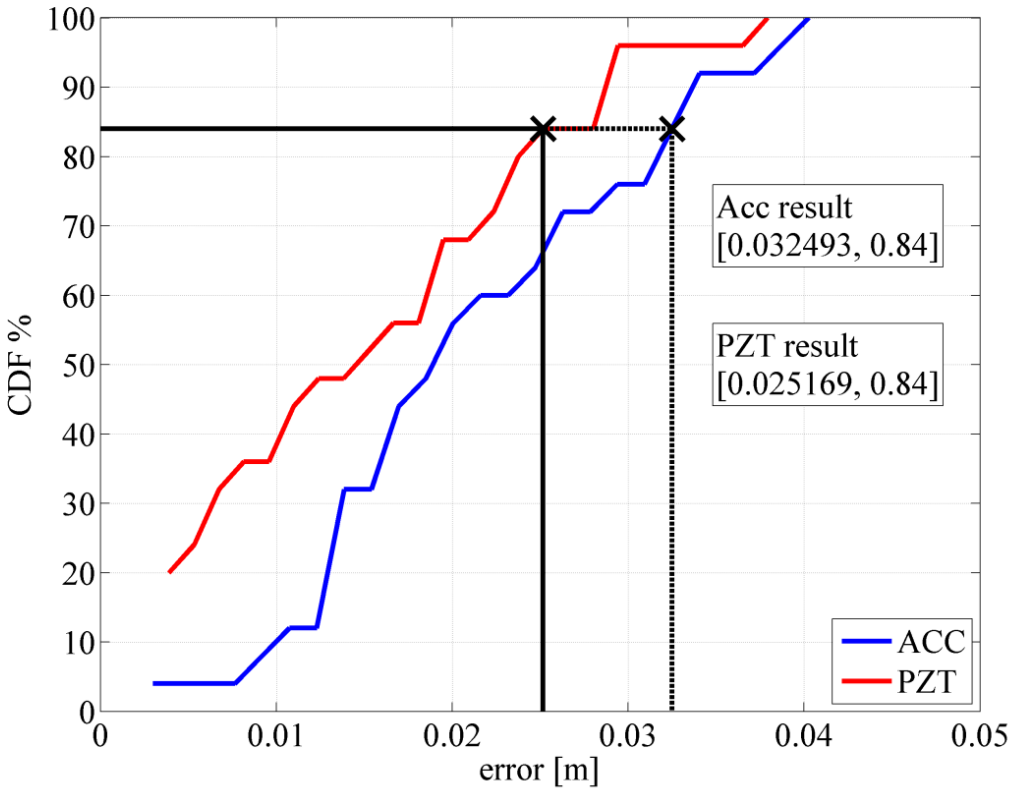

Figure 99: Cumulative distribution functions of the error in the position evaluation.

6.6.1 Comparison between the POD and the integral approaches

Results obtained with the impact location algorithm based on the POD are now compared to those obtained with the integral method based on Equation 5-32. The strain signals were used to perform the comparison. For the analysis based on the integral, all the time response was used, as suggested in [88]. Results show that the POD approach presents a lower value of the error in the impact location for most of the cases. From Figure 100 it is possible to see a comparison between the CDFs for impact location obtained with the two methods. It is evident that the POD-based approach gives better results, in particular for CDF values below 80%.

Analysing each impact location result, it is possible to highlight that the proposed approach provides better accuracy when the impact is located outside the rectangle formed by the sensors; this can be seen in Figure 101. This is a very important result, as the errors in the determination of the location, when an impact occurs outside the sensors' grid, is one of the most challenging aspects for SHM based on a passive approach.

The results obtained with a POD-based approach for impact location showed that this method can improve the techniques which are already present in literature, in particular the one based on the ToA, as no information about the velocity of the wave is needed, and the one based on the integral of the strains, as the errors obtained in the position of impacts are generally smaller with the proposed approach.

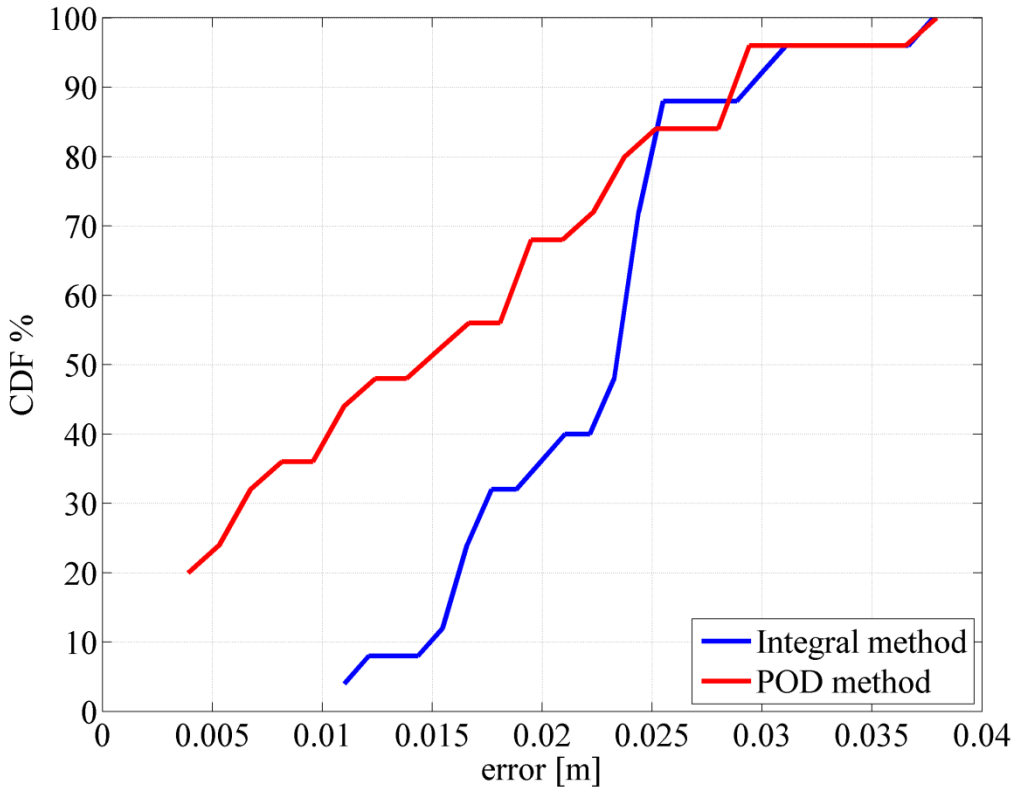

Figure 100: Comparison between the CDFs of the Integral and POD impact location methods.

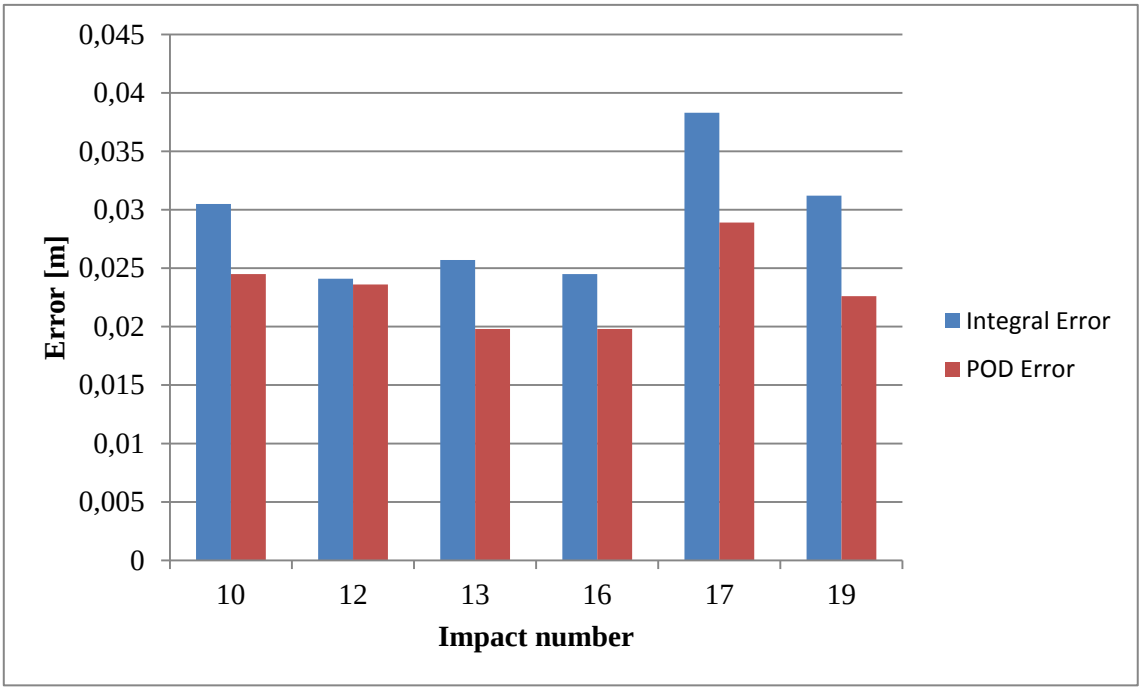

Figure 101: Comparison between the errors for impact positions outside the rectangle formed by the sensors.

6.7 Final remarks on the impact detection and reconstruction results

This chapter proposed some improvements in the branch of SHM dedicated to impact detection and reconstruction. The first part of the analyses was conducted on a simple plate of small dimensions. The results obtained were useful to derive some important information about the applicability of the method. In particular it was highlighted that for low velocity impacts, the frequency domain approach is preferable. In particular it did not only provide better results, but the analyses were faster and the possibility to use a limited number of frequency components could be exploited to overcome the presence of noise in data. The relative position of impact and sensor was also investigated and results showed that if as long as the former occurs inside the sensors' grid, the impact can be located and reconstructed correctly.

The second part of the analyses was focused on the development of an algorithm able to reconstruct impacts with different energies, without losing information on the force amplitude due to the presence of nonlinearities in the system. Different sets of training data were used to build a general transfer function, which resulted to be suitable for a range of impact velocities. Experimental results confirmed that the proposed algorithm is suitable for application also in test cases. Numerical studies on the position of the impactor and on the mismatch between this location and the one at which the transfer function is available showed that the method can be applied also when the impact does not occur in the centre of the plate.

Finally an application of the proper orthogonal decomposition to impact location was proposed. Several impact positions were simulated on a composite panel. The first part of the generated waves was considered when performing the POD. A subset of the sensors' grid was identified for every impact and then the position was estimated. A statistical analysis was conducted in order to verify the performance of the method, both using strains and accelerations. Results showed that the method can locate the impact within a limited error in the position in both cases.

The main conclusions which can be drawn from the analyses conducted are:

- The frequency domain approach is suitable to reconstruct the impact force on composite plates.
- A general transfer function can be determined based on the evaluation of the input-output relationship during different experimental test.
- Small mismatches between the real position of the impactor and the one at which the transfer function is available do not affect much the reconstruction result.
- In order to locate the position of the impact, a novel method based on the proper orthogonal decomposition has proven to be suitable for application on composite plates, regardless of the sensor used to collect the dynamics of the system.

Conclusions

The present thesis developed a research on novel methods for monitoring the integrity of aeronautical structures. The increasing application of composite materials in new aircraft requires the development of new methodologies to guarantee safety of the most critical components. These novel approaches, which improve the capabilities of the conventional non-destructive technique (NDT) methods, are all included in the so-called structural health monitoring (SHM). Structural heath monitoring is a wide field of research which contains different topics, including modelling of new sensors and manufacturing of smart systems and many more. The development of algorithms to monitor the structural integrity of components is the branch of SHM analysed in this PhD research. Two different approaches, active and passive sensing, can be used to achieve this task. In this thesis both of them were investigated. For the first approach, a vibration-based damage detection technique was developed. The proper orthogonal decomposition (POD) of the dynamics of the system under exam was used to detect damage in different structural components. The classic POD was improved with the application of mode shape derivatives and the gapped smoothing method (GSM). For the passive approach, a novel method to determine the transfer function of a component has been investigated. The main objective was the correct reconstruction of the contact force history even when large deformations were present in the system. Finally an innovative impact location algorithm, based on the POD, has been presented. This overcomes the issues related to the direction dependent velocity of wave speed, which is a major concern when working on impact location on composite panels. The major contributions of the thesis are highlighted in this chapter. The structure of the conclusions follows the one of the thesis. First the active and then the passive sensing main results are summarized.

Damage detection based on proper orthogonal decomposition

Cantilever beam

The first part of the research concerned the development of a damage detection approach based on the proper orthogonal decomposition. The presence of defects in different damage components was investigated. The analysis started with the evaluation of possible delamination on a cantilever composite beam. Several positions of damage, both through the thickness and along the length of the beam, were investigated. Results showed that delamination between the mid-plane of the beam produced the highest level of damage index. Moreover this decreased with the distance from the fixed end of the beam. The size of the delamination was also investigated. It was highlighted that when the damage consisted on a full-width delamination, the classic POD could correctly detect it. However, when the damage width was

smaller, the application of the curvature of the proper orthogonal modes was essential to locate the delamination. The gapped smoothing method (GSM) was successfully applied to this analysis. The damage indices computed with the GSM were similar to the ones computed with a comparison between the damaged case and a pristine baseline. The influence of the relative position between sensors and damage was also investigated. It was found out that a delamination between outer layers is much sensitive to the distance from the sensors.

Experimental verification on a cracked homogeneous beam was performed. Results highlighted that the crack could be successfully detected using only the accelerations from the dynamics of the damaged beam. This result is particularly important because it represents the first application of the gapped smoothing method to the derivatives of the proper orthogonal modes.

Cantilever plate

The joined application of POD and GSM was successfully applied also to a bi-dimensional case. A cantilever composite plate was investigated. The damage introduced was a delamination in different positions, both in the plane and through the thickness of the plate. The results obtained confirmed what was obtained for the cantilever beam. In particular the damage index resulted to be higher when the delamination was placed closer to the constraint and in between the 4^{th} and 5^{th} layer of the plate (symmetry plane of the layup). The application of the GSM produced results very similar to the classic POD. It was found that the application of the smoothing technique to the proper orthogonal mode could not locate damage, while with the computation of the curvature, the delamination could be detected.

Experimental verifications on a composite plate highlighted that the damage detection method based on the curvatures of the proper orthogonal modes is sensitive to the presence of noise in data. A modified Laplacian operator was hence introduced. First a comparison with an application present in literature, based on a homogeneous beam, was presented. After the validation of the algorithm, the method was extended to a composite plate. Numerical and experimental verifications showed that the computation of curvatures with modified Laplacian operators can overcome the presence of noise in data.

Stiffened panel

The curvature of a mode shape can highlight local changes in the stiffness of the system. In aeronautical applications, the typical structural component is represented by a stiffened panel. This contains a sharp change in stiffness due to the presence of stringers. The POD analysis was conducted on a composite panel with one stringer. The first simulated damage was a local reduction in the elastic moduli of the material. Three different positions were considered. A second damage was a local debonding of the stiffener. The classic POD was able to detect all types of damage. When the GSM was applied, the influence of the stringer hid the effects due to damage. For this reason a modified algorithm was

proposed. It is based on the exploitation of different recorded data to compute an artificial baseline. Moreover a threshold for the damage index was introduced. The proposed method was able to overcome the presence of the stringer, highlighting only the damage effects. The influence of noise, as well as of the number of sensors, was studied. The method showed good capabilities to detect damage also when noise was present or when fewer nodes where used to perform the damage detection algorithm. The influence of the frequency of the applied load was also investigated when the frequency was close to the first natural one of the system, the algorithm produced better results. This is consistent to what can be found in literature and to the mathematical explanation which was given in the theoretical explanation of the method.

Impact detection and force reconstruction

Reconstruction of impact force on composite panels

The first topic addressed for the passive approach of SHM was to reconstruct the force history of an impact. A preliminary study was performed on a small specimen, the results of which, in terms of impact force, were available from literature. This simple model was useful to determine which method should have been followed for further analyses. Results highlighted that the frequency approach was more suitable than the time one for large mass impacts. The impact force was correctly reconstructed, also when the position of the impact was unknown. However some issues arose. First of all the presence of nonlinearities in the dynamics of the system can prevent a correct reconstruction of the force. Secondly the relative position between the impact and the sensors plays an important role in the reconstruction, when the position of the impact is unknown.

A novel approach has been proposed to overcome the drawback given by the presence of nonlinearities in the dynamics of the system. The transfer function was calculated using different sets of input-output data. The improvements obtained with the proposed method are remarkable and highlight that a classic FRF approach cannot be used for SHM purposes on aeronautical structures. Different parameters were investigated; in particular the impact heights used to evaluate the transfer function, with respect to the velocity of the impact to reconstruct, were considered. Results showed that it is important to evaluate the transfer function from cases which are representative of the real scenario.

The effects of possible mismatches between the real and estimated position of the impact were also analyzed. Results showed that the reconstruction is good even when the impact has a certain offset from the position at which the transfer function is available. This is a good indicator of the accuracy which is requested by an impact location algorithm.

Determination of the impact position

The problem of determining the impact position is the second main concern of a passive approach for SHM. For isotropic materials the application of the triangulation method has proven to be effective and reliable. For composite materials, the direction dependent wave speed prevents the straightforward application of the triangulation. Usually an optimization algorithm is required. Moreover the velocity of waves in different directions must be determined. The method proposed in this thesis overcomes the drawbacks due to the wave speed. It is based on the proper orthogonal decomposition of the response of the plate under impact. Only the first 1ms of the signal was considered. This is in fact the part of the dynamics which can contain information about the distance between the impact and the sensor. Results highlighted that the impacts could be located within a small error between the real and estimated position. Two different signals were used: acceleration and strain. In particular this last response was validated with experimental tests. Results showed that the approach using strain provided lower errors in the determination of the impact position. These results reinforce the capabilities of the proper orthogonal decomposition as mathematical tool in the structural health monitoring field. The POD was in fact before applied to damage detection, but never to impact location.

Final remarks and future works

Different aspects of structural monitoring were addressed in this thesis. Both active and passive techniques were investigated with promising results. Contributions to damage and impact detection were provided in this thesis and in the related publications. The following steps will consist in the application of the proposed techniques to more complicated components. In particular in literature there is a lack of research on curved panels. These represent the typical component of aeronautical structures. However, only few studies have been made on them. A possible prosecution of this thesis is hence the application of the proposed techniques to curved and reinforced panels.

The proposed algorithm to detect damage without a baseline can be even more important when these components are under exam; as the curvature of each panel can have a strong influence in the final result, a comparison between two different panels could be ineffective. Moreover the position of damage through the thickness can have a stronger influence in the damage detection, due to the different stress and strain distribution caused by the curvature of the panel.

For impact detection the problem of curved panels is easily described. Impacts in the inner and outer surfaces produce completely different response of the panel, in terms of both contact force and response. This problem is not so relevant in a flat panel, as the system can be considered symmetric (as long as the layup of the plate is symmetric). The different response can play an important role also in the frequency content of the dynamics. A new study of the most appropriate approach for impact force reconstruction should therefore be performed.

References

[1]. http://aviation-safety.net/index.php.
[2]. Sumant, P. and S. Maiti, *Crack detection in a beam using PZT sensors.* Smart Materials and Structures, 2006. **15**(3): p. 695.
[3]. *http://easa.europa.eu/home.php.*
[4]. Alderliesten, R., *Analytical prediction model for fatigue crack propagation and delamination growth in Glare.* International Journal of Fatigue, 2007. **29**(4): p. 628-646.
[5]. Shim, D., R. Alderliesten, S. Spearing, and D. Burianek, *Fatigue crack growth prediction in GLARE hybrid laminates.* Composites science and technology, 2003. **63**(12): p. 1759-1767.
[6]. Xue, Y., C. Burton, M. Horstemeyer, D. McDowell, and J. Berry, *Multistage fatigue modeling of cast A356-T6 and A380-F aluminum alloys.* Metallurgical and Materials Transactions B, 2007. **38**(4): p. 601-606.
[7]. Wohler, A., *Theorie rechteckiger eiserner Brückenbalken mit Gitterwänden und mit Blechwänden.* Zeitschrift für Bauwesen, 1855. **5**: p. 121-166.
[8]. Wohler, A., *ber die Festigkeitsversuche mit Eisen und Stahl.* Zeitschrift für Bauwesen, 1870. **20**: p. 73-106.
[9]. Staszewski, W., G. Tomlinson, C. Boller, and G. Tomlinson, *Health monitoring of aerospace structures*2004: Wiley Online Library.
[10]. Giurgiutiu, V., *Structural health monitoring with piezoelectric wafer active sensors*2008: Academic Press.
[11]. Adams, D., *Health monitoring of structural materials and components: methods with applications*2007: Wiley.
[12]. Staszewski, W., S. Mahzan, and R. Traynor, *Health monitoring of aerospace composite structures–Active and passive approach.* Composites Science and Technology, 2009. **69**(11): p. 1678-1685.
[13]. Galvanetto, U., C. Surace, and A. Tassotti, *Structural damage detection based on proper orthogonal decomposition: experimental verification.* AIAA journal, 2008. **46**(7): p. 1624-1630.
[14]. Galvanetto, U. and G. Violaris, *Numerical investigation of a new damage detection method based on proper orthogonal decomposition.* Mechanical Systems and Signal Processing, 2007. **21**(3): p. 1346-1361.
[15]. Doebling, S.W., C.R. Farrar, and M.B. Prime, *A summary review of vibration-based damage identification methods.* Shock and Vibration Digest, 1998. **30**(2): p. 91-105.
[16]. Yan, Y., L. Cheng, Z. Wu, and L. Yam, *Development in vibration-based structural damage detection technique.* Mechanical Systems and Signal Processing, 2007. **21**(5): p. 2198-2211.
[17]. Peterson, R.E. and R. Plunkett, *Stress concentration factors.* Journal of Applied Mechanics, 1975. **42**: p. 248.
[18]. International, A.C. *http://www.aci.aero/.*
[19]. Suresh, S., *Fatigue of materials*1998: Cambridge University Press.
[20]. Boller, C., *Ways and options for aircraft structural health management.* Smart Materials and Structures, 2001. **10**(3): p. 432.
[21]. www.airfleets.net.
[22]. Herrera, J.M. and B. Vasigh, *A Basic Analysis Of Aging Aircraft, Region Of The World, And Accidents.* Journal of Business & Economics Research (JBER), 2011. **7**(5).
[23]. Blanchard, B.S., *Design and manage to life cycle cost*1978: M/A Press Portland, OR.
[24]. Toyama, N. and T. Okabe, *Effects of tensile strain and transverse cracks on Lamb-wave velocity in cross-ply FRP laminates.* Journal of materials science, 2004. **39**(24): p. 7365-7367.
[25]. Su, Z. and L. Ye, *Identification of damage using lamb waves: from fundamentals to applications*. Vol. 48. 2009: Springer.
[26]. Chen, J., Z. Su, and L. Cheng, *Identification of corrosion damage in submerged structures using fundamental anti-symmetric Lamb waves.* Smart Materials and Structures, 2010. **19**(1): p. 015004.
[27]. Schubert, L., U. Lieske, B. Frankenstein, and B. Koehler. *Interaction of Lamb waves with impact damaged CFRP's–effects and conclusions for acousto-ultrasonic applications*. in *ECF18, Dresden 2010*. 2013.
[28]. Sharif-Khodaei, Z., M. Ghajari, and M. Aliabadi, *Determination of impact location on composite stiffened panels.* Smart Materials and Structures, 2012. **21**(10): p. 105026.
[29]. Sharif Khodaei, Z. and M. Aliabadi, *Damage Identification Using Lamb Waves.* Key Engineering Materials, 2011. **452**: p. 29-32.
[30]. Sharif Khodaei, Z., R. Rojas-Diaz, and M. Aliabadi, *Lamb-Wave Based Technique for Impact Damage Detection in Composite Stiffened Panels.* Key Engineering Materials, 2012. **488**: p. 5-8.

[31]. Sharif Khodaei, Z., Q. Liu, and M. Aliabadi, *Influence of Adhesive Layer on Actuation of Lamb Wave Signals.* Key Engineering Materials, 2013. **525**: p. 617-620.
[32]. Rocha, B., C. Silva, and A. Suleman, *Development of a PZT phased array and FBG network for structural health monitoring based on guided Lamb waves.* CEAS Aeronautical Journal, 2013: p. 1-10.
[33]. Grondel, S., J. Assaad, C. Delebarre, and E. Moulin, *Health monitoring of a composite wingbox structure.* Ultrasonics, 2004. **42**(1): p. 819-824.
[34]. Baker, A., N. Rajic, and C. Davis, *Towards a practical structural health monitoring technology for patched cracks in aircraft structure.* Composites Part A: Applied Science and Manufacturing, 2009. **40**(9): p. 1340-1352.
[35]. Takeda, S., Y. Aoki, T. Ishikawa, N. Takeda, and H. Kikukawa, *Structural health monitoring of composite wing structure during durability test.* Composite structures, 2007. **79**(1): p. 133-139.
[36]. Park, G., H. Sohn, C.R. Farrar, and D.J. Inman, *Overview of piezoelectric impedance-based health monitoring and path forward.* Shock and Vibration Digest, 2003. **35**(6): p. 451-464.
[37]. Grisso, B.L., D.M. Peairs, and D.J. Inman, *Impedance-based Health Monitoring of Composites.* IMAC XXII Dearborn, MI Jan, 2004: p. 26-29.
[38]. Montalvao, D., N. Maia, and A. Ribeiro, *A review of vibration-based structural health monitoring with special emphasis on composite materials.* Shock and Vibration Digest, 2006. **38**(4): p. 295-326.
[39]. Shen, T., F. Wan, B. Song, and Y. Wu. *Damage location and identification of the wing structure with Probabilistic Neural Networks*. in *Prognostics and System Health Management Conference (PHM-Shenzhen), 2011*. 2011. IEEE.
[40]. Dervilis, N., R. Barthorpe, I. Antoniadou, W. Staszewski, and K. Worden. *Damage detection in carbon composite material typical of wind turbine blades using auto-associative neural networks*. in *Proc. of SPIE Vol*. 2012.
[41]. Ghajari, M., Z. Sharif Khodaei, and M. Aliabadi, *Impact Detection Using Artificial Neural Networks.* Key Engineering Materials, 2012. **488**: p. 767-770.
[42]. Kerschen, G., J. Golinval, A.F. Vakakis, and L.A. Bergman, *The method of proper orthogonal decomposition for dynamical characterization and order reduction of mechanical systems: an overview*. Nonlinear Dynamics, 2005. **41**(1): p. 147-169.
[43]. Karhunen, K., *Über lineare Methoden in der Wahrscheinlichkeitsrechnung*. Vol. 37. 1947: Universitat Helsinki.
[44]. Loève, M., *Fonctions aléatoires du second ordre*1965.
[45]. Kosambi, D., *Statistics in function space.* J. Indian Math. Soc, 1943. **7**(1): p. 76-88.
[46]. Obukhov, A., *Statistical description of continuous fields.* Trudy Geophys. Int. Akad. Nauk. SSSR, 1954(24): p. 3-42.
[47]. Pugachev, V.S., *The general theory of correlation of random functions.* Izvestiya Rossiiskoi Akademii Nauk. Seriya Matematicheskaya, 1953. **17**(5): p. 401-420.
[48]. Lumley, J., *The structure of inhomogeneous turbulent flows.* Atmospheric turbulence and radio wave propagation, 1967: p. 166-178.
[49]. Graham, M.D. and I.G. Kevrekidis, *Alternative approaches to the Karhunen-Loeve decomposition for model reduction and data analysis.* Computers & chemical engineering, 1996. **20**(5): p. 495-506.
[50]. Bayly, P.V., E.E. Johnson, P.D. Wolf, W. Smith, and R. Ideker, *Predicting patterns of epicardial potentials during ventricular fibrillation.* Biomedical Engineering, IEEE Transactions on, 1995. **42**(9): p. 898-907.
[51]. Epureanu, B., K. Hall, and E. Dowell, *Reduced-order models of unsteady viscous flows in turbomachinery using viscous–inviscid coupling.* Journal of Fluids and Structures, 2001. **15**(2): p. 255-273.
[52]. Barnston, A.G. and C.F. Ropelewski, *Prediction of ENSO episodes using canonical correlation analysis.* Journal of Climate, 1992. **5**(11): p. 1316-1345.
[53]. Fitzsimons, P.M. and C. Rui, *Determining low dimensional models of distributed systems.* Advances in Robust and Nonlinear Control Systems, 1993: p. 9-15.
[54]. Kreuzer, E. and O. Kust, *Analysis of long torsional strings by proper orthogonal decomposition.* Archive of Applied Mechanics, 1996. **67**(1): p. 68-80.
[55]. Feeny, B. and R. Kappagantu, *On the physical interpretation of proper orthogonal modes in vibrations.* Journal of Sound and Vibration, 1998. **211**(4): p. 607-616.
[56]. Feeny, B. and Y. Liang, *Interpreting proper orthogonal modes of randomly excited vibration systems.* Journal of Sound and Vibration, 2003. **265**(5): p. 953-966.
[57]. Kerschen, G. and J.C. Golinval, *Physical interpretation of the proper orthogonal modes using the singular value decomposition.* Journal of Sound and Vibration, 2002. **249**(5): p. 849-865.
[58]. Galvanetto, U., L. Monopoli, C. Surace, and A. Tassotti, *Experimental Application of a Damage Localisation Technique Based on Smoothed Proper Orthogonal Modes.* Key Engineering Materials, 2007. **347**: p. 121-126.

[59]. Kerschen, G., V. Lenaerts, and J.-C. Golinval, *Identification of a continuous structure with a geometrical non-linearity. Part I: Conditioned reverse path method.* Journal of Sound and Vibration, 2003. **262**(4): p. 889-906.
[60]. Lenaerts, V., G. Kerschen, and J.-C. Golinval, *Identification of a continuous structure with a geometrical non-linearity. Part II: Proper orthogonal decomposition.* Journal of Sound and Vibration, 2003. **262**(4): p. 907-919.
[61]. Placzek, A., D.-M. Tran, and R. Ohayon, *Hybrid proper orthogonal decomposition formulation for linear structural dynamics.* Journal of Sound and Vibration, 2008. **318**(4): p. 943-964.
[62]. Chelidze, D. and M. Liu, *Dynamical systems approach to fatigue damage identification.* Journal of Sound and Vibration, 2005. **281**(3): p. 887-904.
[63]. Thiene, M., *Studio numerico e sperimentale di una metodologia innovativa per l'individuazione del danneggiamento strutturale*, 2010, University of Padova, Italy.
[64]. Rao, S.S. and F.F. Yap, *Mechanical vibrations*. Vol. 4. 1995: Addison-Wesley Reading, MA.
[65]. Cao, M. and P. Qiao, *Novel Laplacian scheme and multiresolution modal curvatures for structural damage identification.* Mechanical Systems and Signal Processing, 2009. **23**(4): p. 1223-1242.
[66]. Ratcliffe, C.P., *Damage detection using a modified Laplacian operator on mode shape data.* Journal of Sound and Vibration, 1997. **204**(3): p. 505-517.
[67]. Ratcliffe, C.P., *A frequency and curvature based experimental method for locating damage in structures.* Journal of vibration and acoustics, 2000. **122**(3): p. 324-329.
[68]. Wu, D. and S. Law, *Damage localization in plate structures from uniform load surface curvature.* Journal of Sound and Vibration, 2004. **276**(1): p. 227-244.
[69]. Yoon, M., D. Heider, J. Gillespie, C. Ratcliffe, and R. Crane, *Local damage detection using the two-dimensional gapped smoothing method.* Journal of Sound and Vibration, 2005. **279**(1): p. 119-139.
[70]. Sun, E.Q. *Shear locking and hourglassing in msc nastran, abaqus, and ansys*. in *MSC Software Corporation's 2006 Americas Virtual Product Development Conference: Evolution to Enterprise Simulation. July*. 2006.
[71]. Shane, C. and R. Jha, *Proper orthogonal decomposition based algorithm for detecting damage location and severity in composite beams.* Mechanical Systems and Signal Processing, 2011. **25**(3): p. 1062-1072.
[72]. Hilber, H.M., T.J.R. Hughes, and R.L. Taylor, *Improved numerical dissipation for time integration algorithms in structural dynamics.* Earthquake Engineering & Structural Dynamics, 1977. **5**(3): p. 283-292.
[73]. Abaqus_6.8, *Abaqus analysis user's manual*, 2008, SIMULIA.
[74]. Shensa, M.J., *The discrete wavelet transform: wedding the a trous and Mallat algorithms.* Signal Processing, IEEE Transactions on, 1992. **40**(10): p. 2464-2482.
[75]. Limongelli, M., *Frequency response function interpolation for damage detection under changing environment.* Mechanical Systems and Signal Processing, 2010. **24**(8): p. 2898-2913.
[76]. Limongelli, M., *The interpolation damage detection method for frames under seismic excitation.* Journal of Sound and Vibration, 2011. **330**(22): p. 5474-5489.
[77]. Cavalini Jr, A., V. Franco, C. Gonsalez, V. Lopes Jr, and G. De Melo, *Noise influence on damage detection through modal state observers methodology*. Tema Tend Mater Appl Comput. v9 i2, 2008: p. 195-204.
[78]. Bentahar, M., R. El Guerjouma, S. Idijmarene, and M. Scalerandi, *Influence of noise on the threshold for detection of elastic nonlinearity.* Journal of Applied Physics, 2013. **113**(4): p. 043516-043516-11.
[79]. Hensman, J., M. Gherlone, C. Surace, and M. Di Sciuva. *Probabilistic Proper Orthogonal Decomposition*. in *EWSHM*. 2010.
[80]. Matworks, *Matlab 2012 documentation*, 2012.
[81]. Thiene, M., M. Zaccariotto, and U. Galvanetto, *Application of Proper Orthogonal Decomposition to Damage Detection in Homogeneous Plates and Composite Beams.* Journal of Engineering Mechanics, 2013. **139**(11): p. 1539-1550.
[82]. Thiene, M., U. Galvanetto, and C. Surace, *Influence of sharp stiffness variations in damage evaluation using POD and GSM.* Smart Structures and Systems, 2014. **In press**.
[83]. Thiene, M., U. Galvanetto, M. Gherlone, and M.H. Aliabadi, *Application of Laplacian operators on noisy data to compute curvature with proper orthogonal decomposition.* Key Engineering Materials, 2014. **Vols. 577-578**.
[84]. INOUE, H., H. ISHIDA, K. KISHIMOTO, and T. SHIBUYA, *Measurement of impact load by using an inverse analysis technique: comparison of methods for estimating the transfer function and its application to the instrumented charpy impact test.* JSME international journal. Ser. 1, Solid mechanics, strength of materials, 1991. **34**(4): p. 453-458.
[85]. Martin, M. and J. Doyle, *Impact force identification from wave propagation responses.* International journal of impact engineering, 1996. **18**(1): p. 65-77.
[86]. Doyle, J.F., *A wavelet deconvolution method for impact force identification.* Experimental mechanics, 1997. **37**(4): p. 403-408.

[87]. Meo, M., G. Zumpano, M. Piggott, and G. Marengo, *Impact identification on a sandwich plate from wave propagation responses.* Composite structures, 2005. **71**(3): p. 302-306.
[88]. Park, J., S. Ha, and F.K. Chang, *Monitoring impact events using a system-identification method.* AIAA journal, 2009. **47**(9): p. 2011-2021.
[89]. Ghajari, M., Z. Sharif-Khodaei, M.H. Aliabadi, and A. Apicella, *Identification of impact force for smart composite stiffened panels.* Submitted to Smart Materials and Structures, 2012.
[90]. Thiene, M., U. Galvanetto, M. Gahjari, and M. Aliabadi. *A frequency analysis applied to force identification*. in *Fifth International Conference on Structural Engineering, Mechanics and Computation*. 2013. Cape Town.
[91]. LeClerc, J., K. Worden, W. Staszewski, and J. Haywood, *Impact detection in an aircraft composite panel—A neural-network approach.* Journal of sound and vibration, 2007. **299**(3): p. 672-682.
[92]. Worden, K. and W. Staszewski, *Impact location and quantification on a composite panel using neural networks and a genetic algorithm.* Strain, 2000. **36**(2): p. 61-68.
[93]. Sultan, M., K. Worden, S. Pierce, D. Hickey, W. Staszewski, J. Dulieu-Barton, and A. Hodzic, *On impact damage detection and quantification for CFRP laminates using structural response data only.* Mechanical Systems and Signal Processing, 2011. **25**(8): p. 3135-3152.
[94]. Oppenheim, A.V., *Discrete-Time Signal Processing, 2/E*2006: Pearson Education India.
[95]. Oppenheim, A.V., R.W. Schafer, and J.R. Buck, *Discrete-time signal processing*. Vol. 5. 1999: Prentice hall Upper Saddle River.
[96]. Angrilli, F. and S. Debei, *Corso di misure meccaniche, termiche e collaudi*2006: Cedam.
[97]. Doebelin, E.O., *Measurement systems: application and design.* 2003.
[98]. Coverley, P. and W. Staszewski, *Impact damage location in composite structures using optimized sensor triangulation procedure.* Smart materials and structures, 2003. **12**(5): p. 795.
[99]. Ahmari, S. and M. Yang, *Impact location and load identification through inverse analysis with bounded uncertain measurements.* Smart Materials and Structures, 2013. **22**(8): p. 085024.
[100]. Hajzargerbashi, T., T. Kundu, and S. Bland, *An improved algorithm for detecting point of impact in anisotropic inhomogeneous plates.* Ultrasonics, 2011. **51**(3): p. 317-324.
[101]. Azeez, M. and A. Vakakis, *Proper orthogonal decomposition (POD) of a class of vibroimpact oscillations.* Journal of Sound and Vibration, 2001. **240**(5): p. 859-889.
[102]. Pierson, M.O. and R. Vaziri, *Analytical solution for low-velocity impact response of composite plates.* AIAA journal, 1996. **34**(8): p. 1633-1640.
[103]. Ciampa, F. and M. Meo, *Impact detection in anisotropic materials using a time reversal approach.* Structural Health Monitoring, 2012. **11**(1): p. 43-49.
[104]. Ghajari, M., Z. Sharif-Khodaei, M. Aliabadi, and A. Apicella, *Identification of impact force for smart composite stiffened panels.* Smart Materials and Structures, 2013. **22**(8): p. 085014.
[105]. Benedetti, I., A. Milazzo, and M. Aliabadi, *Structures with Surface-Bonded PZT Piezoelectric Patches: a BEM Investigation into the Strain-transfer Mechanism for SHM applications.* SDHM: Structural Durability & Health Monitoring, 2009. **5**(3): p. 251-274.
[106]. Benedetti, I., M. Aliabadi, and A. Milazzo, *A fast BEM for the analysis of damaged structures with bonded piezoelectric sensors.* Computer Methods in Applied Mechanics and Engineering, 2010. **199**(9): p. 490-501.
[107]. Faggiani, A. and B. Falzon, *Predicting low-velocity impact damage on a stiffened composite panel.* Composites Part A: Applied Science and Manufacturing, 2010. **41**(6): p. 737-749.
[108]. Abrate, S., *Modeling of impacts on composite structures.* Composite structures, 2001. **51**(2): p. 129-138.
[109]. SONATEST, *How phased arrays work*, in *Lectures on ultrasound inspections*.

Appendix 1: NDT

Method	Damage type	Advantages	Limitations
Visual inspection	• Fatigue cracks • Delamination	• Simple • Relatively inexpensive	• Time consuming • Low accuracy
Ultrasonics	• Fatigue cracks • BVID • Delamination • Corrosion	• Well established and understood • Sensitive to small damage • Possible damage location • Good depth range • Relatively inexpensive • Possible in flight monitoring	• Requires scanning • Requires coupling • Often does not detect closed cracks • Sensitive to geometry
Eddy current	Fatigue cracks	• Detection of small cracks • Possible non-contact testing • Does not require coupling • Possible data storage • Relatively inexpensive	• Used mostly for crack detection • Requires scanning • Specific monitor skills • Requires calibration • Poor penetration
Acoustic emissions	• Fatigue cracks • BVID • Delamination • Corrosion	• Well established and understood • Large structures can be monitored • Not sensitive to geometry possible in-flight monitoring	• Requires external stimulus • Not reproducible • Not sensitive to small damage
Radiography	• Fatigue cracks • BVID • Delamination • Corrosion	• Fast monitoring • Good penetration • Relatively inexpensive	• Not sensitive to small damage • Not possible for large structure
Thermography	• Fatigue cracks • BVID • Delamination	• Fast monitoring • Suitable for large structures	• Expensive • Not suitable for small damage • Poor penetration
Shearography	• Fatigue cracks • BVID • Delamination • Corrosion	• Fast monitoring • Suitable for large structures	• Very expensive • Not well developed • Need external stimulus

Appendix 2: Ultrasonic inspections

Ultrasonic inspections are based on various properties of ultrasonic waves propagating in monitored structures. Damage detection uses wave's attenuation, reflection, scattering, diffraction and other physical phenomena of an incident wave. Tests are carried out with either pulse-echo approach, using one probe, or as pitch-catch, using two probes. In the first case the probe serves both as actuator and sensor, while in the second one, they move simultaneously, in order to let the second receive the signal emitted by the first.

The technique is often referred to as A-, B- and C-scans. A-scans refer to a single point measurement, B-scans measures along a line (the one defined by the array of sensors) and C-scans provide a collection of B-scans which forms a contour surface plot. This last one has become common practice in industry since the introduction of composite materials. In fact its results are easy to understand and it can be used to verify a large structure in a short time. Traditional ultrasonic inspection approaches use different types of gel to couple the probe and the monitored specimen. Sometimes this coupling material can be avoided if the probe and the specimen are immersed in water. Recent developments in this area include non-contact techniques which use air as coupling. One of the main problems associated with this last coupling is the acoustic impedance mismatch between the air and the specimen, as well as the attenuation of waves in air. Ultrasonic inspections are really sensitive to small surface ad deep flaws in the material. Difficulties with scanning and coupling are the major concerns with this technique. Furthermore sometimes an efficient inspection requires several scans from different directions, increasing the inspection time. Some components in a structure can also be difficult to reach, especially for the pitch catch configuration. In those cases the structure has to be disassembled.

Ultrasound waves are mechanical vibrations induced in an elastic material by a piezoelectric transducer, excited by electric voltage. The typical range of frequency is 0.1-50 MHz, but for industrial application usually this interval restricts to 0.5-15 MHz. The most of ultrasound inspection techniques uses probes with just one transducer, pulse echo configuration, with diverging beams. The basic principle of these inspections is that every time a wave encounters one discontinuity, it is partially reflected back to the transducer. Two main methods can be used to define the location and magnitude of this discontinuity: time of flight and amplitude of the reflected wave. The use of phased array sensors gives much flexibility to the operator, as possibility to define the focal length of the beam as well as the incident angle. The definition of phase array sensor is: a mosaic of transducer elements in which the timing of the elements' excitation can be individually controlled to produce certain desired effects, such as steering the beam axis or focusing the beam. These effects can be achieved applying a correct amplitude and time delay of the signal to each sensor of the array. An example is given in Figure 102.

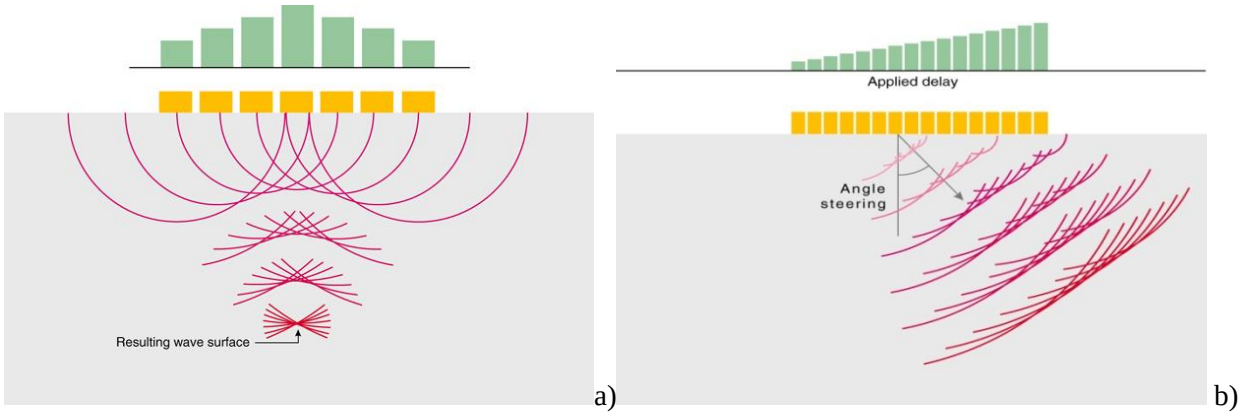

Figure 102: example of beam generation for a phased array probe [109].

One of the most important features of this technique is that it is able not only to detect the position of damage in a surface, but also its position along the thickness. For composite materials this is very important, as delamination can be produced by impacts between different layers. To compute the exact position of damage, however, is not so fast, especially if the structure is wide. Usually a combination of different scan types is required. In particular the C-scan is useful to determine the dimension of damage, as well as its position in the plane. The A scan is useful to determine at which point to define a threshold which is then used to determine the C-scan. This is an important step because from this definition damage can be evaluated or not. It is worth to underline, however, that this limit can be define in the post-processing analysis so that a detailed study about that can be performed. The position of damage through the thickness can be evaluated with the B-scan. Using two orthogonal B-scans it is possible to determine also the dimension of the damage, and possibly its three-dimensional shape. Examples of these types of scans can be found in the following pictures, which were obtained on a composite plate which was impacted at hypervelocity speed. From the B-scan and C-scan delamination is identifiable both in the plane and through thickness.

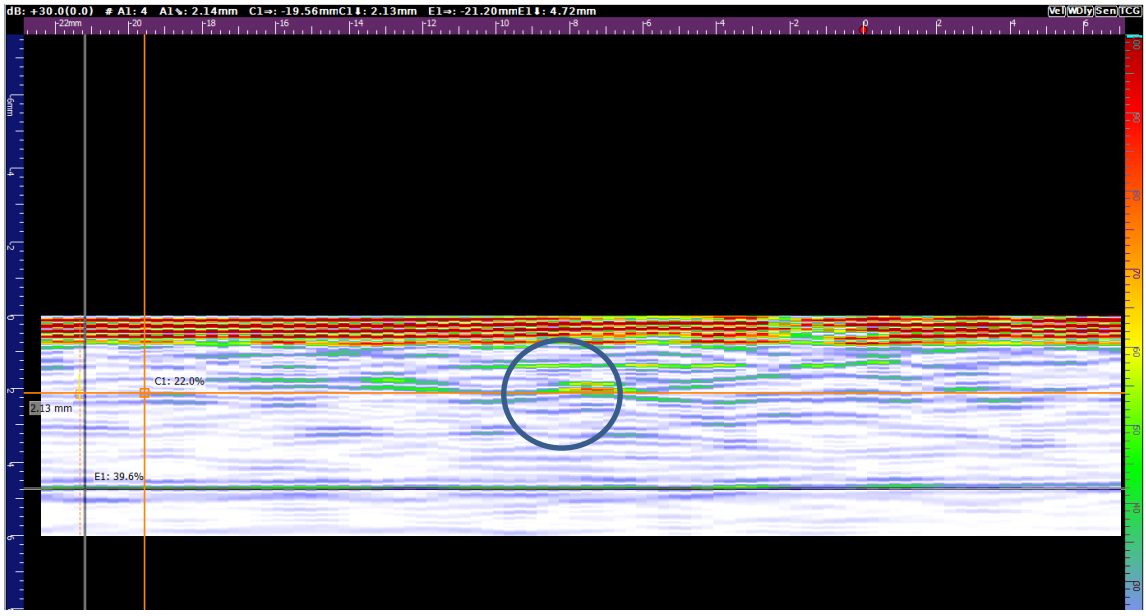

Figure 103: B-scan of a section of a composite plate; highlighted the position of damage.

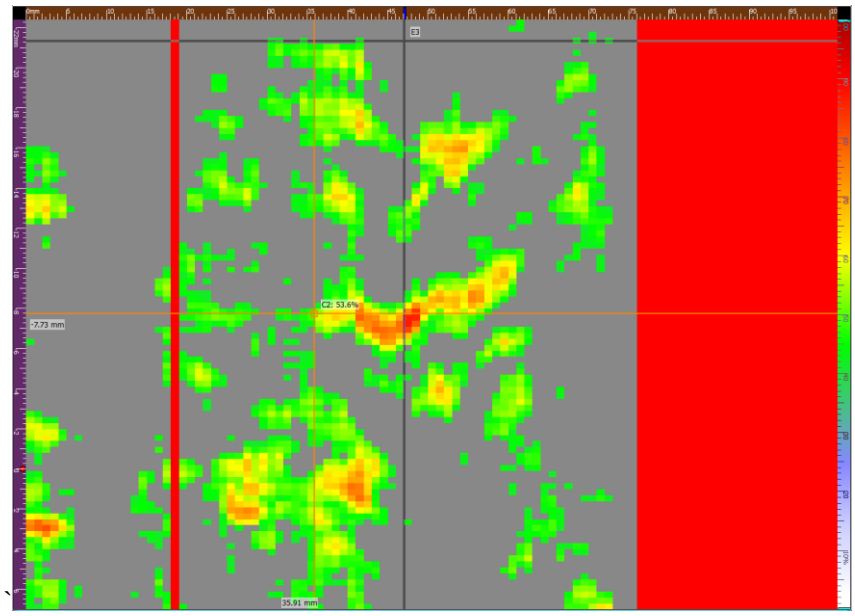

Figure 104: C-scan of the specimen, the delamination is clearly identifiable. Red stripes correspond to missed acquisitions.

Appendix 3: PZT sensors

Electro-active materials have the capability to modify their shape as a response to electric stimuli. They permit induced-strain actuation and strain sensing, which are of considerable importance in SHM. In particular they do not require any mechanism, which can be obviously source of malfunctioning. With piezoelectric strain sensors, strong and clear voltage signals can be obtained without gage bridges or signal modifiers (ex. Amplifiers or conditioners). In dynamics, vibration and audio applications, these properties are particularly important.

In general, polarization is a phenomenon which consists in the separation of positive and negative charges at different ends of a material, after an external stimulus. Different materials present different type of polarization. There can be spontaneous or ferroelectric polarization. Piezoelectricity describes the phenomenon of generating an electric field when the material is subjected to a mechanical stress, or vice versa. Piezoelectric properties occur naturally in some crystalline materials, such as quartz and Rochelle salt. Piezoelectricity is related to permanent polarization and can be attributed to change in permanent polarization being changed when the material undergoes mechanical stress. Conversely, the change in permanent polarization produces a mechanical deformation, i.e. strain.

Piezoelectric wafer active sensors (PWAS) are cheap transducers which operate exploiting piezoelectricity. At the beginning they were used for vibration control, but then their capacity to be also actuators started to be used for damage detection purposes. The application of these sensors to SHM can be basically divided into three steps:

- Modal analysis and transfer function.
- Electromechanical (E/M) impedance.
- Wave propagation.

Piezoelectricity describes the phenomenon of generating an electric field when the material is subjected to mechanical stress (direct effect). On the other hand it works also in the reverse sense, generating mechanical strain in response to an applied electrical field. The direct piezoelectric effect is exploited when PZTs are used as sensors, while the converse piezoelectric effect is useful when they are used as actuators.

For linear piezoelectric materials, the interaction between the electrical field and mechanical variables can be described by a linear relationship. The actuating equations of PZT are:

$$S_{ij} = s_{ijkl}^{E} T_{kl} + d_{kij} E_k + \delta_{ij} \alpha_i^{E} \theta$$

$$D_j = d_{jkl} T_{kl} + \varepsilon_{jk}^{T} E_k + \overline{D}_i \theta \qquad \textbf{A3-1}$$

Where *Sij* and *Tij* are the strain and stresses; *Ek* and *Dj* are the electric field and displacement and θ is the temperature. The stress and strain variables are second order tensors, while the electric field and displacement are first order tensors; s_{ijkl}^{E} is the mechanical compliance of the material measured at zero electrical field (E=0), ε_{jk}^{T} is the dielectric permittivity measured at zero mechanical stress (T=0), d_{kij} represents the piezoelectric coupling effect, α_i is the coefficient of thermal expansion and $\overline{D}_i$ is the electric displacement temperature coefficient.

When PZT are used is sensing mode, the above equations are:

$$S_{ij} = s_{ijkl}^{D} T_{kl} + g_{kij} D_k + \delta_{ij} \alpha_i^{D} \theta$$

$$E_j = g_{ikl} T_{kl} + \beta_{ik}^{T} D_k + \bar{E}_i \theta \qquad \textbf{A3-2}$$

The coefficient g_{ikl} is the piezoelectric voltage coefficient and represents how much electric field is induced per unit stress. The coefficient $\bar{E}_i$ is the pyroelectric voltage coefficient and represents how much electric field is induced per unit temperature change. The superscript *D* indicates that the quantity is measured at zero electric displacement (D=0);

A 7 mm diameter, 0.2 mm thick PWAS weights 78g and costs less than $10. Their performances exceed the ones of strain gages, as PWAS can be used not only as sensors but also as actuators. For a detailed description of PWAS see reference [10].

Appendix 4: Laser scanner vibrometer

The instrumentation used consisted of an Ometron laser scanner vibrometer (LSV), type VPI+, connected to a personal Computer which provided the input command to the shaker and the visualization of the output. The VPI+ Sensor is an industrially engineered 'Michelson' interferometer. The sensor works as a non-contacting velocity transducer capable of remote measurement of the velocity of a solid surface. Velocities up to $\pm$ 2000 mms^{-1} can be measured at working distances of up to 200 m. The main application area for the instrument is vibration measurement on components and structures. A Michelson interferometer uses a laser beam divided into a reference beam and a signal beam. The signal beam is directed onto a vibrating test surface, and back-reflected light is re-combined with the internal reference beam. When the test surface moves, the path difference between the routes followed by the reference and signal beams changes. This results in intensity modulation of the re-combined beam due to interference between the reference and signal beams. One complete cycle of the intensity modulation corresponds to a surface movement of $\lambda/2 = 3.16 \times 10^{-7}$m, half the wavelength of the Helium-Neon laser source; hence the frequency F_d of intensity modulation corresponding with a surface velocity v is given by $F_d = 2v/\lambda$. The re-combined beam is shared between two independent detection channels in such a way that the interferometric path difference presented to one channel is effectively one quarter of a wavelength longer than that presented to the other. This configuration results in a 90° phase shift between the signals from the two channels (denoted 'sin' and 'cos' signals), the direction of motion of the surface determining which signal leads the other in phase. The sin and cos signals at frequency F_d are fed to a dual channel balanced modulator where they are respectively modulated by internally generated sin and cos signals at a carrier frequency F_c. Summation of the two modulated outputs yields a single, frequency shifted output at $F_c + F_d$ or $F_c - F_d$, depending on the direction of motion of the surface. In this way, electronic mixing results in essentially the same frequency shifted Doppler signals as those obtained using optical frequency-shifting techniques, and established frequency tracking methods can be used to derive an analogue voltage representing the instantaneous velocity of the moving surface.

The laser is classified as a Class II, with a Laser Safety Class <1 mW in the visible output. The maximum recommended cable length is no more than 20 metres for analogue output signals. Its general specifications are given in the following tables. More specifications can be found in [105].

Table 18: Range of measurement.

Range	Vibr. Frequency	Error
5 mm/s	< 0.001 Hz - 200 kHz	<1%
20 mm/s	< 0.001 Hz - 200 kHz	<1%
100 mm/s	< 0.001 Hz - 200 kHz	<1%
500 mm/s	< 0.001 Hz - 2 MHz	<1%
2000 mm/s	< 0.001 Hz - 2 MHz	<1%

Table 19: Technical specifications.

Working Distance	Up to 200 m (subject to surface finish)
Field of view	25° x 25°
Signal connectors	Analogue velocity; Doppler; video; RS-232 interface
Unit Dimensions	240 x 380 x 240 mm
Weight	15.2 kg
Power Rating	72VA
Power Requirements	85-264 V_{rms}; 47-63Hz; 0.3A at 240V
Power Safety Requirements	Internal fuse type: 2 x 2A T

Table 20: Signal Outputs.

Name	Type	Output	Connection Type	Source Impedence
Velocity	Analogue	±5V	BNC	50 Ohm
D1 & D2	Analogue	±12V	BNC	50 Ohm
Dropout	Analogue	TTL	BNC	50 Ohm
RS-232	Digital	±5V	9-Way D-Type	

Table 21: Calibration.

Range	Voltage Resolution
5 mms^{-1}	1 $mms^{-1}/V_{(pk)}$
20 mms^{-1}	4 $mms^{-1}/V_{(pk)}$
100 mms^{-1}	20 $mms^{-1}/V_{(pk)}$
500 mms^{-1}	100 $mms^{-1}/V_{(pk)}$
2000 mms^{-1}	400 $mms^{-1}/V_{(pk)}$

Table 22: Environment specifications.

Temperature	+5°C to 40°C (+40°F to + 104°F)
Altitude	up to 2200m (7200ft)
Relative Humidity	up to 90% (non-condensing)

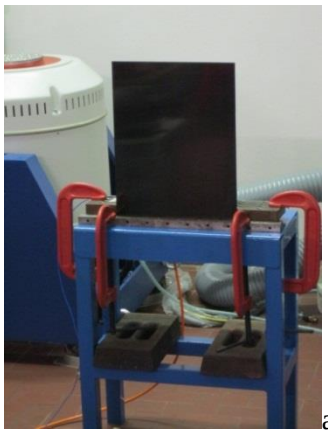
a)
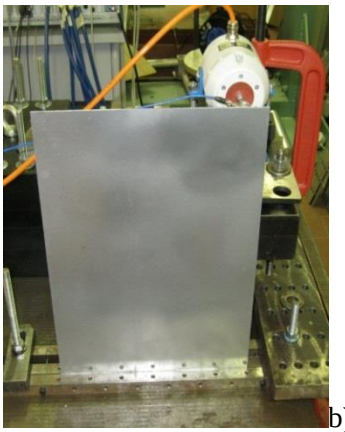
b)


c)

Figure 105: a) Plate in the first support without coating. b) Plate in the second support. c) Vibrometer

Appendix 5: Effects of numerical integration on the POD results

In Chapter 4, which concerned the damage detection using the POD analysis, it was underlined that different numerical integration schemes were used to compute the dynamics of the system, and that sometimes they could affect the damage detection result. In this appendix some examples are given for both the cantilever beam and the stiffened panel cases. Generally damage could be located regardless of the numerical integration applied. However some differences in the damage indices were found. For the composite beam case, only the model were CPS4 elements were used is shown, similar considerations are valid for the CD20r elements.

2-D continuum model of the beam

The following figures present results obtained with implicit and modal integration schemes. No relevant differences were found in the damage detection results. Each picture compares two results obtained with both the techniques. The first three figures refer to damage in different positions, all evaluated with the sensors located in the upper surface of the beam. The last three show the comparison between the evaluations with upper and lower sensors.

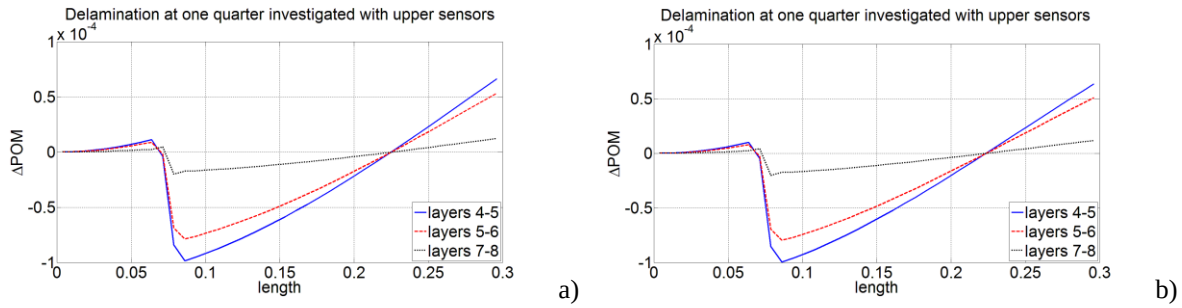

Figure 106: Delamination investigated at one quarter of the length. a) Implicit integration scheme. b) Modal integration scheme.

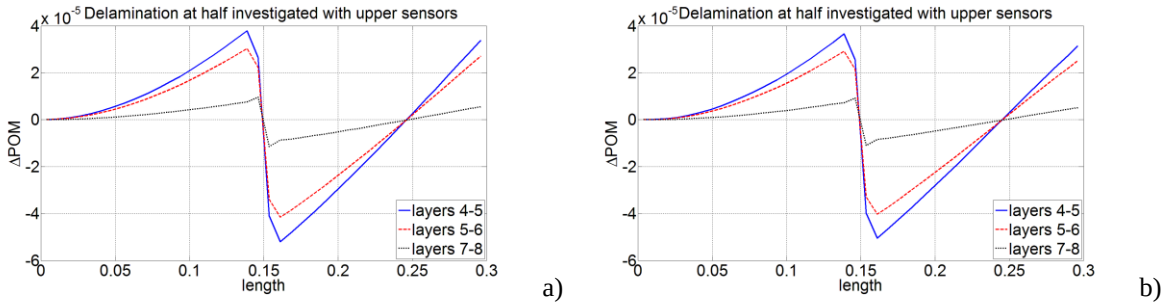

Figure 107: Delamination investigated at half of the length. a) Implicit integration scheme. b) Modal integration scheme.

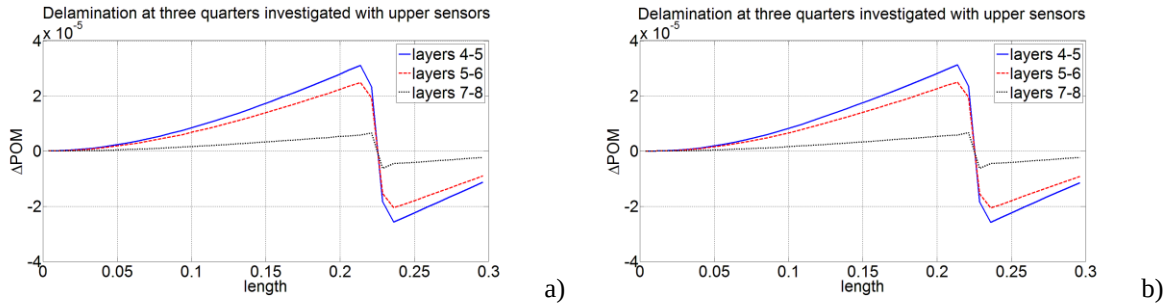

Figure 108: Delamination investigated at three quarters of the length. a) Implicit integration scheme. b) Modal integration scheme.

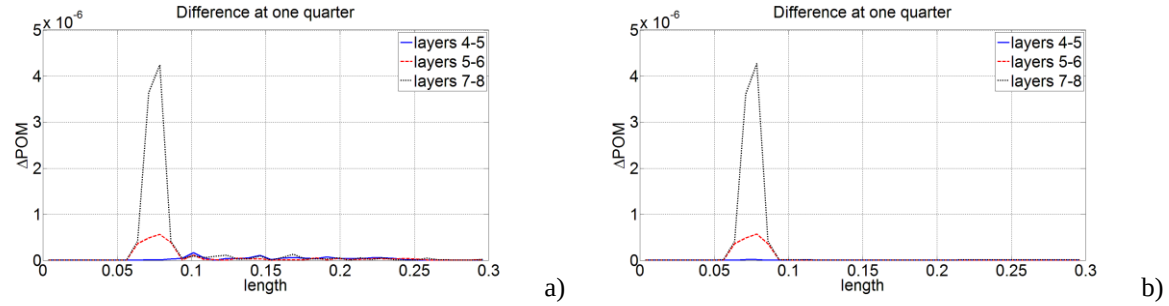

Figure 109: Difference in using upper or lower sensors at one quarter of the length: a) Implicit integration scheme. b) Modal integration scheme.

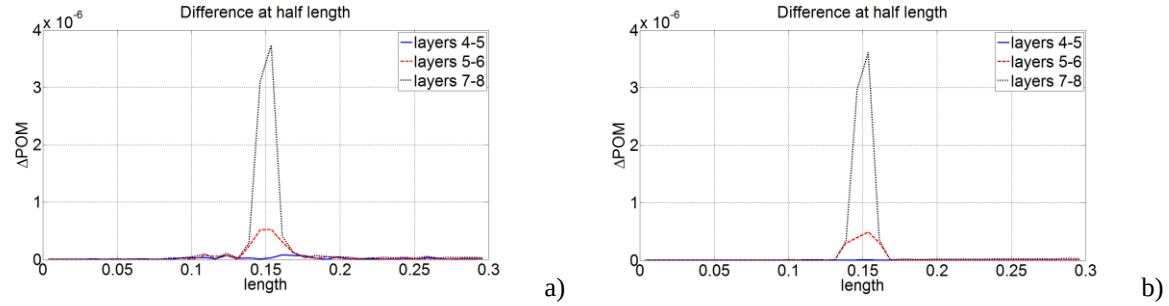

Figure 110: Difference in using upper or lower sensors at half of the length: a) Implicit integration scheme. b) Modal integration scheme.

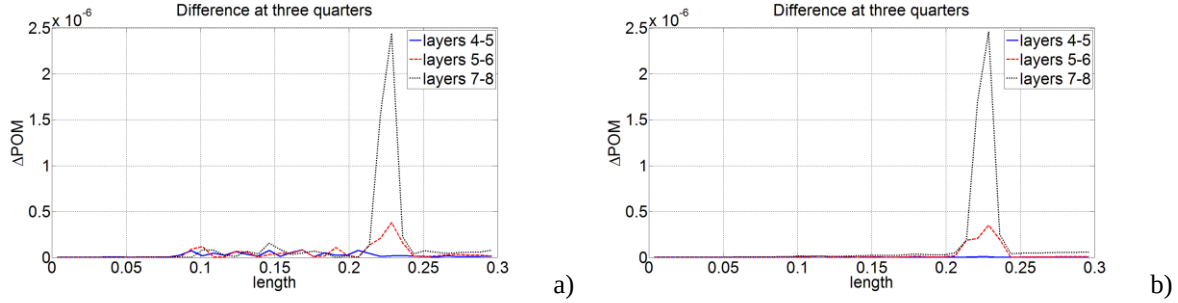

Figure 111: Difference in using upper or lower sensors at three quarters of the length: a) Implicit integration scheme. b) Modal integration scheme.

Stiffened panel

In this case three different methods to evaluate the dynamics of the system were considered: the implicit integration scheme, the modal one and the steady state response of the system. This last calculates the amplitude of the response at a certain frequency and provides also the phase. The dynamics is therefore calculated multiplying the load for that amplitude and applying the correct phase shift. The main

difference between the three methods is that the first is suitable for strong nonlinear dynamics, the second for mild nonlinear dynamics and the third is a linear method. Results obtained for the damage index obtained with the classic POD at three different positions are given in the following figures.

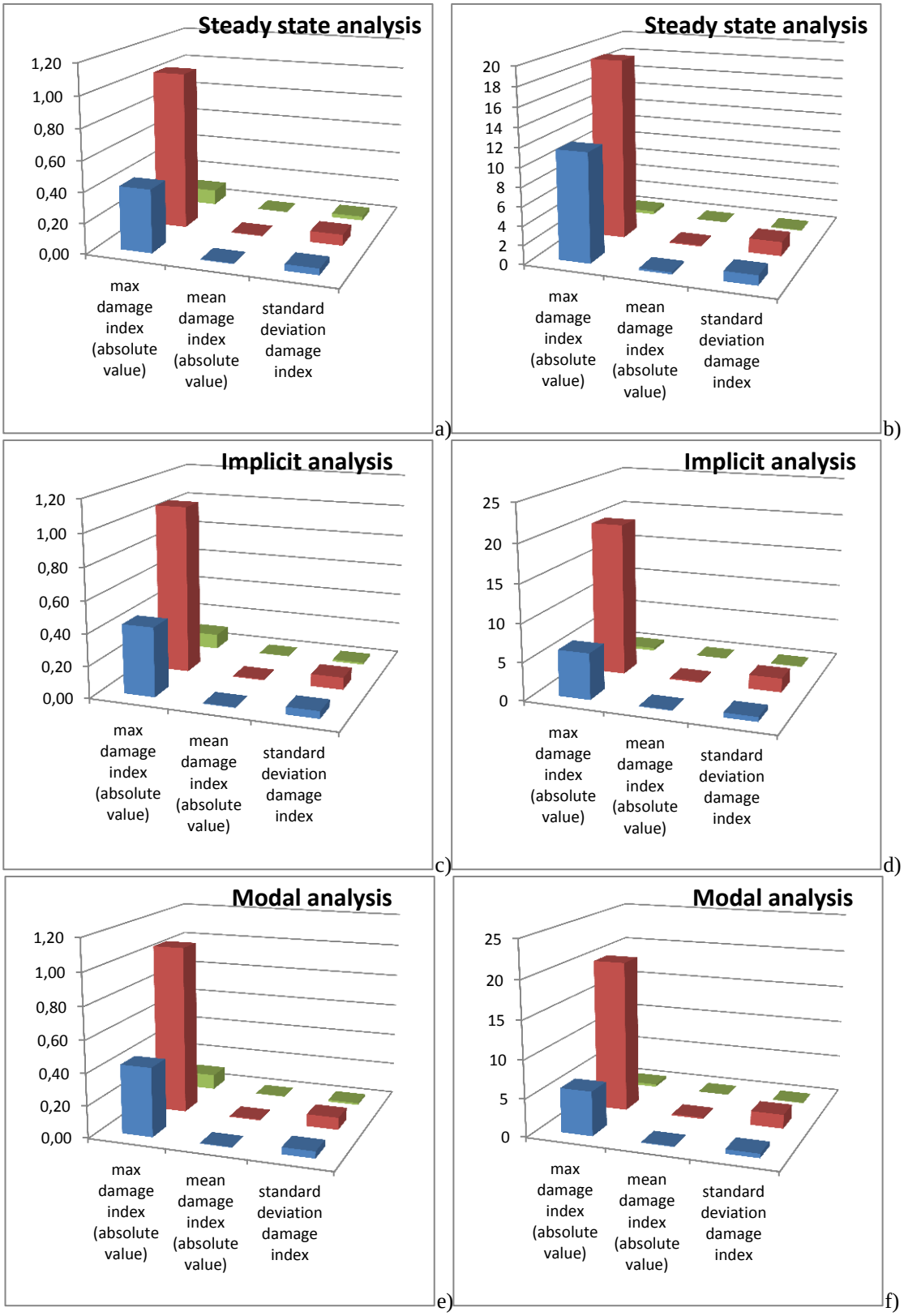

Figure 112: Results obtained with the different techniques. blue) damage 1. red) damage 2. green) damage 3. Fig a) c) e) refer to the low level damage. Fig b) d) f) refer to the high level damage

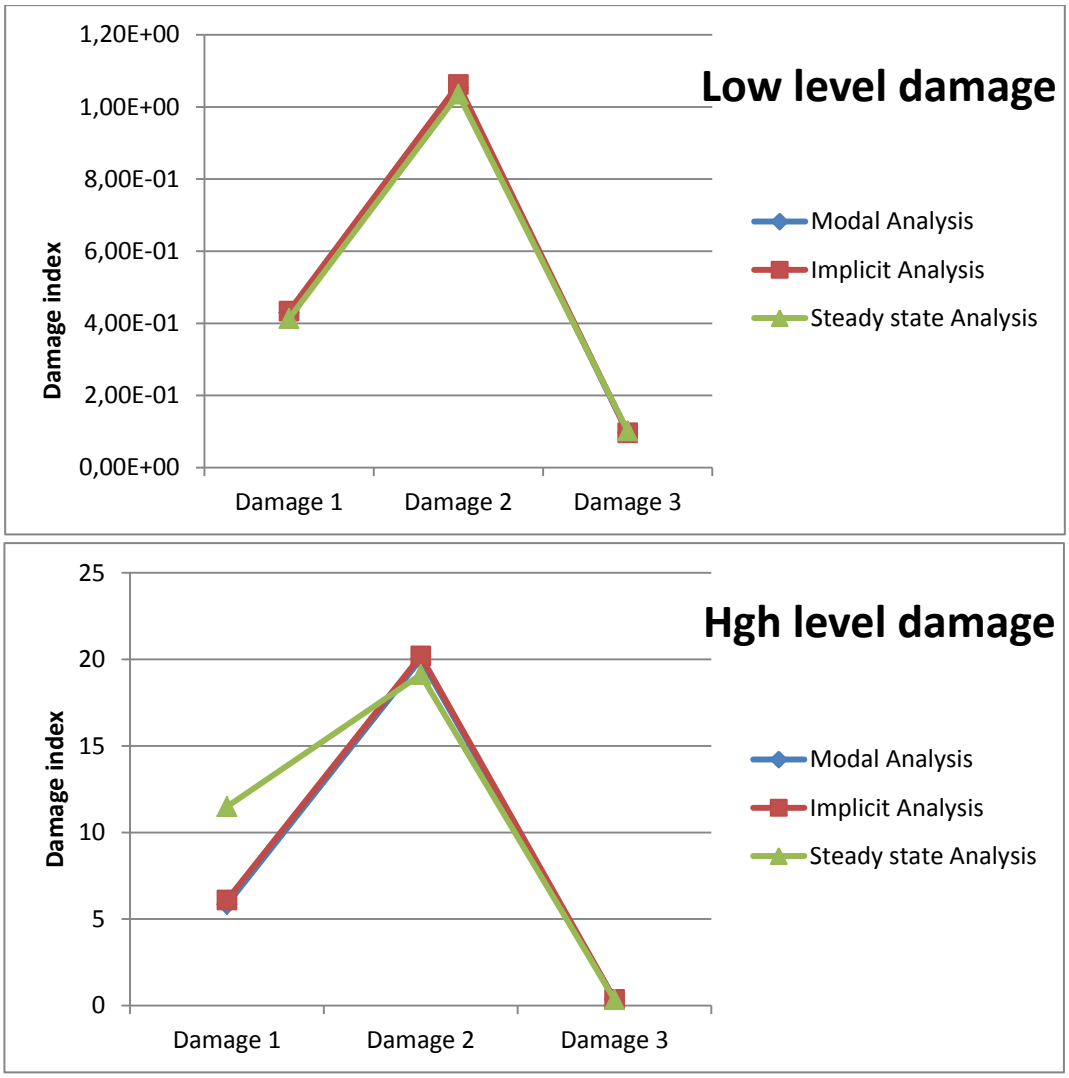

Figure 113: Comparison of the damage indices in the different analysis. a) low level damage. b) high level damage

Figure 112 shows a statistical analysis of the damage detection performance with the three different methods. The damage index indicates that the method can detect the damage. The fact that the average damage index and the standard deviation are very low means that the damage is concentrated in few grid points, hence that the calculated damage index reaches high values only in few points, which are actually the ones close to the actual damage. Figure 113 shows a comparison between the different damage indices, at three positions and for the three integration methods. When the damage is of low entity, there are no substantial differences between the different methods. On the other hand, when the level of damage increases, the steady state analysis provides different results. This can mean that a certain amount of nonlinearity in the dynamics is present. Based on these results for the analyses with the GSM approach, the implicit integration scheme was applied.

Appendix 6: POD GUI

The application of POD in damage detection is of great interest in the scientific field. Part of this PhD consisted in collaborating in a European project denominated Macotech. It involved different partners, including Mare engineering, which had the duty to analyse the impact response of the panel. In this section the part related to the damage detection algorithm, based on the POD, is now presented. To develop a user-friendly code, a graphic user interface (GUI) was developed in Matlab. In this appendix the GUI is presented with the description of how to use it.

The GUI is divided in two main parts: on the left there are all the buttons which control the analysis, create plots and save data. On the right four Cartesian diagrams are available to show different plots simultaneously.

Focusing on the left side, it is subdivided into four parts. The first two provide the POD analysis and compute the curvature for both intact and damaged data and also the smoothing technique for the damaged data. The third part regards the plot options:

- The list box let the user choose which variable must be plotted.
- The underneath popup menu allows to choose which units were given in the model: meters centimetres or millimetres. This is useful to obtain a good contour plot
- The popup menu on the right allows choosing which type of plot the user wants to display while pushing the underneath button, the plot appears in one of the axes on the other part of the GUI. To choose which axes the plot must display just click on it before pushing the PLOT button.
- The slider rotate the azimuth of the pictures

The fourth part concerns the possibility to export one figure, in order to process it, and to save all the calculated data to an external .mat file. The button RESTART allows the user to start again the analysis if anything went wrong, for example when the user loads a wrong file.

Example: simple cantilevered plate

Start the GUI from the Matlab workspace. Push the POD button under the intact data part. A small window appears, asking to insert the number of nodes used for the damage detection and the number of samples for each node; these depend on the analysis performed in the FE software. For this example, type *117* for the number of nodes and *2001* for the number of samples.

When pressing ok a new window opens, asking which type of software or acquisition toolbox were used to generate data. In this case press abaqus and then OK. This list can be updated with other software

reports; in that case also a script providing the reading of the file generated by the other software must be supplied. In the code a commented area provides the possibility to add new software. At this point the script asks the user to choose the file that must be loaded. Go to "Dati per fare le prove"→ "abaqus" and select Torino_integra_vel.rpt.

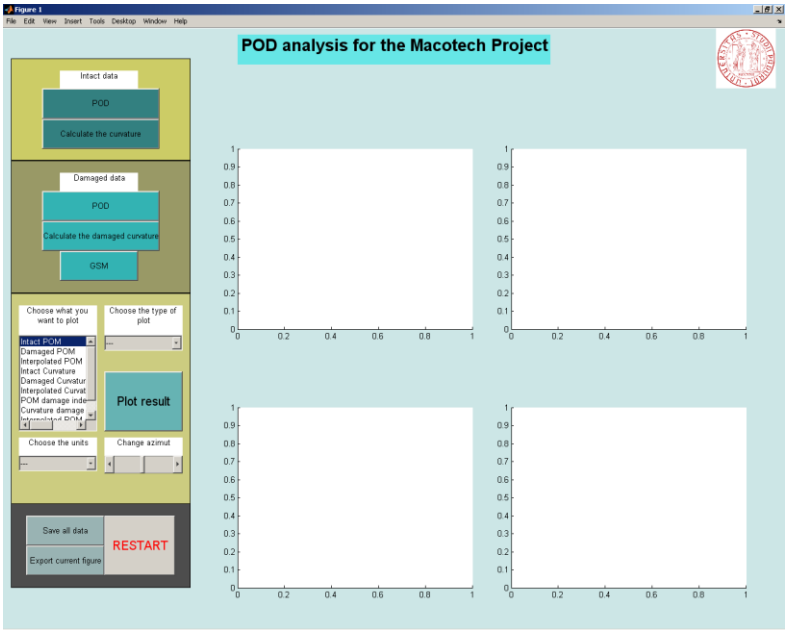

Figure 114: GUI for the Macotech project.

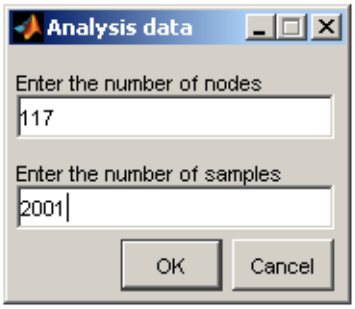

Figure 115: Insert parameters

If the file is loaded correctly a message appears, press Ok. Otherwise check the Matlab command window for possible errors and restart the analysis with the RESTART button. When the file is chosen a new window asks to load the file with the position of the sensors; go to the previous folder and choose the file posizione_nodi_laboratorio_torino.txt. A figure appears, showing one of the loaded data.

The data which are loaded were exported from Abaqus using the tool Report→xy with the option "separate table for each xy data", without exporting the sum. The layout of the file consists into two columns, the first providing the time and the second the value of the variable; the time history of each node is written, once it has finished the following node is written. Three header lines are present at the beginning of the file, while 5 are present between data of subsequent nodes; this layout of the report file is already provided by Abaqus. Regarding the position of the nodes, the layout must provide four columns,

the first with the number of the node, the second with the X coordinate the Y and Z. No header lines are present.

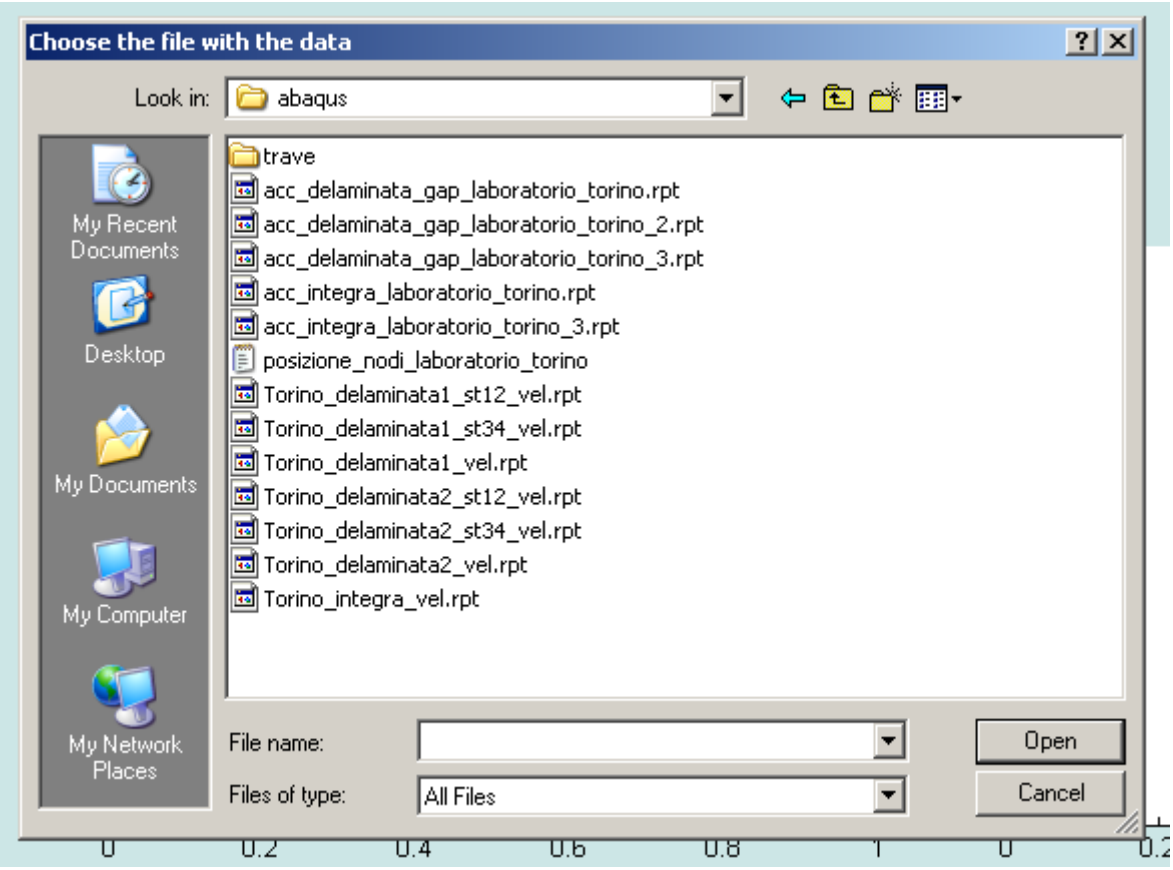

Figure 116: Select data

When also the position of sensors has been loaded a window asks which plane represents the middle plane of the plate (XY, XZ, YZ); this depends to the FEM model. When the window disappears the POD has been implemented. The following step consists on clicking the "Calculate the curvature" button. Follow the same procedure to implement the POD and calculate the curvature for the damaged data (choose file Torino_delaminata1_vel.rpt), and at the end push the GSM button in order to interpolate the damaged POM and curvature. Now it is possible to create the plots:

- Choose what you want to plot
- Choose the units
- Choose the type of plot
- Click on one of the four Cartesian diagrams to choose where the figure will appear.
- Press PLOT
- If you want rotate the graphic using the slider

Be careful on which plot is appearing. If you are trying to plot something that you haven't calculated yet the code displays something, but you should look at the command window in order to be sure that everything is correct (the title of the plot should warn you).

Let's see some plots regarding the comparison with Torino_delaminata1_vel.rpt

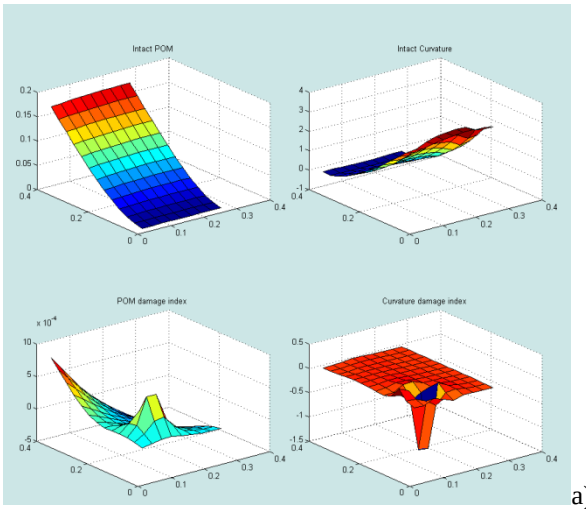

a)

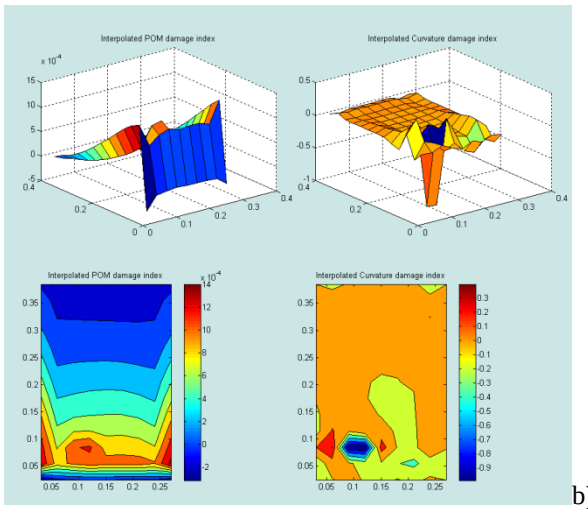

b)

Figure 117: Results. a) Classic POD. b) Smoothing technique

Once you have calculated everything you need, you can save all data with the appropriate button, a window will ask you to define the name and the folder, the format is .mat. If you want to manipulate one figure you can export it into a different window with the button 'Export current figure'. The procedure described above is still valid even if you use just damaged data. In this case don't use the intact data buttons. The data which will be saved consists obviously only in the damaged ones.

Below it is possible to find the main script for the GUI.

```
%This script creates the Graphic User Interface. The window is basically
%divided into two parts. On the left there are the buttons which call all
%the functions while on the right there is space for the graphics. The
%right part is itself divided into four parts. The first one contains two
%buttons, one for computing the POD and another one for calculating the
%curvature. The second part is dedicated to damaged data. More that the two
%buttons present in the previous part, there is also another one which
%calculates the GSM. The third part is dedicated to create the figures
%while the last one enables to export data and figures and to restart the
%analysis
clear all
close all

%%%%%%%%%%%%%%%%%%%%%%%%%%%%%%%%%%%%%%%%%%%%%%%%%%%%%%%%%%%%%%%%%%%%%%%%%%%
%Here I initialize the window so that it fits the whole monitor
f=figure('Units', 'normalized', 'position', [0 0 1 1], 'Color', [0.8 .9 .9]);
%%%%%%%%%%%%%%%%%%%%%%%%%%%%%%%%%%%%%%%%%%%%%%%%%%%%%%%%%%%%%%%%%%%%%%%%%%%



%%%%%%%%%%%%%%%%%%%%%%%%%%%%%%%%%%%%%%%%%%%%%%%%%%%%%%%%%%%%%%%%%%%%%%%%%%%
%This is the title fo the GUI
h_title=uicontrol('units', 'normalized', 'position', [.3 .94 .4 .05],...
    'style', 'text', 'String', 'POD analysis for the Macotech Project',...
    'Fontsize', 20, 'BackgroundColor', [0.4 .9 .9], 'FontWeight', 'bold');
%%%%%%%%%%%%%%%%%%%%%%%%%%%%%%%%%%%%%%%%%%%%%%%%%%%%%%%%%%%%%%%%%%%%%%%%%%%

%%%%%%%%%%%%%%%%%%%%%%%%%%%%%%%%%%%%%%%%%%%%%%%%%%%%%%%%%%%%%%%%%%%%%%%%%%%
%This insert the image of the University of Padua
logo=axes('units', 'normalized', 'position', [.9 .9 .1 .1]);
```

```
imshow('UNIPD_logo.png');

%%%%%%%%%%%%%%%%%%%%%%%%%%%%%%%%%%%%%%%%%%%%%%%%%%%%%%%%%%%%%%%%%%%%%%%%%%%%
%First part. Pristine case
%%%%%%%%%%%%%%%%%%%%%%%%%%%%%%%%%%%%%%%%%%%%%%%%%%%%%%%%%%%%%%%%%%%%%%%%%%%%
h_frame=uicontrol(f, 'style', 'frame', 'Units', 'normalized', 'position',...
    [.01 .78 .23 .17], 'ForegroundColor', 'black', 'BackgroundColor', [.8 .8
.4]);
h_text=uicontrol('style', 'text', 'units', 'normalized', 'position', [.0725
.90 .1 .03], 'String',...
    'Intact data', 'Fontsize', 10, 'BackgroundColor', 'white');
%This is the callback function for the button which performs the POD for
%the pristine case
start_cb=['global folder;'...
'folder=cd;'...
'[POM X1 X2 nr_nodi piastra nodo]=analisi_piastra();'...
'fun=POM;'...
'tit=''POM'';'...
'str_pop={''---''; ''---''}[83];'...
'val_pop=1;'...
'str_unit={''---''; ''---''};'...
'val_unit=1;'];
%This is the button which calls the POD
hstart=uicontrol('style', 'pushbutton', 'units', 'normalized',...
    'position', [0.05 0.85 0.15 0.05], 'Callback', start_cb,...
    'string', 'POD',  'Fontsize', 10, 'BackgroundColor', [.2 .5 .5]);
%%%%%%%%%%%%%%%%%%%%%%%%%%%%%%%%%%%%%%%%%%%%%%%%%%%%%%%%%%%%%%%%%%%%%%%%%%%%

%%%%%%%%%%%%%%%%%%%%%%%%%%%%%%%%%%%%%%%%%%%%%%%%%%%%%%%%%%%%%%%%%%%%%%%%%%%%
%This is the callback function for the button which performs the curvature
%calculation for the pristine case
curv_cb=['curvatura=calcolo_curvatura_bis2(POM, nr_nodi, X1, X2);'];

%Button which calls the curvature calculation
hcurv=uicontrol('style', 'pushbutton', 'units', 'normalized',...
    'position', [0.05 0.80 0.15 0.05], 'Callback', curv_cb,...
    'string', 'Calculate the curvature',  'Fontsize', 10, 'BackgroundColor',
[.2 .5 .5]);
%%%%%%%%%%%%%%%%%%%%%%%%%%%%%%%%%%%%%%%%%%%%%%%%%%%%%%%%%%%%%%%%%%%%%%%%%%%%

%%%%%%%%%%%%%%%%%%%%%%%%%%%%%%%%%%%%%%%%%%%%%%%%%%%%%%%%%%%%%%%%%%%%%%%%%%%%
h_frame=uicontrol(f, 'style', 'frame', 'Units', 'normalized', 'position',...
    [.01 .56 .23 .22], 'ForegroundColor', 'black', 'BackgroundColor', [.6 .6
.4]);
h_text=uicontrol('style', 'text', 'units', 'normalized', 'position', [.0725
.73 .1 .03], 'String',...
    'Damaged data', 'Fontsize', 10, 'BackgroundColor', 'white');
%%%%%%%%%%%%%%%%%%%%%%%%%%%%%%%%%%%%%%%%%%%%%%%%%%%%%%%%%%%%%%%%%%%%%%%%%%%%

%%%%%%%%%%%%%%%%%%%%%%%%%%%%%%%%%%%%%%%%%%%%%%%%%%%%%%%%%%%%%%%%%%%%%%%%%%%%
%This is the callback function for the button which performs the POD for
%the damaged case
start_d_cb=['global folder;'...
'folder=cd;'...
'[POM_d X1_d X2_d nr_nodi_d piastra_d nodo_d]=analisi_piastra();'...
'fun=POM_d;'...
'tit=''POM_d'';'...
'str_pop={''---''; ''---''};'...
'val_pop=1;'];
%Create the button which starts the POD
hstart_d=uicontrol('style', 'pushbutton', 'units', 'normalized',...
```

```
    'position', [0.05 0.68 0.15 0.05], 'Callback', start_d_cb,...
    'string', 'POD',  'Fontsize', 10, 'BackgroundColor', [.2 .7 .7]);
%%%%%%%%%%%%%%%%%%%%%%%%%%%%%%%%%%%%%%%%%%%%%%%%%%%%%%%%%%%%%%%%%%%%%%%%%%%



%%%%%%%%%%%%%%%%%%%%%%%%%%%%%%%%%%%%%%%%%%%%%%%%%%%%%%%%%%%%%%%%%%%%%%%%%%%
%This is the callback function for the button which performs the curvature
%calculation for the damaged case
curv_d_cb=['curvatura_d=calcolo_curvatura_bis(POM_d, nr_nodi_d, X1_d,
X2_d);'];

%Button which calls the curvature calculation
hcurv_d=uicontrol('style', 'pushbutton', 'units', 'normalized',...
    'position', [0.05 0.63 0.15 0.05], 'Callback', curv_d_cb,...
    'string', 'Calculate the damaged curvature',  'Fontsize', 10,
'BackgroundColor', [.2 .7 .7]);
%%%%%%%%%%%%%%%%%%%%%%%%%%%%%%%%%%%%%%%%%%%%%%%%%%%%%%%%%%%%%%%%%%%%%%%%%%%

%%%%%%%%%%%%%%%%%%%%%%%%%%%%%%%%%%%%%%%%%%%%%%%%%%%%%%%%%%%%%%%%%%%%%%%%%%%
%This is the callback function which performs the interpolation
interp_d_cb=['[POM_interpolato]=GSM(POM_d, piastra_d, nodo_d, X1_d, X2_d,
nr_nodi_d);'...
    '[curvatura_interpolata]=GSM(curvatura_d, piastra_d, nodo_d, X1_d, X2_d,
nr_nodi_d);'];

%This is the button for the interpolation
hinterp=uicontrol('style', 'pushbutton', 'units', 'normalized',...
    'position', [.0725 .58 .10 .05], 'string', 'GSM', 'CallBack',
interp_d_cb,  'Fontsize', 10, 'BackgroundColor', [.2 .7 .7]);
%%%%%%%%%%%%%%%%%%%%%%%%%%%%%%%%%%%%%%%%%%%%%%%%%%%%%%%%%%%%%%%%%%%%%%%%%%%

%%%%%%%%%%%%%%%%%%%%%%%%%%%%%%%%%%%%%%%%%%%%%%%%%%%%%%%%%%%%%%%%%%%%%%%%%%%
%This are four clear axes
plot1=axes('units', 'normalized', 'position', [.30 .50 .30 .30]);
plot2=axes('units', 'normalized', 'position', [.65 .50 .30 .30]);
plot3=axes('units', 'normalized', 'position', [.30 .07 .30 .30]);
plot4=axes('units', 'normalized', 'position', [.65 .07 .30 .30]);
%%%%%%%%%%%%%%%%%%%%%%%%%%%%%%%%%%%%%%%%%%%%%%%%%%%%%%%%%%%%%%%%%%%%%%%%%%%

%%%%%%%%%%%%%%%%%%%%%%%%%%%%%%%%%%%%%%%%%%%%%%%%%%%%%%%%%%%%%%%%%%%%%%%%%%%
%Here I put the commands for the graphics
hframe_4=uicontrol('style', 'frame', 'units', 'normalized', 'position',...
    [.01 .18 .23 .38], 'ForegroundColor', 'black', 'BackgroundColor', [.8 .8
.5]);

%Here I insert a list with all the possible variables to be plotted. It
%contains POMs, curvatures and related damage indices
list_cb=['str=get(h_list, ''String'');'...
    'val = get(h_list,''Value'');'...
    'switch str{val};'...
        'case ''Intact POM'';'...
            'fun=POM;'...
            'tit=''Intact POM'';'...
        'case ''Damaged POM'';'...
            'fun=POM_d;'...
            'tit=''Damaged POM'';'...
        'case''Interpolated POM'';'...
            'fun=POM_interpolato;'...
            'tit=''Interpolated POM'';'...
```

```
        'case ''Intact Curvature'';'...
            'fun=curvatura;'...
            'tit=''Intact Curvature'';'...
        'case ''Damaged Curvature'';'...
            'fun=curvatura_d;'...
            'tit=''Damaged Curvature'';'...
        'case ''Interpolated Curvature'';'...
            'fun=curvatura_interpolata;'...
            'tit=''Interpolated Curvature'';'...
        'case ''POM damage index'';'...
            'if max(max(abs(POM-POM_d)))<max(max(abs(POM)));'...
                'fun=POM-POM_d;'...
                'else;'...
                'fun=POM+POM_d;'...
            'end;'...
            'tit=''POM damage index'';'...
        'case ''Curvature damage index'';'...
             'if max(max(abs(curvatura-
curvatura_d)))<max(max(abs(curvatura)));'...
                'fun=curvatura-curvatura_d;'...
            'else;'...
                'fun=curvatura+curvatura_d;'...
             'end;'...
             'tit=''Curvature damage index'';'...
         'case ''Interpolated POM damage index'';'...
            'if max(max(abs(POM_interpolato-
POM_d)))<max(max(abs(POM_interpolato)));'...
                'fun=POM_interpolato-POM_d;'...
            'else;'...
                'fun=POM_interpolato+POM_d;'...
            'end;'...
            'tit=''Interpolated POM damage index'';'...
         'case ''Interpolated Curvature damage index'';'...
             'if max(max(abs(curvatura_interpolata-
curvatura_d)))<max(max(abs(curvatura_interpolata)));'...
                'fun=curvatura_interpolata-curvatura_d;'...
            'else;'...
                'fun=curvatura_interpolata+curvatura_d;'...
             'end;'...
             'tit=''Interpolated Curvature damage index'';'...
    'end;'];
h_list=uicontrol('style', 'list', 'String',...
    {'Intact POM';'Damaged POM'; 'Interpolated POM'; 'Intact Curvature';...
    'Damaged Curvature'; 'Interpolated Curvature'; 'POM damage index';...
    'Curvature damage index'; 'Interpolated POM damage index';...
    'Interpolated Curvature damage index'},...
    'units', 'normalized', 'position', [.02 .33 .1 .16], 'CallBack', list_cb,
'Fontsize', 10, 'BackgroundColor', 'white');
hstatic_list=uicontrol('style', 'text', 'string', 'Choose what you want to
plot',...
    'units','normalized', 'position',  [.02 .49 .1 .05], 'Fontsize', 10,
'BackgroundColor', 'white');
%This is a pop up menu which allows to choose which unit were used in the
%simulation. It is useful for graphic purposes
unit_cb=['str_unit=get(h_unit, ''String'');'...
    'val_unit = get(h_unit,''Value'');'...
    'switch str_unit{val_unit};'...
    'case ''---'';'...
    'msgbox(''Choose the units'', ''Warning'', ''error'');'...
    'case ''m'';'...
    'contourfx=1500;'...
    'change=0.01;'...
```

```
    'case ''cm'';'...
    'contourfx=15;'...
    'change=1;'...
    'case ''mm'';'...
    'contourfx=1.5;'...
    'change=10;'...
    'end;'...
    'integer=exist(''POM'');'...
    'if integer==0;'...
    'X1=X1_d;'...
    'X2=X2_d;'...
    'nr_nodi=nr_nodi_d;'...
    'end;'...
    'set(plot1, ''units'', ''centimeters'');'...
    'conf=get(plot1, ''position'');'...
    'set(plot1, ''units'', ''normalized'');'...
    'if abs(max(X1)-min(X1))*change>conf(3);'...
    'contourfx=contourfx/2.5;'...
    'end;'];
h_unit_text=uicontrol('style', 'text', 'units', 'normalized', 'position',...
    [.02 .29 .1 .03], 'string', 'Choose the units', 'Fontsize', 10,
'BackgroundColor', 'white');

h_unit=uicontrol('style', 'popup', 'units', 'normalized', 'position',...
    [.02 .24 .1 .05], 'string' ,{'---', 'm', 'cm', 'mm'}, 'Fontsize', 10,...
    'Callback', unit_cb);

%callback function for the popup button
pop_cb=['str_pop=get(hpop, ''String'');'...
    'val_pop=get(hpop, ''Value'');'];
%This popup menu allows to choose which type of graphic is going to be
%displayed
hpop=uicontrol('style', 'popup', 'String', {'---'; 'Surf'; 'Mesh';
'Contourf'},...
    'units', 'normalized', 'position', [.13 .44 .1 .05], 'Fontsize', 10,
'CallBack', pop_cb);

hstatic_pop=uicontrol('style', 'text', 'string', 'Choose the type of
plot',...
    'units','normalized', 'position',  [.13 .49 .1 .05], 'Fontsize', 10,
'BackgroundColor', 'white');
%Callback function for the graphic
plot_cb=['integer=exist(''POM'');'...
    'if integer==0;'...
    'X1=X1_d;'...
    'X2=X2_d;'...
    'nr_nodi=nr_nodi_d;'...
    'end;'...
    'pos=get(gca, ''position'');'...
    'set(gca, ''position'', [pos(1) pos(2) .3 .3]);'...
    'X1ord=sort(X1);'...
    'X2ord=sort(X2);'...
    'latoy=find(X2ord==max(X2ord));'...
    'latox=find(X1ord==max(X1ord));'...
    'X_=X1ord(1:max(size(latox)):nr_nodi);'...
    'Y_=X2ord(1:max(size(latoy)):nr_nodi);'...
    'griglia=struct(''X'', {X_}, ''Y'', {Y_});'...
    '[X Y]=meshgrid(X_,Y_);'...
    'switch str_pop{val_pop};'...
    'case ''---'';'...
    'msgbox(''Choose the type of graphic'', ''Warning'', ''error'');'...
```

```
    'case ''Surf'';'...
    'surf(X, Y, fun'');'...
    'title(tit);'...
    'case ''Mesh'';'...
    'mesh(X, Y, fun'');'...
    'title(tit);'...
    'case ''Contourf'';'...
    'contourf(X, Y, fun'');'...
    'colorbar(''location'', ''eastoutside'');'...
    'axis fill;'...
    'title(tit);'...
    'ratio=abs((max(X1)-min(X1))/(max(X2)-min(X2)));'...
    'set(gca, ''units'', ''pixels'');'...
    'set(gcf, ''units'', ''pixels'');'...
    'ax=get(gca, ''position'');'...
    'fi=get(gcf, ''position'');'...
    'dim=get(0, ''screensize'');'...
    'axnew_x=abs(max(X1)-min(X1))*contourfx/1.7;'...
    'axnew_y=axnew_x/ratio;'...
    'set(gca, ''position'', [ax(1) ax(2) axnew_x axnew_y]);'...
    'set(gca, ''units'', ''normalized'');'...
    'set(gcf, ''units'', ''normalized'');'...
    'end;'];
%Graphic button
hplot=uicontrol('style', 'pushbutton', 'units', 'normalized',...
    'position', [.13 .33 .1 .10], 'string', 'Plot result',...
    'Callback', plot_cb,  'Fontsize', 15, 'BackgroundColor', [.4 .7 .7]);

%Callback function fo the slider
slider_cb=['az=get(hslider, ''Value'');'...
    'view(az,30);'];

%slider
hslider=uicontrol('style', 'slider', 'units', 'normalized', 'position',...
    [.13 .26 .1 .03], 'max', 10, 'min', -80, 'Value', -37.5, 'CallBack',
slider_cb);
%hslider2=uicontrol('style', 'slider', 'units', 'normalized', 'position',
[.75 .58 .1 .02], 'max', 10, 'min', -80, 'CallBack', slider_cb);
%hslider3=uicontrol('style', 'slider', 'units', 'normalized', 'position',
[.35 .03 .1 .02], 'max', 10, 'min', -80, 'CallBack', slider_cb);
%hslider4=uicontrol('style', 'slider', 'units', 'normalized', 'position',
[.75 .03 .1 .02], 'max', 10, 'min', -80, 'CallBack', slider_cb);

%Explanation of the aim of the slider
hstatic_slider=uicontrol('style', 'text', 'string', 'Change azimut',
'units',...
    'normalized', 'position',  [.13 .29 .1 .03], 'ForegroundColor', 'black',
'Fontsize', 10, 'BackgroundColor', 'white');

%Fourth part, saving data
h_frame_3=uicontrol(f, 'style', 'frame', 'Units', 'Normalized',...
    'position', [.01 .07 .23 .14], 'ForegroundColor', 'black',...
    'BackgroundColor', [.3 .3 .3]);
export_figure_cb=['g=get(gca, ''position'');'...
    'f=gca;'...
    't=figure(''units'', ''normalized'', ''position'', [0 0 1 1]);'...
    'newax=copyobj(f,t);'...
    'set(newax, ''units'', ''normalized'', ''position'', [.2 .2 2*g(3)
2*g(4)]);'];
hexport_figure=uicontrol('style', 'pushbutton', 'units', 'normalized',...
```

```
    'position', [.03 .09 .1 .05], 'string', 'Export current figure',
'Callback', export_figure_cb,  'Fontsize', 10,  'BackgroundColor', [.6 .7
.7]);
save_data_cb=['if integer==1;'...
                'uisave({''POM'', ''POM_d'', ''curvatura'', ''curvatura_d'',
''POM_interpolato'', ''curvatura_interpolata'', ''griglia''}, ''data'');'...
              'elseif integer==0;'...
                'uisave({''POM_d'', ''curvatura_d'', ''POM_interpolato'',
''curvatura_interpolata'', ''griglia''}, ''data'');'...
              'end;'];
hsave_data=uicontrol('style', 'pushbutton', 'units', 'normalized',...
    'position', [.03 .14 .1 .05], 'string', 'Save all data', 'Callback',
save_data_cb,  'Fontsize', 10,  'BackgroundColor', [.6 .7 .7]);

%restart button which deletes all the variable and goes back to the initial
%folder
clear_cb=['cd (folder);'...
    'clearvars -except -regexp ^h cb$ ^logo ^plot;'...
    'cla (plot1, ''reset'');'...
    'cla (plot2, ''reset'');'...
    'cla (plot3, ''reset'');'...
    'cla (plot4, ''reset'');'];
h_clear=uicontrol('units', 'normalized', 'position', [.13 .09 .09 .1],...
    'style', 'pushbutton', 'string', 'RESTART', 'Fontsize', 15, 'CallBack',
clear_cb,...
    'ForegroundColor', 'red');
```

Appendix 7: Drop tower

Experimental analyses on composite plates were conducted using a drop tower. The specific experimental setup was formed by an Impact test facility provided by Instron, a data logger and a PC. It can be seen in Figure 118. The impact test facility consists of a drop tower which is divided into two different parts. The upper one consists in the actual dropping utilities. A frame formed by two rails holds the magnetic support for the impactor. It can be moved in the vertical direction thanks to the two rails. At the top of the tower two springs are present. Their aim is to increase the impact velocity up to 24 m/s. when the impact occurs, the magnetic force is released and the impactor is free to fall on the specimen. A servomechanism is located at the bottom of this part. It is automatically activated after the impact occurs, in order to prevent multiple impacts on the same specimen. The lower part of the drop tower consists on the chamber in which the specimen is placed. To support this, different sets of frames can be used, depending on the type of specimen under exam. In this case, an extendible tower was used. This allowed the specimen to be moved up, in order to minimize the impact height. Although the machine is configured to reach a minimum height of 30 mm, with the specimen available the lowest one achievable was 33 mm.

Figure 118: Impact facility instrumentation.

The preparation of a test can be divided in different parts. First of all the specimens must be firmly constrained on an appropriate fixture. They must be later placed on the top of the adjustable frame and finally inside the impact chamber. The system can be seen in Figure 119. The impact chamber provides a

hole to bring outside all the cables attached to the plate, in order to connect them to the data logger. The fixture consists of two heavy steel plates, which guarantee that the plate is not moving or rebounding when the impact occurs. The bottom plate of the fixture was fixed to the tower with four screws. The two part of the fixture were connected together with four screws and two pins which have the aim of placing the specimen in the correct position.

The second step of the experiment consisted in preparing a configuration file which is used by the machine to perform the test. This files contains information about the specimen (material, dimensions, thickness), about the energy of the impact (mass, height), about the impactor (dimension, radius) and about the acquisition of data. In particular this part is important to obtain reliable results. An example of the window in which this step is performed is given in Figure 120.

The execution of a test is then relatively simple. Once the user opens the test execution window, the parameters for the impact, which were defined in the previous step, must be loaded. Then the impact can start. Just before releasing the impactor, the software asks to position correctly a photocell, Figure 121, which is used to both trigger the acquisition box and the rebounding mechanism, which prevents multiple impacts on the plate.

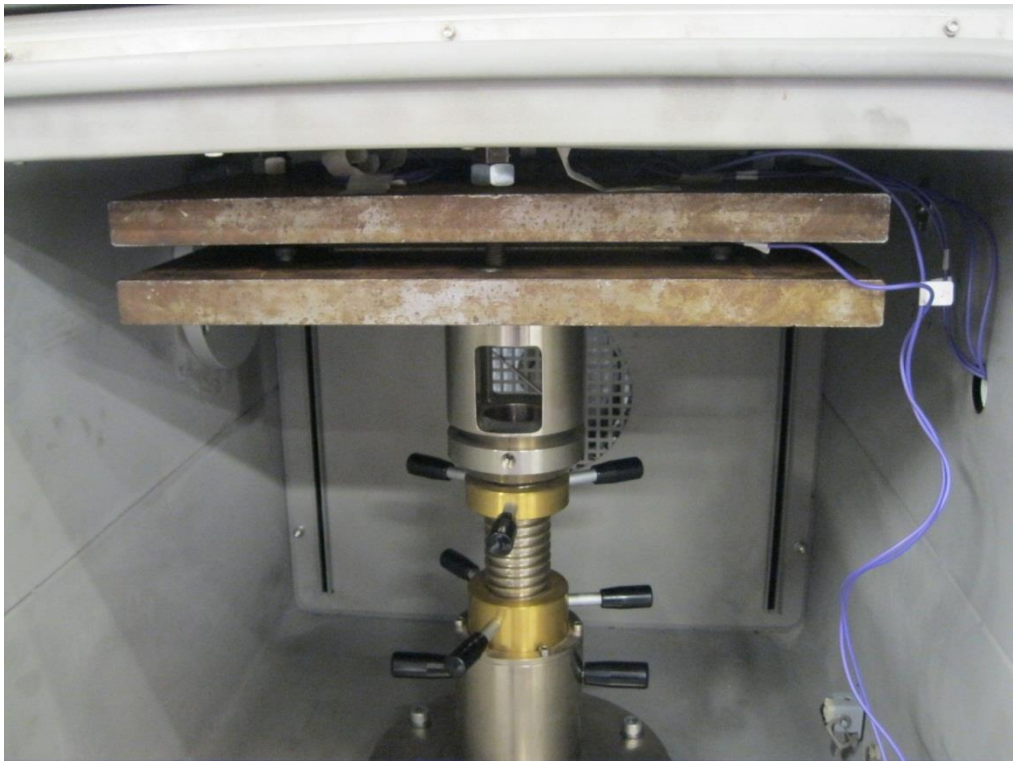

Figure 119: Impact configuration, adjustable tower with fixture and plate on top.

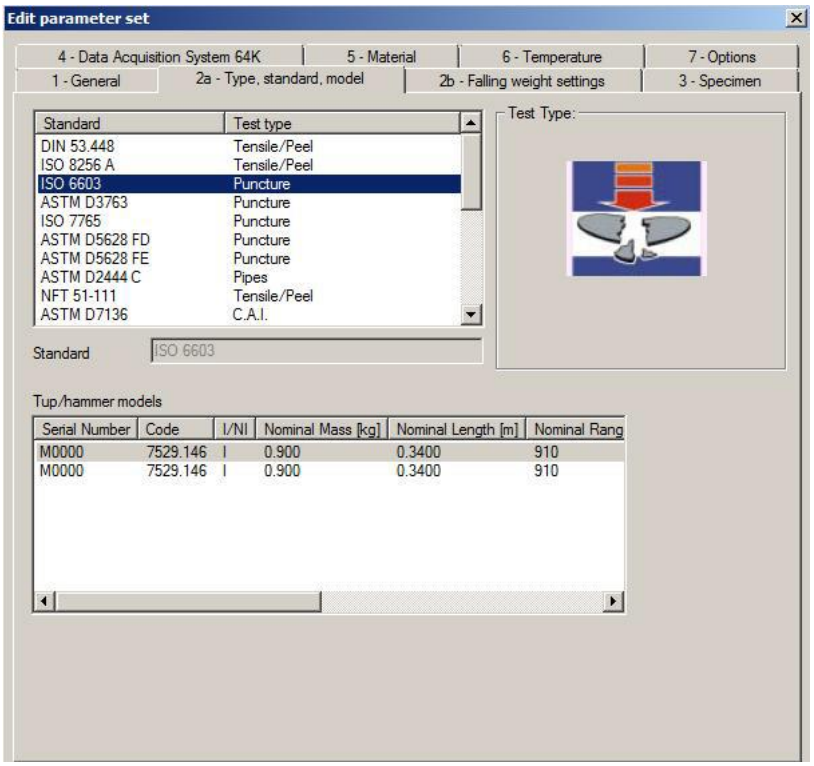

Figure 120: Example of configuration window.

Figure 121: Photocell.

Appendix 8: Examples of force reconstruction

In this appendix some force reconstruction results for the system described in Section are presented. While in that Section the strains of the plate were used to determine the transfer function of the system, in this case the displacements are considered. The results are very similar and indicate that in this case the method can reconstruct accurately the force regardless of the sensors which are available. In all the figures presented the reconstruction technique works properly and the error between the actual and reconstructed force is very small. Figure 122 to Figure 124 can be compared to the ones present in Section 6.5.6 (Figure 86 to Figure 88). The following figures refer to other reconstruction cases, using different sets. In general throughout all the cases which were examined the results are similar to the one proposed. For the error in the force reconstruction, refer to Figure 89. No substantial differences could be found in the errors using the two types of data.

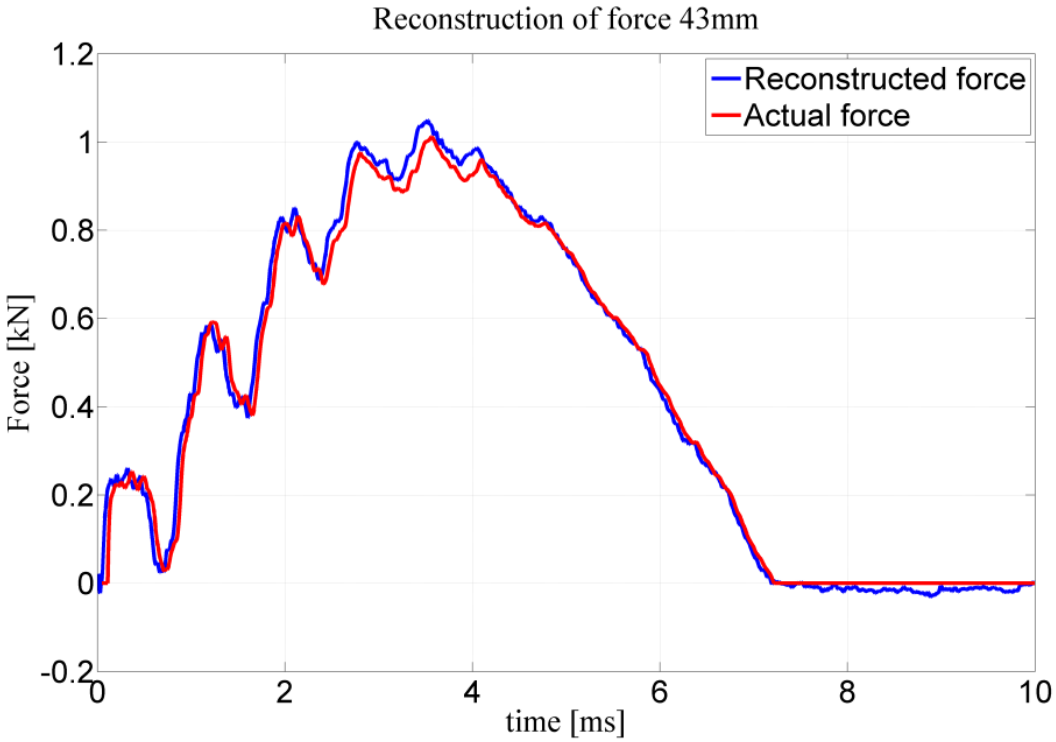

Figure 122: Results using set 1, for the 43 case.

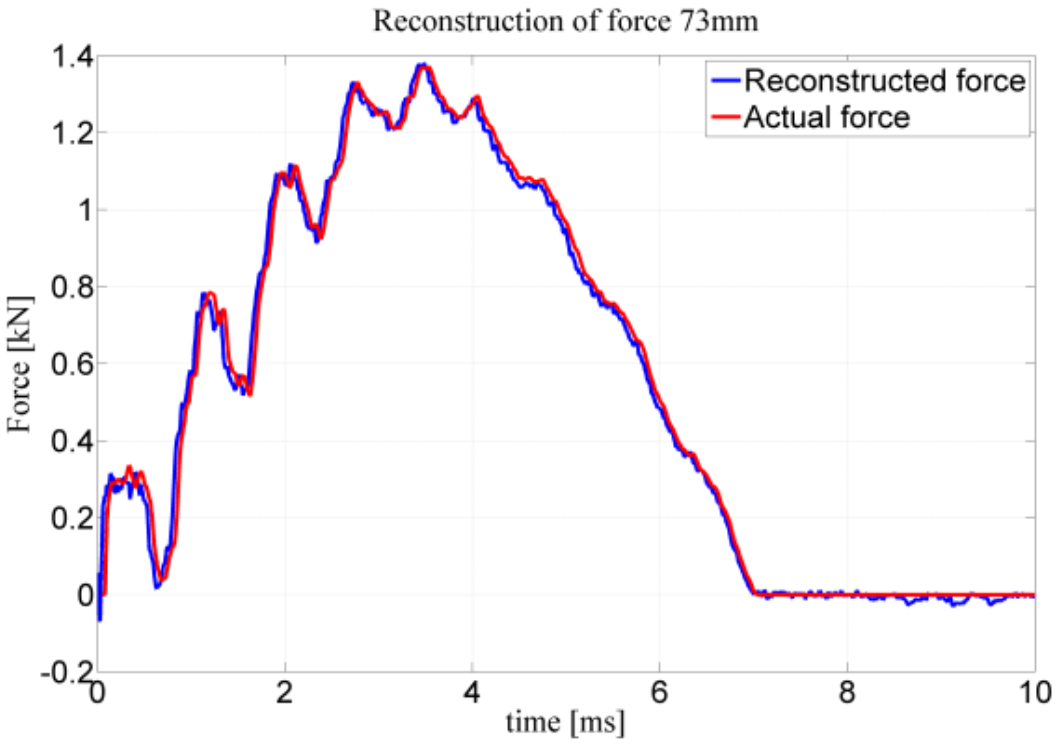

Figure 123: Results using set 1, for the 73 case

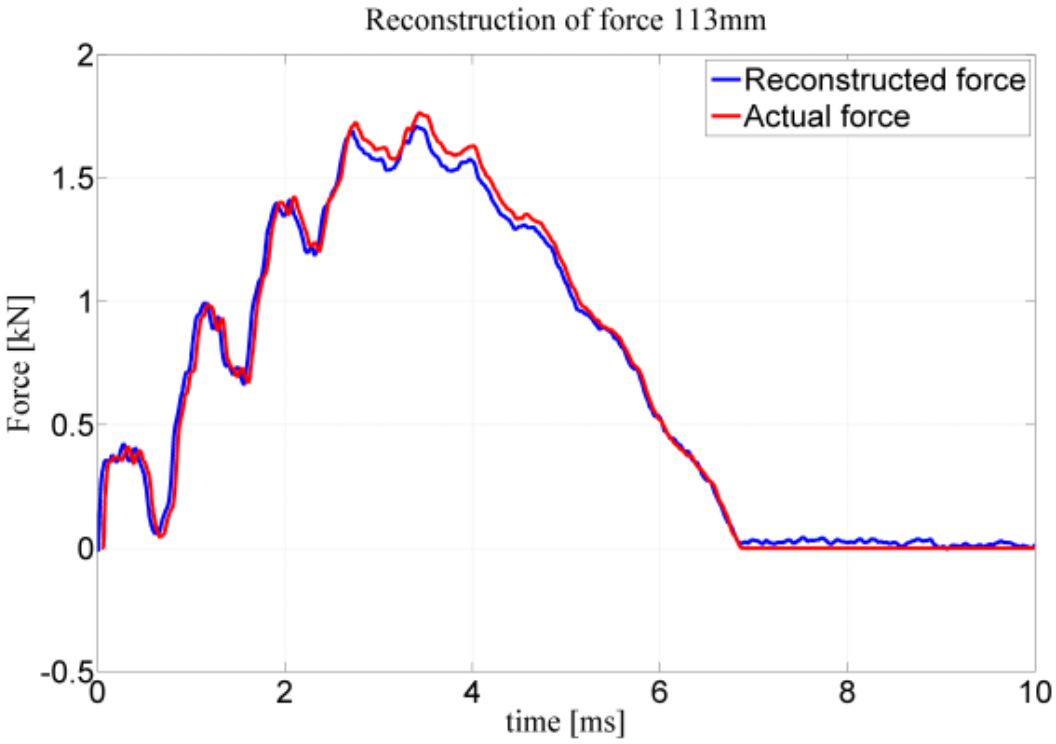

Figure 124: Results using set 1, for the 113 case.

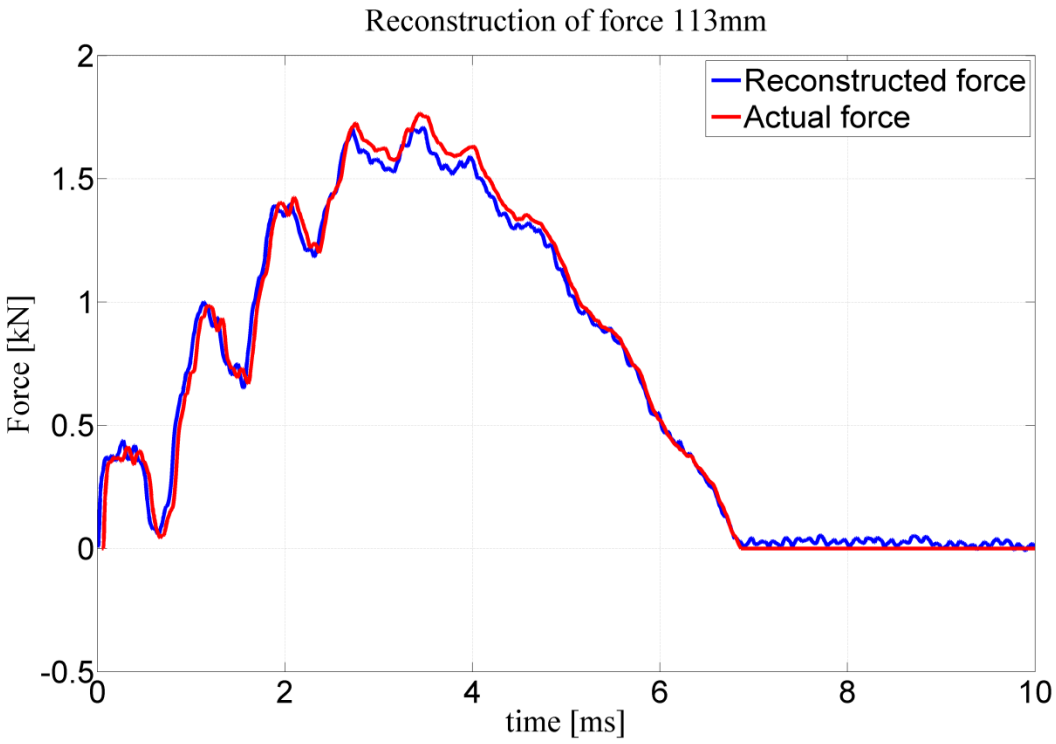

Figure 125: Result using set 2, for the 113 case

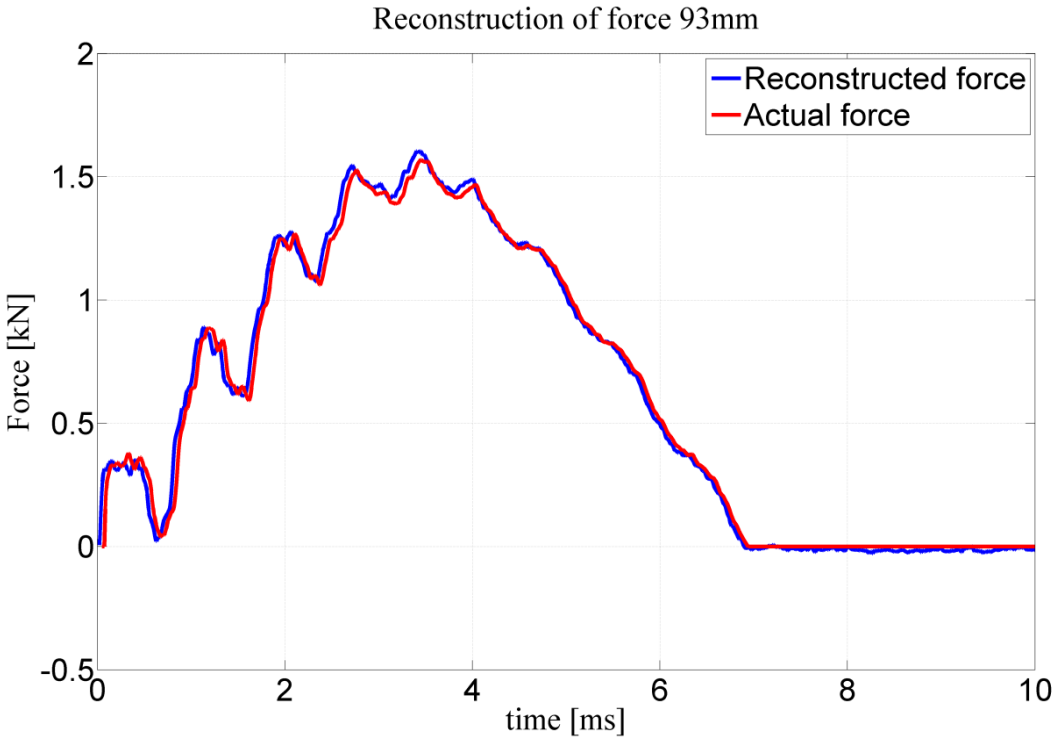

Figure 126: Result using set 4, for the 93 case.